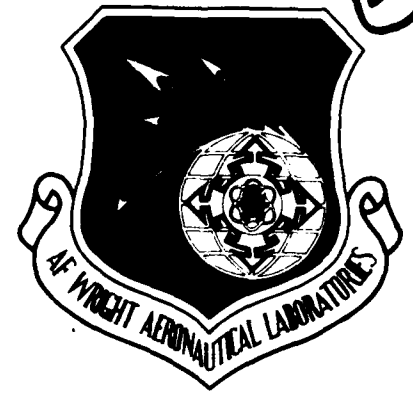


2018 FILE COPY

2



AFWAL-TR-88-1071

**PICOSECOND ELECTROOPTIC INVESTIGATIONS  
OF INTEGRATED CIRCUITS**

Edward L. Ginzton Laboratory  
W. W. Hansen Laboratories of Physics  
Stanford University  
Stanford, CA 94305

January 1989

Final Report for Period September 1986 - December 1987

Approved for public release; distribution is unlimited.

**SDTICD**  
ELECTE  
JUN 13 1989  
HGS

**AVIONICS LABORATORY  
AIR FORCE WRIGHT AERONAUTICAL LABORATORIES  
AIR FORCE SYSTEMS COMMAND  
WRIGHT-PATTERSON AIR FORCE BASE, OHIO 45433-6543**

AD-A209 134

89-6-13-060

UNCLASSIFIED

SECURITY CLASSIFICATION OF THIS PAGE

## REPORT DOCUMENTATION PAGE

Form Approved  
OMB No. 0704-0188

1a. REPORT SECURITY CLASSIFICATION Unclassified			1b. RESTRICTIVE MARKINGS NONE			
2a. SECURITY CLASSIFICATION AUTHORITY			3. DISTRIBUTION/AVAILABILITY OF REPORT Approved for public release; distribution is unlimited			
2b. DECLASSIFICATION/DOWNGRADING SCHEDULE			4. PERFORMING ORGANIZATION REPORT NUMBER(S)			
4. PERFORMING ORGANIZATION REPORT NUMBER(S)			5. MONITORING ORGANIZATION REPORT NUMBER(S) AFWAL-TR-88-1071			
6a. NAME OF PERFORMING ORGANIZATION Stanford University		6b. OFFICE SYMBOL (If applicable)		7a. NAME OF MONITORING ORGANIZATION WRDC/ELET Electronic Technology Laboratory		
6c. ADDRESS (City, State, and ZIP Code) Edward L. Ginzton Laboratory Stanford, CA 94305			7b. ADDRESS (City, State, and ZIP Code) Wright-Patterson AFB, OH 45433-6543			
8a. NAME OF FUNDING/SPONSORING ORGANIZATION		8b. OFFICE SYMBOL (If applicable)		9. PROCUREMENT INSTRUMENT IDENTIFICATION NUMBER Contract F33615-86-C-1126		
8c. ADDRESS (City, State, and ZIP Code)			10. SOURCE OF FUNDING NUMBERS			
			PROGRAM ELEMENT NO. 61101F	PROJECT NO. ILIR	TASK NO. A6	WORK UNIT ACCESSION NO. 02
11. TITLE (Include Security Classification) Picosecond Electrooptic Investigations of Integrated Circuits						
12. PERSONAL AUTHOR(S) Auld, B.A., Bloom, D.M., Freeman, J.L., Majidi-Ahy, R., Rodwell, M.J.W., Weingarten, K.J.						
13a. TYPE OF REPORT Final		13b. TIME COVERED FROM 12/86 TO 2/11/87		14. DATE OF REPORT (Year, Month, Day) January 1989		15. PAGE COUNT 311 pages
16. SUPPLEMENTARY NOTATION						
17. COSATI CODES			18. SUBJECT TERMS (Continue on reverse if necessary and identify by block number)			
FIELD	GROUP	SUB-GROUP	Electrooptic Sampling E/O			
09	03		GaAs Integrated Circuit Testing E/O Probing			
			E/O Sampling			
19. ABSTRACT (Continue on reverse if necessary and identify by block number) The continuing development of integrated electronic circuits operating to 110 GHz, and the development of digital circuits with toggle rates above 20 GHz, has given rise to a commensurate need for instrumentation capable of diagnosing the internal operation of these circuits. These analog microwave and millimeter-wave integrated circuits are critical to the development of compact, low-cost, and frequency agile radar and communication systems for military applications, while the ultrafast digital technologies address the need in military electronic systems to rapidly acquire, digitize, and process very large amounts of data. However, current electronic instrumentation falls far short of the need for internal high-frequency probing capability without severely disturbing circuit operation. Direct electrooptic sampling provides extremely high bandwidth while permitting non-invasive examination of internal node voltages of both digital and microwave GaAs integrated circuits. Characterization of this probe in terms of accuracy, repeatability, and invasiveness, as well as extension of its probing capability to the millimeter regime, is critical to its continued						
20. DISTRIBUTION/AVAILABILITY OF ABSTRACT <input checked="" type="checkbox"/> UNCLASSIFIED UNLIMITED <input type="checkbox"/> SAME AS RPT. <input type="checkbox"/> DTIC USERS				21. ABSTRACT SECURITY CLASSIFICATION Unclassified		
22a. NAME OF RESPONSIBLE INDIVIDUAL Lutz J. Micheel			22b. TELEPHONE (Include Area Code) (513) 255-8642		22c. OFFICE SYMBOL WRDC/ELET	

DD Form 1473, JUN 86

Previous editions are obsolete.

SECURITY CLASSIFICATION OF THIS PAGE  
Unclassified

19. Abstract Continued:

viability as a powerful diagnostic tool.

This report documents work on the 15-month contract in Picosecond Electrooptic Investigations of Integrated Circuits performed at Stanford University. Specific program tasks include: 1) Increase of Electrooptic bandwidth; 2) Improvements to Noise Performance and REpeatability; 3) Evaluation of Spatial Resolution and Signal Crosstalk; 4) Voltage Calibration; 5) Evaluation of the Invasiveness of Electrooptic Sampling; 6) Electrooptic Vector Measurements; and 7) Full Wafer Probing.

This contract was funded under the Independent Laboratory In-House Research (ILIR) project. The work reported and related research provide the basis for setting up in 1989 the Electro-Optic Research Laboratory of the Electronic Technology Laboratory (EL), Wright Research And Development Center (AFSC).



<b>Accession For</b>	
NTIS GRA&I	<input checked="" type="checkbox"/>
DTIC TAB	<input type="checkbox"/>
Unannounced	<input type="checkbox"/>
Justification	
By _____	
Distribution/	
Availability Codes	
Dist	Avail and/or Special
A-1	

Edward L. Ginzton Laboratory  
W. W. Hansen Laboratories of Physics  
Stanford University  
Stanford, California 94305

Final Report  
to  
Wright-Patterson Air Force Base  
on  
A Program of Research  
in  
**Picosecond Electrooptic Investigations  
of Integrated Circuits**

Contract #F33615-86-C-1126

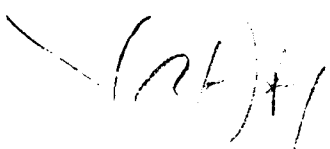
Principal Investigator:  
David M. Bloom  
Associate Professor of Electrical Engineering



## Summary

The continuing development of integrated electronic circuits operating to 110 GHz, and the development of digital circuits with toggle rates above 20 GHz, has given rise to a commensurate need for instrumentation capable of diagnosing the internal operation of these circuits. These analog microwave and millimeter-wave integrated circuits are critical to the development of compact, low-cost, and frequency agile radar and communication systems for military applications, while the ultrafast digital technologies address the need in military electronic systems to rapidly acquire, digitize, and process very large amounts of data. However, current electronic instrumentation falls far short of the need for internal, high-frequency probing capability without severely disturbing circuit operation. Direct electrooptic sampling provides extremely high bandwidth while permitting non-invasive examination of internal node voltages of both digital and microwave GaAs integrated circuits. Characterization of this probe in terms of accuracy, repeatability, and invasiveness, as well as extension of its probing capability to the millimeter regime, is critical to its continued viability as a powerful diagnostic tool.

This report documents work on the 15-month contract in Picosecond Electrooptic Investigations of Integrated Circuits performed at Stanford University. Specific program tasks include: 1) Increase of Electrooptic bandwidth; 2) Improvements to Noise Performance and Repeatability; 3) Evaluation of Spatial Resolution and Signal Crosstalk; 4) Voltage Calibration; 5) Evaluation of the Invasiveness of Electrooptic Sampling; 6) Electrooptic Vector Measurements; and 7) Full Wafer Probing.



# **Program Objectives**

## **1 Overall Program Objectives**

Recently, electrooptical probing techniques for GaAs devices and integrated circuits with picosecond resolution have evolved. These techniques must be further developed in order to make them suitable for practical and reproducible investigations of advanced digital and microwave integrated circuits (ICs) that are needed in future Air Force systems. The objective of this effort is to develop a practical and reproducible picosecond electrooptic measurement system with at least 100 GHz bandwidth that is suitable for measuring all types of ultra high speed GaAs integrated circuits, including ultra high speed digital ICs, monolithic microwave ICs and mm-wave ICs.

## **2 Specific Program Tasks**

### **Increase of Electrooptic Measurement Bandwidth**

The bandwidth of the electrooptic sampler shall be improved to at least 100 GHz, in part by using a new mode-locker laser head that should reduce the laser pulse width by 30 percent. The feasibility of further bandwidth improvements shall be investigated using enhanced timing stabilization feedback loops of feed-forward methods.

### **Improvements to Noise Performance**

Excess amplitude noise can seriously degrade the electrooptic sampler's sensitivity, accuracy, and repeatability. Several approaches to reduce such excess noise shall be investigated, and, if successful, implemented. These approaches shall include at least the following: an optical Faraday isolator between the laser and pulse compressor; employing polarization preserving optical fiber in the pulse compressor; and implementing a differential photodiode receiver using a Faraday isolator.

### **Evaluation of Signal Crosstalk, Spatial Resolution**

Since the focused optical probe beam has a finite cross-section comparable in diameter to the smallest IC metal conductor widths, the electrooptic measurement may be influenced by the potential of adjacent conductors. Such crosstalk and other effects resulting from the

non-zero probe beam diameter shall be investigated. Special test devices shall be designed and fabricated for this investigation that resemble MSI, LSI, and MMIC geometries.

### **Voltage Calibration**

In order to verify the results of the electrooptic measurement and to prove reproducibility, means of absolute voltage calibration shall be investigated, and if feasible, implemented. The goal is a calibration accuracy of better than 5 %.

### **Evaluation of the Invasiveness of Electrooptic Sampling**

A small, optically induced voltage has been observed on GaAs microstrips, and digital IC's exhibited reduced noise margins at high probe beam intensities. The contractor shall investigate the invasiveness of the electrooptic sampling method and model it in terms of optically induced parasitics. Particular attention shall be paid to the causes of optical beam interaction with the IC, e.g., deep-level absorption due to EL2 or impurity doping, and two-photon absorption at high beam energies.

### **Electrooptic Vector Measurements**

Initially, electrooptic probing had been implemented with only a time-waveform mode. However, MMIC and mm-wave IC investigations often require a vector measurement mode. Under this task a vector measurement mode shall be investigated, and if feasible, implemented.

### **Millimeter-wave Wafer Probing**

In order to make the electrooptic measurement approach as practical as possible, the contractor shall study the feasibility of combining it with a high performance full wafer tester such as the Cascade Microtech Model 42 probe station. If shown feasible, the wafer probing configuration shall be documented, but no implementation will be attempted under this program.

# TABLE OF CONTENTS

Section	Page
<b>1. Background</b> .....	1-1
1.1 Motivation .....	1-1
1.2 Review of RF Test Methods .....	1-3
1.2.1 Conventional RF Test Methods.....	1-3
1.2.2 Non-Electrical, Novel Test Techniques.....	1-5
1.3 Direct Electrooptic Sampling in GaAs IC's.....	1-13
1.3.1 Electrooptic Voltage Probing in a GaAs IC Substrate.....	1-13
1.3.2 Probing Geometries in GaAs IC's.....	1-18
1.4 Signal Recovery using Repetitive Sampling.....	1-22
1.4.1 Harmonic Mixing.....	1-23
1.4.2 Equivalent-time Sampling .....	1-28
1.5 Conclusion .....	1-30
References for Section 1.....	1-31
<b>2. Increase of Electrooptic Measurement Bandwidth</b> .....	2-1
2.1 Optical Pulsewidth.....	2-1
2.1.1 Pulse-width reduction.....	2-3
2.2 Timing Jitter.....	2-6
2.3 Transit time.....	2-8
2.4 Effective Receiver Response .....	2-9
2.5 Conclusion .....	2-10
References for Section 2.....	2-10
<b>3. Noise in the Electrooptic Sampler</b> .....	3-1
3.1 Sensitivity and Noise-limited Detection.....	3-1
3.2 Noise sources in the Electrooptic Sampler.....	3-1
3.2.1 Shot Noise.....	3-1
3.2.2 Excess Noise Sources.....	3-2
3.3 Noise Reduction In the Electrooptic Sampler .....	3-9



<b>Section</b>	<b>Page</b>
3.3.1 Fiber Temperature Stabilization.....	3-10
3.3.2 Active Amplitude Stabilization.....	3-10
3.3.3 Faraday Isolator.....	3-12
3.3.4 Ratio Detection.....	3-12
3.3.5 Differential Detection.....	3-13
3.3.6 Optical Biasing.....	3-16
3.4 Conclusion .....	3-18
References for Section 3.....	3-19
<b>4. Spatial Signal Resolution and Crosstalk.....</b>	<b>4-1</b>
4.1 Theoretical tools .....	4-1
4.2 Experimental factors.....	4-3
4.2.1 Noise and stability.....	4-3
4.2.2 Sensitivity to Fabrication .....	4-4
4.2.3 Focusing and Aperturing .....	4-4
4.2.4 Acoustic waves .....	4-5
4.2.5 Fabrication of test structures .....	4-7
4.3 Spatial Resolution .....	4-7
4.3.1 Focused Gaussian Beam Effects.....	4-9
4.3.2 Spot Size Crosstalk.....	4-11
4.4 Backplane Crosstalk.....	4-16
4.4.1 Overview .....	4-16
4.4.2 Coplanar Waveguide Transmission Lines .....	4-19
4.4.3 Digital Geometries.....	4-21
4.4.4 Crosstalk Reduction Mechanisms.....	4-32
4.5 Absolute Signal Calibration .....	4-33
4.6 Conclusion .....	4-37
<b>5. Probe Invasiveness.....</b>	<b>5-1</b>
5.1 Introduction .....	5-1
5.2 Absorption Mechanism .....	5-1
Schottky Diodes .....	5-3
5.3 Perturbations to GaAs MESFET's .....	5-8

<b>Section</b>	<b>Page</b>
5.4 Beam Propagation to an Active Device.....	5-11
5.5 Conclusion .....	5-14
References for Section 5.....	5-14
<b>6. Electrooptic Sampler Measurement Modes.....</b>	<b>6-1</b>
6.1 Vector Mode Measurements.....	6-1
6.1.1 Harmonic Mixing.....	6-1
6.1.2 Traveling-Wave Measurement .....	6-3
6.1.3 Two-port S-parameter Measurements.....	6-4
6.2 Time Waveform Measurements.....	6-8
6.2.1 Signal Chopping.....	6-8
6.2.2 Phase Modulation.....	6-10
6.2.3 Fast-Offset and Averaging.....	6-13
6.3 Conclusion .....	6-16
References for Section 6.....	6-17
<b>7. Wafer Probe Station for Electrooptic Probing.....</b>	<b>7-1</b>
7.1 Wafer Probe Station.....	7-1
7.2 Microwave Circuit Measurements.....	7-5
7.2.1 One-Port Measurements .....	7-5
7.2.2 Two-port S-parameter Measurements.....	7-5
7.2.3 Potential Mapping for Circuit Modeling .....	7-9
7.2.4 Microwave Amplifiers .....	7-9
7.2.5 Nonlinear Transmission Line .....	7-14
7.2.6 Transmission line Mode Characterization.....	7-14
7.3 Millimeter-Wave Wafer Probing.....	7-21
7.3.1 Active Probe Development .....	7-21
a) Introduction .....	7-21
b) CPW Circuit Design Considerations.....	7-22
c) Nonlinear Device Modelling .....	7-29
d) Scaled model frequency multiplier design.....	7-34
7.4 Millimeter wave circuit measurements .....	7-53
7.4.1 Standing wave measurements.....	7-53
7.4.2 CPW and Slot line Dispersion Characteristics .....	7-53
7.5 Conclusion .....	7-54
References for Section 7.....	7-54

<b>Section</b>	<b>Page</b>
<b>8. Conclusion</b> .....	8-1
 <b>Appendix I</b>	
Laser Timing Stabilization System Design Considerations.....	AI-1
 <b>Appendix II</b>	
Optical System Analysis using Jones-Vector Representation .....	AII-1
 <b>Appendix III</b>	
Traveling wave coefficient calculation .....	AIII-1
 <b>Appendix IV</b>	
"Full-field modeling of the longitudinal electrooptic probe" .....	AIV-1
 <b>APPENDIX V</b>	
"Gallium Arsenide Integrated Circuit Testing Using Electrooptic Sampling" [Ref. 1.47, 5.12].....	AV-1
(1) Accuracy, Crosstalk, and Spatial Resolution	
(2) Linearity	
(3) Invasiveness of the Electro-Optic Probing Beam	
(4) References	
(5) The Electro-Optic Probing System	
(6) Integrated Circuit Measurements	

## LIST OF ILLUSTRATIONS

<u>Figs.</u>	<u>Title</u>	<u>Page</u>
1.1	Charge-sensing system schematic	1-7
1.2	Hybrid electrooptic sampling system	1-9
1.3	Transverse-field electrooptic needle probe; for on-wafer measurements	1-10
1.4	Needle probe sampling system for on-wafer measurements	1-11
1.5	Principal axes and cleave planes of (100)-oriented gallium arsenide	1-15
1.6	Gallium arsenide transmission light modulator	1-16
1.7	Reflection probing geometries for IC's	1-19
1.8	Coaxial optical arrangement for separation of incident and reflected beams	1-20
1.9	Electrooptic harmonic mixing	1-26
1.10	Equivalent-time sampling	1-27
2.1	Autocorrelation of the pulse compressor output	2-4
2.2	Magnitude of the spectral content of the pulse compressor output pulse	2-5
3.1	Typical spectrum of intensity noise for a mode-locked Nd:YAG laser	3-4
3.2	Dispersion-induced walkoff between the pump pulse and the Raman pulse from the 1 km fiber	3-6
3.3	Raman pulse build-up	3-7
3.4	Periodic noise spectrum from parasitic fiber-Raman laser when the compressor is operated near the Raman threshold	3-8
3.5	Excess intensity noise due to misadjustment of the polarization from the output of the pulse compressor fiber	3-8
3.6	Low frequency laser intensity noise reduction by the amplitude stabilizer	3-11
3.7	Coaxial optical arrangement for separation of incident and reflected beams for differential detection	3-14
3.8	Block diagram of a differential and ratio detection receiver	3-15

<u>Fig.</u>	<u>Title</u>	<u>Page</u>
4.1	Illustration of a spatial harmonic; where the penetration is related to the transverse frequency	4-2
4.2	Variation in crosstalk measurement with frequency due to acoustic modes and capacitive coupling	4-6
4.3	Deviations in the filter response for very tight beams and very low frequency	4-8
4.4	Parameters for a focused gaussian beam	4-10
4.5	Operation of spot-size crosstalk	4-12
4.6	Calculated crosstalk for the general structure of Fig 4.4 with 2 $\mu\text{m}$ lines	4-13
4.7	Calculated crosstalk for the general structure of Fig. 4.4 with 4 $\mu\text{m}$ lines	4-14
4.8	Structure for measuring spot-size crosstalk	4-15
4.9	Decay of a surface potential due to spatial harmonics	4-17
4.10	Mechanism of backside crosstalk	4-18
4.11	Calculated and measured signals for backside crosstalk on CPW's	4-20
4.12	Structure for measuring backside calibration errors	4-22
4.13	Results from measurements on the structure of Fig. 4.11 plotted versus line thickness	4-23
4.14	Results from measurements on the structure of Fig. 4.11 plotted versus signal to ground spacing	4-24
4.15	Structure for measuring backside crosstalk in a 2-conductor configuration	4-25
4.16	Results of 2-conductor crosstalk, plotted vs. signal line separation	4-26
4.17	Results of 2-conductor crosstalk, plotted vs. signal to ground separation	4-27
4.18	Structure for measuring many-conductor crosstalk	4-29
4.19	Many-line crosstalk vs. number of intervening lines	4-30
4.20	Sketch of the potential at one frequency for a many-conductor structure	4-31
4.21	Sketch of a window for reducing backside crosstalk	4-34
4.22	Mechanism for leakage of unwanted light to the photodetector	4-36

<u>Fig.</u>	<u>Title</u>	<u>Page</u>
5.1	I-V curve for a schottky diode illuminated by a high intensity 1.06 $\mu\text{m}$ laser	5-4
5.2	Optical intensity dependence of the short circuit current in a schottky diode	5-5
5.3	As in Fig. 5.5, but for a diode where the depletion depth is known well	5-6
5.4	Time response of a schottky diode to an impulse of 1.06 $\mu\text{m}$ light	5-7
5.5	Intensity dependence of the 82 MHz component of $I_{\text{SC}}$ at 2 different gate conditions	5-9
5.6	Intensity dependence of the DC component of $I_{\text{SC}}$	5-10
5.7	Mechanism for propagation of scattered radiation in the Gaussian tails of the beam to the active region of a distant device	5-12
5.8	2D scan of the change in drain current of a MESFET as a function of beam position	5-13
6.1	Receiver block diagram	6-2
6.2	Frequency converter schematic	6-2
6.3	Integrated circuit S-parameter test structure for the electrooptic probe	6-5
6.4	Error model for the S-parameter test structure	6-5
6.5	Fast scan rate signal processing block diagram	6-14
6.6	Block diagram of the fast averager	6-15
7.1	Front view of microwave wafer probe station	7-2
7.2	Front view closeup of the Cascade microwave probe station	7-3
7.3	Schematic diagram of microwave probe station	7-4
7.4	Slot line standing wave	7-6
7.5	CPW standing wave at 20 GHz	7-7
7.6	Measured $S_{11}$ using electrooptic sampling	7-8
7.7	Transverse scan of microstrip	7-10
7.8	Transverse potential distribution of slot line measured using electrooptic sampling	7-11
7.9	Distributed amplifier using coplanar waveguide transmission line interconnects	7-12

<b><u>Fig.</u></b>	<b><u>Title</u></b>	<b><u>Page</u></b>
7.10	Small-signal voltages on the coplanar 2-18 GHz distributed amplifier	7-13
7.11	Saturation at drains 4 and 5 of a microstrip distributed amplifier	7-15
7.12	Saturation at drain 3 of a microstrip distributed amplifier at 21 GHz drive	7-15
7.13	Shock-wave formation/falltime compression on the nonlinear transmission line with a sinusoidal input waveform	7-16
7.14	Shock-wave formation/falltime compression on two cascaded nonlinear transmission lines	7-16
7.15	CPW transverse scan and cross section	7-18
7.16	Magnitude and phase of the odd (CPW) mode standing wave on the center conductor	7-19
7.17	CPW even mode standing wave	7-20
7.18	CPW lowpass filter circuit layout	7-23
7.19	CPW lowpass filter (with bond wires) measurement results	7-24
7.20	CPW lowpass filter (without bond wires) measurement results	7-25
7.21	Schematic and simulation results of CPW bandpass filter with series CPW gaps	7-27
7.22	Measurement results of CPW bandpass filter	7-28
7.23	Millimeter wave diode equivalent circuit	7-30
7.24	Millimeter wave diode impedance vs. driving voltage	7-31
7.25	Voltage and current waveforms at 25 GHz with +30 dBm input power	7-32
7.26	Voltage and current waveforms at 25 GHz with +10 dBm input power	7-33
7.27	Schematic and simulation results of CPW lowpass filter	7-35
7.28	Schematic and simulation results of CPW bandpass filter	7-37
7.29	Measurement results of CPW bandpass filter	7-38
7.30	Diode input impedance and the simplified model impedance vs. frequency	7-39
7.31	Diode output impedance and the simplified model impedance vs. frequency	7-40
7.32	Schematic and simulation results of input matching network	7-42

<u>Fig.</u>	<u>Title</u>	<u>Page</u>
7.33	Schematic and simulation results of output matching network	7-43
7.34	Scaled model quintupler circuit layout	7-44
7.35	Scaled model quintupler output with 3.0 GHz input	7-45
7.36	Scaled model quintupler output with 3.432 GHz input	7-46
7.37	Scaled model quintupler output with 4.374 GHz input	7-48
7.38	Millimeter wave quintupler circuit layout	7-49
7.39	GaAs quintupler input signal at 20 GHz	7-51
7.40	GaAs quintupler output signal at 100 GHz	7-52
7.41	100 GHz standing wave	7-55
7.42	40 GHz standing wave	7-56
7.43	CPW odd mode dispersion characteristics	7-57
7.44	Dispersion characteristics of CPW even mode	7-57
7.45	Free space-to-guide wavelength ratio vs. frequency for CPW even and odd mode	7-58
7.46	Slot line dispersion characteristics	7-58



# 1. Background

## 1.1 Motivation

Gallium arsenide (GaAs) has been the "material of the future" for integrated circuit (IC) technology for at least the last decade, starting with the first fabrication of a GaAs transistor more than two decades ago [1.1]. For microwave applications, such as broadband amplifiers, oscillators, diode switches, and mixers in microwave/millimeter-wave radar and communication systems, GaAs IC's and components clearly have outpaced competition from silicon IC's. For digital applications, such as fiber optic digital data transmission at gigahertz rates, high-speed data acquisition, and faster digital logic for high-speed computers and signal processors, GaAs IC's have a small but growing niche for high-performance functions that outperform silicon IC's. In addition, the advent of two new epitaxial growth techniques for GaAs and other III-IV compound semiconductors, molecular beam epitaxy (MBE) and organo-metallic chemical vapor deposition (OMCVD, also known as vapor phase epitaxy, VPE) [1.2], allow for control of the growth of semiconductor structures with atomic layer resolution and the semiconductor bandgap energy. These growth techniques promise much higher performance devices based on heterostructures and quantum-size effects, such as heterojunction bipolar transistors (HBT's), high electron mobility transistors (HEMT's) or modulation-doped field effect transistors (MODFET's), resonant tunneling diodes (RTD's), and multi-quantum well devices. The devices developed with these new fabrication techniques and IC's developed for high performance applications are creating new challenges for the high-speed test instrumentation used to characterize their electrical response.

One need is for increased instrument time resolution or frequency bandwidth. GaAs metal-semiconductor field-effect transistors (MESFET's) have demonstrated a maximum frequency of oscillation,  $f_{max}$ , in excess of 110 GHz [1.3], InGaAs/AlGaAs MODFET's [1.4] have shown power-gain bandwidth products which extrapolate to give  $f_{max} = 200$  GHz, resonant tunnelling diodes have oscillated at 56 GHz [1.5], and HBT's and permeable base transistors should show similar performance. The  $f_{max}$  of these devices, often greater than the 100 GHz bandwidth of commercial millimeter-wave network analyzers, is usually estimated by extrapolation from measurements at lower frequencies. Propagation delays and transition times of 1-10 ps (picosecond,  $10^{-12}$  seconds), well below the resolution of commercial sampling oscilloscopes, is expected for switching

circuits using these devices. In either the time or the frequency domain, the speed of the device exceeds the speed of the measurement instrument.

A second need is for a noninvasive probe of internal signals in high-speed integrated circuits. GaAs digital IC's of medium-scale integration (MSI) complexity with 1-5 GHz clock rates and monolithic microwave integrated circuits (MMIC's) of small-scale integration (SSI) complexity with 1-20 GHz bandwidths are now available commercially. More complex large-scale integration (LSI) digital circuits are under development, and experimental SSI digital circuits operating with 18-26 GHz clock rates [1.6,7] have been demonstrated. In contrast to silicon LSI integrated circuits, operating at clock rates in the tens and hundreds of megahertz, GaAs high-speed circuits are hampered both by poorly refined device models and by layout-dependent circuit parasitic impedances at high frequencies of operation. A test instrument providing noninvasive measurements within the integrated circuit would permit better characterization of such complex high-speed IC's.

In the last decade, however, optical techniques for ultrashort pulse generation have outpaced electronic pulse generation techniques. Researchers at Bell Laboratories have generated 6 fs (femtosecond,  $10^{-15}$  seconds) optical pulses [1.8], and many research laboratories routinely generate picosecond pulses at a number of optical wavelengths. One method to make electrical measurements using light is through the linear electrooptic effect, first described by Pockels in the late 1800's. This effect allows for the modulation of light with electrical signals, for applications such as light modulators, known as the Pockels cell. The advantages of using light to monitor high-speed electrical signals (subnanosecond) launched onto a Pockels cell was known in the early 1970's [1.9] and first implemented in the early 1980's, achieving sub-picosecond time resolution for measurements of the response of optoelectronic devices [1.10,11]. A high-repetition rate laser was used in these systems to repetitively sample the electrical waveforms, hence the term "electrooptic sampling." Kolner and Bloom at Stanford University realized that the substrate of GaAs IC's was suitable as the electrooptic material for a Pockels cell, and demonstrated the feasibility of direct optical probing of voltage signals in a GaAs substrate using a short-pulse infrared laser [1.12,13] in 1984. The first GaAs IC was electrooptically probed in 1985 [1.14].

## 1.2 Review of RF Test Methods

### 1.2.1 Conventional RF Test Methods

Conventional RF test instruments have capabilities and characteristics determined by two features - the electrical probe that connects the test instrument to the circuit and the test instrument itself. The electrical probe has its own intrinsic bandwidth that may limit the test method. In addition, the probe also determines an instrument's ability to probe internal to the IC due to its size (limiting its spatial resolution) and influence on circuit performance (loading of the circuit from the probes characteristic and parasitic impedances). The test instrument sets the available bandwidth given perfect electrical probes or packaged circuits, and defines the type of electrical test, such as measuring time or frequency response.

#### Contact Probes

Connection of a test instrument to an IC begins with the external connectors, typically 50  $\Omega$  coaxial cable with a microwave connector, such as SMA and APC-3.5, standard microwave connectors, or K-connector (to 46 GHz) and APC-2.4 (to 50 GHz). *Contact probes* are the electrical transitions from the coaxial cable to some type of contact point with a size comparable to an IC bond pad. Low-frequency signals are often connected with needle probes. At frequencies greater than several hundred megahertz these probes have serious parasitic impedances, due to shunt capacitance from fringing fields and series inductance from the long, thin needle. The parasitic impedances and the relatively large probe size compared to IC interconnects limit their effective use to low-frequency external input or output signals at the bond pads. By reducing the probe size and maintaining coaxial line with a ground connection as near the tip and the IC as possible, the performance of needle probes can extend to 1-2 GHz. Active needle probes, consisting of an IC FET mounted near the probe tip, provide a way to increase the probe impedance and reduce its series inductance, allowing internal-node probing up to  $\approx$ 1 GHz. The small probe (for contact to small internal interconnects) is typically very fragile and the FET must be well-characterized over the desired frequency range. Transmission line probes, such as the recently developed Cascade Microtech probe [1.15,16], have demonstrated IC connections to millimeter-wave frequencies of 50 GHz. The probe consists of a coaxial connector with a transition to 50  $\Omega$  coplanar waveguide (CPW) transmission line that then tapers to bond pad size contacts. They offer good mi-

crowave performance, but their size limits test points to IC bond pads and their 50  $\Omega$  characteristic impedance limits their use to input or output sections of the IC.

Thus, contact probes pose a measurement dilemma. Good high-frequency probes use transmission lines to control the line impedance from a coaxial transition to the IC bond pad and to reduce parasitic impedances. The characteristic impedance of such lines (typically 50  $\Omega$ ) and their size limits their use to input/output stages designed for matched (50  $\Omega$ ) loads. High-impedance probes suitable for probing internal circuit nodes have significant parasitic impedances at microwave frequencies, severely loading the circuit, perturbing its operation and affecting the measurement accuracy, or requiring a FET for active probing that has a well characterized frequency response greater than the circuit under test. Large needle probes are limited to test points at the circuit's input/output pads, while small needle probes are very fragile and can damage the circuit mechanically.

### **Microwave Test Instruments**

Conventional test instruments for measuring high-speed electrical signals consist of sampling oscilloscopes, spectrum analyzers, and network analyzers. Sampling oscilloscopes, based on step recovery diode technology, can measure the time response of repetitive signals with a resolution slightly less than 20 ps (or a corresponding bandwidth of  $\approx$ 20 GHz). Combined with transmission line probes this instrument measures either time domain reflectometry (electrical echoes from circuit elements and interfaces) or signal waveforms of an IC's external response, but has neither the time resolution required for state-of-the-art GaAs IC's nor the ability to measure the internal node response of IC's. A promising note is the recent introduction of a new sampling oscilloscope from Hypres, Inc., based on Josephson Junction superconducting technology [1.17], that offers a time resolution of about 8 ps. As with slower sampling oscilloscopes, however, the 50  $\Omega$  connectors limit its use to external characterization of IC's, and the coaxial cabling and connectors probably limit the instrument's time resolution more than the sampling speed of the Josephson junction switches.

Spectrum and network analyzers measure the response of circuits in the frequency domain, with a range of 26.5 GHz typically and limited extension through the millimeter-wave frequencies to 300 GHz. A spectrum analyzer measures the power spectrum of a signal, while network analyzers measure the vector transfer function of a network (magnitude and phase) as a function of frequency. The small-signal, linear characteristics of microwave devices and circuits measured with a network analyzer are usually expressed in terms of the scattering parameters. These provide a measure (often extrapolat-

ed) of  $f_{max}$ , a device's maximum frequency of oscillation, and  $f_t$ , the unity current gain frequency, figures of merit of a device's speed of operation. The frequency range of these instruments can be extended to millimeter-wave frequencies (300 GHz for the spectrum analyzer, 100 GHz for the network analyzer) using external source multipliers, mixers and waveguide connectors, but the frequency coverage is limited to waveguide bandwidths (having upper and lower cutoff frequencies in the ratio of 1.5:1) and the waveguide connectors require a hybrid mount of the IC in a waveguide package, preventing wafer level testing of the IC (wafer measurements are possible to 50 GHz using the Cascade probes). Network analyzers can provide time-domain measurements of a network's small-signal step or impulse response by performing a Fourier transform of the small-signal frequency response. For large-signal measurements, where the network is no longer linear, the principle of superposition does not hold and Fourier transform theory cannot be applied, preventing calculation of the large-signal time response from its frequency response. For example, the network analyzer cannot determine the IC's time waveform response due to amplifier saturation. Although spectrum analyzers can measure the harmonic spectrum magnitude of saturated or large-signal circuit responses, the phases of the harmonics are not measured, and the large-signal time waveforms again cannot be determined. Both instruments also rely on 50  $\Omega$  connectors and contact probes, limiting their ability to probe an IC to its external response. For network analysis, a further issue is de-embedding the device parameters (both magnitude and phase) from the connector and circuit fixture response, a task which grows progressively more difficult at increasing frequencies, particularly for millimeter-wave testing.

### **1.2.2 Non-Electrical, Novel Test Techniques**

With the objective of either increased bandwidth or internal node IC testing with high spatial resolution (or both) a number of new test techniques have been introduced and demonstrated.

#### **Voltage-contrast Scanning Electron Microscope**

One method of measuring a voltage on IC conductors is to energy analyze secondary electron emission. To test logic level signals in VLSI silicon IC's researchers in the late 1960's developed the voltage contrast scanning electron microscope (SEM) or E-beam probing [1.18,19]. This technique uses an electron beam from an SEM to stimulate secondary electron emission from surface metalization. For a metal conductor at ground or negative potential, the electrons have sufficient energy to be collected by a detector

shielded by an energy analyzer grid. Metal lines at a positive potential retard the emitted electrons, lowering their energy and reducing the number of electrons detected. The detected signal is small for IC voltage levels; to improve time resolution the signal is sampled with electron beam pulses and averaged to improve signal-to-noise ratio.

Commercial voltage contrast SEM's have sensitivities of 1-10 mV, bandwidths up to 2 GHz or time resolutions of  $\approx 1$  ns, and a spatial resolution as small as 20 nm. Compared to typical operating speeds of commercial silicon VLSI (clock rates of 10 to 100 MHz) this technique has good time resolution, acceptable sensitivity, and excellent spatial resolution. One particular feature of these systems is the normal SEM imaging, which provides an excellent picture of the IC for both visual inspection and for positioning the E-beam probe. The system's time resolution is set by gating the E-beam from the thermionic cathodes of standard SEM's. For decreasing electron beam duration (required for increased time resolution), the average beam current decreases, degrading measurement sensitivity and limiting practical systems to a time resolution of several hundred picoseconds. To overcome this limitation, a technique which uses a photocathode triggered by an intense picosecond optical pulse to generate short, high-current electron pulses [1.20] has been demonstrated. This approach has experimentally demonstrated a time resolution of 5 ps, a sensitivity of  $3 \text{ mV}/\sqrt{\text{Hz}}$ , and a spatial resolution of  $0.1 \mu\text{m}$  [1.21]. The major drawback of SEM testing is its vacuum system, lowering system throughput.

### **Photoemissive Sampling**

Photoemissive sampling, based on analyzing secondary electron emission from IC conductors similar to E-beam testing, uses intense, energetic light from a pulsed laser focused on an IC conductor to generate photoelectrons. An extraction/retarding grid combination placed in close proximity to the conductor energy analyzes the electrons, with a resulting secondary electron emission varying with the conductor potential. The feasibility of this new approach is made possible by picosecond pulsewidth, high peak power lasers, and offers a potential improvement in time resolution and sensitivity over the SEM probe. The technique is not available commercially, but researchers have experimental evidence of time resolution as short as 5 ps with good spatial resolution and a sensitivity of  $10 \text{ mV}/\sqrt{\text{Hz}}$  [1.22-24]. With both electron-beam and photoemissive sampling, electron beams and electron extraction fields may produce charge concentrations within the semiconductor substrate through charging of deep levels, or at its surface, through field-induced surface inversion.

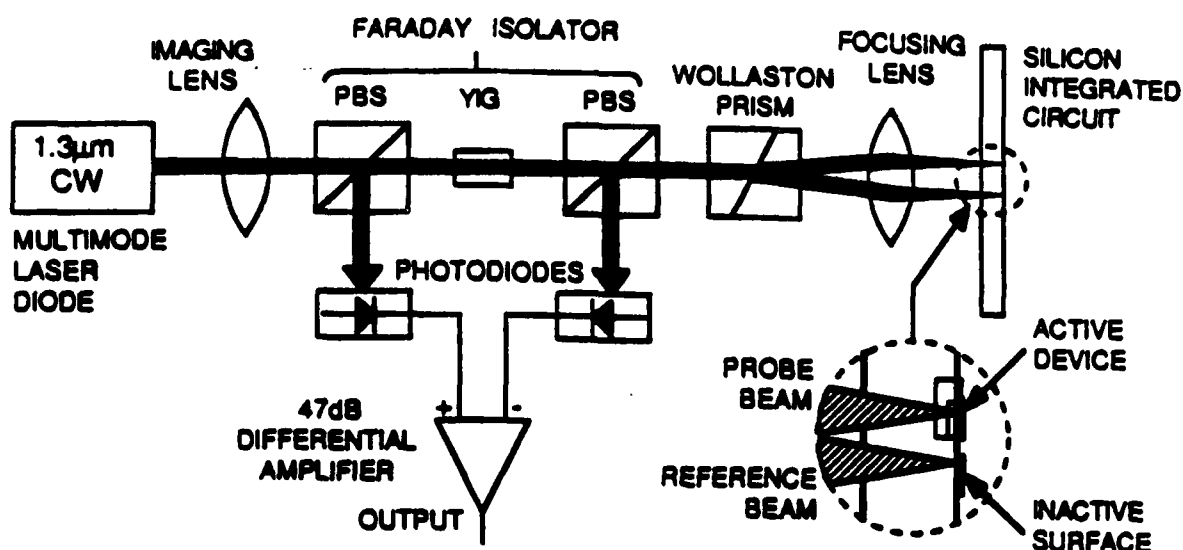


Fig. 1.1. Charge-sensing system schematic; [1.25-27]. The Wollaston prism separates the input beam into a probe beam and a reference beam, forming an optical interferometer. In silicon IC's, the presence of free carriers in the probe beam path results in a change in output intensity at the photodiodes proportional to the charge concentration as described by (1.1).

## Charge Sensing

A technique which optically senses free-carrier charge density was recently developed for measurements of silicon IC devices [1.25,26]. Because of its centrosymmetric crystal structure, silicon exhibits no bulk second-order optical nonlinearities, such as the electrooptic effect, to use as a basis for an optical measurement system. Third-order effects, such as voltage-dependent second-harmonic generation or the optical Kerr effect, are in general very weak and result in systems with poor measurement sensitivity and impractical experimental implementations. Most semiconductor devices function by modulating charge density within a control region, which contributes to material index of refraction in silicon devices as described by the plasma-optical relation

$$n = n_0 \sqrt{1 - \frac{\omega_p^2}{\omega^2}} \quad (1.1)$$

where

$$\omega_p^2 = \frac{q^2 N}{\epsilon_s m_e^*} + \frac{q^2 P}{\epsilon_s m_h^*} \quad (1.2)$$

$n_0$  is the bulk index of refraction,  $\omega$  is the optical probe frequency,  $\omega_p$  is the plasma resonance frequency,  $N$  is the electron concentration in the conduction band,  $P$  is the hole concentration in the valence band,  $\epsilon_s$  is the permittivity of the substrate material, and  $m_e^*$  and  $m_h^*$  are the electron/hole conductivity effective masses. The change in charge density is detected with a compact optical interferometer using a 1.3  $\mu\text{m}$  wavelength (the absorption minimum in silicon) semiconductor laser as the probe, shown schematically in Fig. 1.1. In contrast to electrooptic techniques, where typical probe beam intensity modulation is on the order of 0.1%, for the charge density typical of integrated silicon bipolar transistors the probe beam modulation in the charge-sensing system is on the order of 1-10%. This sensitivity has allowed the demonstration of single-shot (i.e. no repetitive sampling) detection of a silicon bipolar junction transistor's switching signal with a 200 MHz bandwidth [1.27] and repetitive sampling measurements using a pulsed semiconductor laser with 1 GHz measurement bandwidth [1.28]. This technique is applicable to GaAs and other III-IV-type IC's and shows promise for studying device characteristics and carrier dynamics.



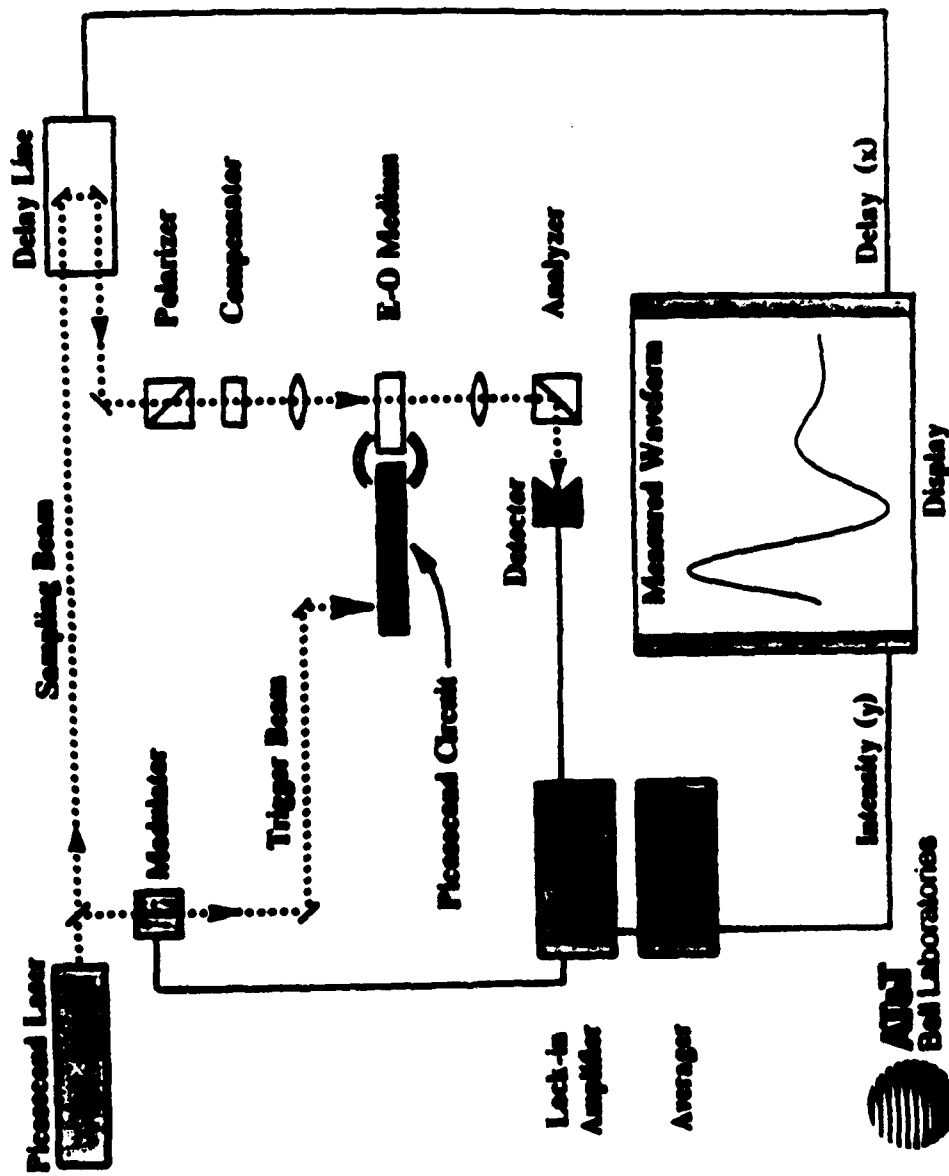


Fig. 1.2. Hybrid electrooptic sampling system, using an electrooptic modulator connected to test circuit through wire bonds or some other hybrid assembly technique. The E-O medium, typically LiTaO<sub>3</sub>, is transparent at visible light wavelengths, allowing use of ultrashort (<100 fs) light pulses from CPM lasers. Diagram courtesy of J.A. Valdmanis, AT&T Bell Laboratories.

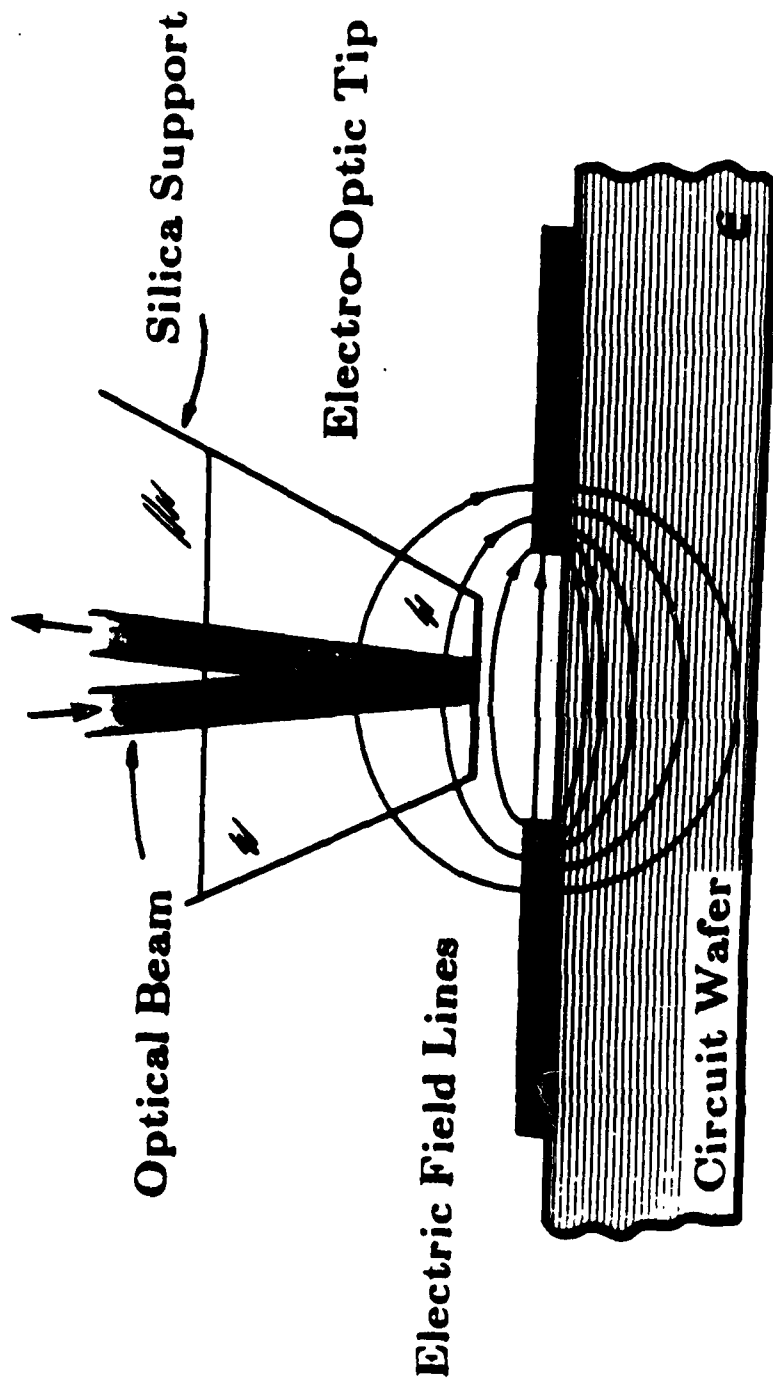


Fig. 1.3. Transverse-field electrooptic needle probe; for on-wafer measurements [1.32-33]. Because the probe senses transverse fields, calibration and crosstalk between nearby conductors depends on the spacing between the conductors.

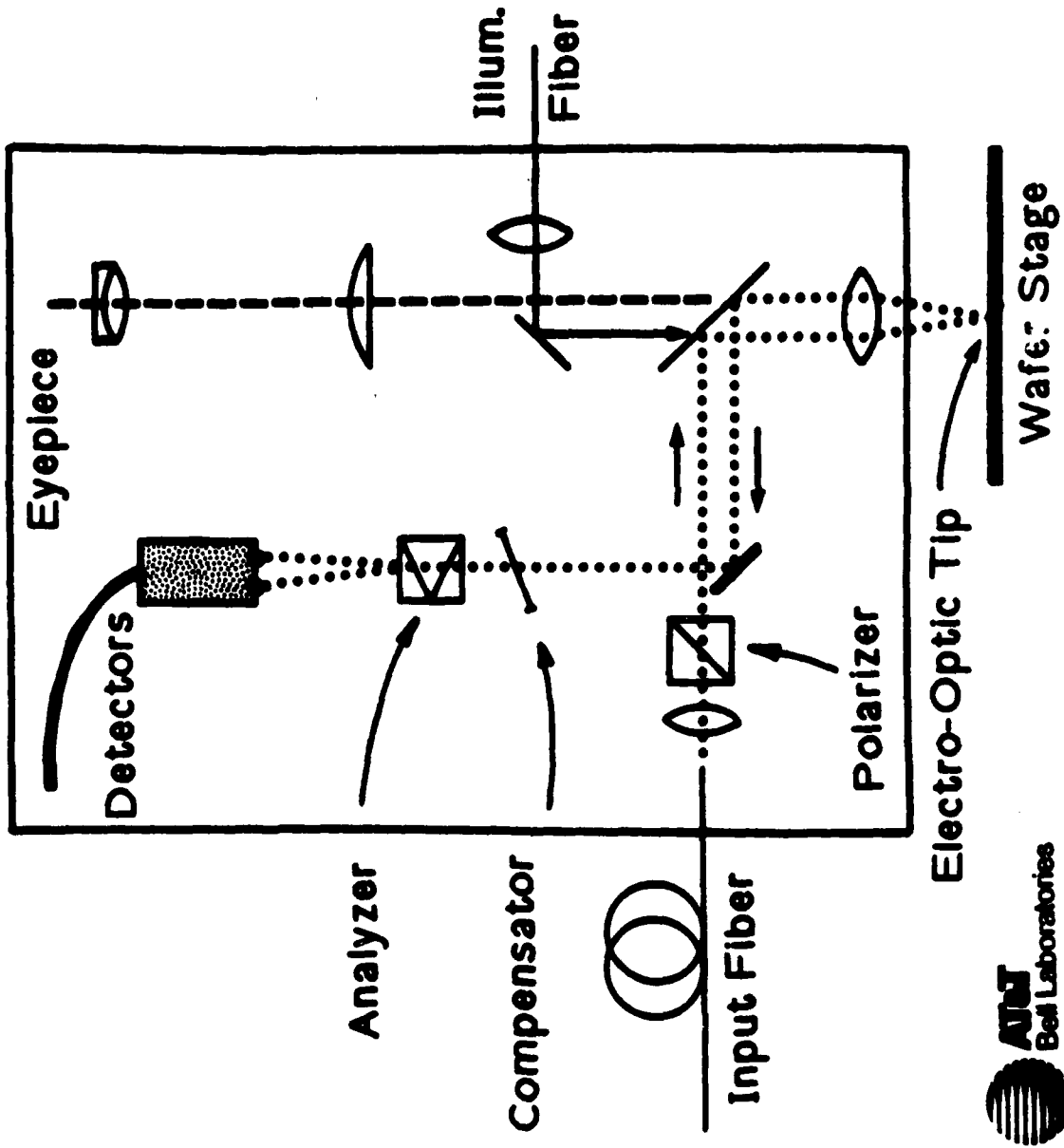


Fig. 1.4. Needle probe sampling system for on-wafer measurements. The probe beam is delivered to the test station with an optical fiber, and a novel viewing system allows for imaging through the needle probe for positioning of the test point. Diagram courtesy of

J A Valdmann AT&T Bell Laboratories



## **Electrooptic Sampling**

Another optical probe scheme is electrooptic sampling, which uses an electrooptic light modulator to intensity modulate a probe beam in proportion to an electrical signal. The technique was initially developed to measure the response of photoconductors and photodetectors faster than the time resolution of sampling oscilloscopes [1.10,11,29,30] and used an external electrooptic modulator (typically lithium tantalate,  $\text{LiTaO}_3$ ) connected to the device under test. A polarized optical probe beam passes through an electrooptic crystal, whose index of refraction changes due to the presence of an electrical signal (Fig. 1.2). The polarization of the light after passing through the electrooptic crystal depends on the signal driving the modulator, and passing the probe beam through a polarizer results in a signal-dependent intensity modulation. The approach exhibits very short time resolution ( $<0.5$  ps) due to the use of ultrashort pulses from the colliding-pulse mode-locked (CPM) laser and the very high intrinsic speed of the electrooptic effect. Combined with a cryogenic system, optical measurements of electrical signals have been made at liquid helium temperatures[1.31]. However, the hybrid lithium tantalate electrooptic modulator requires connecting the test point on the IC to the transmission line of the modulator, restricting its use to external test points. Unless carefully designed, the system's time resolution is degraded by the hybrid connection between the modulator and the device under test, due to the loading of the test point from the relatively low characteristic impedance of the transmission line and the parasitic impedances of the bond wires.

Using an electrooptic needle probe (Figs. 1.3, 1.4) [1.32], the technique has been extended to internal node probing of IC's. The needle, a fused silica rod with a  $40 \times 40$  micron tip of  $\text{LiTaO}_3$  coated for high reflection of the probe beam, is brought close to a conductor, introducing fields within the probe tip. As with the hybrid electrooptic technique, the electric fields change the polarization of the probing beam, and the reflected beam is analyzed by a polarizer. The  $\text{LiTaO}_3$  electrooptic material, transparent to visible wavelength light, allows the use of ultrashort sampling pulses from a CPM laser, and a signal risetime of less than 300 fs has been measured[1.33]. Because the probe relies on no optical or electrical properties of the circuit under test, circuits of any substrate material can be tested without sample preparation. The probe exhibits circuit invasiveness through capacitive loading on the order of 10 femtofarads, due to the proximity of the  $\text{LiTaO}_3$  probe tip of dielectric constant  $\epsilon_r = 40$ . The polarization shift in lithium tantalate, proportional to the lateral electric field, may make the probe sensitive to signals from nearby conductors in addition to the signal of the probed conductor, limiting its ability to spatially resolve closely spaced conductors due to measurement crosstalk.

Direct electrooptic sampling uses the substrate of the GaAs circuit under test as the electrooptic modulator, eliminating electrical parasitics associated with external electrooptic elements and providing voltage measurements of points internal to the IC with picosecond time resolution and micron spatial resolution. This method's principles, capabilities, and circuit measurement results are described in the remainder of this section.

### 1.3 Direct Electrooptic Sampling in GaAs IC's

This subsection describes the concepts and theory of electrooptic voltage probing in GaAs IC's, sampling principles for time and frequency response measurements, the characteristics that define the probe's time resolution, its sensitivity based on noise-limited detection, and signal processing schemes to achieve noise-limited detection.

#### 1.3.1 Electrooptic Voltage Probing in a GaAs IC Substrate

The electrooptic effect is an anisotropic variation in a material's dielectric constant due to an applied electric field. A variety of non-centrosymmetric crystals exhibit this effect, such as GaAs, InP and AlAs, used for high-speed semiconductor devices, and lithium niobate ( $\text{LiNbO}_3$ ), lithium tantalate ( $\text{LiTaO}_3$ ) and potassium dihydrogen phosphate ( $\text{KH}_2\text{PO}_4$ ), used for nonlinear optical devices. Centrosymmetric crystals, such as silicon and germanium, do not exhibit the electrooptic effect. The change in refractive index of electrooptic materials due to applied electric field can be used for optical phase-modulation, and from this, polarization-modulation or intensity-modulation [1.34,35]. Direct electrooptic sampling uses the electrooptic effect in GaAs to obtain voltage-dependent intensity modulation of a probe beam [1.36,37].

GaAs is one of simplest electrooptic crystals, a zincblende with crystal symmetry  $\bar{4}3m$ . It has a cubic crystal structure and no birefringence under stress-free and field-free conditions. The electrooptic tensor in GaAs, symmetric with equal-valued elements, is [1.38]

$$r_{jk} = \begin{pmatrix} 0 & 0 & 0 \\ 0 & 0 & 0 \\ 0 & 0 & 0 \\ r_{41} & 0 & 0 \\ 0 & r_{41} & 0 \\ 0 & 0 & r_{41} \end{pmatrix} \quad (1.3)$$

An applied electric field induces a birefringence described by the index ellipsoid

$$\frac{x^2}{n_0^2} + \frac{y^2}{n_0^2} + \frac{z^2}{n_0^2} + 2r_{41}E_x yz + 2r_{41}E_y xz + 2r_{41}E_z xy = 1 \quad (1.4)$$

where  $n_0$  is the zero-field refractive index,  $r_{41}$  is the electro-optic coefficient for GaAs,  $x$ ,  $y$ , and  $z$  correspond to the [100], [010], and [001] directions of the GaAs cubic Bravais lattice, and  $E$  is the applied electric field in the direction indicated by its subscript. The intersection of the index ellipsoid and a plane normal to the optical propagation direction defines an ellipse whose major and minor axes give the allowed (eigenvector) polarization directions and their refractive indices.

To relate this to an IC substrate, Fig. 1.5 shows the principal crystal axes of a (100) oriented GaAs substrate, the industry standard for IC fabrication. The  $x$ ,  $y$ , and  $z$  axes are aligned with the  $\langle 100 \rangle$  directions of the GaAs cubic Bravais lattice, while the  $y'$  and  $z'$  axes are aligned with the  $[01\bar{1}]$  and  $[011]$  directions parallel to the cleave planes of the a GaAs wafer (along which individual IC's are scribed) and  $45^\circ$  to the [010] and [001] directions. For an optical plane wave traveling in the  $x$  direction, the intersection of the index ellipsoid and the  $x=0$  plane normal to its direction of propagation defines an ellipse in the  $(y', z')$  plane

$$y'^2 \left( \frac{1}{n_0^2} - r_{41}E_x \right) + z'^2 \left( \frac{1}{n_0^2} + r_{41}E_x \right) = 1 \quad (1.6)$$

The  $y'$  and  $z'$  axes are the eigenvectors of the electrooptic effect and form the natural coordinate system for describing electrooptic sampling in GaAs IC's. The refractive indices  $n_{y'}$  and  $n_{z'}$  in the  $y'$  and  $z'$  directions are

$$n_{y'} \cong n_0 + \frac{n_0^3 r_{41} E_x}{2}$$

$$n_{z'} \cong n_0 - \frac{n_0^3 r_{41} E_x}{2} \quad (1.7)$$

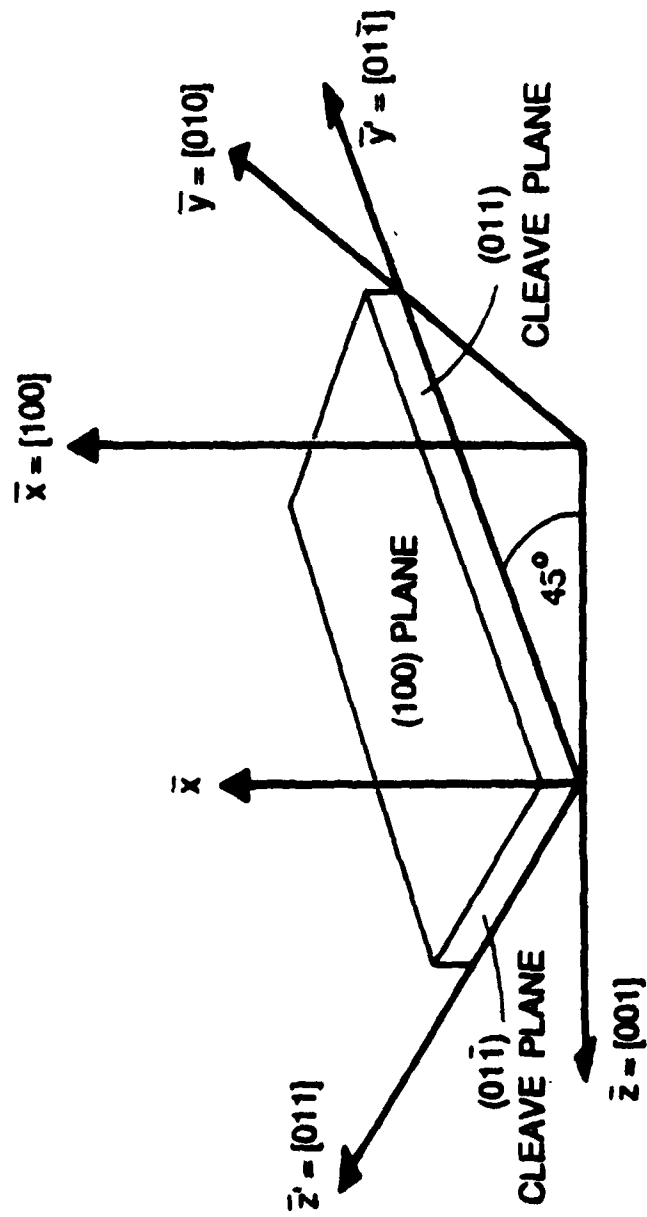


Fig. 1.5. Principal axes and cleave planes of (100)-oriented gallium arsenide; the industry-standard wafer orientation. IC's are fabricated on the (100) plane.

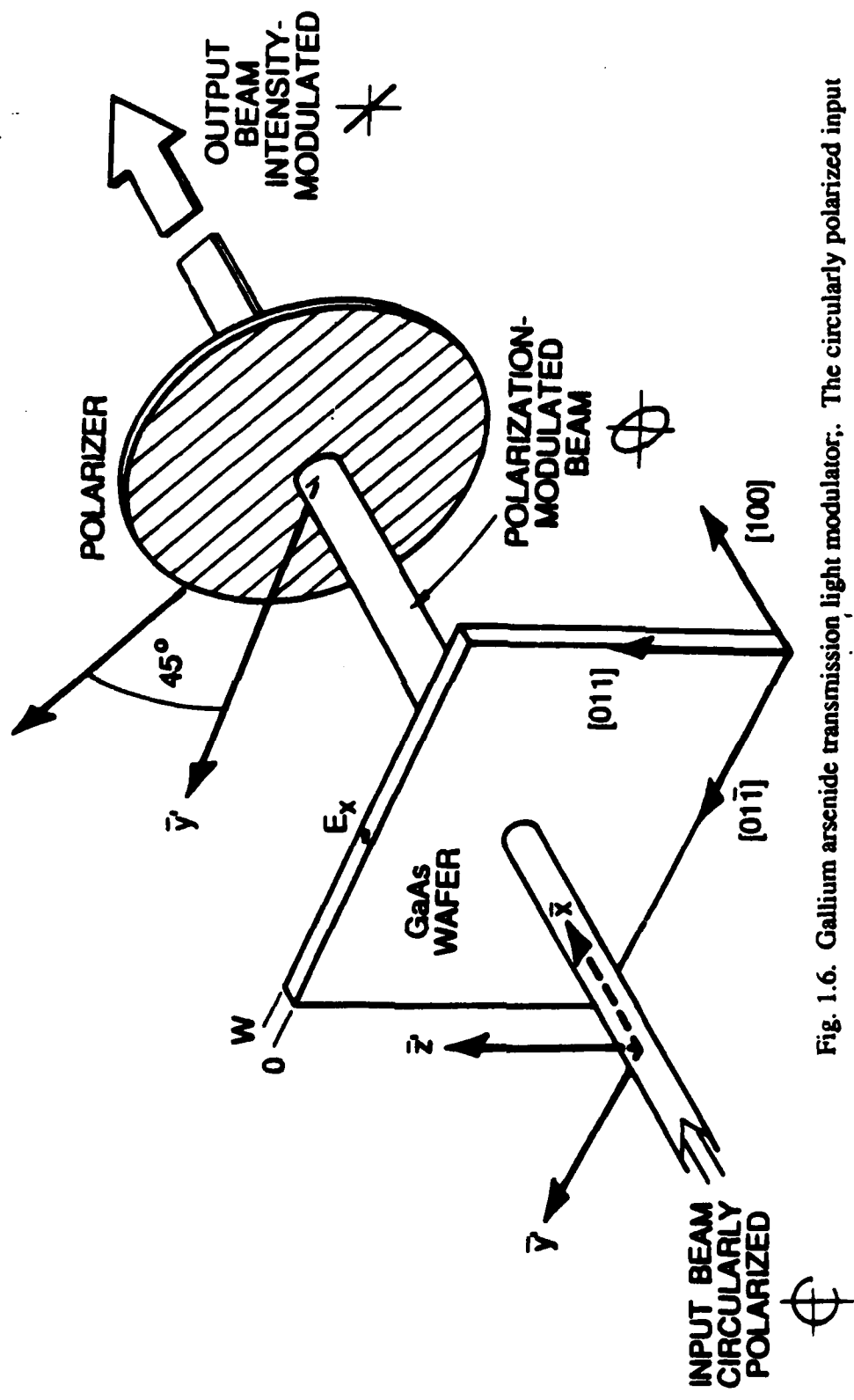


Fig. 1.6. Gallium arsenide transmission light modulator. The circularly polarized input beam becomes elliptically polarized due to the voltage-induced birefringence in the GaAs. A crossed polarizer (45° to the y' and z' directions) after the GaAs results in an output beam intensity that varies in proportion to the substrate voltage as described by (1.10)



and these field-dependent refractive indices result in differential phase shift for beam polarizations in the  $y'$  and  $z'$  directions.

Consider the transmission electrooptic amplitude modulator shown in Fig. 1.6. A circularly-polarized plane wave propagating through the substrate receives a change in phase between the  $y'$  and  $z'$  polarizations after passing through the GaAs

$$\Delta\phi = \int_0^W \frac{2\pi}{\lambda_0} n_0^3 r_{41} E_x dx \quad (1.8)$$

such that the beam emerging from the substrate has changed from circular to slightly elliptical polarization. This expression holds for a general field distribution; a plane-wave optical beam propagating along a  $\langle 100 \rangle$  direction experiences a differential change in phase shift proportional to the longitudinal electric field only.

Since the integral of the electric field over the substrate is just the voltage difference between the front and back of the substrate, the change in phase is

$$\begin{aligned} \Delta\phi &= \frac{2\pi n_0^3 r_{41}}{\lambda_0} E_x W \\ &= \frac{\pi}{V_\pi} V \end{aligned} \quad (1.9)$$

where

$$V_\pi = \frac{\lambda_0}{2n_0^3 r_{41}} \quad (1.10)$$

is the half-wave-voltage or the voltage causing a  $180^\circ$  phase shift between the  $y'$  and  $z'$  polarizations. For GaAs,  $V_\pi \cong 10$  kV at a wavelength of  $1.064 \mu\text{m}$ , for  $n_0 = 3.6$ , and  $r_{41} = 1.4 \cdot 10^{-12}$  m/V [1.39]; [1.47], Appendix V.

To measure the voltage-induced polarization change, the beam emerging from the GaAs is passed through a polarizer oriented at  $45^\circ$  to the  $y'$  and  $z'$  axes. The intensity of the output beam from the modulator is then [1.40]

$$P_{out}(V) = P_0 \left[ 1 + \sin\left(\frac{\pi V}{V_\pi}\right) \right] \quad (1.11)$$

where  $P_0$  is the output intensity with zero field in the substrate. The argument of the sine expression is small for typical voltages on integrated circuits, and (1.11) can be approximated by

$$P_{out} \cong P_0 \left[ 1 + \frac{\pi V}{V_\pi} \right] \quad (1.12)$$

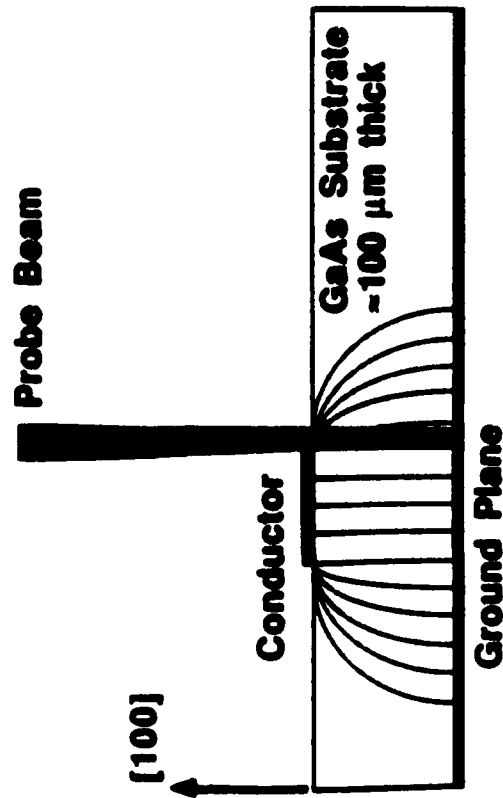
For substrate voltages up to several hundred volts, the output beam intensity is nearly linear and changes in direct proportion to the voltage across the substrate. The change in intensity of the output beam, detected by a photodiode, is then a measure of the voltage across the substrate of the IC.

### 1.3.2 Probing Geometries in GaAs IC's

The transmission modulator of Fig. 1.6 requires separate lenses for focusing and collecting the probe beam, precisely aligned on opposite sides of the wafer for IC measurements. Also, high-density interconnections on the circuit side of digital IC's and backside metalization on many microwave IC's would obstruct passage of the beam through the wafer. Reflection-type probing geometries as shown in Fig. 1.7 provide better access to IC's, using a single lens for focusing and using the IC metalization for reflection. The frontside geometry is suitable for probing microstrip transmission lines of MMIC's. The backside geometry permits focusing of the probe beam to a diameter limited by the numerical aperture of the focusing lens for probing closely spaced conductors.

For microstrip transmission lines typically used in MMIC's, the fields extend laterally from the conductor roughly a distance equal to the substrate thickness, and the probe beam is focused from the top of the substrate through the fringing fields to a spot size diameter approximately one-tenth of the substrate thickness, so that it overlaps well with the fringing fields. Other MMIC's use planar transmission lines such as coplanar waveguide (CPW) for microwave interconnects. MSI/LSI circuits typically use thin metal lines (3 to 10  $\mu\text{m}$ ), and the electric field distribution around the conductors is a strong function of their layout. For these types of interconnects and for planar transmission lines, the penetration of the fields into the substrate is on the order of the distance between signal conductors and grounds. Typical IC substrate thickness (400 to 500  $\mu\text{m}$ ) is much greater than conductor spacings. The electric fields lie near the substrate surface, and the back of the substrate is nearly at an equipotential with respect to individual conductors on the IC surface (this approximation is discussed further in the next section).

# Frontside Probing



# Backside Probing

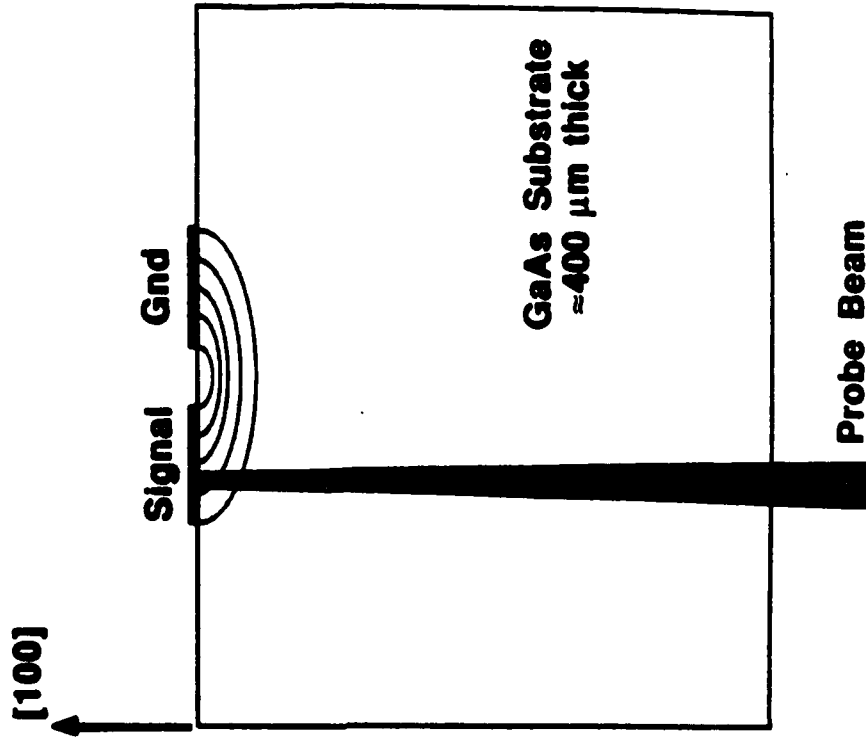


Fig. 1.7. Reflection probing geometries for IC's. Frontside probing is for circuits with microstrip transmission line, and the spot size is focused to 10-20  $\mu\text{m}$  typically. Backside probing is for circuits with planar transmission line such as coplanar waveguide, or circuits with standard metal interconnects. The spot size is typically 3-5  $\mu\text{m}$  in this case.

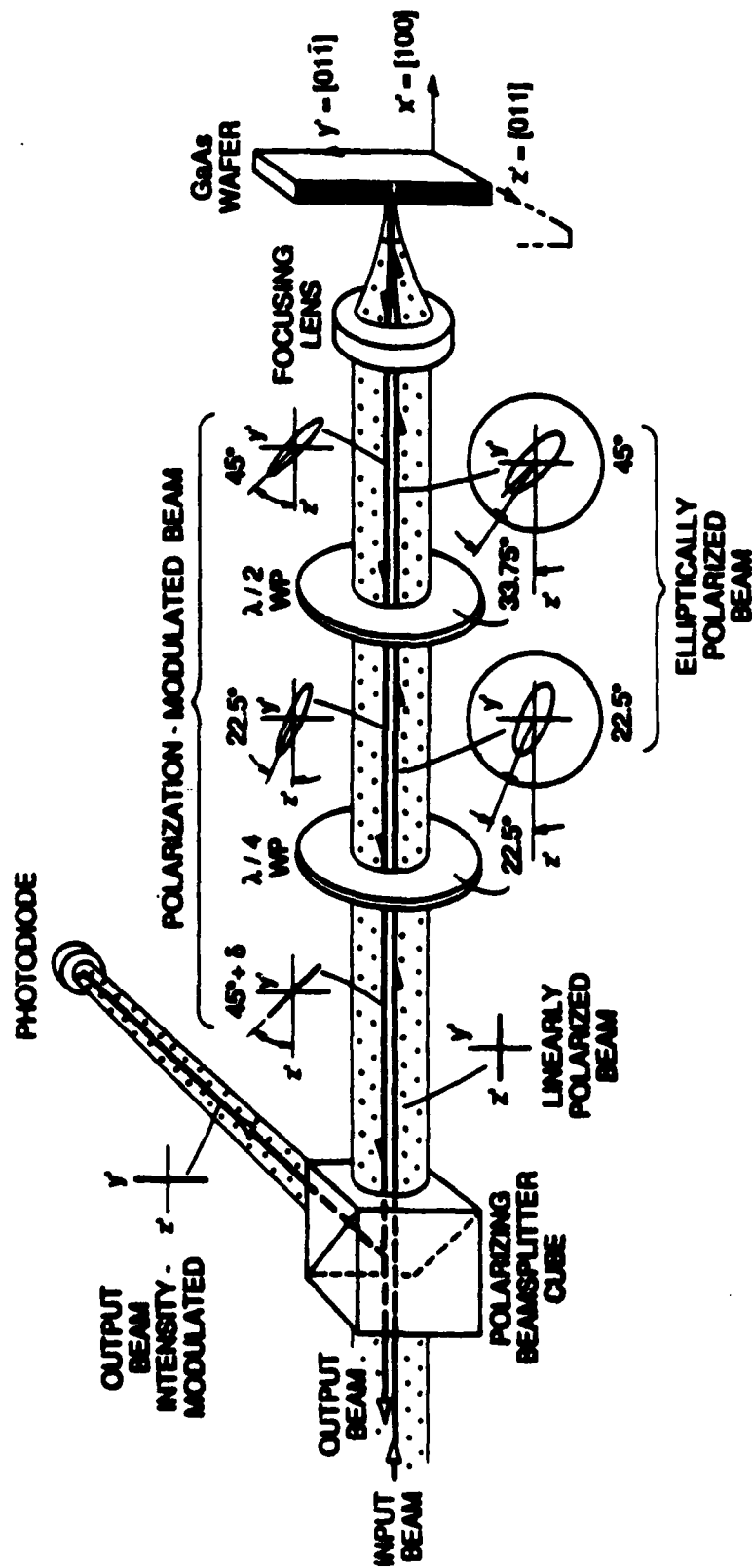


Fig. 1.8. Coaxial optical arrangement for separation of incident and reflected beams for the IC probing geometries of Fig. 1.7. The text gives a description of the polarization states.

The optical probe, focused through the back of the substrate to a spot diameter less than or equal to the conductor width, is modulated by the voltage on the conductor nearly independent of signals from nearby conductors [1.41].

In both cases the optical probe is reflected from metalization on the IC. The signal is proportional to the amount of light reflected, and if the reflectivity of the metalization varies, the signal strength also varies. The signal can be normalized to the amount of reflected light, but metalization such as ohmic contacts, which may be very rough, will cause poor signal sensitivity if a large fraction of the probe beam is scattered. Second level metal, which may rest on a thin layer of dielectric such as  $\text{SiO}_2$  or  $\text{SiN}_2$  (silicon nitride), can degrade the signal due to the voltage drop across the dielectric (reducing the voltage across the GaAs substrate) and a change in the reflectivity of the probe beam.

The optical quality of the wafer surfaces must also be considered for optical probing. Because IC's are patterned by optical lithography, the wafer top surface has an excellent optical finish. For backside probing, the back of the wafer may require polishing to prevent scatter of the probe beam, depending on the wafer vendor (many wafers are supplied with both sides polished) and the IC process (for example, a wafer may be thinned by lapping with a coarse abrasive, leaving the backside rough and of poor optical quality). Backside polishing is easily accomplished with a one-step mechanical-chemical polish. For frontside probing the ground plane should be sufficiently reflective to provide a good return beam - most MMIC's tested at Stanford have shown adequate ground-plane reflectivity.

In reflection-mode probing, the incident and reflected beams are separated by manipulation of their polarizations (Fig. 1.8). The advantages of this arrangement for IC probing are on-axis focusing for diffraction-limited spot size, ease-of-alignment, and efficient use of the optical signal (in contrast to using a non-polarizing beamsplitter to separate the incident and return beams, which attenuates the optical power by one-half on each pass). The polarization states of this arrangement are analyzed using the Jones-vector notation, and are qualitatively described as follows. A linearly polarized probe beam from the polarizing beamsplitter passes through a quarter-wave plate, oriented at  $22.5^\circ$  to the axis of the beamsplitter, producing an elliptical polarization with its major axis oriented at  $22.5^\circ$ . A half-wave plate oriented at  $33.75^\circ$  then rotates the elliptical polarization an additional  $22.5^\circ$ , to align its major axis at  $45^\circ$  to the [011] direction of the GaAs substrate (i.e. oriented at  $45^\circ$  to the substrate cleave planes). The on-axis probe beam is focused by a microscope objective next to a conductor (frontside probing) or on the conductor (backside probing). The reflected beam passes back through the lens and

the wave plates, producing a linear polarization at 45° to the axes of the polarizing beam-splitter, and half of the light is directed by the beamsplitter onto a photodiode. The probed conductor voltage changes the polarization of the return beam through the electrooptic effect by changing the *angle* of the linearly polarized light prior to the polarizer, and thus the intensity incident upon the photodiode. The resulting intensity varies as in (1.11) where  $V_{\pi}$  is now

$$V_{\pi} = \frac{\lambda_0}{4n_0^3 r_{41}} \cong 5 \text{ kV} \quad (1.12)$$

giving twice the sensitivity for the reflection-mode cases. The on-axis return beam may be separated from the incident beam with a Faraday isolator. The signal from this beam is out-of-phase with the first beam allowing for differential detection to further improve signal sensitivity.

#### 1.4 Signal Recovery using Repetitive Sampling

The longitudinal reflection-mode geometries provide intensity modulation proportional to voltage. With a continuous optical probe beam, the output intensity incident upon the photodiode will be a large steady-state intensity plus a small intensity change proportional to the voltage of the probed conductor. Microwave-frequency or picosecond-risetime signals result in microwave-frequency or picosecond-risetime modulation of the probe beam. Detection of such signals requires a photodiode/receiver system with bandwidth comparable to that of the detected signal. A system using commercial sampling oscilloscopes and state-of-the-art infrared photodiodes, each limited to about 20 GHz, has insufficient bandwidth for many high-speed and microwave GaAs circuits. In addition, the small modulation provided by the electrooptic effect results in extremely poor signal-to-noise ratio using direct detection at microwave bandwidths, and thus very poor instrument sensitivity. Repetitive sampling techniques eliminate these problems. Cf. [1.47].

Mode-locked laser systems in conjunction with optical pulse compressors can generate extremely short optical pulses. At visible wavelengths, pulses as short as 6 fs [1.42,1.43] have been generated, while at the infrared wavelengths (where GaAs is transparent), pulses as short as 19 fs have been generated [1.44,1.45]. Sampling techniques using a pulsed optical probe can achieve a time resolution set by the optical pulse duration and the circuit-probe interaction time, with potential instrument bandwidths

exceeding 100 GHz. The following section describes how repetitive pulse trains are used to measure microwave/millimeter-wave signals in the frequency domain and picosecond risetime signals in the time domain. Repetitive sampling in the frequency domain can be described as *harmonic mixing*, where the electrooptic sampler measures the amplitude and phase of sinusoidal voltages, as with a microwave network analyzer. In the time domain, repetitive sampling, also termed synchronous sampling, allows an equivalent-time measurement of voltage waveforms, as with a sampling oscilloscope. [ 1 . 47 ]

This section begins with a simple, ideal description of a mode-locked, pulse-compressed laser suitable for describing signal recovery using repetitive sampling. The laser's output intensity is modeled as a train of perfect (i.e. no amplitude noise or pulse-to-pulse jitter) delta functions.

$$p(t) = P_0 T_0 \sum_{n=-\infty}^{+\infty} \delta(t - nT_0) \quad (1.13)$$

which has a frequency domain representation of

$$P(f) = P_0 \sum_{n=-\infty}^{+\infty} \delta(f - nf_0) \quad (1.14)$$

where  $T_0$  is the pulse-to-pulse period and  $f_0 = 1/T_0$  is the pulse repetition rate. In the following sections of this chapter, this model for the laser pulse train will be extended to include its pulsewidth and noise characteristics.

#### 1.4.1 Harmonic Mixing

Harmonic mixing is used to recover the magnitude and phase of the measured signal response at the circuit drive frequency, i.e. to determine the *small-signal response* of the DUT. The measured signal is

$$v(t) = |\tilde{v}_s| \cos(2\pi f_s t + \phi) \quad (1.15)$$

or, using complex exponential notation,

$$v(t) = \frac{\tilde{v}_s}{2} \exp(+j2\pi f_s t) + \frac{\tilde{v}_s^*}{2} \exp(-j2\pi f_s t) \quad (1.16)$$

where  $\tilde{v}_s = |\tilde{v}_s| \exp(j\phi)$  and  $\phi = \tan^{-1} \left[ \frac{\text{Im}(\tilde{v}_s)}{\text{Re}(\tilde{v}_s)} \right]$

represents an arbitrary magnitude and phase of the signal,  $f_s$  is the signal frequency, and the asterisk \* represents the complex conjugate. The frequency-domain representation of this signal is

$$V(f) = \frac{\tilde{v}_s}{2} \delta(f - f_s) + \frac{\tilde{v}_s^*}{2} \delta(f + f_s) \quad (1.17)$$

The intensity-modulated optical output is then (1.12) as a function of time,

$$P_{out}(t) = P(t) \left[ 1 + \frac{\pi}{V_\pi} v(t) \right] \quad (1.18)$$

and has a frequency spectrum determined by the spectrum of the laser *convolved* with the spectrum of the measured signal [1.46]. In the frequency domain

$$P_{out}(f) = P(f) * \left[ \delta(f) + \frac{\pi}{V_\pi} V(f) \right] \quad (1.19)$$

where  $P_{out}(f)$  is the intensity spectrum out of the polarizer,  $P(f)$  is the laser intensity spectrum,  $\delta(f)$  is a delta function, and \* represents the convolution operation. Substituting (1.14) and (1.17) into (1.19) gives

$$P_{out}(f) = P_0 \sum_n \delta(f - nf_0) * \left\{ \delta(f) + \frac{\pi}{V_\pi} \left[ \frac{\tilde{v}_s}{2} \delta(f - f_s) + \frac{\tilde{v}_s^*}{2} \delta(f + f_s) \right] \right\} \quad (1.20)$$

If the signal frequency  $f_s$  is set to an exact multiple  $N$  of the laser repetition rate  $f_0$ ,  $f_s = Nf_0$ , then



$$P_{out}(f) = P_0 \sum_n \delta(f - nf_0) \left[ 1 + \frac{\pi}{V_\pi} \left( \frac{\tilde{v}_s}{2} + \frac{\tilde{v}_s^*}{2} \right) \right] \quad (1.21)$$

This has spectral components at DC and multiples of the laser repetition rate, due to the transmitted part of the laser intensity, plus small changes at each multiple of the laser rep rate corresponding to the measured signal  $v(t)$ . The DC value is

$$P_{DC} = P_0 \left[ 1 + \frac{\pi}{2V_\pi} (\tilde{v}_s + \tilde{v}_s^*) \right]$$

or

(1.22)

$$P_{DC} = P_0 \left( 1 + \frac{\pi}{V_\pi} |\tilde{v}_s| \cos\phi \right)$$

Because the modulation due to the typical signals is small (for signal levels of 1 V, the amount of modulation is about  $\pi/V_\pi = 0.06\%$ ), detecting this small change in the DC spectral component is rather impractical. Instead, the signal frequency is set to an exact multiple of the laser repetition rate plus some frequency offset  $\Delta f$

$$f_s = Nf_0 + \Delta f \quad (1.23)$$

The signal component then lies in a frequency range separate from the laser intensity spectrum. In addition, the frequency offset is chosen to lie in a spectral region free of spurious noise (to allow shot-noise limited detection as discussed Section 3.2), and where conventional photodiode receivers and radio-frequency synchronous detectors can be used. The resulting output intensity is

$$P_{out}(f) = P_0 \sum_n \left\{ \delta(f - nf_0) + \frac{\pi}{V_\pi} \left[ \frac{\tilde{v}_s}{2} \delta(f - nf_0 - \Delta f) + \frac{\tilde{v}_s^*}{2} \delta(f + nf_0 + \Delta f) \right] \right\} \quad (1.24)$$

Figure 1.9 shows a graphic representation of harmonic mixing. The signal appears in the output intensity spectrum as amplitude-modulation sidebands around each laser harmonic, scaled by  $\pi/V_\pi$ . The magnitude and phase of the signal is recovered from the baseband

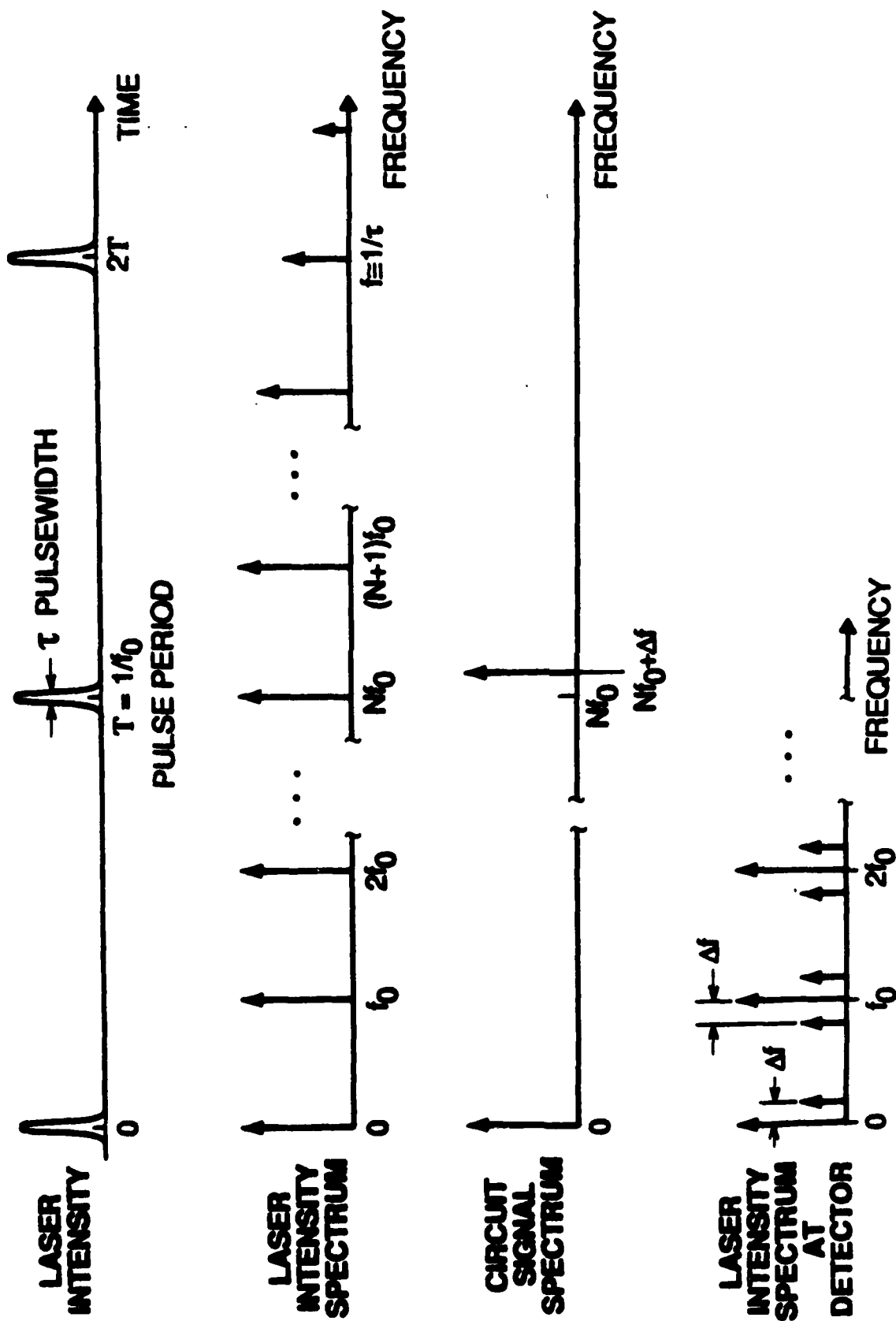
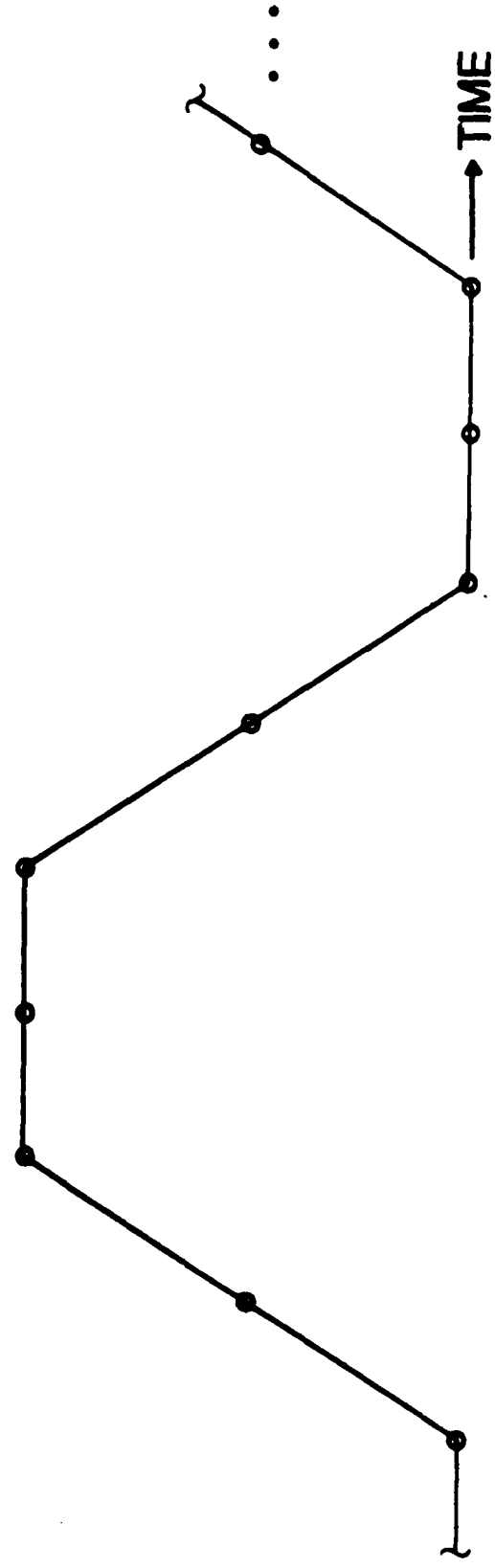
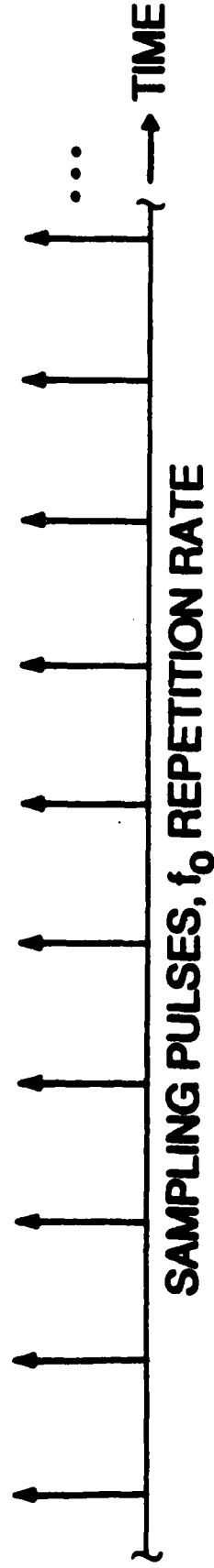
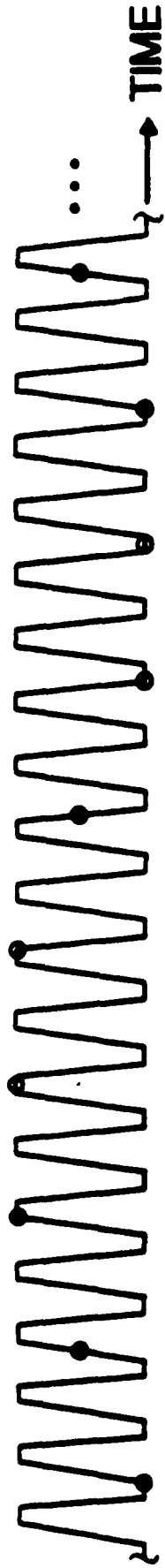


Fig. 1.9. Electrooptic harmonic mixing. The signal spectrum mixes with the laser intensity spectrum to produce replicas of the signal spaced by  $\Delta f$  around each laser harmonic. The recovered baseband signal is a replica of the actual signal with scaled magnitude and equal phase as described by (1.24).

SIGNAL WAVEFORM,  $N \cdot f_0 + \Delta f$  REPETITION RATE (N=2)



SAMPLED WAVEFORM,  $\Delta f$  REPETITION RATE

Fig. 1.10. Equivalent-time sampling. Typically,  $f_0 \approx 82$  MHz,  $0 \leq \Delta f \leq 500$ , and  $\Delta f \approx 10$  Hz.

harmonic with a RF photodiode and a synchronous detector. The baseband signal (the signal term at  $n = 0$ ) is

$$P_{BB} = \frac{P_0\pi}{V_\pi} \left[ \frac{\tilde{v}_s}{2} \delta(f - \Delta f) + \frac{\tilde{v}_s^*}{2} \delta(f + \Delta f) \right] \quad (1.25)$$

and its time domain representation is

$$\begin{aligned} P_{BB}(t) &= \frac{P_0\pi}{V_\pi} \left[ \frac{\tilde{v}_s}{2} \exp(+j2\pi\Delta f t) + \frac{\tilde{v}_s^*}{2} \exp(-j2\pi\Delta f t) \right] \\ &= \frac{P_0\pi}{V_\pi} |\tilde{v}_s| \cos(2\pi\Delta f t + \phi) \end{aligned} \quad (1.26)$$

Equation (1.26) verifies that the measured signal is a replica of the actual signal, with its frequency-scaled to  $\Delta f$ , its amplitude-scaled by  $P_0\pi/V_\pi$  and its phase preserved. The offset  $\Delta f$  is set above the low-frequency laser noise, but in the range of conventional synchronous receivers.

#### 1.4.2 Equivalent-time Sampling

Equivalent-time or synchronous sampling is used to recover the time waveform of the measured signal and to determine the circuit's *large-signal response*. In equivalent-time sampling, an optical pulse samples a repetitive voltage waveform. If the waveform repeats at *exactly*  $Nf_0$ , an integer multiple of the probe repetition rate, an optical pulse interacts with the waveform every  $N^{\text{th}}$  period at a fixed point within its cycle. Over many repetitions, the pulses sample the voltage waveform at the same time within the cycle, producing an equal modulation of each pulse. The resulting change in the average intensity of the probe beam is proportional to the signal, allowing detection by a photodiode receiver whose bandwidth is much less than the pulse repetition rate. To detect the entire time waveform, the signal frequency is increased by a small amount  $\Delta f$  (Fig. 1.10). The probe pulses are then slowly delayed with respect to the waveform, sampling successively delayed points, so that the average output intensity changes in proportion to the waveform, but repeating at a rate  $\Delta f$ . A photodiode receiver averages (by low-pass filtering) the output intensity over a period much longer than pulse-to-pulse period  $T$ , eliminating the individual pulses and measuring the change in intensity due to the signal.

The signal  $v(t)$  is now an arbitrary waveform that repeats with a period

$$T_s = \frac{1}{f_s} = \frac{1}{Nf_0 + \Delta f} \quad (1.27)$$

so that

$$v(t) = v(t - T_s) \quad (1.28)$$

The output intensity is now

$$P_{out}(t) = P_0 T_0 \sum_n \delta(t - nT_0) \left[ 1 + \frac{\pi}{V_\pi} v(t) \right] \quad (1.29)$$

and is non-zero only when  $t = nT_0$

$$P_{out}(t) = P_0 T_0 \sum_n \delta(t - nT_0) \left[ 1 + \frac{\pi}{V_\pi} v(nT_0) \right] \quad (1.30)$$

Since  $v(t)$  is periodic with period  $T_s$ , its argument can be shifted by any integer multiple of  $T_s$ , such as  $nNT_s$ . Then, the argument of  $v$  in (1.30) becomes

$$\begin{aligned} nT_0 - nNT_s &= \frac{n}{f_0} - \frac{nN}{f_s} \\ &= \frac{nf_s - nNf_0}{f_0 f_s} \\ &= \frac{\Delta f}{f_s} nT_0 \end{aligned} \quad (1.31)$$

and (1.30) is then

$$P_{out}(t) = P_0 T_0 \sum_n \delta(t - nT_0) \left[ 1 + \frac{\pi}{V_\pi} v\left(\frac{\Delta f}{f_s} t\right) \right] \quad (1.32)$$

The signal  $v(t)$  has been scaled in time by the factor  $\Delta f/f_s$ , slowing it to an equivalent time set by the repetition rate  $\Delta f$ , chosen to be much less than  $f_0$ . The receiver low-pass filters

the output intensity to measure the average intensity, removing the train of optical pulses and giving

$$P_{DC}(t) = P_0 \left[ 1 + \frac{\pi}{V_{\pi}} v \left( \frac{\Delta f}{f_s} t \right) \right] \quad (1.33)$$

The probe varies with  $v(t)$  but at a scaled-down equivalent time set by the ratio  $\Delta f/f_s$ . Typically,  $f_0$  is  $\approx 82$  MHz,  $N$  varies from 1 to 500 for circuit drive frequencies up to 40 GHz, and  $\Delta f$  is 10 to 100 Hertz.

A frequency-domain analysis of equivalent time sampling, similar to the harmonic mixing analysis, also yields the same result. The signal voltage is expressed as the sum of weighted harmonics at multiples of its fundamental frequency

$$V(f) = \sum_{n=-n_{max}}^{n_{max}} [\tilde{v}_n \delta(f - nf_s)] \quad (1.34)$$

where  $\tilde{v}_n = \tilde{v}_n^*$ . Again,  $f_s$  is set to  $Nf_0 + \Delta f$ ; each signal at  $nf_s$  mixes to a frequency as in the harmonic mixing case of  $n\Delta f$ , and the resulting baseband signal of the output intensity is

$$P_{BB} = P_0 \left\{ \delta(f) + \frac{\pi}{V_{\pi}} \sum_{-n_{max}}^{n_{max}} [\tilde{v}_n \delta(f - n\Delta f)] \right\} \quad (1.35)$$

This has a time-domain representation identical to (1.33).

## 1.5 Conclusion

Traditional electronic test techniques do not provide the capabilities needed to examine internal node voltages in the microwave and millimeter-wave regime. Direct electrooptic sampling passes picosecond infrared laser pulses through the GaAs substrate to non-invasively sense frontside potentials. Sampling techniques permit signal recovery in either a harmonic-mixing or equivalent-time sampling mode for vector or time measurements, respectively.

## 1.6 References for Section 1

- 1.1 P.T. Greiling: "High-speed digital IC performance outlook, " *IEEE Trans. Microwave Theory Tech.*, vol. MTT-35, pp. 245-259, 1987.
- 1.2 R.E. Williams, *GaAs IC Processing Techniques*, Dedham, MA: Artech House, 1984, pp. 44-47.
- 1.3 H.Q. Tserng and B. Kim, "110 GHz GaAs FET Oscillator," *Elec. Lett.*, vol. 21, pp. 178-179, 1985.
- 1.4 T. Henderson, M.I. Aksun, C.K. Peng, Hadis Morkoc, P.C. Chao, P.M. Smith, K.-H. G. Duh, and L.F. Lester, "Microwave performance of a Quarter-Micrometer Gate Low-Noise Pseudomorphic InGaAs/AlGaAs Modulation-Doped Field Effect Transistor," *IEEE Elect. Dev. Lett.*, vol. EDL-7, pp. 649-651, 1986.
- 1.5 T.C.L.G. Sollner, E.R. Brown, W.D. Goodhue, and H.Q. Le, "Observation of millimeter-wave oscillations from resonant tunneling diodes and some theoretical considerations of ultimate frequency limits", *Appl. Phys. Lett.*, vol. 50, pp. 332-334, 1987.
- 1.6 J.F. Jensen, L.G. Salmon, D.S. Deakin, and M.J. Delaney, "Ultra-high speed GaAs static frequency dividers," Technical Digest of the 1986 International Electron Device Meeting, pp. 476-479.
- 1.7 K.C. Wang, P.M. Asbeck, M.F. Chang, G.J. Sullivan, and D.L. Miller, "A 20 GHz frequency divider implemented with heterojunction bipolar transistors," *IEEE Elec. Dev. Lett.*, vol. EDL-8, pp. 383-385, 1987.
- 1.8 R.L. Fork, C.H. Brito-Cruz, P.C. Becker, and C.V. Shank, "Compression of optical pulses to six femtoseconds by using cubic phase compensation," *Opt. Lett.*, vol. 12, pp. 483-485, 1987.
- 1.9 J.B. Gunn, "Sampling system utilizing electrooptic techniques," U.S. Patent no. 3,614,451, issued Oct. 1971.
- 1.10 J.A. Valdmanis, G.A. Mourou, and C.W. Gabel, "Picosecond electro-optic sampling system," *Appl. Phys. Lett.*, vol. 41, pp. 211-212, 1982.
- 1.11 B.H. Kolner, D.M. Bloom, and P.S. Cross, "Electro-optic sampling with picosecond resolution," *Elect. Lett.*, vol. 19, pp. 574-575, 1983.
- 1.12 B.H. Kolner and D.M. Bloom, "Direct electro-optic sampling of transmission-line signals propagating on a GaAs substrate," *Elect. Lett.*, vol. 20, pp. 818-819, 1984.
- 1.13 B.H. Kolner, "Picosecond electro-optic sampling in gallium arsenide," *Ph.D. Thesis*, Stanford University, Stanford, CA, 1985.

- 
- 1.14 K.J. Weingarten, M.J.W. Rodwell, H.K. Heinrich, B.H. Kolner, and D.M. Bloom, "Direct electro-optic sampling of GaAs integrated circuits," *Elect. Lett.*, vol. 21, pp. 765-766, 1985.
  - 1.15 E.W. Strid, K.R. Gleason, and T.M. Reeder, "On-wafer measurement of gigahertz integrated circuits," *VLSI Electronics: Microstructure Science, Vol 11*, New York: Academic Press, 1985, pp. 265-287.
  - 1.16 Cascade Microtech, Inc., P.O. Box 2015, Beaverton, OR 97075.
  - 1.17 Hypres, Inc., 175 Clearbrook Rd., Elmsford, NY 10523.
  - 1.18 "Electron-beam testing of VLSI chips gets practical," *Electronics*, March 24, 1986, pp. 51-54.
  - 1.19 R. Iscoff, "E-beam probing systems: filling the submicron gap," *Semiconductor International*, Sept. 1985, pp. 62-68.
  - 1.20 P. May, J.-M. Halbout, and G. Chiu, "Laser pulsed E-beam system for high speed IC testing," *Picosecond Electronics and Optoelectronics*, New York: Springer-Verlag, 1987.
  - 1.21 P. May, J.-M. Halbout, and G. Chiu, "Picosecond photoelectron scanning electron microscope for noncontact testing of integrated circuits," *Appl. Phys. Lett.*, vol. 51, pp. 145-147, 1987.
  - 1.22 R.B. Marcus, A.M. Weiner, J.H. Abeles, and P.S.D. Lin, "High-speed electrical sampling by fs photoemission," *Appl. Phys. Lett.*, vol. 49, pp. 357-359, 1986.
  - 1.23 J. Bokor, A.M. Johnson, R.H. Storz, and W.M. Simpson, "High-speed circuit measurements using photoemission sampling," *Appl. Phys. Lett.*, vol. 49, pp. 226-228, 1986.
  - 1.24 A.M. Weiner, P.S.D. Lin, and R.B. Marcus, "Picosecond temporal resolution photoemissive sampling," *Appl. Phys. Lett.*, vol. 51, pp. 358-360, 1987.
  - 1.25 H.K. Heinrich, D.M. Bloom, and B.R. Hemenway, "Noninvasive sheet charge density probe for integrated silicon devices," *Appl. Phys. Lett.*, vol. 48, pp. 1066-1068, 1986.
  - 1.26 H.K. Heinrich, "A noninvasive optical probe for detecting electrical signals in silicon integrated circuits," *Ph.D. Thesis*, Stanford University, Stanford, CA, 1987.
  - 1.27 B.R. Hemenway, H.K. Heinrich, J.H. Goll, Z. Xu, and D.M. Bloom, "Optical detection of charge modulation in silicon integrated circuits using a multimode laser-diode probe," *IEEE Elect. Dev. Lett.*, vol. EDL-8, pp. 344-346, 1987.
  - 1.28 A. Black, C. Courville, G. Schultheis, and H. Heinrich, "Optical sampling of GHz charge density modulation in silicon bipolar transistors," *Elec. Lett.*, vol. 23, pp. 783-784, 1987.



- 
- 1.29 J.A. Valdmanis, G.A. Mourou, and C.W. Gabel, "Subpicosecond electrical sampling," *IEEE J. Quantum Elect.*, vol. QE-19, pp. 664-667, 1983.
- 1.30 J.A. Valdmanis and G. Mourou, "Subpicosecond electrooptic sampling: principles and applications," *IEEE J. Quantum Elect.*, vol. QE-22, pp. 69-78, 1986.
- 1.31 D.R. Dykaar, R. Sobolewski, J.F. Whitaker, T.Y. Hsiang, G.A. Mourou, M.A. Hollis, B.J. Clifton, K.B. Nichols, C.O. Bozler, and R.A. Murphy, "Picosecond characterization of ultrafast phenomena: new devices and new techniques," *Ultrafast Phenomena V*, ed. by G.R. Fleming and A.E. Siegman, Springer Ser. Chem. Phys., Vol. 46, New York:Springer-Verlag, 1986 pp. 103-106.
- 1.32 J.A. Valdmanis and S.S. Pei, "A non-contact picosecond prober for integrated circuit testing," *Picosecond Electronics and Optoelectronics*, New York: Springer-Verlag, 1987.
- 1.33 J.A. Valdmanis, "1 THz-bandwidth prober for high-speed devices and integrated circuits," *Elec. Lett.*, vol. 23, pp. 1308-1310, 1987.
- 1.34 I.P. Kaminow, *An Introduction to Electro-Optic Devices*. New York: Academic Press, 1974.
- 1.35 I.P. Kaminow and E.H. Turner, "Electrooptic light modulators," *Proc. IEEE*, vol. 54, pp. 1374-1390, 1966.
- 1.36 B.H. Kolner and D.M. Bloom, "Direct electrooptic sampling of transmission-line signals propagating on a GaAs substrate," *Elect. Lett.*, vol. 20, pp. 818-819, 1984.
- 1.37 B.H. Kolner and D.M. Bloom, "Electrooptic sampling in GaAs integrated circuits," *IEEE J. Quant. Elect.*, vol. QE-22, pp. 79-93, 1986.
- 1.38 A. Yariv and P. Yeh, *Optical Waves in Crystals*, New York: New York: John Wiley & Sons, Inc, 1984, pp. 286-287.
- 1.39 *Ibid*, p. 230.
- 1.40 *Ibid*, pp. 241-243.
- 1.41 J.L. Freeman, S.K. Diamond, H. Fong, and D.M. Bloom, "Electrooptic sampling of planar digital integrated circuits," *Appl. Phys. Lett.*, vol. 47, pp. 1083-1084, 1985.
- 1.42 W.H. Knox, R.L. Fork, M.C. Downer, R.H. Stolen, and C.V. Shank, "Optical pulse compression to 8 fs at a 5-kHz repetition rate," *Appl. Phys. Lett.*, vol. 46, pp. 1120-1121, 1985.
- 1.43 C.H. Brito-Cruz, R.L. Fork, and C.V. Shank, "Compression of optical pulses to 6 fs using cubic phase distortion compensation," *Technical Digest of the 1987 Conference on Lasers and Electrooptics*, pp. 12-13.
- 1.44 A.S. Gouveia-Neto, A.S.L. Gomes, and J.R. Taylor, "Generation of 33-fsec pulses at 1.32  $\mu\text{m}$  through a high-order soliton effect in a single-mode optical fiber," *Optics Letters*, vol. 12 pp. 395-397, 1987.

---

1.45 B. Zysset, W. Hodel, P. Beaud, and H.P. Weber, "200-femtosecond pulses at 1.06  $\mu\text{m}$  generated with a double-stage pulse compressor," *Optics Letters*, vol. 11, pp. 156-158, 1986.

1.46 Bracewell, p. 110.

1.47 K.J. Weingarten, "Gallium Arsenide Integrated Circuit Testing Using Electrooptic Sampling," Ph.D. Thesis, Stanford University, Stanford CA, 1987.  
Excerpts are reprinted in APPENDIX V of this report.

## 2. Increase of Electrooptic Measurement Bandwidth

A key feature of the electrooptic sampler is its large bandwidth. Electronic systems lack the short pulse generation capability to make time-mode measurements below 5 ps, while optical pulses in the infrared can be subpicosecond. To extend the bandwidth of the electrooptic sampler to the picosecond level, several improvements have been made: replacement of the acousto-optic mode-locker; and refinement of the timing stabilization system. This section describes the limiting factors to electrooptic measurement bandwidth and reports on these improvements.

With equivalent-time sampling, the signal repeats  $N$  times between probe pulses (in contrast to pump/probe sampling, which has one probe pulse for every pump signal). Because the pulse repetition rate is harmonically related to the signal repetition rate, Nyquist's sampling theorem (which states that the maximum recoverable signal bandwidth is half the sampling rate) does not apply in setting the bandwidth of this measurement. Instead, the bandwidth is determined by the sampling pulsewidth, the pulse-to-pulse jitter relative to the signal driving the circuit, the interaction time of the probe pulse and the electrical signal, and the effective receiver response time.

For a generalized description, the response of the electrooptic probe can be described as a temporal and spatial cross-correlation between the electrical signal and optical probe [2.1]. For this analysis, Gaussian distributions are assumed so that each term can be considered separately. The overall time resolution is then approximately the root-mean-square sum of these values. That is,

$$\tau_{total} = \sqrt{\tau_{PW}^2 + \tau_J^2 + \tau_{IT}^2 + \tau_{Rec}^2} \quad (2.1)$$

where  $\tau_{PW}$  is the optical pulsewidth,  $\tau_J$  is the pulse-to-pulse timing jitter,  $\tau_{IT}$  is the interaction time of the pulse through substrate, and  $\tau_{Rec}$  is the effective receiver impulse response time. Note that these values must be expressed in the same form, such as full-width at half maximum or in standard deviation (or rms).

### 2.1. Optical Pulsewidth

The optical pulse train is modeled as a train of perfect (i.e. no amplitude noise of pulse-to-pulse jitter) delta function

$$p(t) = P_0 T_0 \sum_{n=-\infty}^{+\infty} \delta(t - nT_0) \quad (2.2)$$

The finite pulse width can be included in (2.2) as

$$p(t) = \hat{p}(t) * P_0 T_0 \sum_{n=-\infty}^{+\infty} \delta(t - nT_0) \quad (2.3)$$

where  $\hat{p}(t)$  is the optical pulse shape. If the pulse is Gaussian,

$$\hat{p}(t) = \frac{1}{\tau_{fwhm}} \sqrt{\frac{4 \ln 2}{\pi}} \exp \left[ -4 \ln 2 \left( \frac{t}{\tau_{fwhm}} \right)^2 \right] \quad (2.4)$$

where  $\tau_{fwhm}$  is the full-width at half maximum pulsewidth. The frequency bandwidth of the Gaussian pulse as measured with a photodiode receiver is then

$$\tau_{fwhm} = \frac{0.312}{f_{3dB}} \quad (2.5)$$

where  $\tau_{fwhm} = 2.35\tau_{rms}$  relates the full width at half-maximum to its rms or standard deviation value, and  $f_{3dB}$  is the half power frequency. The time-bandwidth product from (2.5) is lower by a factor of  $1/\sqrt{2}$  than the time-bandwidth product of 0.441 from the pulse itself because of the square-law photodetector response. That is, the optical intensity of the pulse is converted to a current in the receiver with a resulting power spectrum proportional to the square of this current.

The pulshape of most mode-locked lasers is well-described by a Gaussian. However, the optical pulshape after pulse compression (Section 2.1.1) typically is not Gaussian but some more complicated shape. Additionally, the compressed pulse is usually too short to directly measure (with a fast photodiode, for example) and must be measured with indirect methods such as an optical intensity autocorrelator. This gives the optical pulshape's intensity autocorrelation

$$A(t) = \hat{p}(t) \star \hat{p}(t) = \int_{-\infty}^{\infty} \hat{p}(u) \hat{p}(u-t) du \quad (2.6)$$

The power spectrum of the optical pulse can then be calculated [2.1]

$$\mathcal{F}\{A(t)\} = |P(f)|^2 \quad (2.7)$$

to determine the half-power frequency. Note that from this information the response of the optical pulse *cannot* be deconvolved from the optically measured signal, because the auto-correlation gives no information about the pulse's phase response. A best-case approximation, however, would be to assume zero phase, inverse Fourier transform, then use this pulse shape for deconvolution.

### 2.1.1 Pulse-width reduction

In December of 1986, a new commercial Spectra-Physics mode-locker was installed. It succeeded in reducing the pulse width from the laser to 90 ps from about 110 ps, and the resulting compressed pulse is 1.5 to 1.75 ps, as opposed to  $\geq 2$  ps previously. The stability of the mode-locker with respect to its drive frequency was increased, requiring adjustment of less than 100 Hz as the laser warmed-up, as opposed to several hundred hertz previously. The new mode-locker has substantially lower open loop jitter but the closed loop jitter is essentially unchanged.

In November of 1987 a new, prototype, modelocker was placed in the Spectra Physics Nd:YAG mode locked laser. The new modulator resulted in a factor of two decrease in pulse width from the laser, from 90 ps to  $\approx 45$  ps. This results in several benefits for the present electro-optic sampling system. First, it is now possible, with a re-design of the pulse compressor, to have sub-picosecond pulses. Second, even without a re-designed compressor, the shorter laser pulses input into the compressor result in less Raman noise, due to the shorter interaction length between the pulse in the fiber and the stimulated Raman emission. Finally, the shorter pulses into the compressor see a greater amount of group velocity dispersion in the fiber creating a more linear frequency chirp and less power in the wings of the compressed pulses. The reduction in wings alone has increased the 3 dB

# Laser pulse Autocorrelation

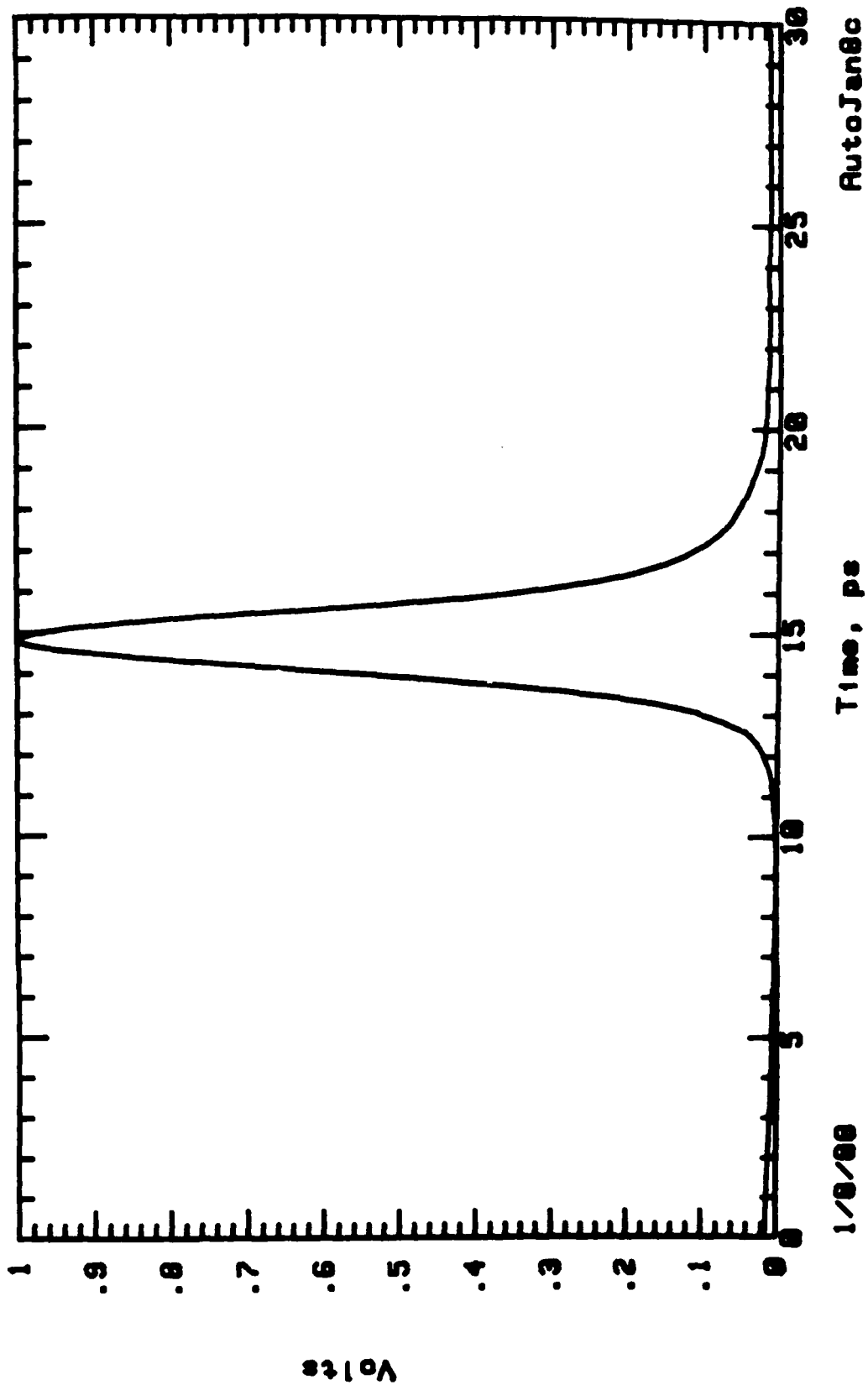


Fig. 2.1: Autocorrelation of the pulse compressor output. The deconvolved full-wid half-maximum is 1.25 ps.

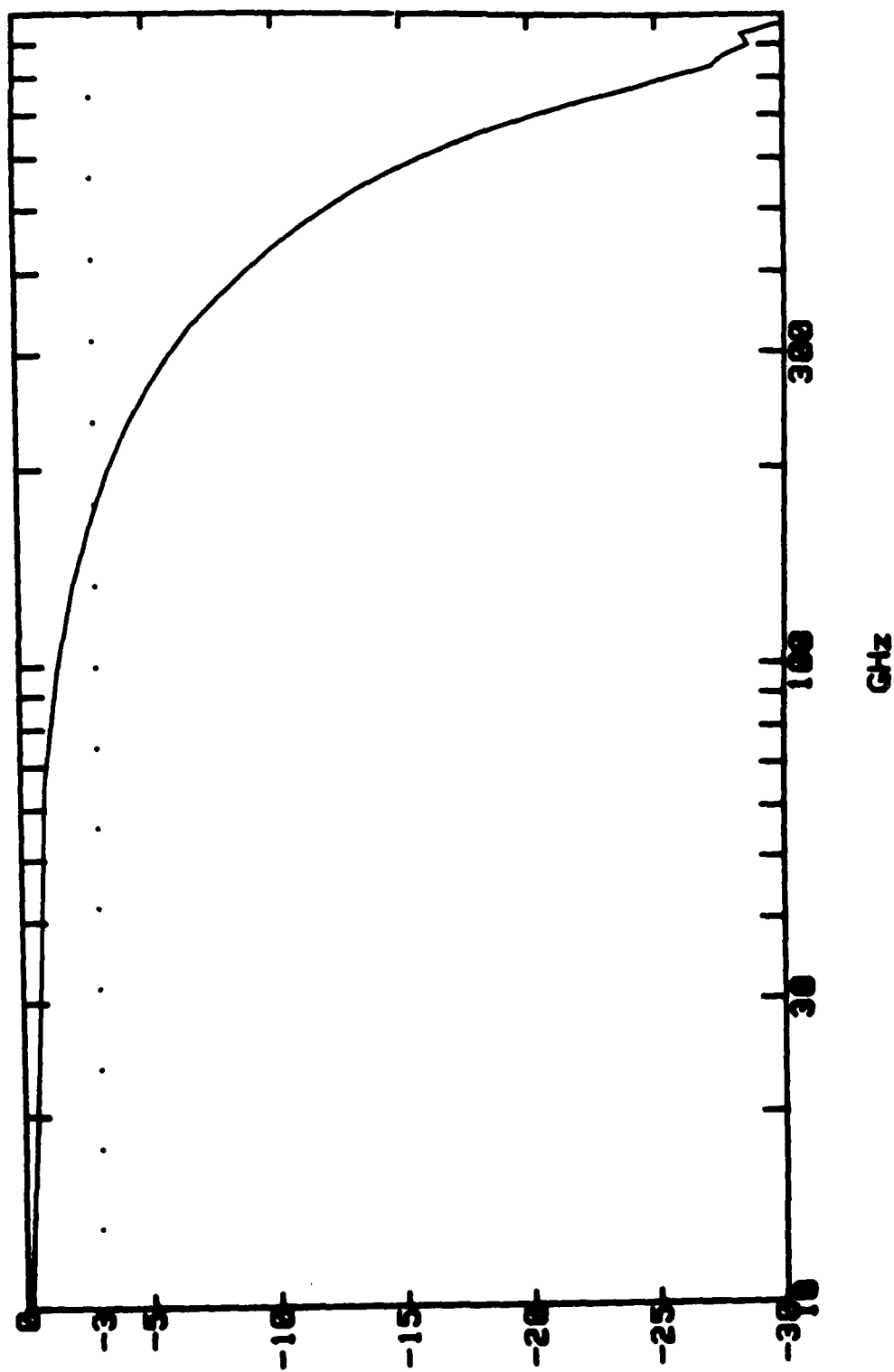


Fig 2.2: Magnitude of the spectral content of the pulse compressor output. The -3 dB point is almost 200 GHz.

bandwidth of the sampling system about 20%. There will be further work to re-design the pulse compressor for shorter sampling pulses to realize the first benefit outlined here.

Figure 2.1 presents the most recent autocorrelation of the pulse compressor output. At present the large spectral width of the pulse is being apodized by several optical components in the pulse compressor, increasing the final output width. Minor changes in component layout should permit complete recompression of the spectral content, resulting in shorter pulses. Already, simple adjustments in component alignment have resulted in a 20 % improvement in pulse width, from 1.4 ps to 1.25 ps. The frequency content of the pulse is shown in Figure 2.2. The -3 dB point has been extended to nearly 200 GHz. More extensive reworking of the compressor for optimum fiber length and grating delay promises sub-picosecond pulses.

The bandwidth of the sampling system is particularly evident in several recent measurements. Falltimes as fast as 3.5 ps have been measured on a nonlinear transmission line (cf. Section 7.2.5). Similarly, standing waves at frequencies as high as 100 GHz have been measured (Section 7.4.1). These data exhibit the large, useful bandwidth of the sampler in real applications.

## 2.2 Timing Jitter

If the optical pulse train consists of ideal delta functions but has variations in its pulse-to-pulse timing with respect to the measured signal, the time resolution is effectively degraded, smeared out by the probability distribution of its arrival time. Stabilization of the laser timing by phase-locking the laser to a high-stability reference oscillator is required to reduce the timing jitter to an amount less than the optical pulsewidth. Timing jitter also degrades signal sensitivity, introducing noise proportional to the time derivative of the measured waveform. Appendix I presents in detail the analysis of timing jitter, together with the design of a stabilizer to significantly reduce it [2.2].

The time resolution due to timing jitter is estimated by assuming a Gaussian probability distribution for the timing jitter

$$J(t) = \frac{1}{\sqrt{2\pi} \tau_{JT}} \exp\left(-\frac{t^2}{2\tau_{JT}^2}\right) \quad (2.8)$$

The optical pulsetrain is then



$$p(t) = P_0 T_0 \sum_{n=-\infty}^{+\infty} \delta[t - nT_0 - J(t)] \quad (2.9)$$

and has a power spectrum approximated to second order in  $nf_0\tau_{JT}$  by [2.3]

$$S_p(f) \cong P_0^2 \sum_n \left\{ \left[ 1 - (2\pi n f_0 \tau_{JT})^2 \right] \left[ \delta(f - n f_0) \right] + (2\pi n f_0)^2 S_J(f - n f_0) \right\} \quad (2.10)$$

where  $\tau_{JT}$  is the rms timing fluctuations and  $S_J(f)$  is the power spectral density of the timing jitter, or the phase noise.

This timing jitter can be the dominant noise term in determining the sampler bandwidth. To reduce random timing fluctuations, a timing stabilizer feedback system has been constructed. Figure 2.3 shows the block diagram of this stabilizer system [2.4]. A photodiode monitors the 82 MHz laser pulse train, and the phase of the 82 MHz fundamental component is compared to the reference oscillator, generating a phase error signal. The 41 MHz signal required for driving the laser's acousto-optic (AO) cell is generated by frequency division from the 82 MHz standard, and its timing (phase) is adjusted with a voltage-controlled phase-shifter controlled by the amplified and frequency-compensated phase error signal. With an error-free phase detector, the laser timing fluctuations are suppressed in proportion to the loop gain of the feedback system (see Appendix I).

The timing jitter is calculated by measuring the phase noise of one of the laser harmonics using a photodiode and a spectrum analyzer. The harmonic number is chosen to be great enough so that phase noise (which increases with the harmonic number) dominates the intensity noise (which is constant with harmonic number). Figure 2.4 shows the measured phase noise of the 20<sup>th</sup> harmonic of the laser with an HP 8662 low-phase noise synthesizer as the reference for the feedback system. From this measurement the timing jitter is calculated [2.4] from the relation

$$\Delta t_{rms} = \frac{T_0}{2\pi n} \sqrt{\frac{P_{SB}}{P_a}} \quad (2.11)$$

where

$$P_{SB} = 2 \int_{f_1}^{f_2} \frac{P_b(f)}{B} df \quad (2.12)$$

is the integrated phase noise power from a low frequency limit  $f_1$  to an upper frequency limit  $f_2$ ,  $P_a$  is the carrier power,  $P_b$  is the phase noise power at some frequency offset  $f$ ,  $T_0 = 1/f_0$  is the pulse period,  $n$  is the harmonic number, and  $B$  is the spectrum analyzer resolution. In practice, the calculation is done with the spectrum analyzer under control of a desktop computer [2.5]. From data similar to Fig. 2.4 the calculated timing jitter is 250 fs rms (0.6 ps FWHM to express it on the same terms as the optical pulsewidth) from  $f_1 = 50$  Hz to  $f_2 = 25$  kHz. One limitation of an RF spectrum analyzer (Hewlett Packard 8566B) is a lower frequency limit of about 50 Hz, due to the 10 Hz minimum resolution bandwidth. Jitter components at rates less than 50 Hz cannot be measured in this fashion. Long term timing drift, on the order of seconds or minutes, can be monitored with the receiver system, measuring drift of the phase of a measured sinusoid.

### 2.3. Transit time

The interaction time of the optical pulse and the electrical signal in the GaAs substrate comes from several factors: the response time of the electrooptic effect, the electrical transit time, and the optical transit time. The electrooptic effect in GaAs arises primarily from its electronic polarizability and is intrinsically very fast, with a response time on the order of 10 femtoseconds. The electrical transit time is the propagation time of the electrical signal as it traverses the spatial extent of the probe beam. For typical IC values this time is on the order of 60 fs [2.4]. The optical transit time is the propagation time of the optical pulse as it traverses the electric fields within the GaAs substrate. For frontside probing of microstrip lines, where the field is nearly uniform through the substrate, the optical transit time is proportional to the substrate thickness.

$$\tau_{\pi} = \frac{2nL}{c} \quad (2.13)$$

where  $n$  is the index of refraction of the GaAs,  $L$  is the substrate thickness, and  $c$  is the free-space speed of light. The factor of 2 is due to the reflection probing geometry which doubles the transit time (and halves  $V_{\pi}$ , the switching voltage). For backside probing of coplanar transmission lines or planar interconnections, the voltage drop in the substrate scales with the conductor spacing. In this case the optical transit time is not a function of substrate thickness but of the conductor spacing. Because the optical and microwave dielectric constants in GaAs are nearly equal, microwave transmission lines have a cutoff frequency for higher-order modes roughly equal the inverse of the optical transit time.

Well-designed microwave circuits operate at frequencies well below the multimode cutoff frequency. Only when measuring interconnects near or above the cutoff frequency (where dispersive characteristics are of interest) must the optical transit time be considered. For example, the optical transit time for a 125  $\mu\text{m}$  thick substrate, typical of MMIC's operating at frequencies below 40 GHz, is 3 ps, corresponding to a 3 dB response rolloff of >100 GHz.

#### 2.4. Effective Receiver Response

The effective receiver impulse risetime arises from the constraint put on the receiver bandwidth by the required system sensitivity. The receiver is assumed to have an ideal Gaussian impulse response

$$h(t) = \frac{1}{\sqrt{2\pi}\tau} \exp\left(\frac{-t^2}{2\tau^2}\right) \quad (2.14)$$

where  $\tau$  is the rms duration. Then, the receiver frequency response

$$H(f) = \exp\left(\frac{-f^2}{2B^2}\right) \quad (2.15)$$

has an rms bandwidth  $B = 1/2\pi\tau$ . Because the sampled signal at frequency  $f_s$  is translated to a lower frequency  $\Delta f$  at the receiver, the effective receiver impulse response for equivalent-time sampling is

$$\tau_{Rec} = \frac{\Delta f}{f_s} \tau = \frac{\Delta f}{f_s} \frac{1}{2\pi B} \quad (2.16)$$

Given a required time resolution  $\tau_{total}$  the data acquisition rate of the system is then limited. For a fixed time resolution, larger receiver bandwidths  $B$  (or shorter receiver time constants) permit faster waveform acquisition rates, but degrade the measurement sensitivity, as discussed in the next section.

## 2.5 Conclusion

The determinants of electrooptic bandwidth have been discussed. Two key contributors to bandwidth have been improved: optical pulsewidth has been reduced to 1.25 ps by incorporation of a new mode-locker, and timing jitter has been reduced to below 250 fs by active feedback stabilization. Further pulsewidth reductions are expected as the pulse compressor is modified to fully utilize the large spectral spread of the fiber output.

## 2.6 References for Section 2

---

- 2.1 R.N. Bracewell, *The Fourier Transforms and its Applications*, New York: McGraw-Hill, 1978, p. 115-116.
- 2.2 M.J.W. Rodwell, "Picosecond Electrical Wavefront Generation and Picosecond Optoelectronic Instrumentation," PhD Thesis, Stanford University (1987).
- 2.3 M.J.W. Rodwell, K.J. Weingarten, D.M. Bloom, T. Baer, and B.H. Kolner, "Reduction of timing fluctuations in a mode-locked Nd:YAG laser by electronic feedback," *Optics Letters*, vol. 11, pp. 638-640, 1986.
- 2.4 B.H. Kolner and D.M. Bloom, "Electrooptic sampling in GaAs integrated circuits," *IEEE J. Quant. Elect.*, vol. QE-22, 1986, pp. 79-93.
- 2.5 Program and calculation courtesy of B.K. Kolner, Hewlett-Packard Laboratories.

## 3. Noise in the Electrooptic Sampler

### 3.1. Sensitivity and Noise-limited Detection

If the measurement bandwidth provided by the electrooptic sampler is to be useful, the instrument must also provide sufficient sensitivity to observe signal voltages typical of high-speed GaAs circuits. As in any system, sensitivity is determined by the signal to noise ratio; the instrument's sensitivity, or minimum detectable voltage, is the signal voltage which has a measured value equal to the measurement system's noise signal. Most noise sources, with power spectral densities independent of frequency ("white" noise), have a noise voltage proportional to the square root of the signal acquisition bandwidth, and a minimum detectable voltage expressed in units of volts per root Hertz ( $V/\sqrt{\text{Hz}}$ ). Smaller minimum detectable voltages allow faster measurement acquisition for a fixed measurement accuracy. With appropriate system design and signal processing, the various sources of noise in the electrooptic sampler can be reduced or eliminated, permitting low-noise voltage measurements with fast data acquisition.

### 3.2. Noise sources in the Electrooptic Sampler

#### 3.2.1. Shot Noise

A fundamental limiting noise source in electrooptic sampling is the shot noise of the probe beam. The output intensity generates a photodiode current proportional to the intensity

$$i_{out}(t) = rp(t) = I_0 \left[ 1 + \frac{\pi}{V_{\pi}} v(t) \right] \quad (3.1)$$

where  $r$  is the responsivity of the photodiode in amperes/watt. The shot noise of the output intensity is observed as shot noise of the photodiode quiescent current  $I_0$ , and has a variance

$$\overline{i_{SN}^2} = 2qI_0B \quad (3.2)$$

where  $q$  is the electron charge, the horizontal bar denotes the statistical expectation, and  $B$  is the receiver's equivalent noise bandwidth. If the signal current  $I_0 \pi v_{min} / V_\pi$  is set equal to the shot noise current, the minimum detectable voltage is

$$v_{min} = \frac{V_\pi}{\pi} \sqrt{\frac{2qB}{I_0}} \quad (3.3)$$

For the reflection-mode probing geometries,  $V_\pi \approx 5 \text{ kV}$ , while a typical average photocurrent  $I_0$  is  $1 \text{ mA}$ . Then, normalizing to a  $1 \text{ Hz}$  receiver bandwidth, the minimum detectable voltage is

$$v_{min} = 31 \frac{\mu\text{V}}{\sqrt{\text{Hz}}} \quad (3.4)$$

### 3.2.2. Excess Noise Sources

Typically,  $v_{min} \approx 70 \mu\text{V}/\sqrt{\text{Hz}}$  is observed experimentally due to  $\approx 10 \text{ dB}$  of residual noise from the system (mainly from excess amplitude noise of the pulse compressor). This sensitivity is sufficient to acquire measurements at scan rates of  $10\text{-}100 \text{ Hz}$  with a noise floor of a few millivolts. The actual measurement system has a number of additional excess noise sources to contend with to achieve  $70 \mu\text{V}/\sqrt{\text{Hz}}$  sensitivity, such as intensity noise of the probe beam from laser fluctuations and the pulse compressor, timing jitter of the probe pulses (phase noise), and receiver noise. The noise terms representing the intensity noise and pulse-to-pulse timing jitter are included in the expression for the laser pulse train as

$$p(t) = P_0 T_0 [1 + N(t)] \sum_n \delta[t - nT_0 - J(t)] \quad (3.5)$$

where  $N(t)$  is the normalized intensity noise and  $J(t)$  is the pulse timing jitter. The laser intensity then has a power spectral density  $S_p(f)$  approximated to second order in  $nf_0\tau_{JT}$  by

$$S_p(f) \cong P_0^2 \sum_n \left\{ \left[ 1 - (2\pi n f_0 \tau_{JT})^2 \right] \left[ \delta(f - n f_0) + S_N(f - n f_0) \right] + (2\pi n f_0)^2 S_J(f - n f_0) \right\} \quad (3.6)$$

where  $S_N(f)$  is the power spectral density of the intensity noise  $N(t)$  and  $S_J(f)$  is the power spectral density of the timing jitter  $J(t)$ . The spectrum of the laser intensity is the discrete spectral lines at multiples of  $f_0$ , plus spectra resulting from amplitude-noise sidebands  $S_N(f-nf_0)$  and phase-noise sidebands  $(2\pi nf_0)^2 S_J(f-nf_0)$ .

With these amplitude and timing fluctuations, the photocurrent  $i_{out}(t)$  is

$$i_{out}(t) = I_0 \left[ 1 + \frac{\pi}{V_\pi} v(t) \right] + i_{SN} + i_{LO} + i_{L1} + i_{PN} \quad (3.7)$$

where

$$i_{LO} = I_0 N(t) \quad (3.8)$$

is the background (zero-order) laser intensity noise,

$$i_{L1} = N(t) \frac{\pi I_0}{V_\pi} v(t) \quad (3.9)$$

is a multiplicative (first-order) intensity noise from the product of laser intensity fluctuations and the signal voltage, and

$$i_{PN} = J(t) \frac{\pi I_0}{V_\pi} \frac{dv}{dt} \quad (3.10)$$

is phase noise arising from the laser timing fluctuations, assuming  $\Delta f \ll Nf_0$ , and omitting terms in  $N(t)J(t)$  as negligible.

A typical spectral density  $S_N(f)$  of the laser intensity noise  $N(t)$  is shown in Fig. 3.1. At frequencies below 10 kHz, the laser intensity noise is 60-70 dB greater than the shot noise of a 0.5 mA receiver photocurrent. At higher frequencies the noise power decreases, reaching an asymptote 5-15 dB above the shot noise level at frequencies greater than  $\approx 100$  kHz. The excess noise at frequencies above 100 kHz arises from Raman scattering and polarization noise in the optical pulse compressor. If the sampled signal were detected at DC or a low frequency near DC, the background laser intensity noise  $i_{LO}$  would degrade the minimum detectable voltage by  $10^3:1$ . Signal processing methods, such as signal

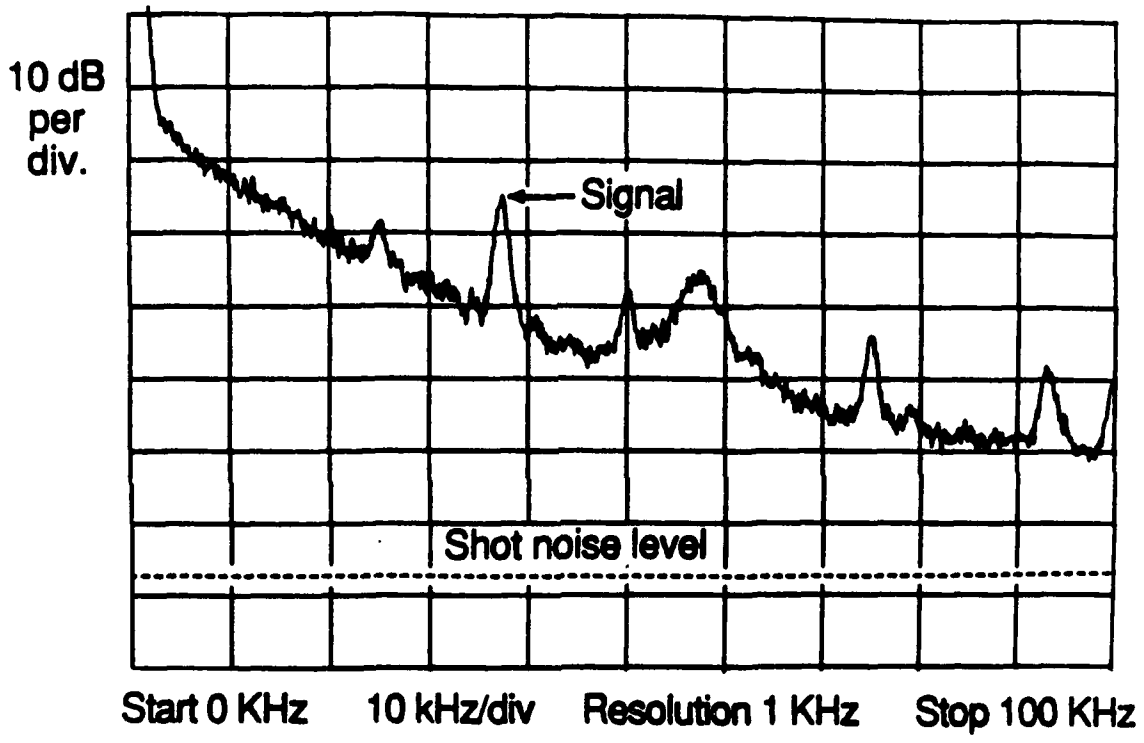


Fig.3.1. Typical spectrum of intensity noise for a mode-locked Nd:YAG laser, measured with a photodiode and spectrum analyzer. The photocurrent is 0.5 mA. At low frequencies the intensity is  $\geq 60$  dB above the shot noise of 0.5 mA photocurrent.



chopping, are required to suppress the background laser intensity noise as described in Section 3.3.

### Sources of Noise from Fiber-Grating Pulse Compressor

Excess intensity noise can increase on the compressed pulsetrain due to stimulated Raman scattering and other nonlinear processes, degrading the signal-to-noise ratio for electrooptic measurements. Stimulated Raman scattering (SRS) has gain proportional to the pump intensity and interaction length, setting an upper limit to the intensity in the fiber and an upper limit to pulse compression. SRS has a frequency shift in glass of  $440 \text{ cm}^{-1}$ , a wavelength shift from  $1.06 \text{ }\mu\text{m}$  to  $1.12 \text{ }\mu\text{m}$ . The Raman threshold pump power is predicted to be [3.1]

$$P_{th} = \frac{30A}{GL} \quad (3.11)$$

where  $A$  is the effective core area of the fiber,  $G$  is the Raman gain  $9.2 \times 10^{-12}$ , and  $L$  is the effective interaction length in the fiber. The fiber has a core diameter of approximately  $7 \text{ }\mu\text{m}$ , dispersion of  $35 \text{ ps/nm}\cdot\text{km}$  at  $1.06 \text{ }\mu\text{m}$ , and an interaction length is set by dispersion-induced walkoff between the pump and Raman pulses. One advantage of the long  $1 \text{ km}$  fiber is that SPM occurs over the entire fiber length by SRS is limited by the dispersion-induced walkoff length. The interaction length could be estimated as the time for a Raman pulse to walk-off a pump pulse by one FWHM. However, this tends to underestimate the interaction length because the pump pulse broadens as it propagates through the fiber through SPM and the dispersion. A better way to determine the interaction length is to determine the temporal separation between the pump pulse and the Raman pulse at the output of the fiber. From this measurement, shown in Fig. 3.2, the walkoff length is calculated to be  $140 \text{ meters}$ , and the Raman threshold is  $P_{th} = 90 \text{ W}$ . For the pump pulses repeating at an  $82 \text{ MHz}$  rate, the average power resulting in this peak power

$$P_{avg} = \sqrt{\frac{\pi}{4 \ln 2}} T_{fwhm} f_0 P_{peak} \quad (3.12)$$

is  $P_{avg} = 700 \text{ mW}$ , where  $T_{fwhm}$  is the pulsewidth,  $f_0$  is the pulse repetition rate, and  $P_{peak}$  is the peak power.

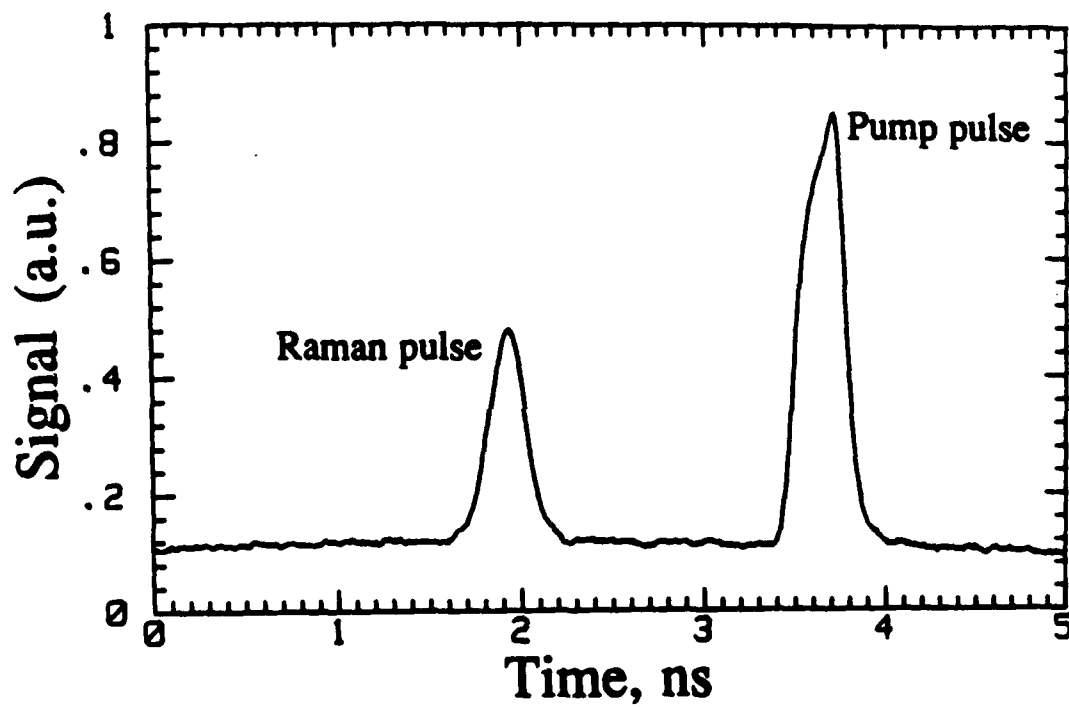


Fig.3.2. Dispersion-induced walkoff between the pump pulse and the Raman pulse from the 1 km fiber, causing a 1.8 ns separation.

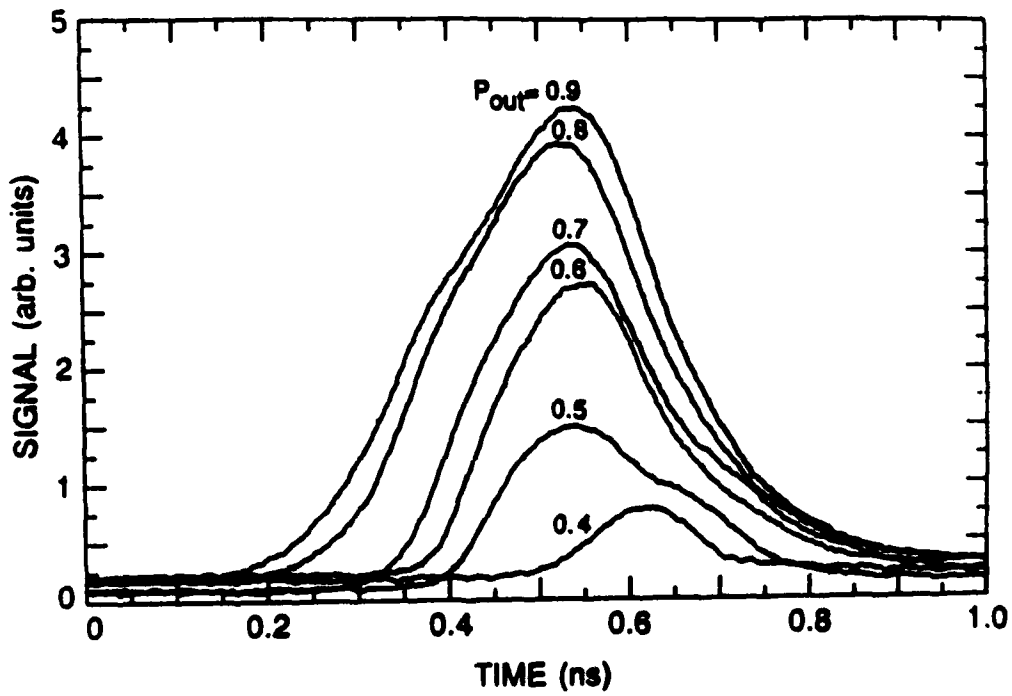


Fig.3.3. Raman pulse build-up as a function of the average power from the fiber output  $P_{out}$  before trimming the fiber to defeat the parasitic fiber-Raman laser synchronism condition.

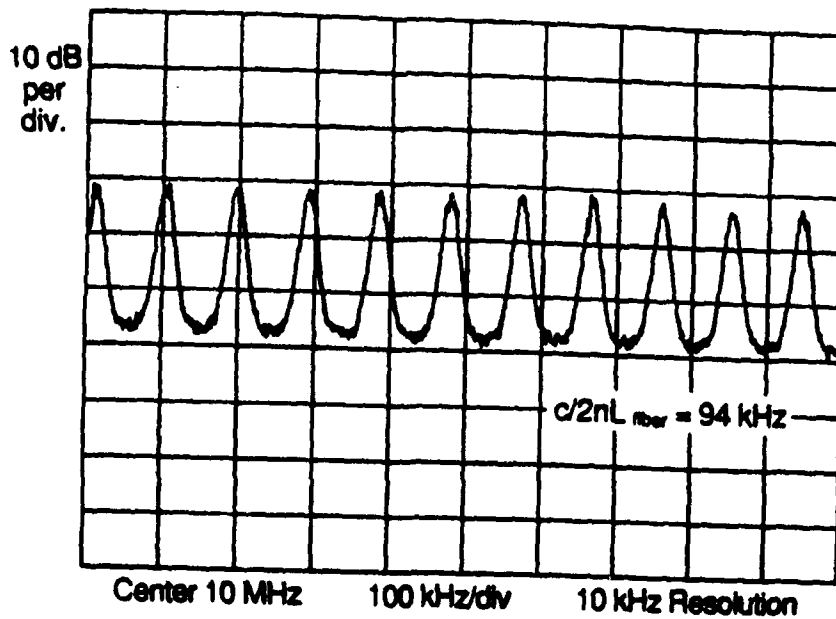


Fig.3.4. Periodic noise spectrum from parasitic fiber-Raman laser when the pulse compressor is operated near the Raman threshold. The peaking at 95 kHz corresponds to the free spectral range of the 1 km fiber.

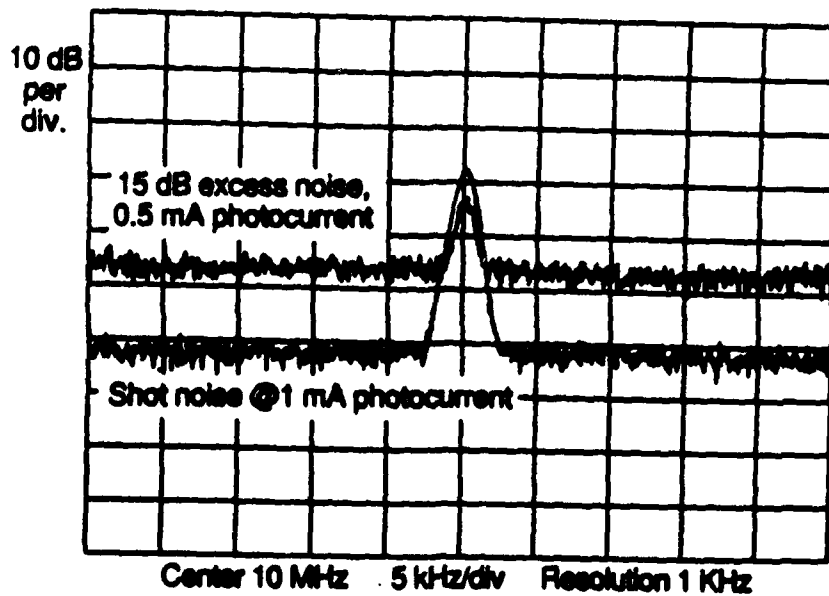


Fig.3.5. Excess intensity noise due to misadjustment of the polarization from the output of the pulse compressor fiber.

In addition, a resonant effect in longer fibers can further reduce the Raman threshold. The high gain of the SRS and 4% Fresnel reflection at each end facet form a parasitic synchronously-pumped fiber-Raman laser [3.2]. Dispersion sets the pump walkoff length of  $\approx 140$  meters for SRS and also causes the  $1.06 \mu\text{m}$  pump and the  $1.12 \mu\text{m}$  Raman pulse to separate by 1.8 ns over the length of the 1 km fiber. The weakly reflected Raman pulse is further amplified if, after its first round trip through the fiber, it is synchronized to within 1.8 ns of a pump pulse. With this condition the Raman threshold with the 1 km fiber is 350-400 mW average fiber output power. Fig. 3.3 shows the Raman pulse buildup with pump power for this condition. Trimming the fiber length a few inches defeats this synchronism and increases the Raman threshold to about 700 mW. A compression ratio of 60X is then routinely obtained at  $\approx 400$  mW average power from the fiber output, well below the Raman threshold.

The pulse compressor introduces excess intensity noise on the compressed pulsetrain due to a variety of causes. The excess intensity noise in general increases with increasing pulse compression from either increased fiber length or increased optical power launched into the fiber. As the pump intensity approaches the SRS threshold, a substantial increase in intensity noise above the shot noise limit is observed, as shown in Fig. 3.4. The frequency period of the repetitive noise spectrum in this figure corresponds to the free spectral range of the 1 km fiber, indicative of the parasitic fiber-Raman laser.

In addition to SRS the fiber generates broadband polarization noise, possibly arising from guided acoustic wave Brillouin scattering [3.3] or some other nonlinear process in the fiber. The polarization noise is converted to amplitude noise after passing through the grating pair in the compressor, which has polarization dependent reflectivity. Adjusting the polarization from the fiber to maximize transmission through the grating path results in second-order intensity variations due to polarization fluctuations, reducing this excess noise to a level near the shot noise limit (Fig. 3.5). However, this excess noise typically adds 10-15 dB of broadband background noise above the shot noise limit.

### 3.3. Noise Reduction In the Electrooptic Sampler

To improve the sensitivity and dynamic range of the electrooptic sampler, several modifications have been made to the system. Key among these is the reduction of pulse-to-pulse timing jitter below 300 fs by a refined phase-lock-loop, and the insertion of a Faraday Isolator. Since the timing jitter leads to limitations in bandwidth, it is discussed in more

detail in Section 2.1. We consider here methods both for reducing noise, and for reducing the effects of noise on electrooptic measurement.

### **3.3.1. Fiber Temperature Stabilization**

Temperature change of the fiber contributes to timing drift of the pulses, since the pulse compressor is "outside" the timing stabilizer feedback loop. The temperature coefficient of refractive of fused silica is  $11.8 \times 10^{-6}/^{\circ}\text{C}$  [3.4] resulting in an expected timing drift ( $\Delta t = \Delta n L/c$ ) of 39 ps/ $^{\circ}\text{C}$  for the 1 km fiber. To suppress polarization and timing drift, the non-polarization-preserving fiber is placed in an insulated container that is temperature-stabilized to  $\approx 0.1$   $^{\circ}\text{C}$ . However, temperature drift of the fiber probably accounts for most of the 2-4 ps per minute long-term timing drift observed with the system.

### **3.3.2. Active Amplitude Stabilization**

One approach to reducing low-frequency amplitude noise is to insert an active stabilizer, or "noise-eater" in the output beam. Two fundamentally different commercial laser amplitude stabilizers were evaluated. The Spectra Physics model 3260 laser amplitude stabilizer monitors the laser output with an external photodetector and uses a feedback loop to control the pumping lamp current. The evaluation results indicated that using this amplitude stabilizer a significant reduction in the low frequency intensity noise of the laser was not achieved.

The second laser amplitude stabilizer evaluated was the Cambridge Research Instrumentation model LS200. This amplitude stabilizer uses an external electrooptic modulator and a feedback loop consisting of a beam splitter, a photodiode and control electrical circuit block connected to the modulator. Fig. 3.6 shows the best performance achieved with this amplitude stabilizer. Low frequency noise reduction of 15 dB was consistently achieved with this stabilizer. However, this performance was very sensitive to the laser output power and the beam alignment. The overall conclusion was that this stabilizer required extremely fine alignment to achieve the desired level of noise reduction.

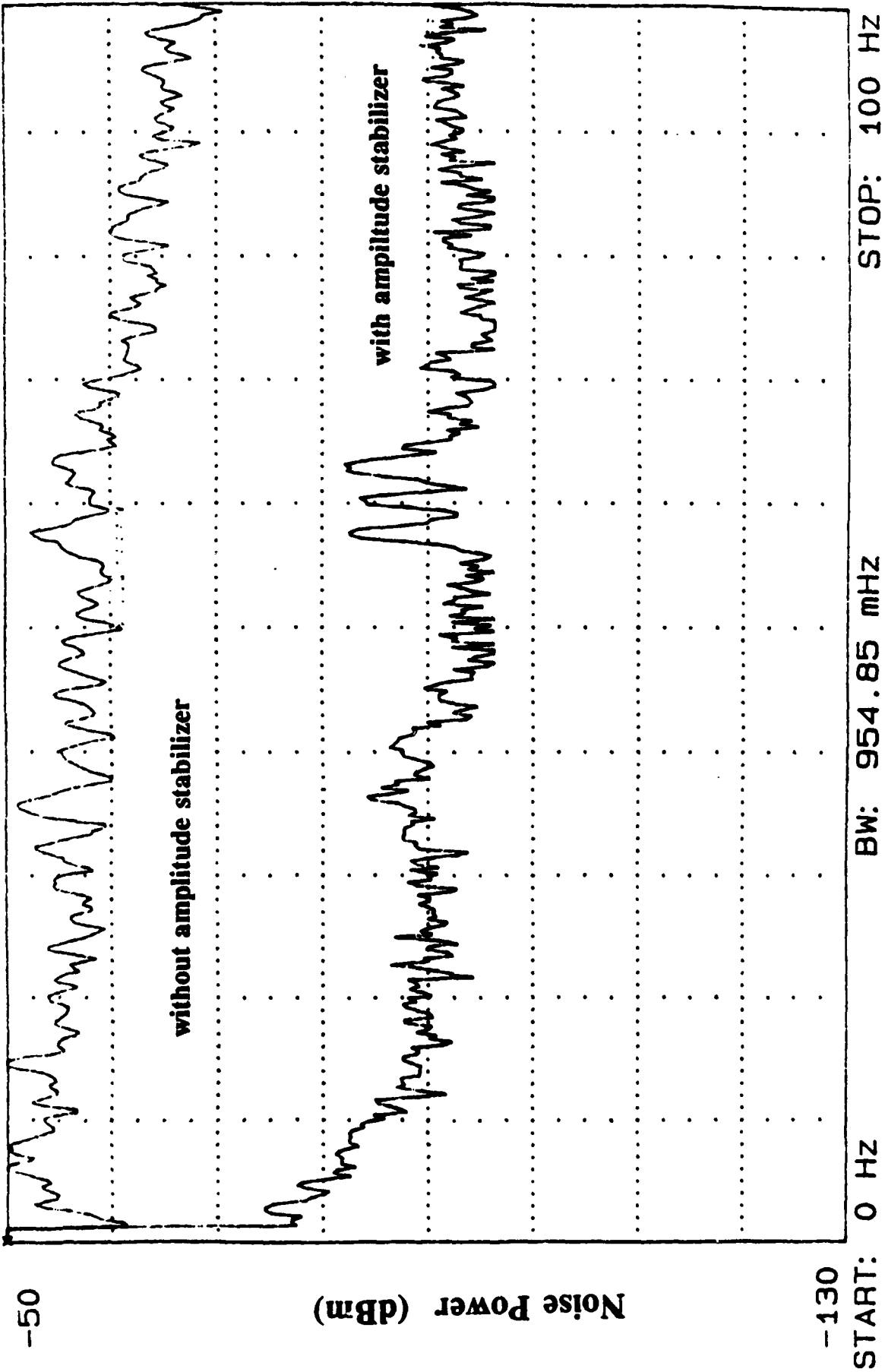


Fig. 3.6. Low frequency laser intensity noise reduction by the amplitude stabilizer

### 3.3.3. Faraday Isolator

A consequence of replacing the mode-locker with the more powerful one, described in Section 2, was a large increase in the noise sidebands. This was traced to feedback from some portion of the pulse compressor back to the laser. Particularly strong were 60 KHz relaxation oscillations aggravated by this feedback. Though normally present some 60 dB below carrier, these oscillations increased to -25 dBc when the beam was allowed to enter the fiber. Reflections from both fiber ends was eliminated as a possible source of the feedback, leaving only some continuous process such as Rayleigh scattering as a suspect mechanism. Since simple adjustments of laser to fiber distances to prevent feedback at the "open" portion of the mode-locker cycle are not possible for such a continuous mechanism, elimination of all feedback by addition of a Faraday Isolator was employed. Such a tact had been considered previously, but never pursued for lack of a clear necessity. With the assistance of Electro-optic Technology, a unit was procured and inserted in the beam path immediately after the laser. The result was suppression of the 60 KHz sidebands almost 40 dB, and significant enhancement of the autocorrelation trace stability. Low-frequency amplitude noise, and long-term mode-lock frequency drift were both reduced far below levels encountered with any of the mode-lockers. This permits much faster potential scans (cf. Section 4), as well as faster time-waveform acquisition. Such noise reduction also reopens the possibility of successfully using a commercial amplitude stabilizer.

### 3.3.4. Ratio Detection

The first-order intensity noise can be suppressed by normalizing the measured signal to the intensity fluctuations. Suppose a common mode signal is generated.

$$V_c = V_1 + V_2 = I_0 (A + B) + I_0 (A - B) \delta V \quad (3.13)$$

The ratio of  $V_d$  to  $V_c$  is

$$\frac{V_d}{V_c} = \frac{(V_1 - V_2)}{(V_1 + V_2)} = \frac{(A - B) + (A + B) \delta V}{(A + B) + (A - B) \delta V} \quad (3.14)$$

Since  $\delta V \ll 1$  and  $A = B$ , this expression to first order in  $\delta V$  is



$$\frac{V_d}{V_c} = \frac{(A-B)}{(A+B)} + \delta V \left\{ 1 - \frac{[(A-B)]^2}{[(A+B)]^2} \right\} \quad (3.15)$$

With perfect balance,  $A = B$ , and then

$$\frac{V_d}{V_c} = \delta V \quad (3.16)$$

and the signal is recovered independent of laser intensity noise.

The above discussion is an idealized case. Representative numbers for a practical experiment might be 40 dB of common mode rejection, i.e.  $A - B = 0.01$  and  $A + B = 2$ . Then,

$$\frac{V_d}{V_c} = 0.005 + \delta V (1 - 2.5 \times 10^{-5}) \quad (3.17)$$

reducing the background noise by 46 dB, and effectively eliminating multiplicative noise.

### 3.3.6. Differential Detection

Differential detection is one method to suppress background laser intensity noise. The optical system described in Fig. 3.7 provides differential signals when a Faraday isolator is used to recover the return beam. Fig. 3.8 shows a block diagram of a receiver system for differential and ratio detection.

The receivers provide a voltage signal proportional to the intensity as measured by a photocurrent  $I_0 = rP_0$

$$V_1 = AI_0(1 + \delta V) \quad (3.18)$$

$$V_2 = BI_0(1 - \delta V)$$

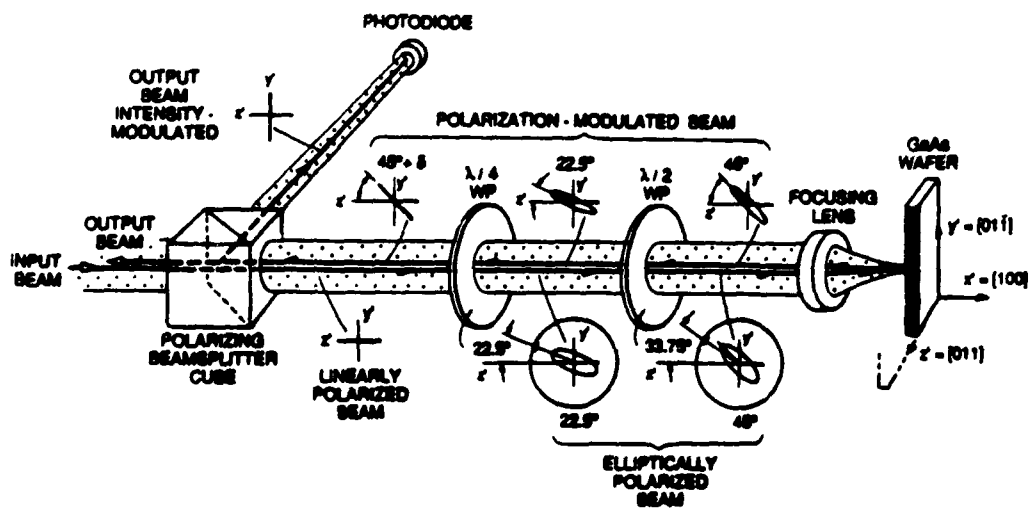


Fig. 3.7: Coaxial optical arrangement for separation of incident and reflected beams for differential detection.

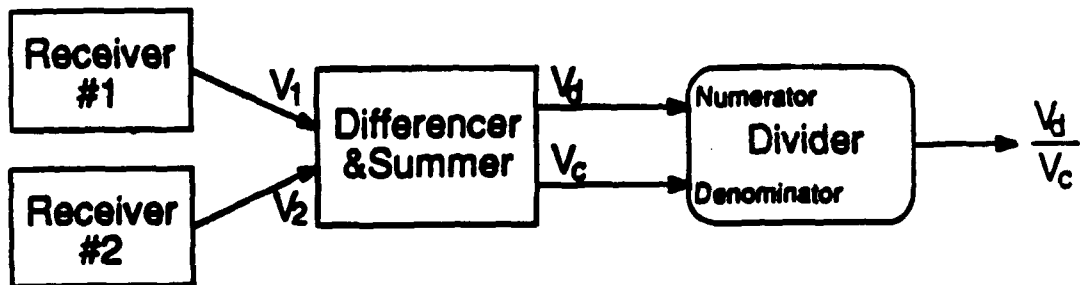


Fig. 3.8. Block diagram of a differential and ratio detection receiver

where  $V_1$  is the signal from the first receiver,  $V_2$  is the signal from the second receiver,  $I_0$  is the photocurrent,  $A$  and  $B$  are the effective receiver gains to account for imbalances in the receiver electronics and the optical system,  $\delta = \pi/V_{\pi}$  and  $V$  is the signal voltage. With an ideal differential amplifier, the difference signal is

$$V_d = V_1 - V_2 = I_0(A - B) + I_0(A + B)\delta V \quad (3.19)$$

If the receivers are perfectly balance,  $A = B = 1$ , then

$$V_d = 2I_0\delta V \quad (3.20)$$

and the background laser intensity noise from the photocurrent term is eliminated. However, the first-order intensity noise still affects the measured signal, i.e. if  $I_0$  has 1% fluctuations, then  $V_d$  will vary by the same 1%.

### 3.3.7. Optical Biasing

An alternative method to suppress intensity noise is through careful optical biasing of the quarter-wave plate (QWP) in the electrooptic modulator. From Appendix II, the expression for the y-output intensity (II.15) is

$$I_y = I_m \left[ \sin^2(2\theta) + \delta \sin(4\theta) \sin(2\theta - 4\phi) \right] \quad (3.21)$$

where  $I_m$  is the maximum photocurrent,  $\theta$  is the angle of the QWP,  $\phi$  is the angle of the half-wave plate, and  $\delta = \pi V/2V_{\pi}$ . The signal and noise terms are then

$$I_{sig} = I_m \delta \sin(4\theta) = 2I_m \delta \sin(2\theta) \cos(2\theta)$$

$$I_{DC} = I_m \sin^2(2\theta)$$

(3.22)

$$\overline{i_{SN}^2} = 2qI_{DC} = 2qI_m \sin^2(2\theta)$$

$$\overline{i_{\lambda N}^2} = K^2 I_{DC}^2 = K^2 I_m^2 \sin^4(2\theta)$$

where  $I_{DC}$  is the DC photocurrent,  $\overline{i_{SN}^2}$  is the mean-square shot noise current, proportional to the photocurrent,  $\overline{i_{\lambda N}^2}$  is the mean-square intensity noise current, which scales as the square of the photocurrent,  $K$  is a proportionality constant for the intensity noise, and  $q$  is the electron charge. Note that the  $\sin(2\theta - 4\phi)$  term is dropped because the half-wave plate can always be set so that  $\sin(2\theta - 4\phi) = 1$ . The signal-to-noise ratio is then

$$S/N = \frac{i_{sig}^2}{\overline{i_{SN}^2} + \overline{i_{\lambda N}^2}} = \frac{4I_m \delta^2 \cos^2(2\theta)}{2q + I_m K^2 \sin^2(2\theta)} \quad (3.23)$$

At the quarter wave bias point,  $\theta = 22.5^\circ$  and the  $S/N$  is (neglecting the intensity noise)

$$S/N = \frac{I_m \delta^2}{q} \quad (3.24)$$

corresponding to the shot noise limit (where  $I_m = 2I_0$ ) when  $S/N = 1$ . When the intensity noise is included, the  $S/N$  at the quarter wave bias is

$$S/N = \frac{I_m \delta^2}{q + \frac{1}{4} I_m K^2} \equiv \frac{4\delta^2}{K^2} \quad (3.25)$$

for  $\frac{1}{4} I_m K^2 \gg q$ . For intensity noise much larger than the shot noise, the  $S/N$  ratio does not depend on the photocurrent.

If the optical bias is adjusted so that  $\theta \rightarrow 0$ , the  $S/N$  is then

$$S/N = \frac{I_m \delta^2}{\frac{q}{2} + I_m K^2 \theta^2} \quad (3.26)$$

The intensity noise decreases as  $\theta^2$  and equals the shot noise when

$$\theta = \sqrt{\frac{q}{2I_m K^2}} \quad (3.27)$$

If the intensity noise is some multiple of the shot noise  $P_n$ , measured at  $\theta = 45^\circ$  (the half-wave bias), then

$$K^2 = \frac{qP_n}{I_m} \quad (3.28)$$

and the bias point where the intensity noise equals the shot noise is simply

$$\theta = \frac{1}{\sqrt{2P_n}} \quad (3.29)$$

For example, suppose the intensity noise is measured to be 60 dB greater than the shot noise with the QWP set to  $45^\circ$ , so that  $P_n = 10^6$ . Then, the QWP angle must be set to  $\theta = 0.7$  mrad to suppress the intensity noise to the shot noise level.

Several practical limitations exist for this scheme. First, precisely adjusting the QWP angle to less than a milliradian may be difficult. Second, as the QWP angle approaches zero, the linear range of the modulator decreases. Finally, reducing the bias point reduces the signal level, requiring the photocurrent load resistor in the receiver to be increased to keep the shot noise above its thermal noise level, and resulting in a reduced receiver bandwidth (due to increasing the photodiode capacitance/load resistance time constant).

### 3.4 Conclusion

The noise terms in electrooptic sampling have been discussed. Reduction of timing jitter to below 300 fs has been accomplished by construction and refinement of a timing feedback loop. Amplitude noise has been significantly reduced by addition of a Faraday Isolator between the laser and pulse compressor, and construction of a fiber-temperature stabilizer. If warranted, additional noise suppression could be accomplished through insertion of a commercial amplitude stabilizer as well as by implementation of ratio and differential detection.

### 3.5. References for Section 3

- 
- 3.1 P.M.W. French, A.S.L. Gomes, A.S. Gouveia-Neto, and J.R. Taylor, "Picosecond stimulated raman generation, pump pulse fragmentation, and fragment compression in single-mode optical fibers," *IEEE J. Quant. Elect.*, vol. QE-22, pp. 2230-2235.
  - 3.2 M.N. Islam, L.F. Mollenauer, and R.H. Stolen, "Fiber raman amplification soliton laser (FRASL)," *Ultrafast Phenomena V*, ed. by G.R. Fleming and A.E. Siegman, Springer Ser. Chem. Phys., Vol. 46, New York:Springer-Verlag, 1986, pp. 46-50.
  - 3.3 R.M. Shelby, M.D. Levenson, and P.W. Bayer, "Guided acoustic-wave Brillouin scattering," *Phys. Rev. B*, vol. 31, pp. 5244-5252, 1985.
  - 3.4 *American Institute of Physics Handbook*, 3<sup>rd</sup> ed., D.E. Gray, ed., McGraw-Hill Book Company, New York, p. 6-29.

## 4. Spatial Signal Resolution and Crosstalk

### 4.1 Theoretical tools

Previous approaches to understanding the interaction of the optical beam with the electric fields in the GaAs substrate assumed a infinitesimally thin cylinder of light as a probe. To provide a more powerful tool for studying such interactions in a general sense, an analysis was developed which permitted inclusion of general microwave and optical fields. Details of the theory are presented in Appendix III, which is a reprint of a publication in *Optics Letters*.

The advantage of the approach taken in this theory is its generality. Expressions of the optical fields may be used which represent the actual Gaussian profile of the focused light, including the finite waist, conic focused section, gaussian transverse decays, and increasing longitudinal field components in the conic region. Interaction of these components with applied microwave fields of an equally anisotropic nature may be considered as well. Although a zeroth-order Hermite-Gaussian optical field was used for this work, higher-order modes could also be considered, if, for example, the effect of spatially varying wafer surface reflections are examined. Finally, optical interactions in electrooptic systems where the eigenvalue problem for the new polarizations and refractive indices is intractable may be evaluated.

Although the optical fields used in probe beam are described in terms of rather simple analytical expressions, the quasi-static microwave circuit fields arising from the set of conductors on the surface are usually too complex for closed-form description. Numerical integration over the volume of the GaAs substrate being difficult to corroborate intuitively as well as computationally intensive, we chose to express the fields within the substrate as a weighted sum of spatially periodic terms derived from the surface source potentials. This yields physically understandable behavior of field components whose weightings are determined from structure to structure by finite difference calculations.

The basic principle of the spatial harmonic representation is described in the following equation

$$\phi(x,z) = \sum_n A_n \cos(\alpha_n x) e^{-\alpha_n z} \quad (4.1)$$



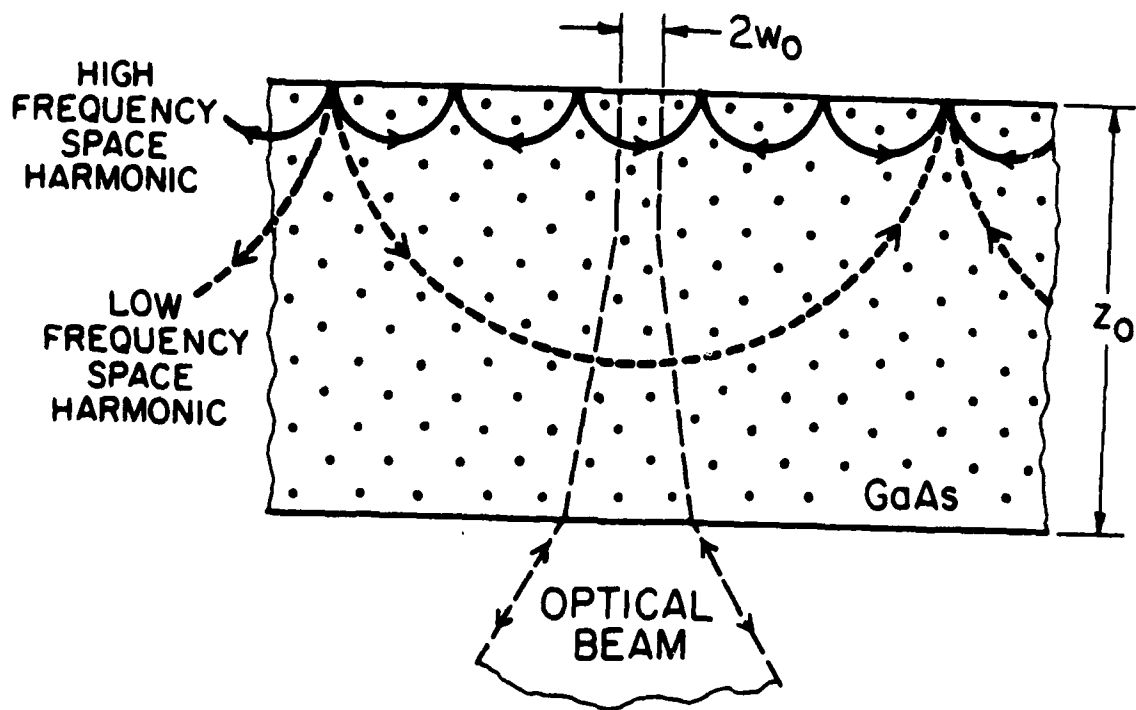


Fig. 4.1: Illustration of a spatial harmonic; where the penetration is related to the transverse frequency.

where  $\alpha_n$  is the spatial frequency,  $z$  is into the substrate, and  $x$  is along the surface. The expression, a solution of Laplace's equation provides a link between the nature of the potential at the surface and its decay towards the back of the wafer. Figure 4.1 illustrates this action.

A modification to Eq. (4.1) must take place when the volume considered is not semi-infinite, but bounded at the backside of the wafer by a dielectric-air interface. An analytical formulation can again be achieved if the  $\epsilon$ , the dielectric constant, is assumed to be infinite (a good approximation for GaAs,  $\epsilon = 13$ ). Then we write

$$\phi(x,z) = \sum_n A_n \cos(\alpha_n x) \frac{\cosh[\alpha_n(z_0-z)]}{\cosh(\alpha_n z_0)} \quad (4.2)$$

The difference between the two expressions is a somewhat higher backside potential for the *cosh* case, since the normal derivative at the boundary must be zero. Later we will see the size of this effect.

## 4.2 Experimental factors

Measuring the accuracy of the electrooptic sampler required attention to points heretofore ignored. In many cases, simple changes to the system configuration can yield improvements in measurement repeatability as well as noise performance. In other cases, awareness of the difficulties inherent in electrooptic measurements can guide the user to more reliable and useful data.

### 4.2.1 Noise and stability

Some of the first measurements made to ascertain the sampler accuracy were on simple coplanar waveguide (CPW) transmission lines. Transverse scans of the potential difference between the front and back sides are made and the magnitude of the side conductor signal relative to that on the center is characterized. Since these scans require on the order of tens of seconds for completion, the low-frequency amplitude noise of the laser introduced large fluctuations on the scan that make accurate magnitude determinations difficult. In addition, changes in surface reflectivity can lead to misleading signal magnitude changes. Finally, photodiode "normalization" conducted over the IEEE-488 interface bus (see Section 3.3), has a bandwidth of only a few tens of hertz and represents division by photocurrent at a slightly different time in the scan.

A straightforward, though some distasteful solution is to increase the acquisition time. The lock-in amplifier may be used in the 300 ms to 1 s time constant range, and a simple RC filter used before the digital voltmeter (DVM) monitoring the photocurrent signal. The two time constant should be nearly equal, much larger than the difference in acquisition times, and less than the time between data points in the scan. Normalization then acts to remove reflectivity anomalies and long-term amplitude drift, while the long acquisition time averages out more rapid amplitude fluctuations. Scans with sufficient signal-to-noise can be made in several minutes.

A more elegant solution is, of course, to remove the offending noise to begin with. With the addition of the Faraday Isolator (cf. Section 3.1), significant improvements in the low-frequency noise are evident. Scans can be made in tens of seconds. Differences in acquisition moments then make photocurrent normalization problematic. If the portions of the scan of interest are under identical metallization, and if the reflectivity variations are small, normalization can be neglected. Most of the crosstalk data was taken in this way due to the excellent long-term stability and low amplitude noise of the system with the isolator.

#### **4.2.2 Sensitivity to Fabrication**

These reflectivity variations under the metallization are in general attributable to defects in fabrication. Residue under the metallization leads to scattering of the coherent probe beam with unpredictable results. Measured signals have been observed to increase and decrease under such defects, while the photocurrent invariably diminishes. Although a trustworthy time-mode measurement could conceivably be made in such a region, a calibrated measurement or an accurate scan which included in this region would be impossible. Differences were also noted between test patterns made with crude emulsion masks and simple lithography, and those made with chrome e-beam masks and refined submicron lithography techniques.

#### **4.2.3 Focusing and Aperturing**

Scans of potential profiles are also susceptible to inaccuracies from poor spot imaging. With a gaussian beam incident on a circular aperture of the focusing lens, the focused spot size is not limited by the numerical aperture (NA) of the lens, as it would be for a plane wave. This leads to observable structure in the reflected beam if the reflection is not uniform. In backside probing, 100% reflectivity can be obtained at a GaAs-metal interface, and 30% at a GaAs-air interface. Passivation layers of  $\text{SiO}_2$  ( $\epsilon = 1.46$ ) or  $\text{Si}_3\text{N}_4$  ( $\epsilon = 2.05$ )

can either increase or decrease the reflectivity at the surface, depending on their thickness. Either way, maximum beam structure will occur on passing over a conductor edge.

The focal point -- where the beam is reflected -- and the recollimated beam incident on the photodiode are fourier transform pairs; uniform reflection corresponds to a delta function convolved with the gaussian back at the detector, while any other reflection gives a broader function to be convolved with the gaussian. The result is increased optical power near the edges of the spot and decreased power near the center, as the edge is traversed. If the receiving photodetector is inopportunately aligned, such that it examines a small enough portion of the beam to be sensitive to these fluctuation, a distorted signal at the conductor edges will result. If placed near the outer edges, it will peak unrealistically; if near the center, it will dip, though this dip will probably be lost in the much larger falloff as the conductor is passed.

The solution is relatively simple: place a gentle focusing lens before the detector so that the entire beam front is integrated at the detector. Similarly, overfocusing at the detector can lead to saturation or melting at higher powers. Care must be taken to avoid significant apodization of the returning beam at any point for the same reasons.

#### 4.2.4 Acoustic waves

The test structures discussed later were originally designed for testing at low frequencies -- below 100 MHz. This effectively eliminates any real, electrical coupling between line, permitting any remaining crosstalk to be attributed to measurement, or electrooptic, crosstalk. At these low frequencies however, the electric field applied to the piezoelectric GaAs gives rise to acoustic waves in the material, which can setup standing waves in modes determined by the shape of the sample. At the frequencies of operation typical of circuits tested by electrooptic sampling, these waves are not of consequence. However, between 100 MHz and 1 GHz, these signals can be 10% of the electrooptic signal, and will scale with both electric and optical power. Below 20 MHz, they can completely dominate the potential scan, and may lead to waveform distortion due to their potential strength away from the central conductor. Typically, they are most apparent in transverse potential scans across structures like CPW's, manifesting themselves as ripples across the ground plane sections, with a period inversely proportional to the drive frequency. Their effect in smaller structures is more difficult to determine, since the potential is varying more rapidly. To avoid these effects, crosstalk and calibration measurements must be made above approximately 800 MHz. Clearly, the higher the frequency the smaller the effect of these acoustic modes.

### Variation of Crosstalk with Frequency

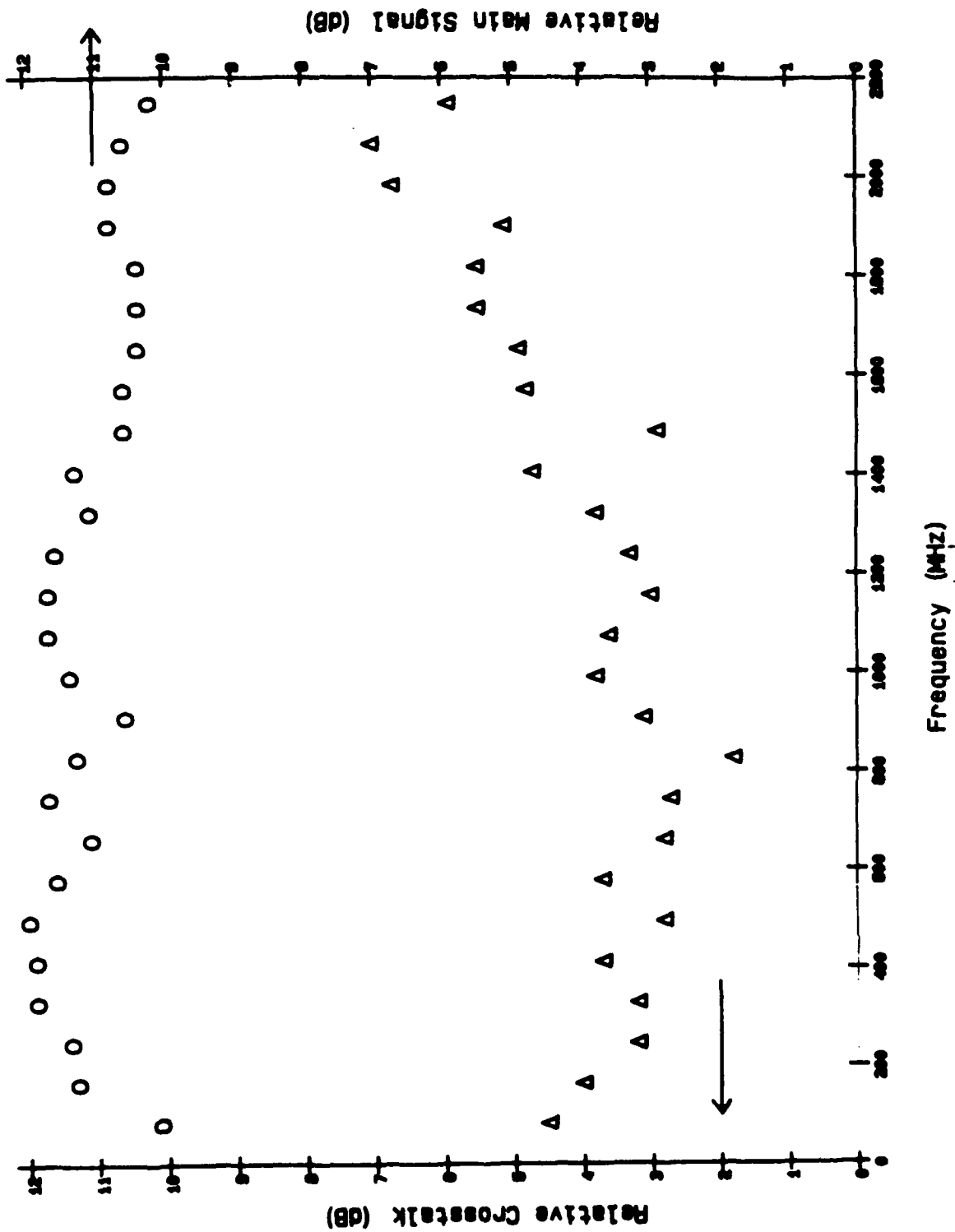


Fig. 4.2: Variation in crosstalk measurement with frequency due to acoustic modes and capacitive coupling.

At higher frequencies, however, real capacitive coupling can arise between the lines. Some test structures extend several millimeters in length in order to avoid bond pad effects while varying the separation of two conductors. The choice of an operating frequency, then, is a compromise between the desire to be above acoustic modes but low enough to avoid significant capacitive coupling. Figure 4.2 illustrates the change in the crosstalk,  $\omega_2$ , on the structure of Figure 4.15 as a function of harmonic number. The variation of the crosstalk signal with increasing frequency is attributed to decreasing acoustic wave excitation, followed by increasing capacitive coupling. Note that the main signal at frequency  $\omega_1$  is not significantly changed. To minimize both effects, we generally choose an operating point near the minimum in Figure 4.2, or 800 MHz to 1.2 GHz.

#### 4.2.5 Fabrication of test structures

The test structures used in these experiments were designed with OCT/VEM on a DEC VaxStation GPX color workstation. They were then translated to MEBES format and dumped to a 1600 bpi magnetic tape. An on-campus MEBES-1 produced a four inch square glass mask with resolution below 1  $\mu\text{m}$ . Hoect 5214e positive photoresist was used with exposure on a Karl Süss MJB3 aligner. Liftoff processing of the resist was accomplished with a well-characterized chlorobenzene process. Finally, .5 to 1  $\mu\text{m}$  Ti/Au metallization was evaporated by electron beam and lifted off with acetone soaking. Lines and spacings of 1  $\mu\text{m}$  were resolved, as well as multiple instances of each test structure. Two mask sets were produced, with the second incorporating improvements discerned from testing the first as well as CPW's that were previously made with a poorer process. The size of a die was approximately 1 cm by 1.5 cm.

### 4.3 Spatial Resolution

Since the electrooptic probe acts by integrating the phase change along the path of the beam, portions of the beam other than that at the front surface are involved in determining the actual measurement made. Additionally, this probing beam is focused at an angle  $\theta$  in the substrate. Determining the actual resolution of the probe requires consideration of the interplay of the optical fields with the spatially harmonic circuit fields both transversely and longitudinally.

Filter deviations for Very Tight Beams

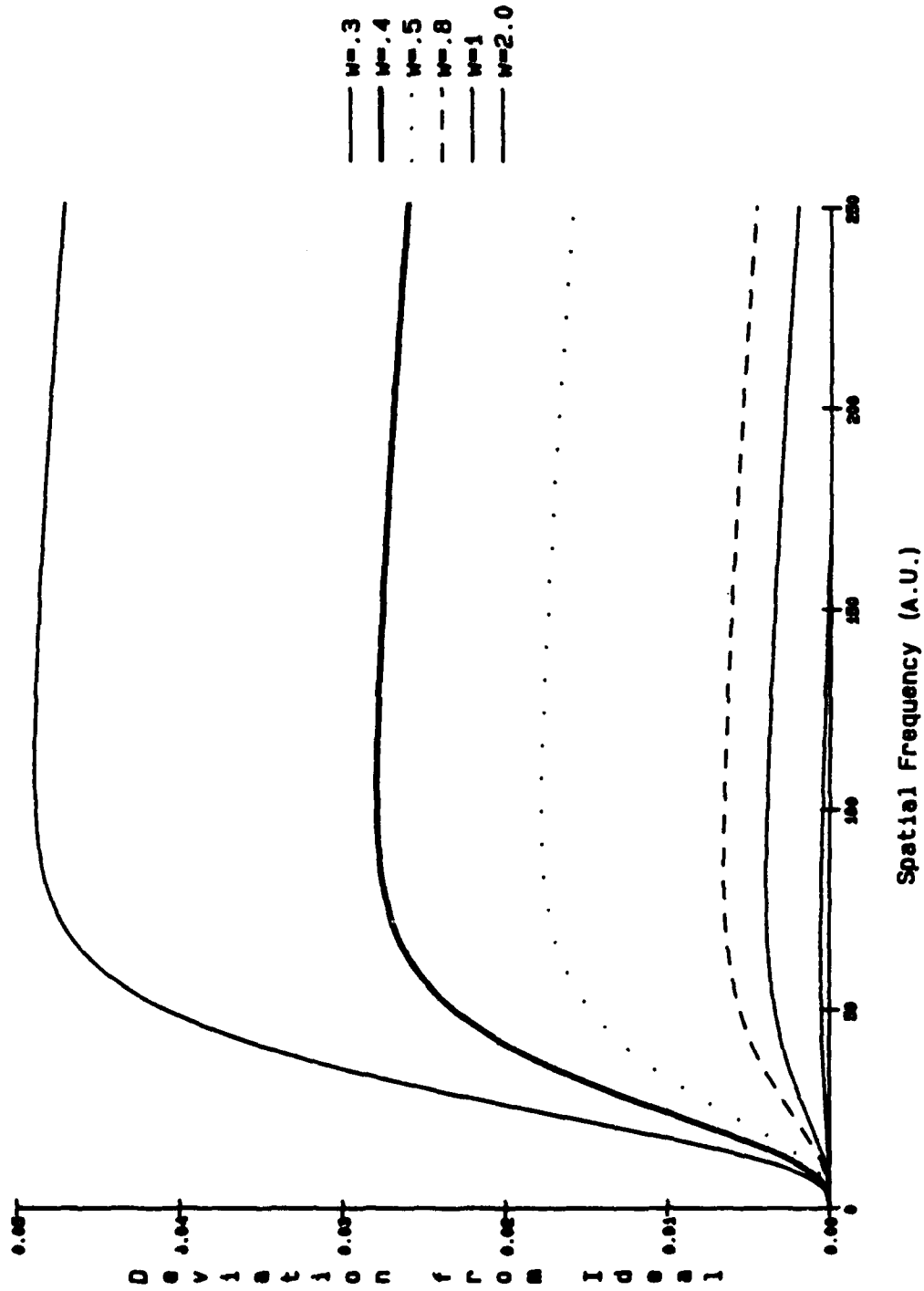


Fig. 4.3: Deviations in the filter response for very tight beams and very low frequency.

### 4.3.1 Focused Gaussian Beam Effects

A typical gaussian beam within a wafer is illustrated in Figure 4.3. We note that the final spot size is determined by the NA of the objective and remains constant upon passage into the dielectric. This arises from the reduction of the wavelength in the material balancing the Snell's law change in angle. Several of the most relevant parameters are included in a table for various spot sizes. Typically, spot radii of 1.5 to 2  $\mu\text{m}$  can be obtained with standard microscope objectives. The smallest radii are not obtainable without some type of immersion lens due to the large change in  $\epsilon$  at the interface. Frontside probing uses large radii --  $\approx 4 \mu\text{m}$  in order to have a small spot at the top surface. The column 'Spot at 100  $\mu\text{m}$ ' then better represents the actual probing resolution.

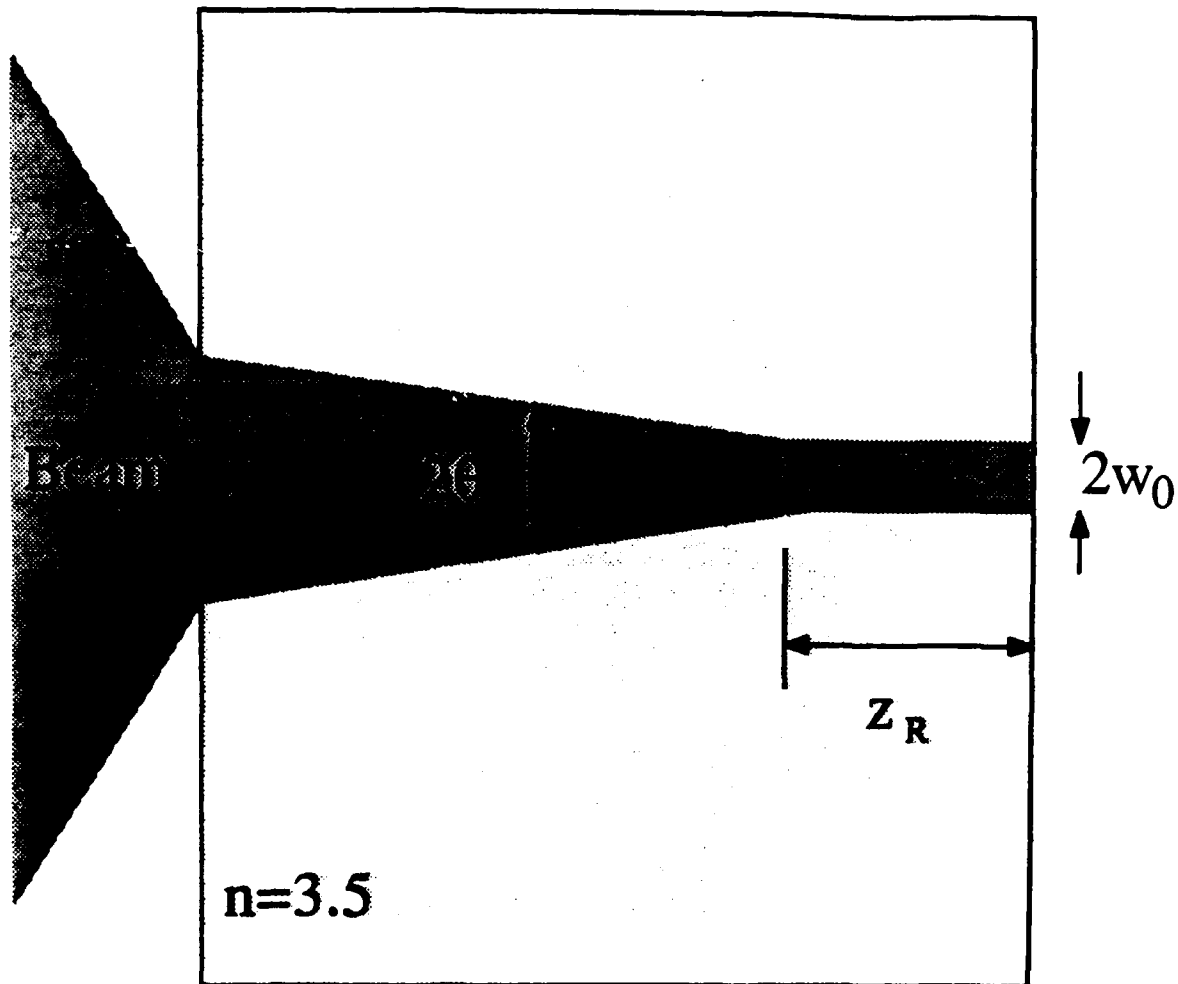
#### Interplay of falloff and beam expansion

Much of the initial investigation of focused Gaussian beams centered on the large spot at the backplane. It was reasoned that this must result in a larger effective spot size that would be expected from the front spot alone. Computations using the theory described in the Appendix III, however, revealed filter functions and measured potentials that differed imperceptibly from those expected for a non-expanding beam of the same radius, in the range of beam radius normally used. This result can be understood in a simpler physical fashion through the use of spatial harmonics. Harmonics with rapid transverse variation also suffer rapid decay into the substrate and hence are probed only by the waist of the beam. In contrast, slowly varying spatial harmonics have a period large in comparison with even the larger backside spot. This can be expressed mathematically by examining the ratio of the beam diameter at the 1/e point of a space harmonic (Fig. 4.1) to the period of the space harmonic:

$$\frac{2w(z=L/2\pi n)}{L/n} = \frac{\lambda}{2\pi^2 w_0} \approx \frac{.03}{w_0} \quad (4.3)$$

where  $w_0$  is the waist radius at the focus. Note that this ratio is independent of  $n$  and will generally be much less than 1 for all but the smallest  $w_0$ . This means that any portion of the electric field seeing a portion of the optical field will have a transverse variation that is broad in comparison with the beam.





Spot Radius	Angle	Waist Length	Spot at 100 $\mu\text{m}$	Spot at 450 $\mu\text{m}$
0.25	22.2	0.6	38.7	174.3
0.5	11.1	2.6	19.4	87.2
1	5.6	10.3	9.7	43.6
1.5	3.7	23.2	6.6	29.1
2	2.8	41.3	5.2	21.9
3	1.9	92.9	4.4	14.8
4	1.4	165.2	4.7	11.6
5	1.1	258.1	5.4	10.0

$w_0$  is the waist radius (in  $\mu\text{m}$ );  $\theta$  is the paraxial angle (in deg.);  $z_R$  is the Rayleigh range or waist length. The last two columns represent the spot radius at the backside of different thickness substrates

Fig. 4.4: Parameters for a focused gaussian beam.

A rough comparison of the effect of even very tightly focused beams can be made by examining the magnitude of the probe spatial filtering function near zero spatial frequency. The higher frequency portion of the filter is of course determined by the spot-size; the very low frequency regions, though, are well removed from the high-frequency gaussian roll-off and are attributable to other forms of averaging. In Figure 4.4, the filter function for several spot sizes ( $w_0$ ) have been subtracted from that of a 3.0  $\mu\text{m}$  radius beam. The 3.0  $\mu\text{m}$  beam is taken as a standard of negligible extra averaging; the validity of this statement is confirmed by the near-zero difference between 3.0  $\mu\text{m}$  and 2.0  $\mu\text{m}$  beams in this region. Since the maximum of the filter function is 1.0, the vertical axis represents the fractional error. We conclude from this that averaging from the beam focusing (apart from the surface spot size) is still below 1% for beams 3 to 4 times tighter than currently used. Since the error is relatively flat in frequency, though, the effect will simply be to reduce the signal amplitude uniformly, rather than yielding crosstalk.

#### 4.3.2 Spot Size Crosstalk

The dominant form of electrooptic measurement error due to the gaussian beam is the finite spot width. Rapidly spatially varying potentials are smoothed by the finite spot size and lead to the crosstalk error illustrated in Figure 4.5. The structure has a 2  $\mu\text{m}$  center conductor (only half is shown), a 3  $\mu\text{m}$  gap, and a second 2  $\mu\text{m}$  line. A ground plane is 50  $\mu\text{m}$  away. The center conductor has 1 V applied in both traces, while the side conductor has 1V applied in trace (a), and -1 V in trace (b). The rising and falling of the side conductor represent the maximum excursions of the potential on that conductor for a fixed center potential. This permits a DC analysis. The difference in the measured signal on the center conductor is the crosstalk due to the finite spot size and of course depends on the spot size as well as the structure under consideration.

An equivalent value of crosstalk can be arrived at by considering the center conductor in Fig. 4.5 to be at zero volts and the side conductor at 1 V. This offers the benefit of a single structure in calculation. Evaluating the signal on the center line for a large variety of spot size, and several worst-case structures gives the plots of Figures 4.6 and 4.7. For 2  $\mu\text{m}$  lines probed by 1.5 to 2.0  $\mu\text{m}$  spots (typical), we expect a crosstalk of about 3 %, or -30 dB.

#### Experimental spot-size crosstalk measurements

The structure of Figure 4.8 is designed to measure the crosstalk calculated above. An earlier structure was much shorter, but proved to be dominated by backplane effects from

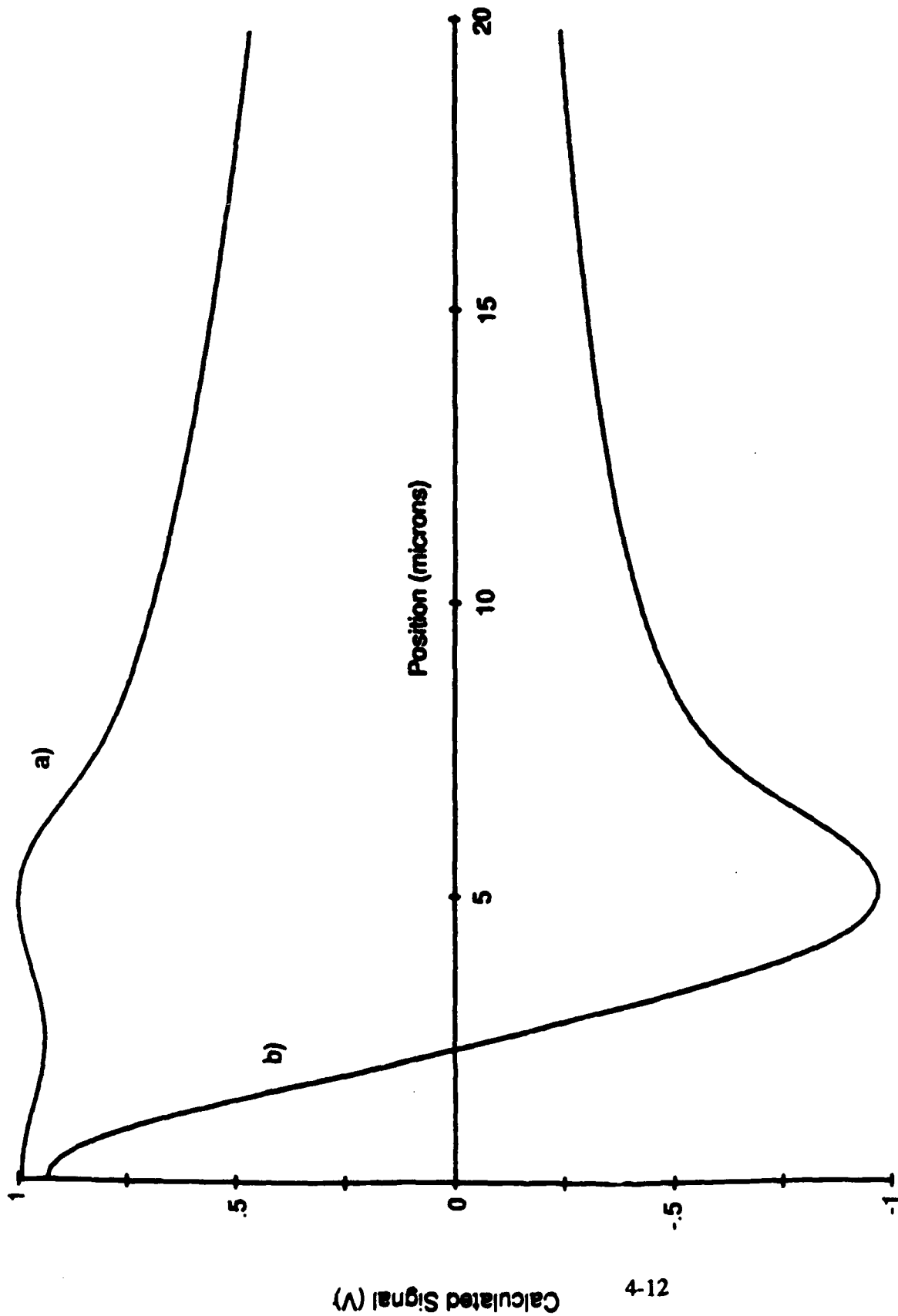


Fig. 4.5: Operation of spot-size crosstalk.. One conductor is from 0 to 1  $\mu\text{m}$ , at 1 V; the second from 4 to 6  $\mu\text{m}$  at a) 1 V, b) -1 V.

Spot size Crosstalk -- 2 micron lines

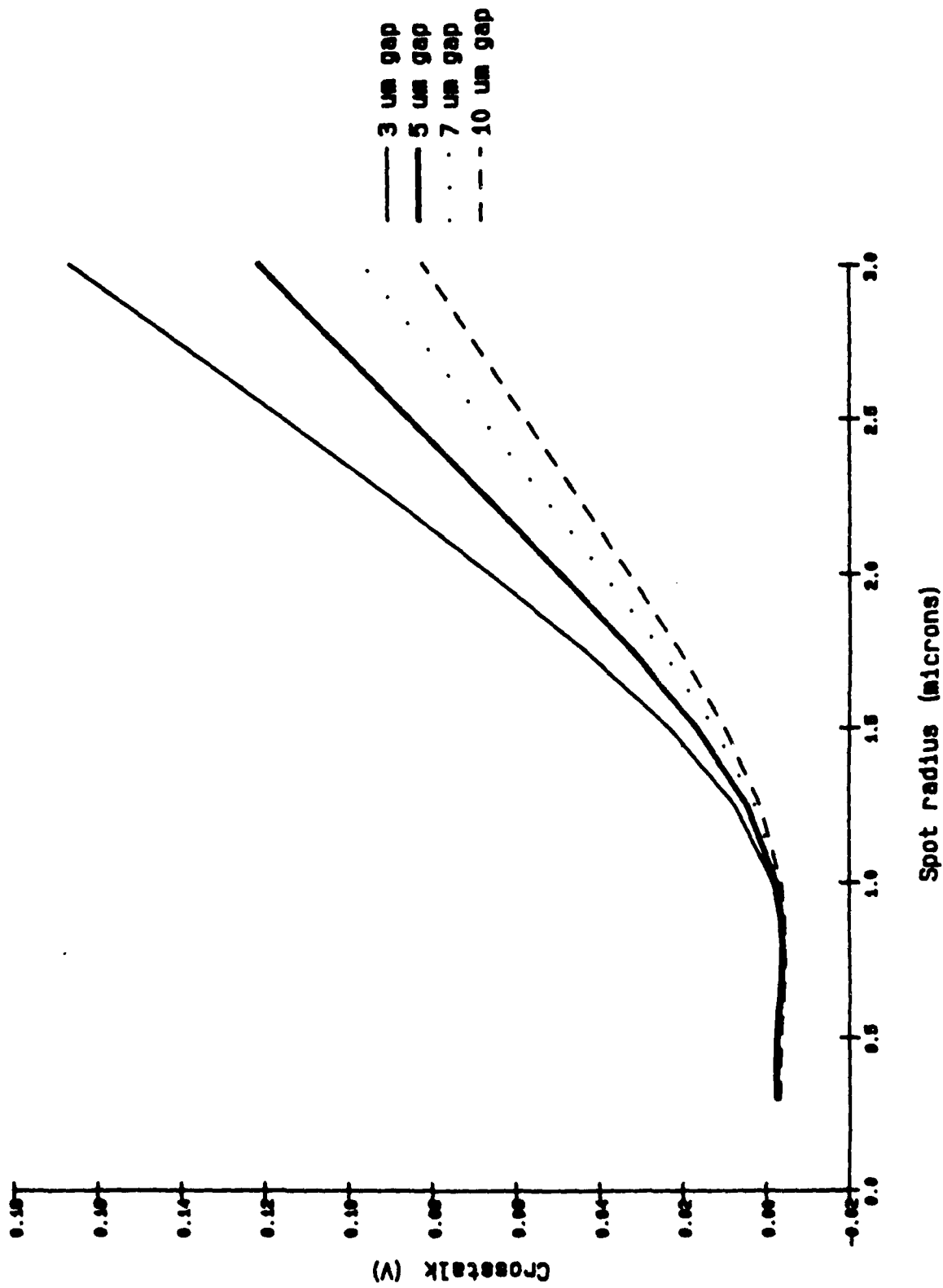


Fig. 4.6: Calculated crosstalk for the general structure of Fig. 4.4 with 2 mic lines.

Spot size Crosstalk -- 4 micron lines

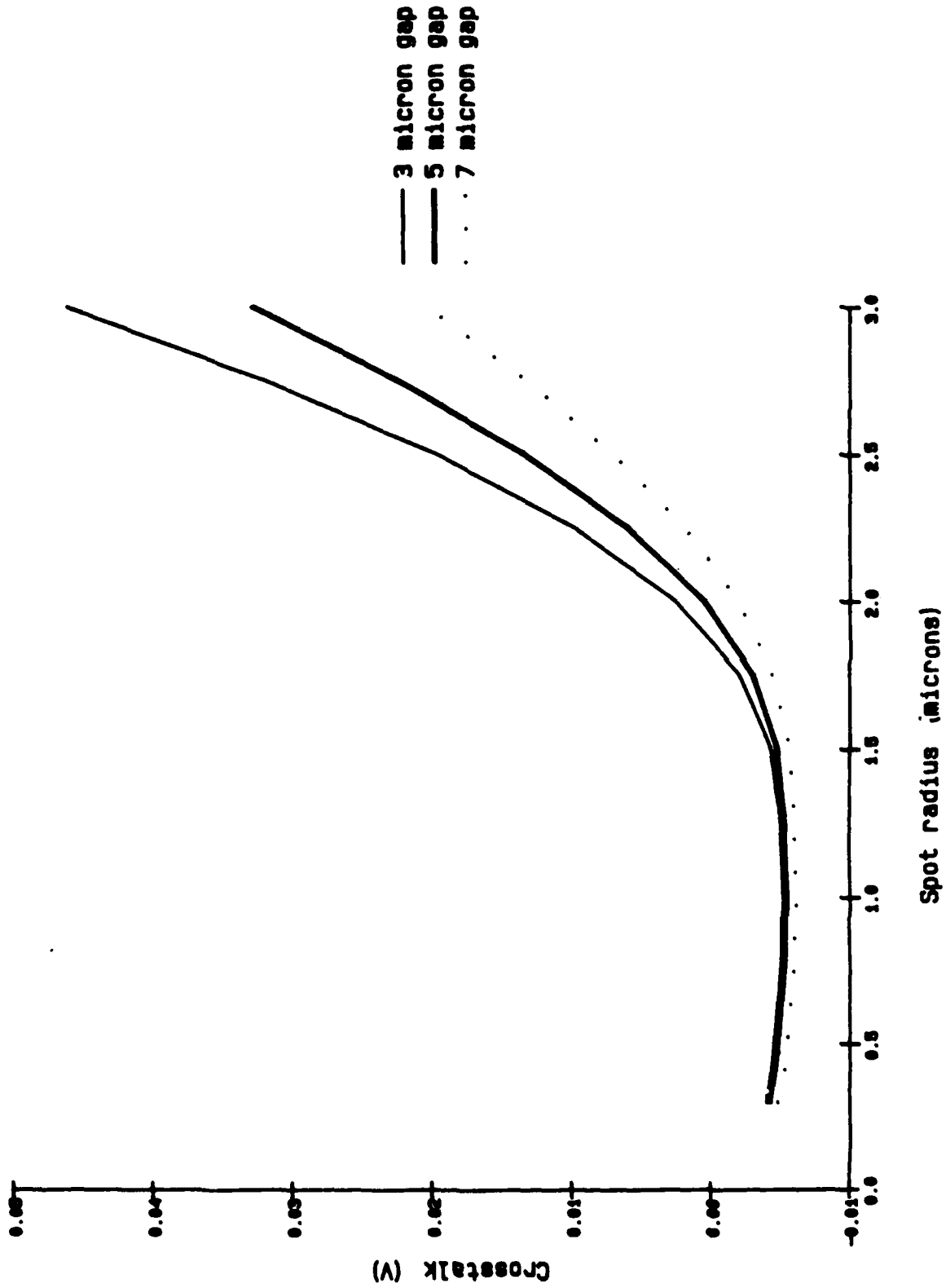


Fig. 4.7: Calculated crosstalk for the general structure of Fig. 4.4 with 4 μm lines.

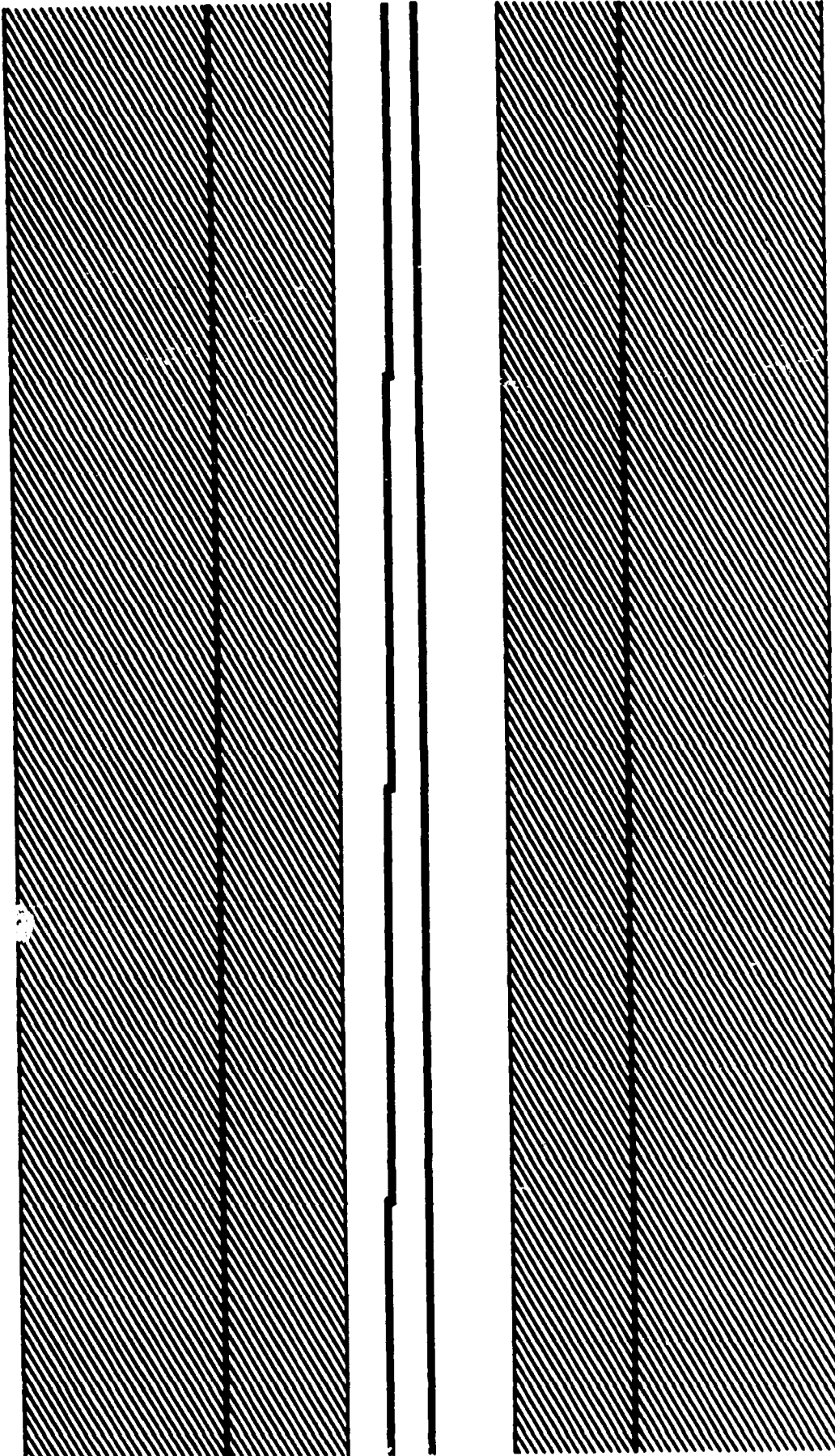


Fig. 4.8: Structure for measuring spot-size crosstalk. Different frequencies are placed on the two conductors.

the large bond pads that were of necessity present. It is worth noting that the two effects may be separated by their sign: backside crosstalk is opposite in sign to its source, while spot-size crosstalk is of the same sign.

Measurements on structures like that of Figure 4.8 reveal that spot-size crosstalk becomes apparent only for the most difficult of probing situations. For ground spacings greater than 10 microns, clear sensing of the adjacent, strong potential is evident. Strongest, as expected, on 2  $\mu\text{m}$  lines, the spot-size crosstalk appears at the -18 dB level for those structure in which it is evident. We draw two conclusions from this: spot-size crosstalk will rarely be the dominant mechanism in circuits with ungrounded backplanes; and secondly, that a ground will be required on the back if more detailed information on spot-size crosstalk is desired.

## 4.4 Backplane Crosstalk

The dominant source of error in the electrooptic measurement is the finite potential on the backside of a GaAs circuit. It is a ubiquitous term of magnitude -20 to -30 dB and is difficult to eliminate by top-side configurations. This section will describe the underlying physical mechanism for this effect, its magnitude in a variety of digital and microwave structures, and suggest some solutions that may be applicable to certain cases. [ 5 . 1 2 ]

### 4.4.1 Overview

Backside crosstalk arises from the variable decay of different spatial harmonics into the substrate. If all harmonics decayed at the same rate, the potential below a given line would be proportional to the signal at the surface, and the result would be a simple attenuation of the measured signal, not a distortion. As Figure 4.9 illustrates, however, high spatial frequency components die out quickly, leaving a very smoothed version of the surface potential farther into the material. Usually, by the time the backplane is reached, a given source on the surface has resulted in a broad, gaussian-like backside.

Given this backside potential, the electrooptic measurement then takes the difference between the frontside potential and the backside. The result is as in Figure 4.10. The key point is the negative signal beneath the center conductor and the reduced signal beneath the side conductor. This sign change permits ready identification of the crosstalk signal, since it implies a zero crossing when magnitude only is measured (as on a spectrum analyzer). Any *electrical* coupling between the lines will be a *positive* signal that will reduce the perceived electrooptic crosstalk.

Decay of surface potentials

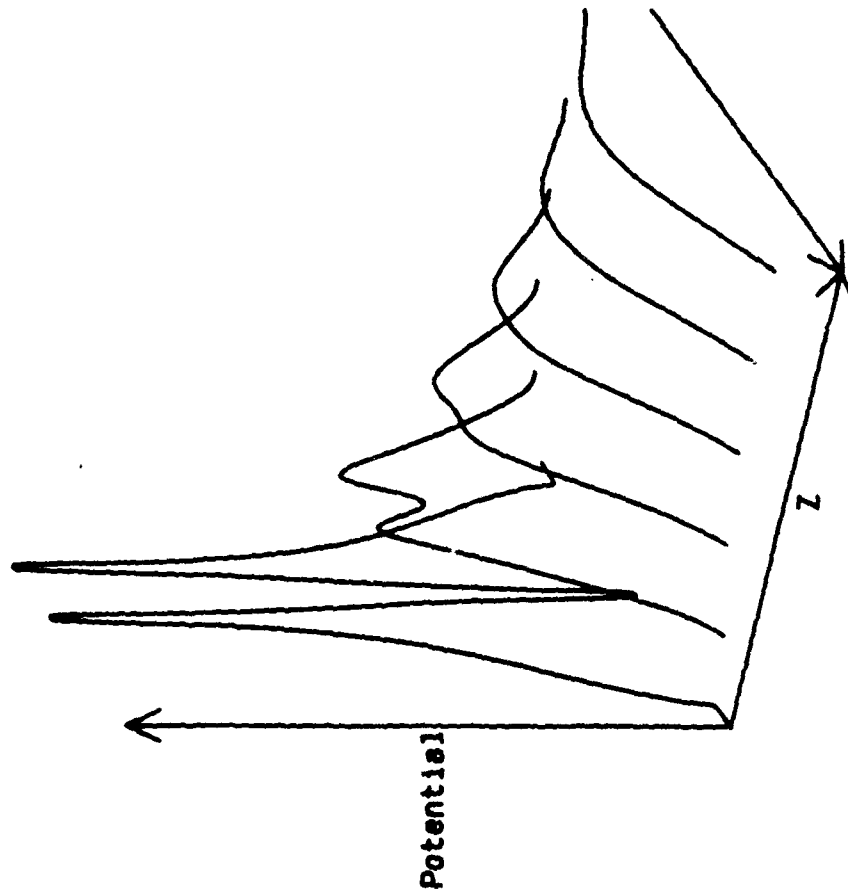


Fig. 4.9: Decay of a surface potential due to spatial harmonics. There are 3 thin conductors, at 1 V, 0 V, and 1 V. Increasing  $z$  is into the substrate.



Mechanism of backside Crosstalk

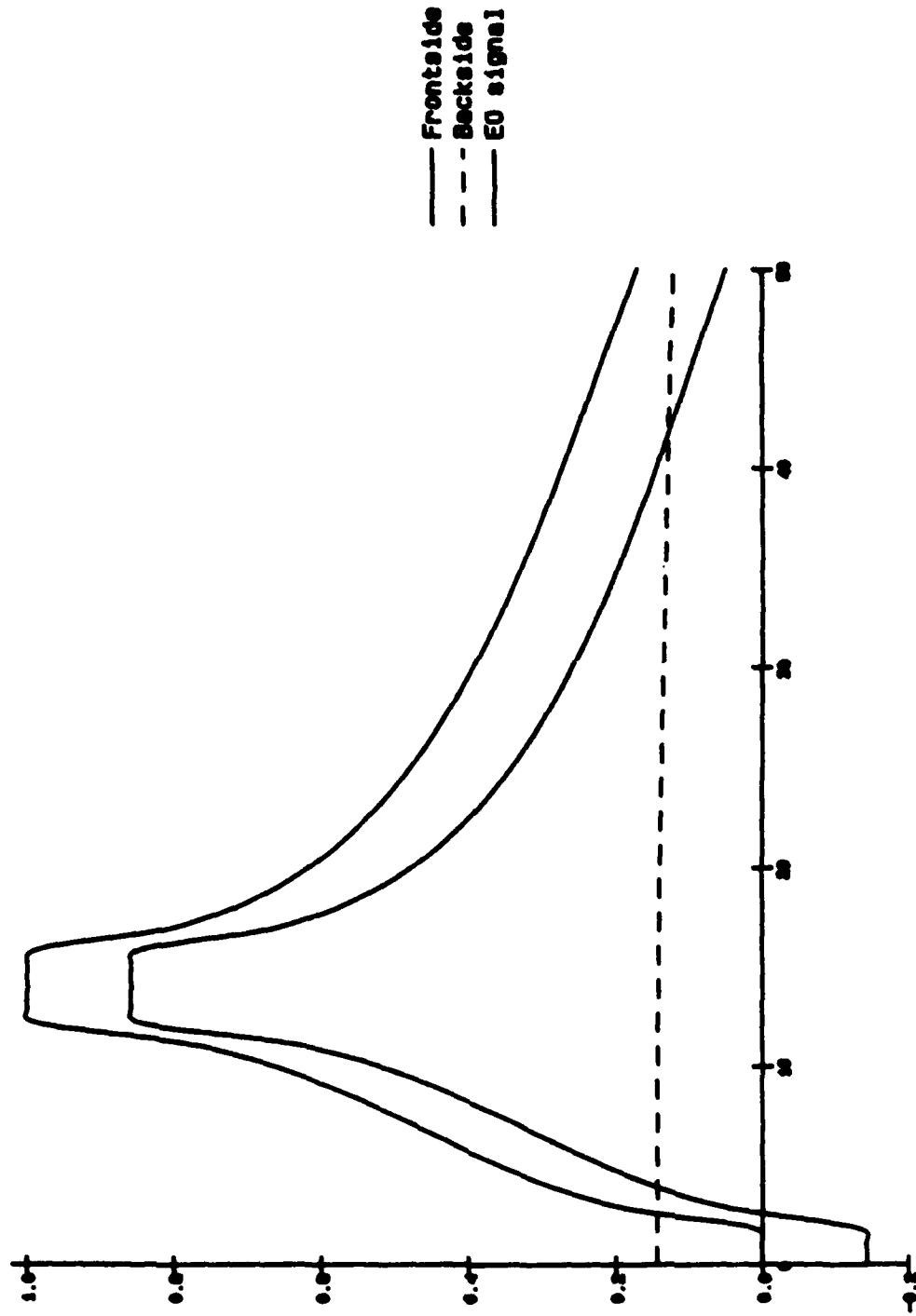


Fig. 4.10: Mechanism of backside crosstalk.. A conductor from 0 to 2  $\mu\text{m}$  is grounded, while the one at 12 to 14  $\mu\text{m}$  is 1 V applied.

#### 4.4.2 Coplanar Waveguide Transmission Lines

For microwave transmission lines, the relative parameter is not so much crosstalk as it is measured signal under the ground plane when no signal is really present. This arises, as before, from a smoothed, positive backside potential that is subtracted from the front to give a electrooptic signal beneath a ground plane. Since transverse scans of the potential of such lines are often used to study moding and field distribution, identification, and characterization, these spurious signals are critically important.

An estimate of the magnitude of the backside signal can be made by assuming a rectangular potential profile  $\phi(x) = \text{rect}(x/w)$  at the surface and using the analytic form of its spatial fourier transform to calculate the potential at a given distance  $z$  into the substrate. We then write

$$\phi(x,z) = \int_{-\infty}^{\infty} \frac{\sin(\pi\alpha w)}{\pi\alpha} \exp(-\alpha z) \exp(-i2\pi\alpha x) d\alpha \quad (4.4)$$

where we have approximated the true cosh dependence by an exponential. We can then evaluate

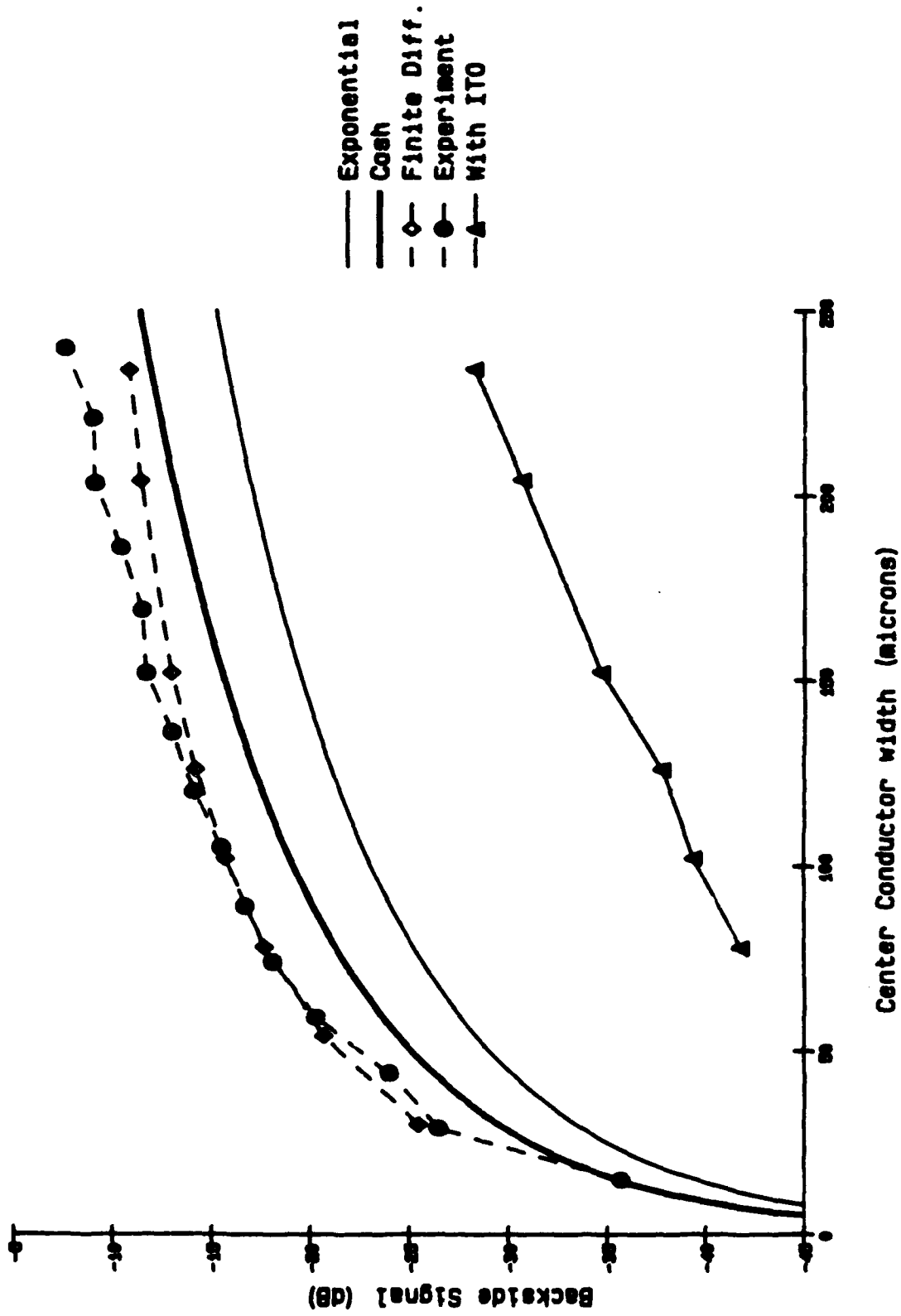
$$\frac{\phi(0,d)}{\phi(0,0)} = \frac{2}{\pi} \tan^{-1} \left( \frac{w}{2d} \right) \approx \frac{w}{\pi d} \quad (4.5)$$

as the ratio of the potential at the front surface to the potential at a distance  $d$  into the substrate. A more accurate consideration of the boundary condition at the backside requires use of a *cosh* dependence on  $z$  (cf. Section 4.1). In this case the integral is more difficult, though still tractable, and gives:

$$\frac{\phi(0,d)}{\phi(0,0)} = \frac{4}{\pi} \tan^{-1} \left[ \exp(\pi w/4d) \right] - 1 \quad (4.6)$$

These two functions are plotted in Figure 4.11. Since an exponential is appropriate for an interface where  $\Delta n = n_1 - n_2$  is zero, and a cosh for  $\Delta n \rightarrow \infty$ , the actual value would be near the cosh curve.

Backside Signals on 50 Ohm CPW's



Substrate is 450 microns thick

Fig. 4.11: Calculated and measured signals for backside crosstalk on CPW's.

Figure 4.11 also summarizes the measurements and calculations on 50  $\Omega$  CPW's fabricated on a 450  $\mu\text{m}$  substrate. Shown are measurements on 15 CPW's of different center conductor widths, finite difference calculations on 8 CPW's, and measurements on 8 CPW's with ITO is on the backside (see Section 4.4.4). Since the backside potential cannot be measured directly, but it is known that it is slowly varying over the backside, it can be estimated by measuring the value beneath the ground plane alone. Since the simple relationships described above assume  $\text{Rect}(x/w)$ , some discrepancy is expected. A compensating factor could be used to adjust  $w$  as appropriate for a true CPW potential.

#### 4.4.3 Digital Geometries

Digital structures are much more complex, with many parameters determining the backside potential. Although the lines are generally much thinner, they exist in much greater number, and with ground planes placed much less frequently, and, often, are much narrower. We have examined digital structures in two distinct categories: 1) where the number of conductors is few, but the relationship between them is varied over large ranges; and 2) where the number of conductors is large, with a fixed relationship to one another.

##### Type 1: Few conductors, many parameters

The first type of structure is similar to the microwave CPW, but is now of much greater impedance, though unspecified. We examine two subcategories of backplane effects: *calibration* and *crosstalk*. The first category, calibration, considers the ability to measure an absolute potential on a conductor, relative to some other point, and the deviation from accuracy due to conductor geometry. The second, crosstalk, adds a conductor to the first structure and considers the effect of the second conductor on the first. In each, the various factors in the geometry must be controlled.

In calibration, we identify two factors: conductor width, and conductor to ground spacing. Figure 4.12 presents a structure for varying conductor width for a fixed spacing. 8 of these structures are made with identical center pieces, but different spacings. Experimentally, the beam is centered each segment of the middle conductor, and the signal magnitude is measured on a spectrum analyzer or a lock-in. Figure 4.13 plots the results versus the center conductor width. At the low end, an upturn is seen as the large bond pad is approached (see Figure 4.12); at the high end, the dip is probably due to extra ground plane on the other side of the bond pad. Figure 4.14 plots the same data against the center to ground spacing. One conclusion that we draw from this data is that the ground plane

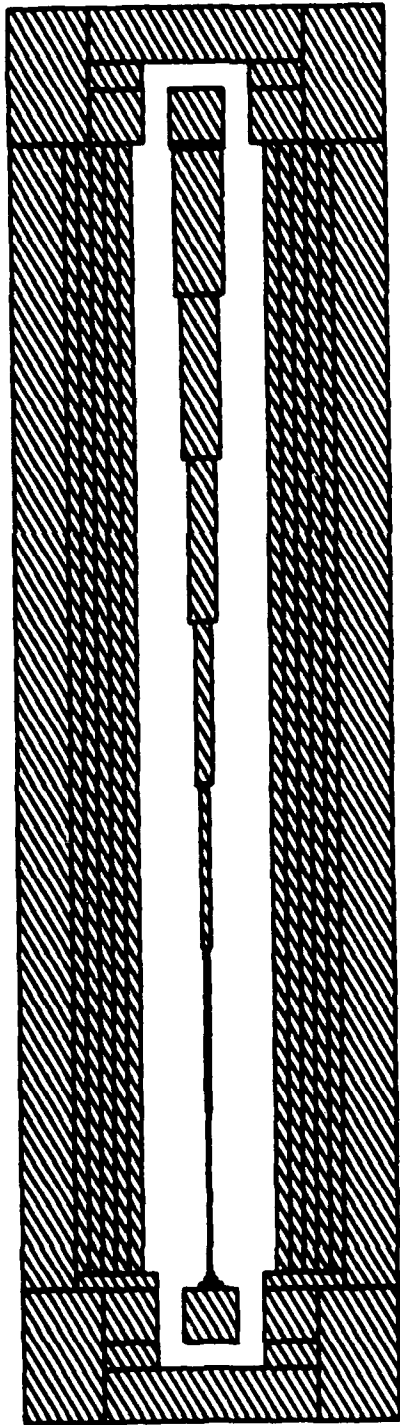


Fig. 4.12: Structure for measuring backside calibration errors.

Backside signal in Calibration

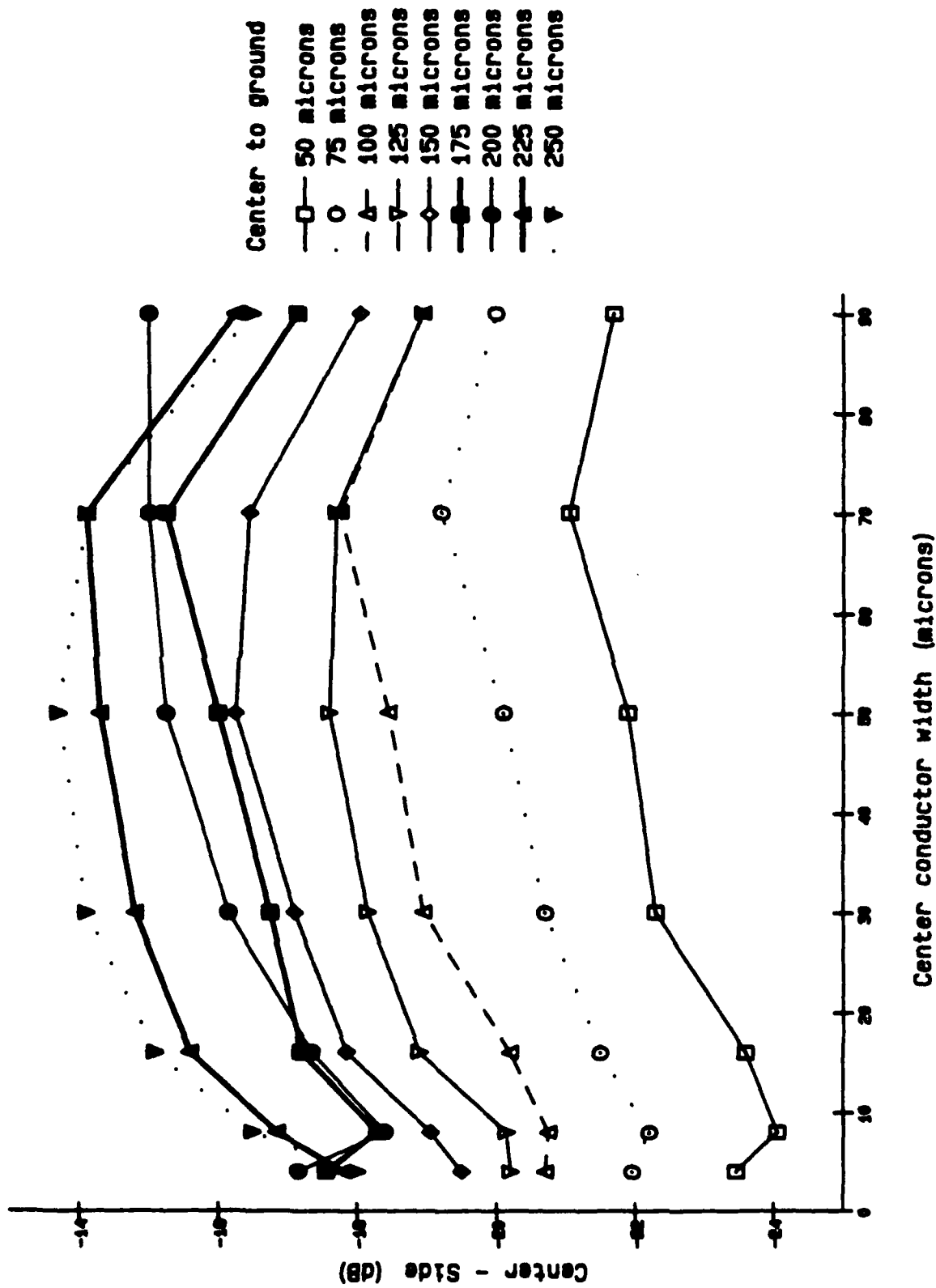


Fig. 4.13: Results from measurements on the structure of Fig. 4.11 plotted versus line thickness.

Backside signal in Calibration

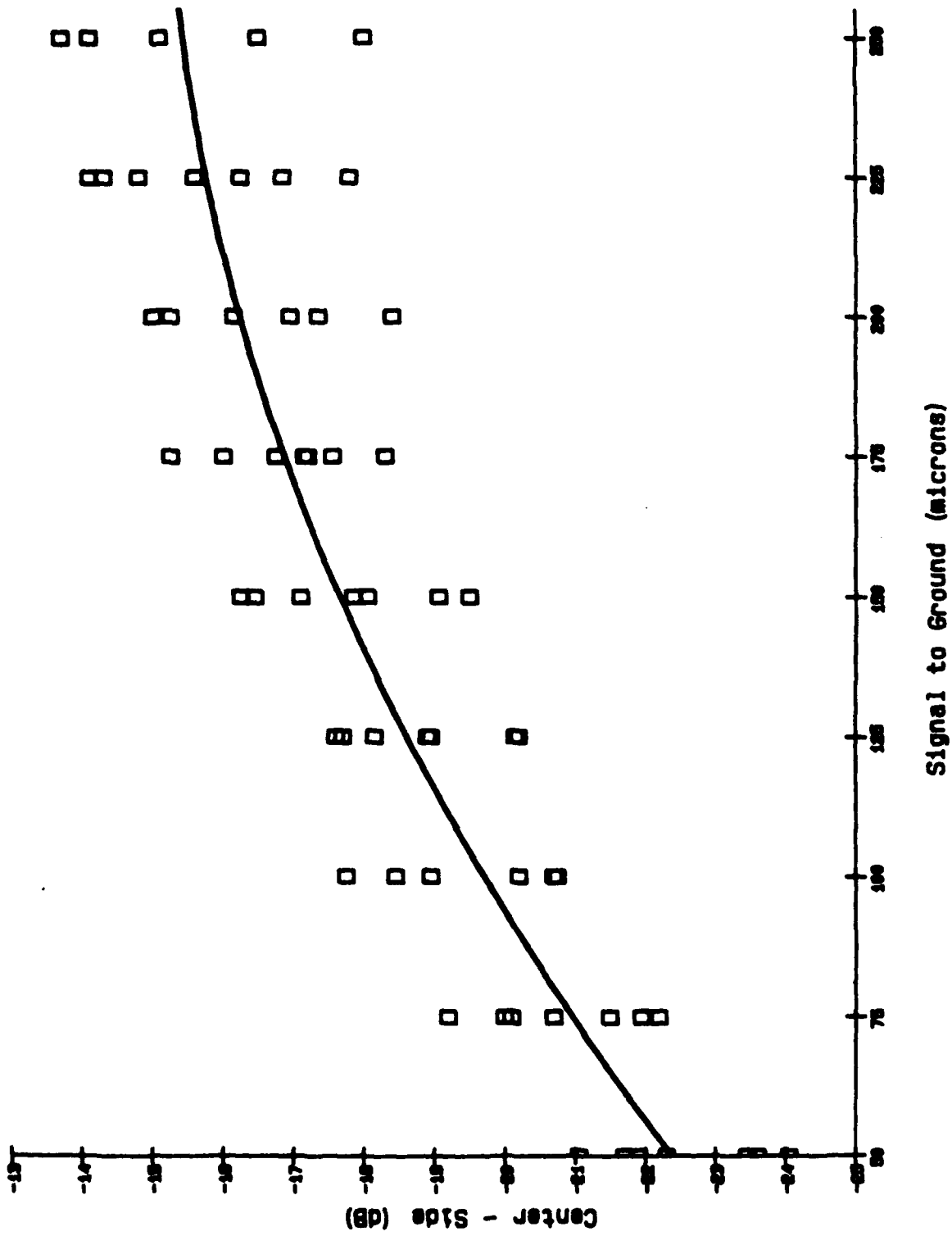


Fig. 4.14: Results from measurements on the structure of Fig. 4.11 plotted versus signal to ground spacing.

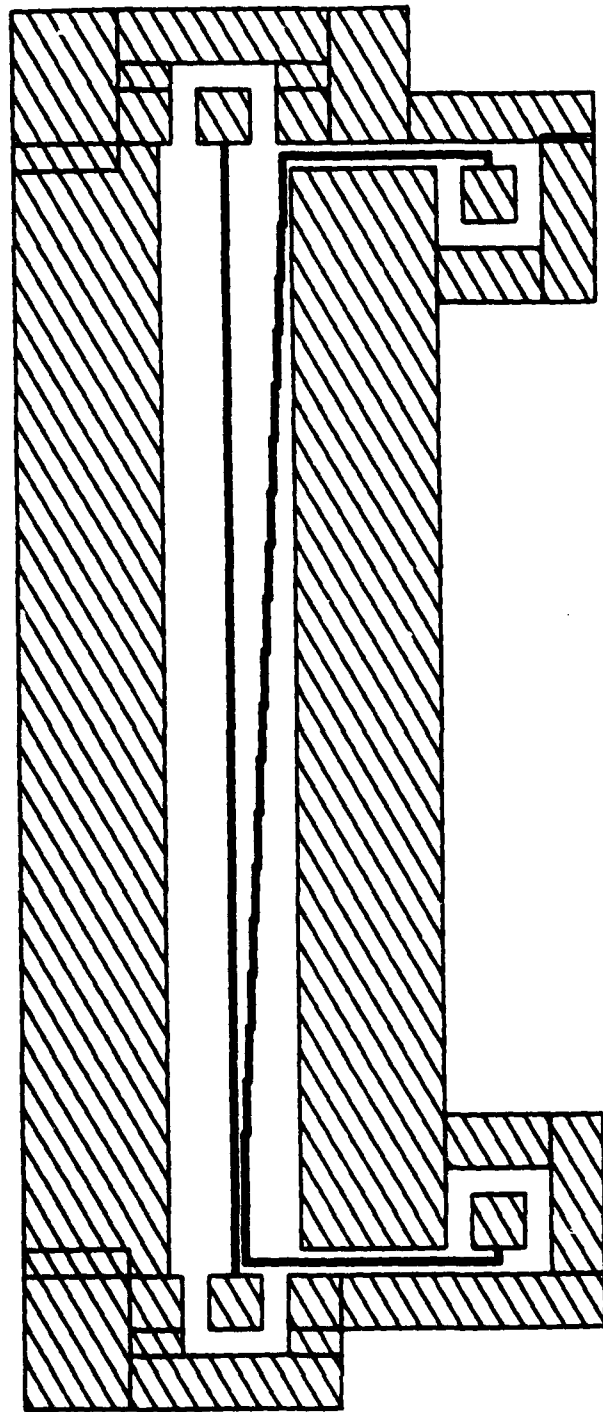


Fig. 4.15: Structure for measuring backside crosstalk in a 2-conductor configuration.



# 2 conductor Crosstalk

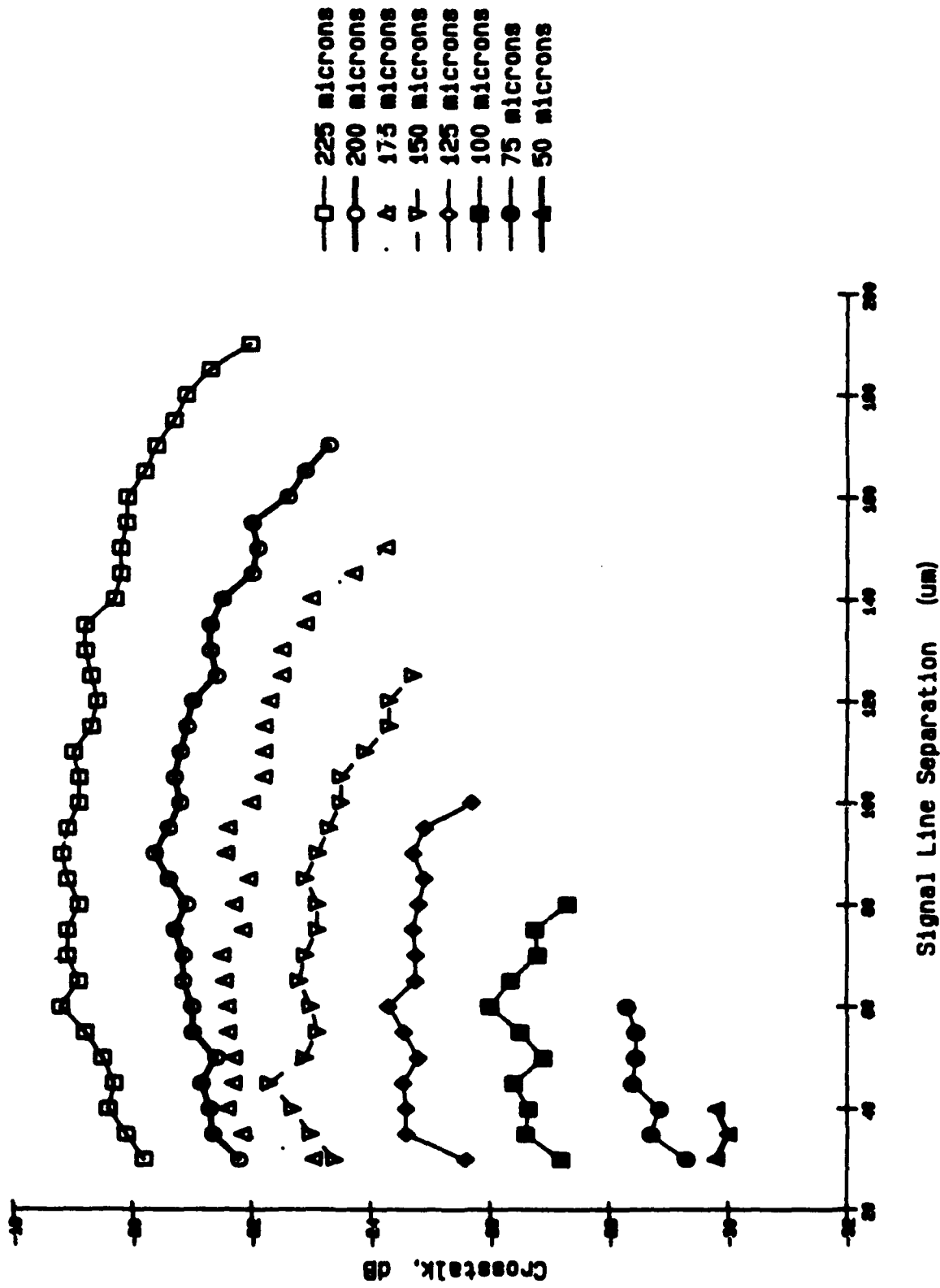


Fig. 4.16: Results of 2-conductor crosstalk, plotted vs. signal line separation.

## 2 Conductor Crosstalk

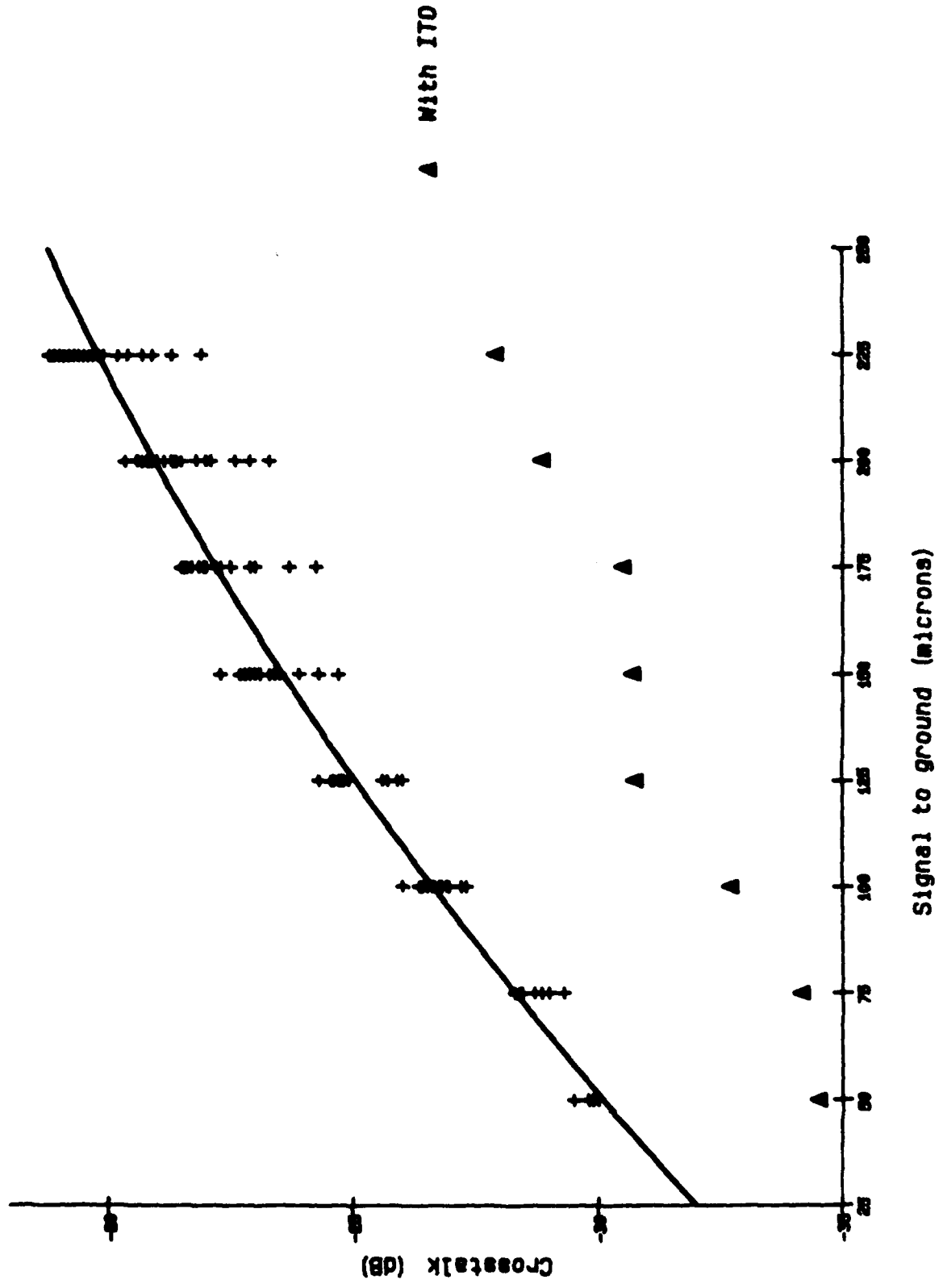


Fig. 4.17: Results of 2-conductor crosstalk, plotted vs. signal to ground separation.

spacing is a much stronger factor in determining backside signal than is the size of the center conductor.

Similar measurements can be made to determine crosstalk. Since the conductor width is a weak variable, we fix it at a value that will permit a range of signal 1 to signal 2 spacings: here, 5  $\mu\text{m}$ . A segment of a structure permitting the variation of S1 to S2 spacings is shown in Figure 4.15. As in calibration, we repeat this structure with different ground plane spacing to monitor the second variable. Since crosstalk is now the issue, different frequencies,  $\omega_1$  and  $\omega_2$ , are applied to the center and side lines, respectively. With a separation  $\omega_1 - \omega_2$  of  $\approx 1$  kHz, both signals can be observed (after electrooptic down-conversion) simultaneously on the spectrum analyzer. The beam is centered on a center line segment by maximizing the negative crosstalk signal ("zero" crossings on both sides), and the difference between the peaks at  $\omega_1$  and  $\omega_2$  is measured. Note that as the ground spacing become smaller, the range of available S1 to S2 spacings is restricted.

Figure 4.16 presents the crosstalk data for these few-line structures. As with the calibration structures, dips at the ends of the structure are attributable to the effects of the bond pads. A weak trend of decreasing crosstalk for larger signal line separations can be noted, but the dominant factor is clearly again the signal to ground spacing. Figure 4.17 confirms the strong dependence on the ground plane spacing for crosstalk, as before with calibration.

#### **Type 2: Many conductors in a pattern**

Since digital circuits consist of so many independent conductors, in a manhattan (orthogonal) layout, crosstalk should also be studied with an array of small lines. To simplify the problem to two variables, we use the structure of Figure 4.18. The line width is again fixed at 5  $\mu\text{m}$ , and the number of intervening lines and the line spacing are varied. A signal at  $\omega_1$  is applied to the center (solid) conductor, at a signal at  $\omega_2$  is applied to a conductor which moves step-wise closer to the center conductor. All other lines are held at ground potential. Figure 4.19 shows the results from probing such a structure. The case of directly adjacent lines is difficult to study accurately, since spot-size crosstalk, electrical coupling, and acoustic waves obscure the backside signal. Of these, only spot-size crosstalk would be problematic in a real circuit.

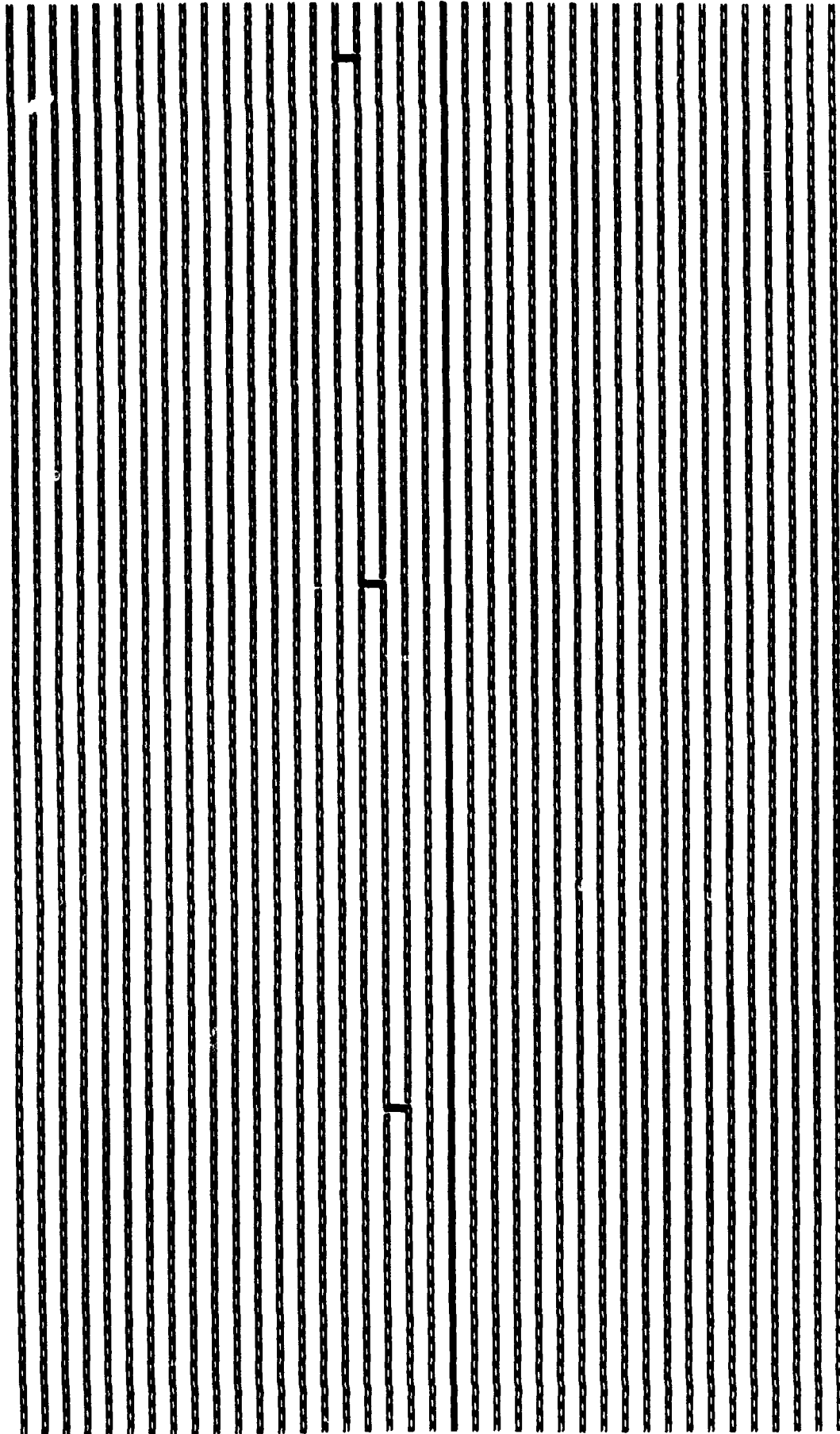


Fig. 4.18: Structure for measuring many-conductor crosstalk.. The main signal line is solid, and the second signal line can be seen moving in one segment at a time.

# Many-line crosstalk

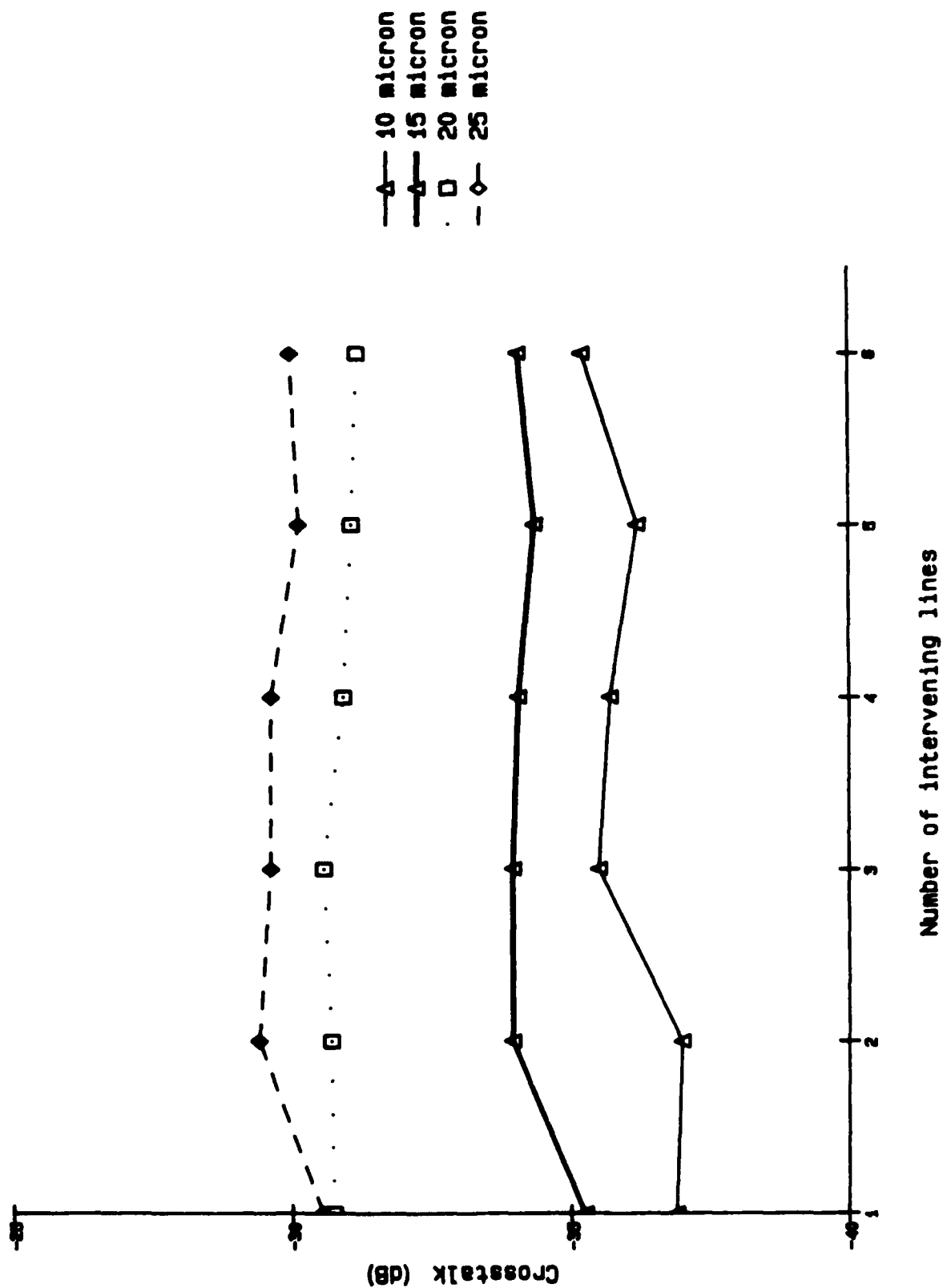


Fig. 4.19: Many-line crosstalk vs. number of intervening lines. The primary dependence is the line spacing.

# Profile of Frontside Potential for an array of lines

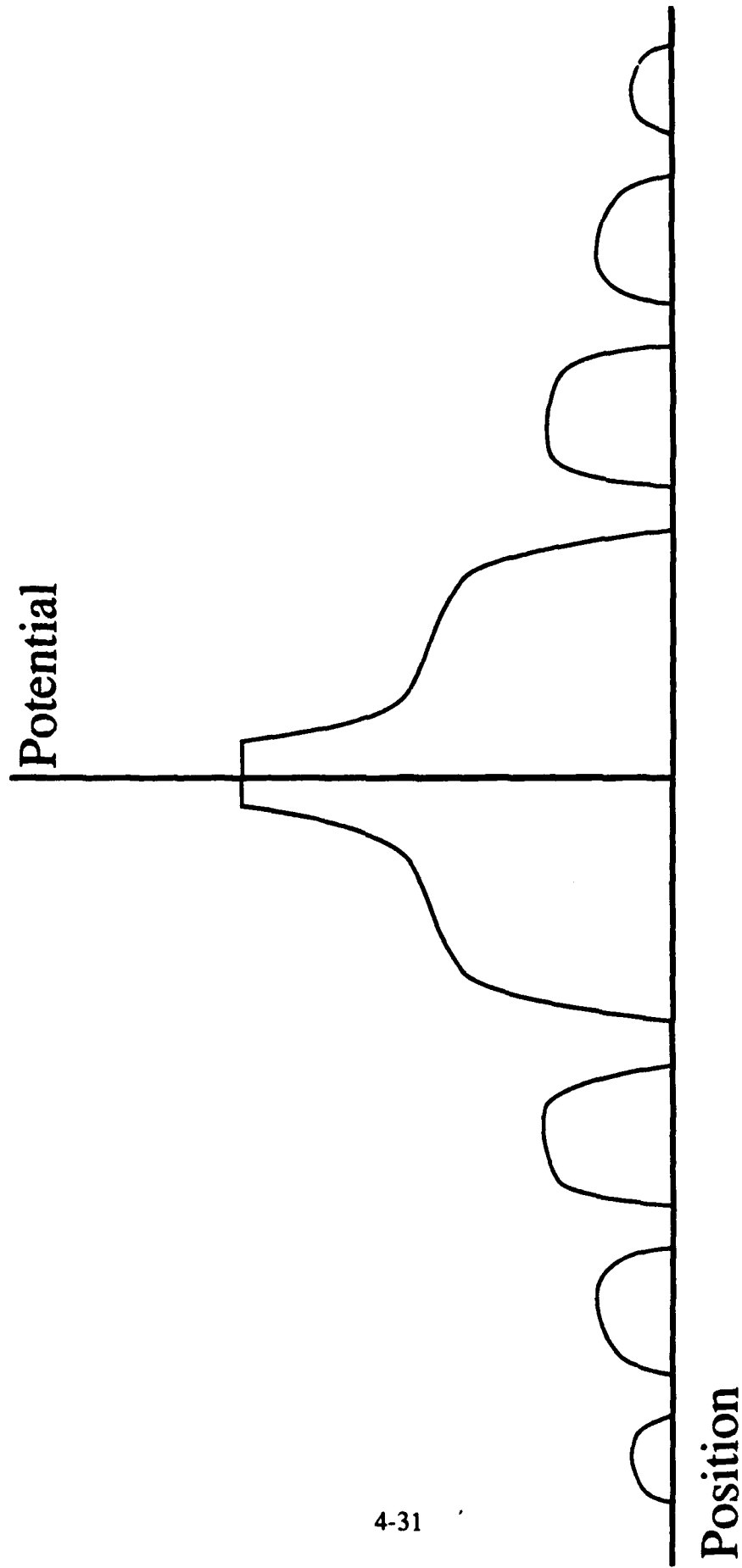


Fig. 4.20: Sketch of the potential at one frequency for a many-conductor structure where all the side lines are grounded. Note the resulting periodic nature.

The reduction in crosstalk for the smaller spacings can be explained in terms of spatial harmonics. Figure 4.20 shows a rough sketch of the potential across several grounded conductors. Between the grounded metallization, the potential rises, yielding a potential profile with a strongly periodic component. In terms of spatial harmonics, the broader the period of this profile, the greater the penetration and the greater the backside signal, as in Figure 4.1. As seen previously, the effect of a single conductor is a very broad potential on the backside; hence, it's position with respect to the line of interest is only a weak factor in a homogeneous ground surrounding as in this case. The primary difference between the multi-line structures and the few-line structures, then, is the nature of the ground, which, as shown before, is the dominant determinant of crosstalk.

#### 4.4.4 Crosstalk Reduction Mechanisms

Spot-size crosstalk is difficult to overcome without smaller spots. Fortunately, it is small in magnitude, and can be avoided by probing larger lines. Backplane crosstalk generally dominates, and is more amenable to reduction. We discuss in this section some of the alternatives available.

Several practical techniques may be considered to reduce calibration and crosstalk problems. Since the presence of a backside potential is the dominant cause of such problems, its effect must somehow be minimized. One alternative is to place a conductive layer next to the backside of the substrate. This alternative offers the advantage of in some ways mimicking the actual final packaging of the die, where a conductive epoxy is attached to a conductive package. To achieve such a conducting layer, several options are available that are compatible with electrooptic probing: apply metallization to the backside, with an opening behind the region to be probed; deposit Indium Tin Oxide (ITO) or a similar transparent conductive coating on the backside; implant the backside to form a conductive layer; or place the chip/wafer on a transparent window which is coated with ITO. The last alternative is shown in Figure 4.21. It offers the advantage of one-time processing and ease-of-use. Both the surface with ITO and the back surface must be AR coated for  $1.06 \mu\text{m}$  to avoid etalon effects between the window and the GaAs. If such is the case, it can be shown that the total reflection from the window/GaAs system is the same as that from simply the GaAs. The potential difficulty of a window is that the potential will drop across any gap between the window and GaAs 13 times faster than in the GaAs itself. Vacuum mounting or probe pressure might be sufficient to keep this effect small. In addition, AR coating the ITO on glass can be difficult since the index of ITO depends strongly on the deposition conditions. A problem common to any method of backside grounding is that

forcing the potential to zero also perturbs the impedance of surface transmission lines, degrading circuit performance.

The effect of ITO on the back surface is noted in Figures 4.11 and 4.17, for CPW's and 2-conductor crosstalk, respectively. In both cases, the ITO reduces the crosstalk to -30dB or below, corresponding to 3 % error. Note that a unique feature of a backside ground is the possibility of compensating for the error signal. Since the backside will be constant at any instant of time, placing the beam beneath a ground plane, noting the time waveform (or vector magnitude), and then subtracting it from a measurement made beneath a signal line gives a very accurate electrooptic measurement.

A second approach to crosstalk reduction is to extend the extent of the electrooptic medium sufficiently to integrate over the entire potential falloff. Although inclusion of all the field is most likely impractical, backside errors can at least be minimized or the perturbation to line impedance reduced by effectively increasing the substrate thickness. Again an AR coating must be applied to the second GaAs segment to eliminate etalon effects. A small error will arise from the potential falloff in the AR coating and in any air gap. Since the GaAs window is being probed together with the wafer, the crystallographic axes must be aligned between the two samples, or signal will be lost.

Finally, such errors can be minimized by intelligent design of circuits. Large field penetration is detrimental to transmission line moding and electrooptic transit-time in addition to the accuracy questions above. Although it is difficult to completely remove the backside potential for realistic structures, more liberal inclusion of ground planes will reduce it significantly. A "probe point" which could be included in layouts at those points in the circuit where a good measurement was desired is difficult to achieve. Due to the broad nature of the backside potential, large areas of ground plane would be needed to ensure a proper backside zero; then, a thin line, very close to ground on both sides could be introduced, and run sufficiently far to escape other potentials. Unfortunately, this is a disastrous microwave segment.

#### **4.5 Absolute Signal Calibration**

Although we have had little call for absolute signal level measurement in our work, the question is often raised about the ability to do so. The key issue in such measurements is system stability. So many factors affect the measured signal, that all must be frozen to permit comparison of signal levels made at different moments. Practically speaking, this is simple for measurements made within a given circuit at one sitting, but very difficult when



# Window for backside crosstalk reduction

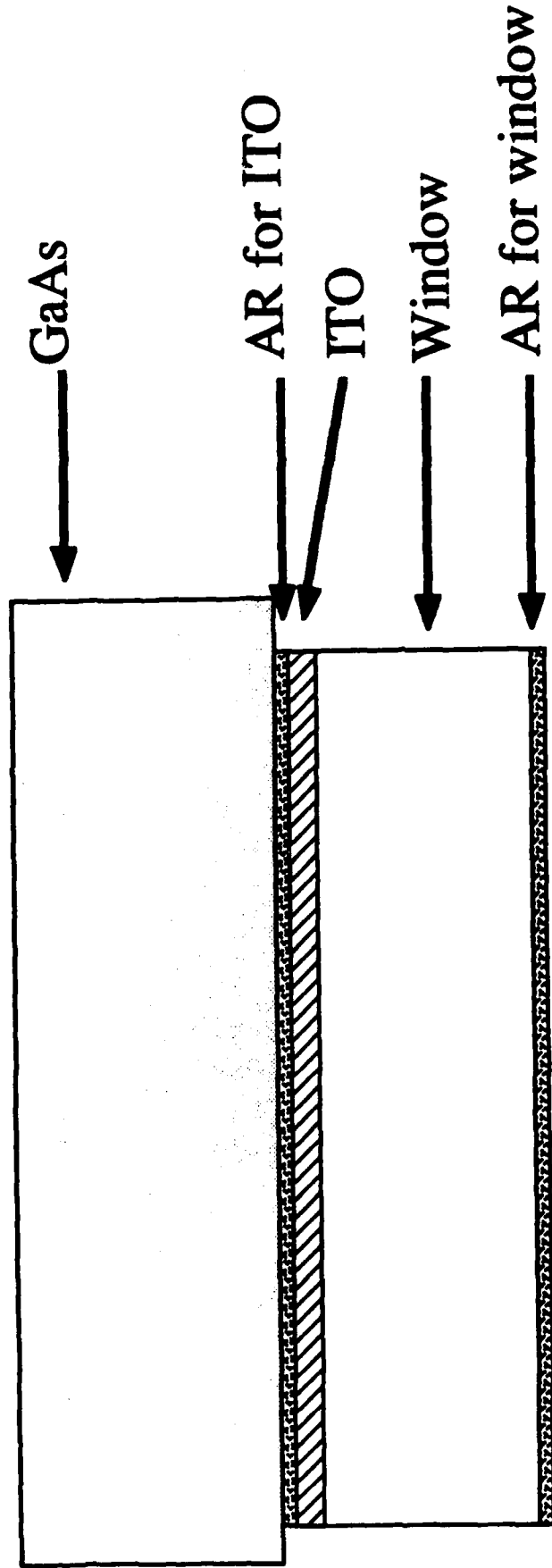


Fig. 4.21: Sketch of a window for reducing backside crosstalk without additional processing of wafers to be probed. ITO = Indium Tin Oxide, AR = anti-reflection.

made at different sittings. Most of the issues have been previously discussed; we present here their impact on absolute signal measurements.

Amplitude noise is an obvious deterrent to accurate, repeatable measurements. Particularly difficult are the very long term drifts in polarization and amplitude that require readjustment of the pulse compressor. Photodiode "normalization" is most useful in resolving *this* problem, as opposed to the more rapid amplitude fluctuations. Attention must be paid to the power dissipation of the photodiode for high bias detectors (e.g. YAG-100 at -180 V) to prevent operation in a nonlinear region where a 2x reduction in laser power is not equally reflected in the DC and AC components of the photodiode. If it is linear, consistent normalization can give excellent results.

To ensure the proportionality of the DC and AC components of photocurrent, spurious DC elements must be eliminated. These arise from several sources and can be significantly reduced by careful optical setup. The simplest is careful choice of polarizing beamsplitter orientation. In Figure 4.22 a beam with a large s-polarization component and a smaller p-component (from setting the waveplates for small photocurrent for low shot noise) should have a pure p component reflected. Due to the large size of the s-component, however, the inherent several percent leakage results in a spurious orthogonal component. This adds to the photocurrent, and, since, the s polarization has a phase shift  $180^\circ$  from the p, the signal magnitude is reduced. The problem is easily solved by insertion of a second polarize to reject the undesired component. Reduction of photocurrent and increases in signal magnitude of  $\approx 25\%$  been observed in this way.

Additional photocurrent can also arise from reflection from the GaAs backside. Unless this surface is AR coated, this reflection is unavoidable. Since the backside is not at the focus, however, the reflected light is not recollimated by the objective but is slightly diverging. Placement of a variable aperture at some distance from the focusing lens allows attenuation of that portion which has diverged outside of the properly collimated returning beam. The result is a simple reduction in photocurrent, since this component has no electrooptic phase information. Typical reductions are 15 to 20 %. Over-apodization leads to spot distortion and exaggerated imaging effects like those discussed in Section 4.2.3.

When a good linearity has been established, normalization may proceed by any of several means, as discussed in Section 3. Some form of normalization is required not only because of amplitude drift, but also because of the variable reflectivities present in circuits. Ohmic metal, schottky metal, and bare GaAs all present different reflectivities, but support electrooptic probing. Absolute calibration will require compensation for these differences.

## Leakage of s-polarization into reflection

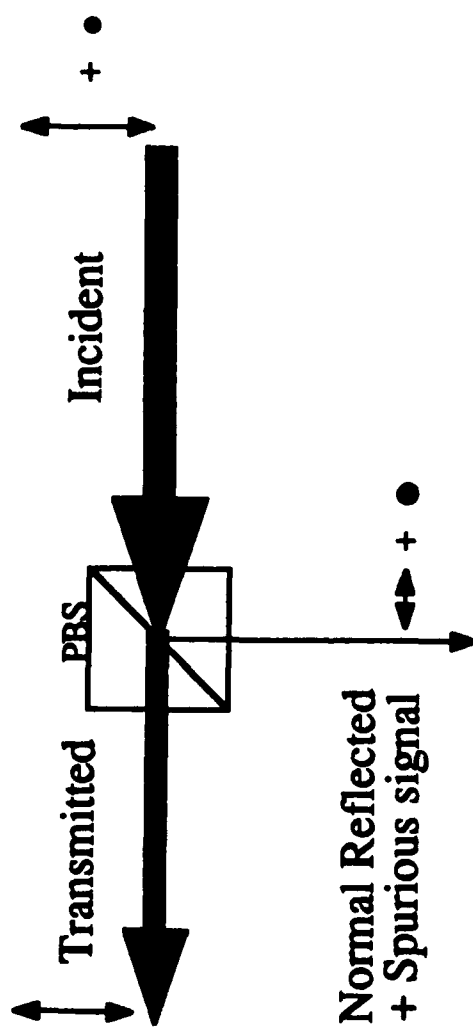


Fig. 4.22: Mechanism for leakage of unwanted light to the photodetector. It is solved by addition of a polarizer, increasing signal and reducing shot noise.

## 4.6 Conclusion

The primary contributor to electrooptic measurement error is the non-zero backplane potential. Spot-size crosstalk is generally obscured by the larger backplane signals, and effects from the focused Gaussian beam are negligible. Backplane crosstalk and calibration errors are predominantly determined by signal to ground spacing, and are generally 20 to 30 dB down. Conductive backsides offer an excellent crosstalk reduction technique for circuits where line impedances are either non-critical or independent of backside condition. Cf. [5.12], Appendix v.

## 5. Probe Invasiveness

### 5.1 Introduction

As with any probe, one question that must be resolved is its degree of invasiveness, and in what form it is manifested. Low-frequency probes placed on a small microwave interconnect introduce additional capacitance and inductance, and have poor time resolution; faster microwave probes have excellent time resolution but load the node with 50  $\Omega$ . The electrooptic needle probe [1.32,33] (cf. Section 1.2.2) exhibits invasiveness through the high dielectric present above an interconnect, leading to capacitive loading. Finally, the silicon charge-sensing probe [1.25-27], because it probes directly within an active device, has a small degree of invasiveness from charge generation. However, since silicon is a much higher quality material, and since the probe beam is cw and low power, the perturbation is very small.

Circuit perturbation during electrooptic probing occurs by charge generation through deep-level absorption or two-photon absorption within the channel of an active device. This charge then acts to increase the drain current of the MESFET through both photoconductivity and back-gating. Light can reach the active device either directly, from the gaussian shape of the pulse, or by scattering from surface irregularities. The following sections describe these processes in detail.

### 5.2 Absorption Mechanism

At 1.06  $\mu\text{m}$ , the optical probing beam is well below bandgap. Thus, single-photon band-to-band transitions are forbidden. Several other processes are allowed, however, that lead to charge generation in the vicinity of a probe beam: deep-level absorption and two-photon absorption. Cf. [5.12], Appendix V.

In deep-level absorption, carriers are excited from a deep level to a band. Since both electrons and holes can make this transition, we can imagine transitions of electrons from the valence band to the trap or from the trap to the conduction band, or both. The second then becomes a two-photon, trap-assisted process with a single-photon intensity dependence. In GaAs, the primary optical deep level [5.1] is EL2 [5.2, thought to be an Arsenic anti-site [5.3] (Arsenic on a Gallium site). Its position of 0.82 eV below the conduction band permits transitions to both bands [5.4] with the 1.17 eV energy of 1.06  $\mu\text{m}$  light. LEC-grown material typically possesses EL2 at the level of  $1-2 \times 10^{16} \text{ cm}^{-3}$

[5.5], while newer, In-"doped" materials below  $3 \times 10^{15} \text{ cm}^{-3}$ . Chemical vapor deposition also exhibits EL2 [5.6], though LPE and MBE grown material do not [5.7]. The only other deep-level present in GaAs to demonstrate significant optical absorption at  $1.06 \mu\text{m}$  is  $\text{Cr}^{3+}$  [5.8, and it is now used only rarely by commercial vendors.

The second process contributing to charge generation in GaAs is two-photon absorption (TPA). Due to the high intensities of the picosecond pulse, transitions can occur to the conduction band through the use of two photons. As a result, this process exhibits a quadratic dependence on optical power, and can be separated from the linear dependence of deep-level absorption through intensity studies. Although several authors have calculated or measured two-photon coefficients [5.9, 10] for  $1.06 \mu\text{m}$  radiation in GaAs, significant disparity still exists. The best estimate appears to be  $.04 \text{ cm/MW}$ .

An expression can be derived which calculates the crossover point between deep-level absorption and TPA. We express the pulse as

$$I(x,y,t) = \frac{P_{\text{avg}}\tau_{\text{rep}}}{w_0^2 t_0 \sigma \tau^{3/2}} \exp\left(-t^2/t_0^2\right) \exp\left(-\frac{x^2+y^2}{w_0^2}\right) \quad (5.1)$$

where  $P_{\text{avg}}$  is the average optical power,  $\tau_{\text{rep}}$  is the time between pulses,  $w_0$  is the beam radius at the focus, and  $t_0$  is the pulse half-width. Using the two-photon coefficient  $\beta$ , the deep-level cross-section  $\sigma_n$ , and the number of deep levels,  $N_{\text{dl}}$ , we can calculate the number of carriers per unit length of waist for deep levels

$$\bar{n}_{\text{dl}} = \frac{\sigma_n N_{\text{dl}} P_{\text{avg}} \tau_{\text{rep}}}{h\nu} \quad (5.2)$$

and, similarly, for two-photon absorption

$$\bar{n}_{\text{tpa}} = \beta \frac{P_{\text{avg}}^2 \tau_{\text{rep}}^2}{4h\nu w_0 t_0 \sigma \tau^{3/2}} \quad (5.3)$$

The point where TPA and deep-level absorption are equal is given by

$$P_{avg} = \frac{4w_0^2 t_0 \pi^{3/2} \sigma_n N_{dl}}{\beta \tau_{rep}} \quad (5.4)$$

For  $w_0 = 2 \mu\text{m}$ ,  $t_0 = .75 \text{ ps}$ ,  $\tau_{rep} = 12.1 \text{ ns}$ ,  $\sigma_n \approx 1 \times 10^{-16}$ ,  $N_{dl} = 1 \times 10^{16}$ ,  $\beta = .04 \text{ cm/MW}$ ,  $P_{avg}$  for the crossover is about 1 mW. Since  $N_{dl}$  and  $\beta$  are poorly known, though, this is an order of magnitude estimate.

### Schottky Diodes

An evaluation of the relative strengths of the two optical absorption mechanisms can be made by examining a simple diode. The diode is a large area Schottky diode that is part of a Varian microwave test mask [5.11]. The N<sup>-</sup> layer is 300 Å thick beneath the large center contact, which is etched back through the ohmic layer. A 1 μm buffer layer of undoped epitaxial layer is beneath that; it and the other epitaxial layers were grown by MOCVD. We measure the current and voltage across the unbiased diode for different loads with simple volt and ammeters, for an average optical power on the diode of approximately 40 mW. The resulting curve of Figure 5.1 exhibits the type of photodiode behavior expected.

Since the induced short-circuit current  $I_{sc}$  is proportional to the generated charge in the region, we can measure  $I_{sc}$  versus optical intensity to reveal the optical absorption mechanisms. Figure 5.2 illustrates the dependence on a log-log plot. If the mechanism is TPA, we expect a slope of 2, as shown in the high power region of the curve. If it is deep-level, we expect a slope of one, as shown in the lower power portion. The crossover here is about 2 mW. The significant contribution of deep levels to the absorption indicates the presence of traps in the depletion region of the diode, as expected for CVD material.

A second diode was also examined. It placed the N<sup>+</sup> layer beneath a .6 μm MBE-grown N<sup>-</sup> layer, permitting an accurate assessment of the depletion region when fully depleted. Figure 5.3 illustrates intensity dependencies of  $I_{sc}$  for this diode at two different biases. The curve upwards on both at high powers indicates the onset of two-photon absorption, although the reason for the change in crossover point is not clear. Since the material is MBE, this may be due to traps created at the surface in processing, whose effect becomes progressively less of the whole as the depletion region expands into purer MBE material. From a current of 4 μA, and a volume of 7.5 μm<sup>3</sup>, based on the beam spot and the known thickness of the depletion region at punch-through, we find an equilibrium charge flux of  $8 \times 10^{24} \text{ carriers/sec/cm}^3$ .

I-V curve for 1.06  $\mu\text{m}$  illuminated Schottky barrier

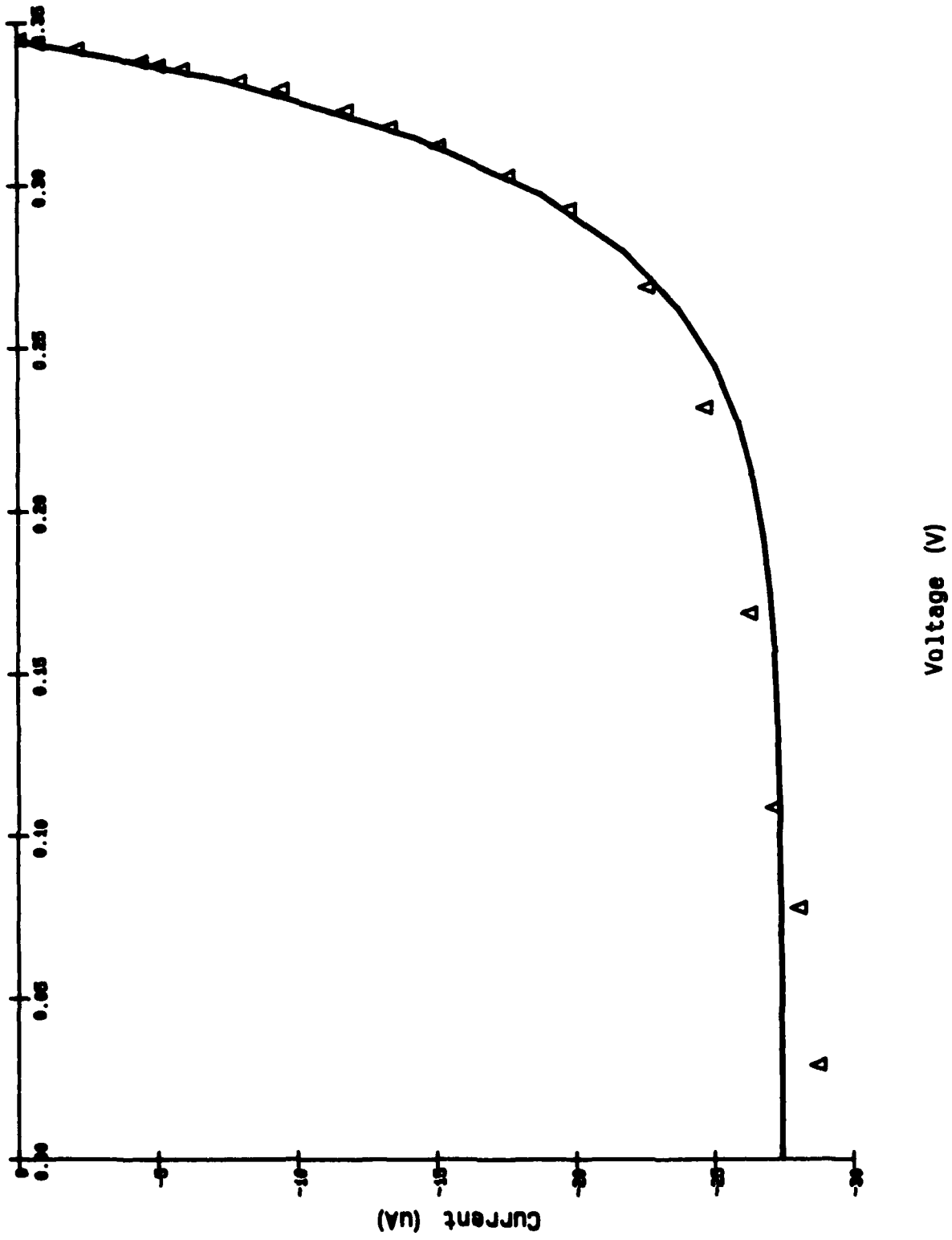
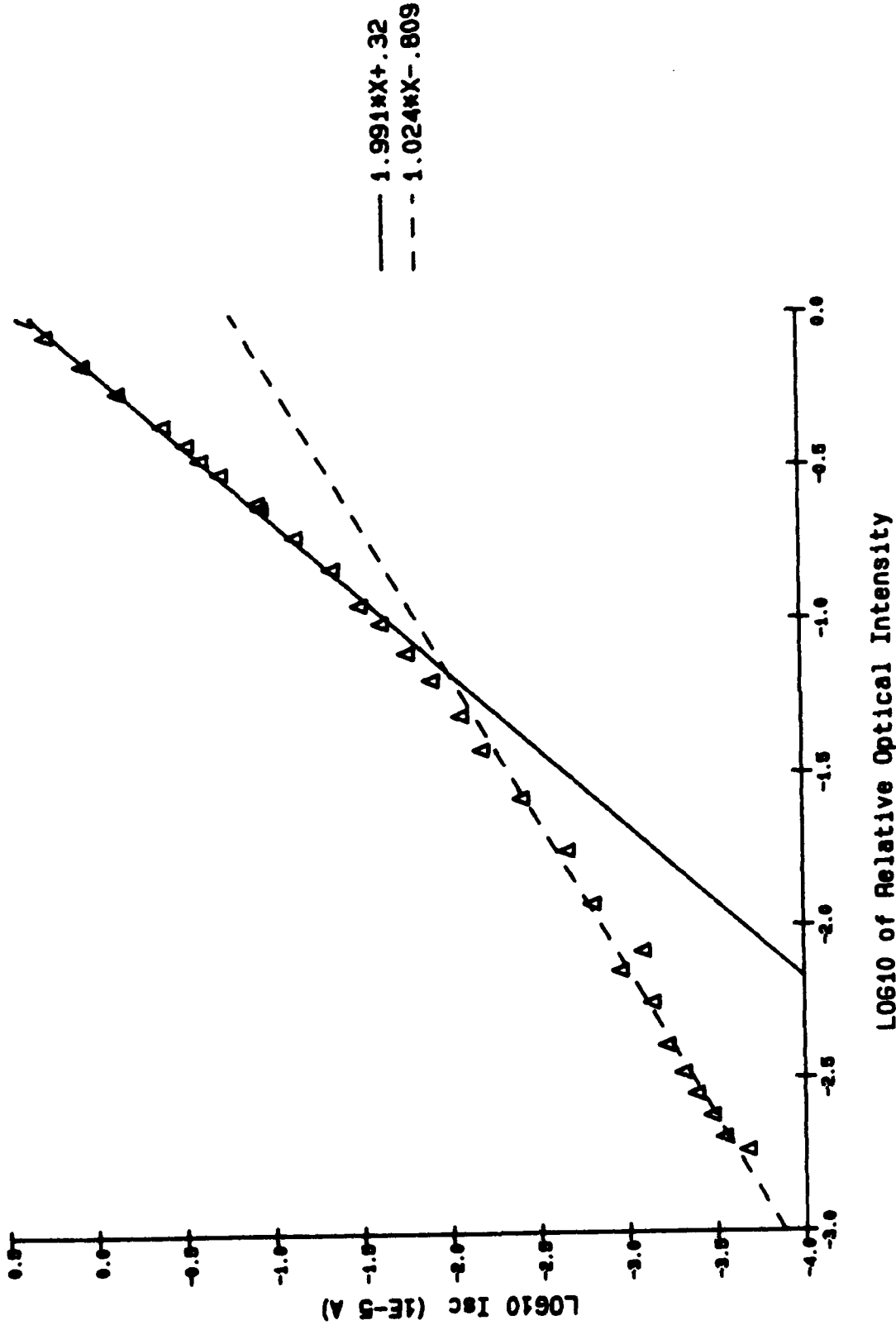


Fig. 5.1: I-V curve for a schottky diode illuminated by a high intensity 1.06  $\mu\text{m}$  laser.



Deep Level to TPA transition in Diode Isc



Optical Power Normalized to 41 mW  
 Fig. 5.2: Optical intensity dependence of the short circuit current in a schottky diode. A clear transition from deep-level absorption to two-photon absorption is indicated by the change in slope.

# Isc in Schottky Diode

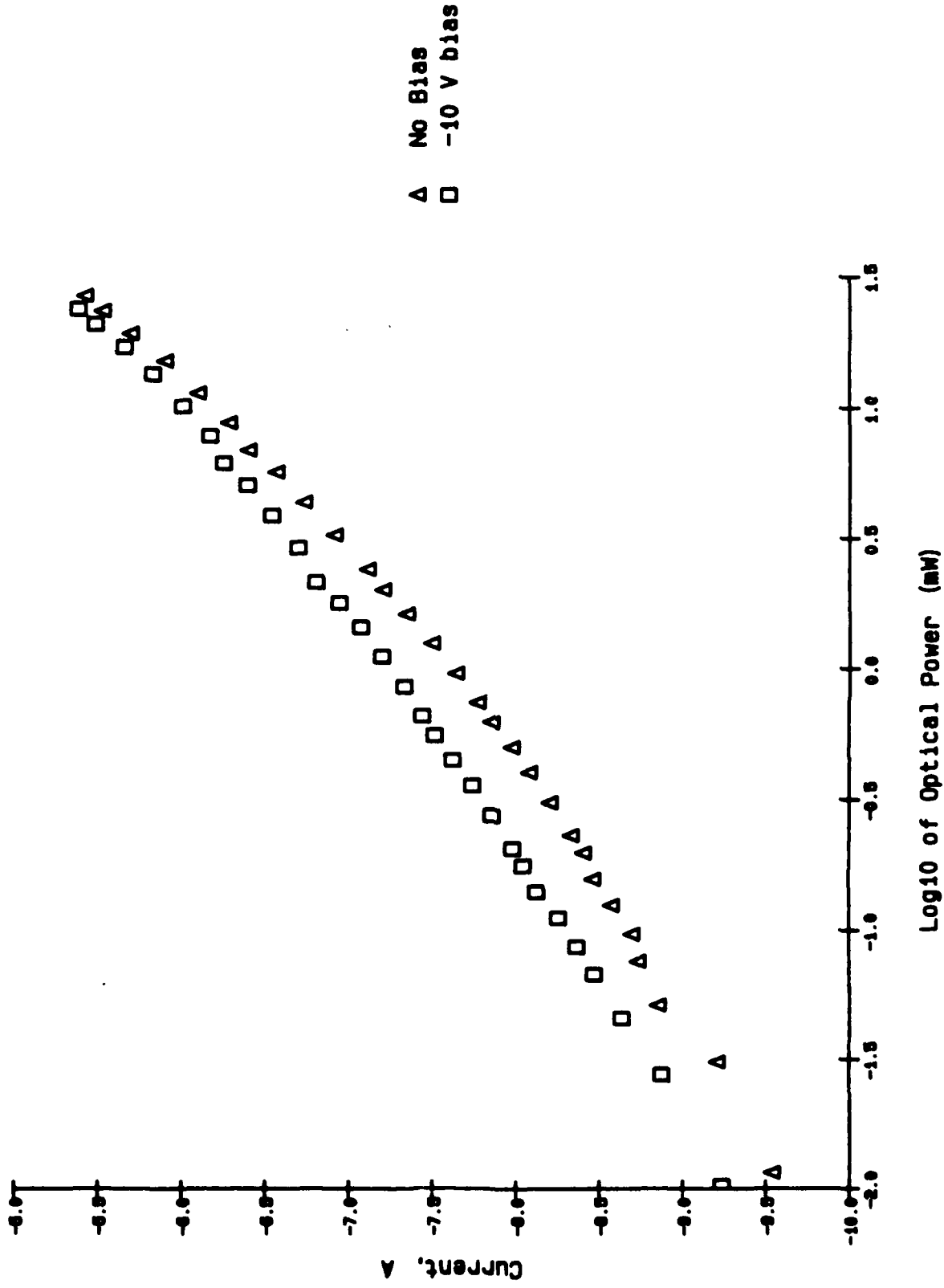
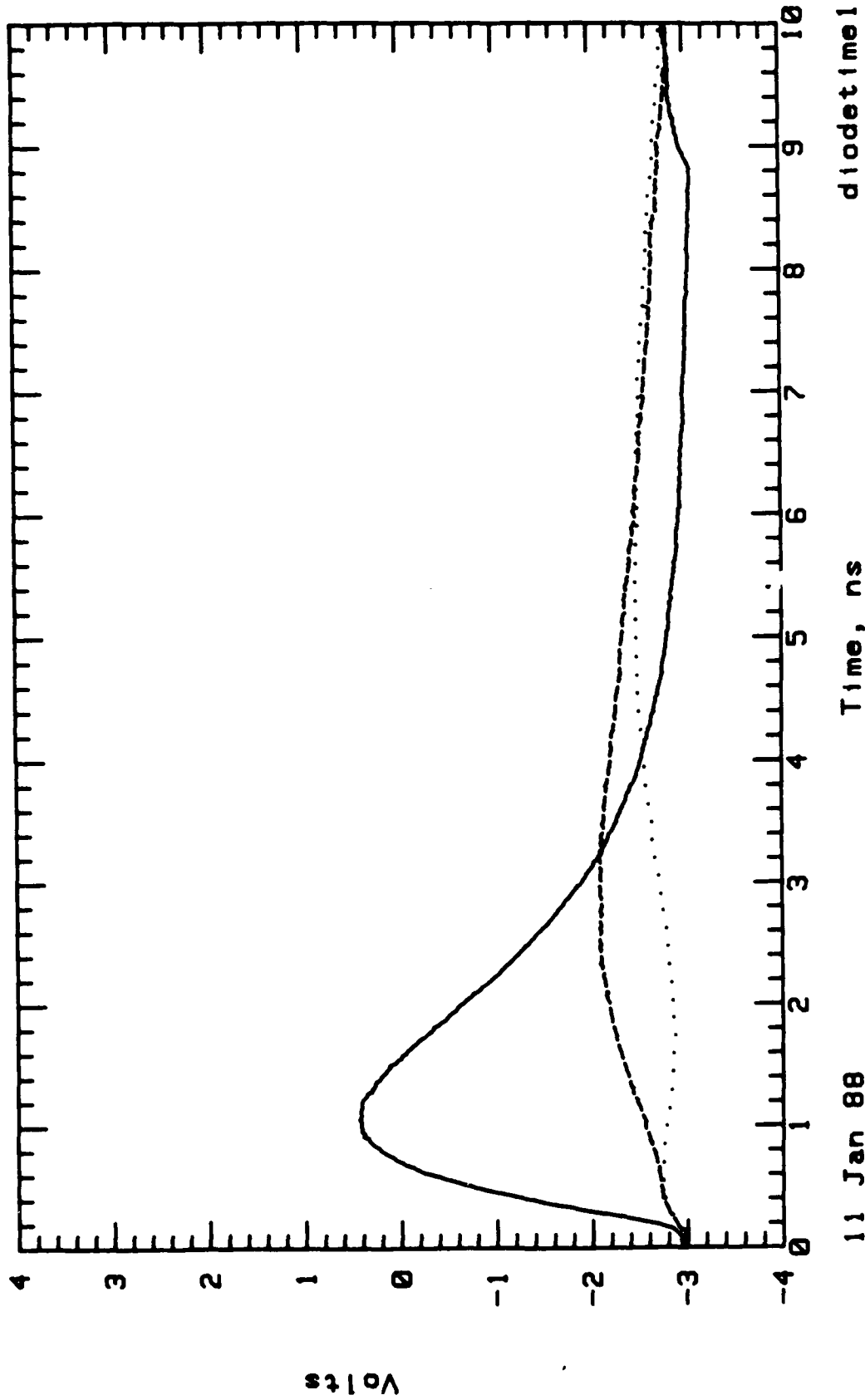


Fig. 5.3: As in Fig. 5.5, but for a diode where the depletion depth is known well, and at different biases.

Diode current variation with position



11 Jan 88

Fig. 5.4: Time response of a schottky diode to an impulse of  $1.06 \mu\text{m}$  light. The shape of the pulse depends on the position within the diode. Vertical scale: 1 V corresponds to 1 mA.

Time-resolved measurements of the induced current can also be made. Figure 5.4 presents several different waveforms as the beam is moved to different portions of the diode. The solid trace is with the beam at the edge of the Schottky region, and the dashed and dotted lines record the waveform as the beam moves to the center of the Schottky contact. The variation in the waveform is attributed to the different velocities of electrons and holes in GaAs, and on transit-time to the Schottky and ohmic contacts. A key conclusion can be drawn from these waveforms: the AC component of the current decays before the next pulse, 12 ns later. Thus, though the device is perturbed, the measurement of its state is independent of this fast component. Significantly, similar changes in the AC component of the drain current  $I_d$  are evident as the beam is moved within the channel of a MESFET.

### 5.3 Perturbations to GaAs MESFET's

As a more complex device, the MESFET is more difficult to analyze. Beam perturbations are sensitive to position, gate bias, drain bias, as well as terminal loading. Nevertheless, several key points can be made in characterizing the effect of the 1.06  $\mu\text{m}$  probe beam on a FET. The first is that the primary perturbation is to the drain current  $I_d$ . Increases in current are observed with both an AC, pulse-to-pulse component similar to Fig. 5.4, and a constant background component. Simple curve tracer depiction of the I-V properties of the device shows a marked jump equivalent to a negative gate bias upon application of a high-power beam directly within the active device.

The two components of the perturbation -- AC and DC -- can be studied separately for their intensity dependence. Figure 5.5 shows the change of the 82 MHz component of the AC signal as measured on a spectrum analyzer. The change in slope around 1 mW reveals the two-photon crossover again. Note especially the relatively fast falloff with power. This is also reflected in the fact that the AC perturbation is only strong within the active device itself, and then falls off rapidly to the sides. Since electrooptic probing occurs on interconnects rather than within a device, the AC contribution will be quite small.

The DC effect is of a much different nature. Figure 5.6 plots the change in the drain current, in mA, as a function of optical intensity. The baseline drain current is about 12 mA. The significant difference is the intensity dependence: The DC effect varies  $\approx 8$  dB for a decade of optical power, while the AC effect varies over 25 dB. This DC effect will then be significant even at large distance from the FET, and can be induced even for scattered light (see Section 5.4).

Intensity Dependence of AC part of  $I_{sd}$

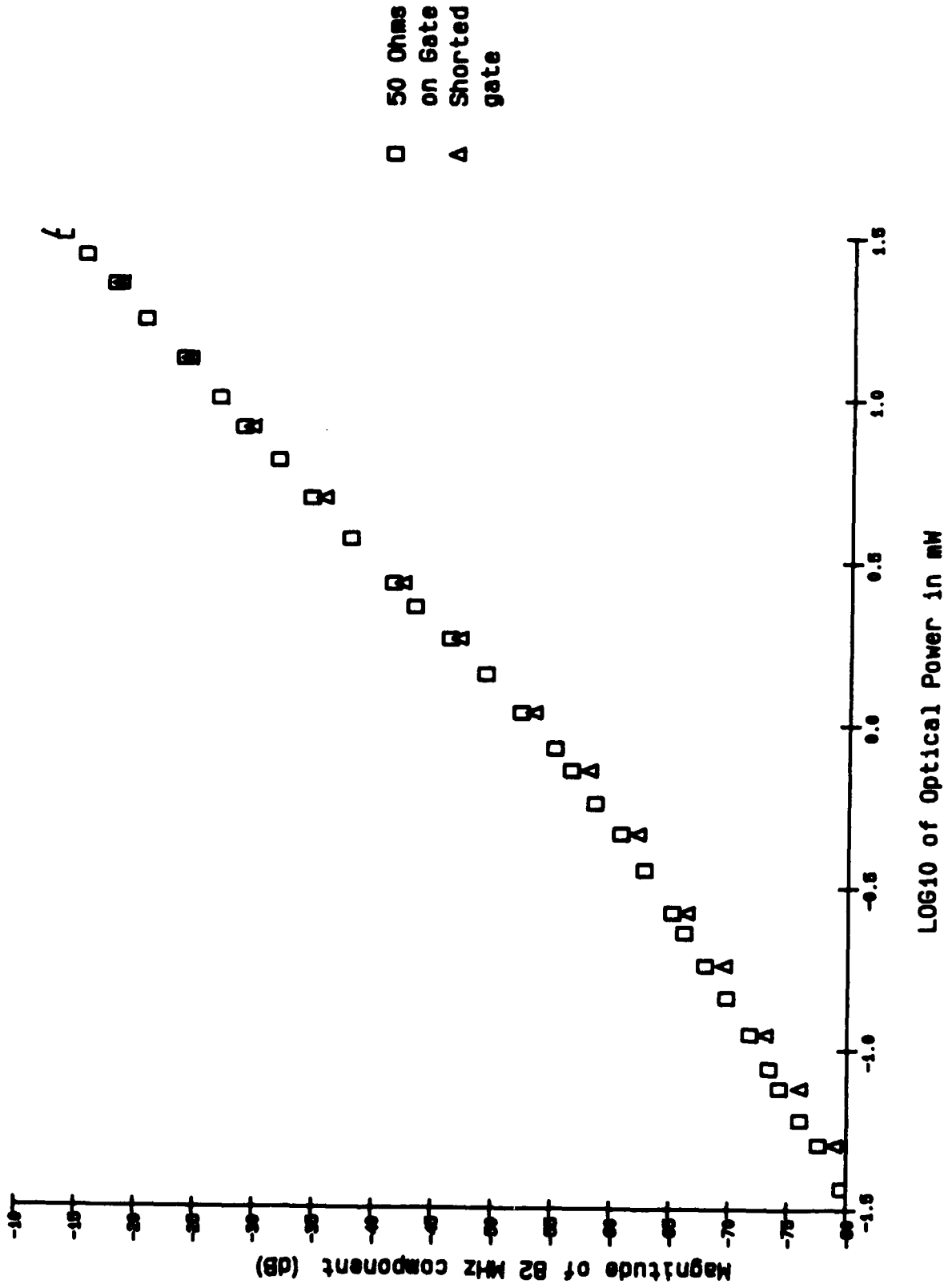


Fig. 5.5: Intensity dependence of the 82 MHz component of  $I_{sc}$  at 2 different gate conditions. Note the rapid falloff with intensity.  $V_{sd} = .75$  V.

# Intensity Dependence of DC part of $I_{sd}$

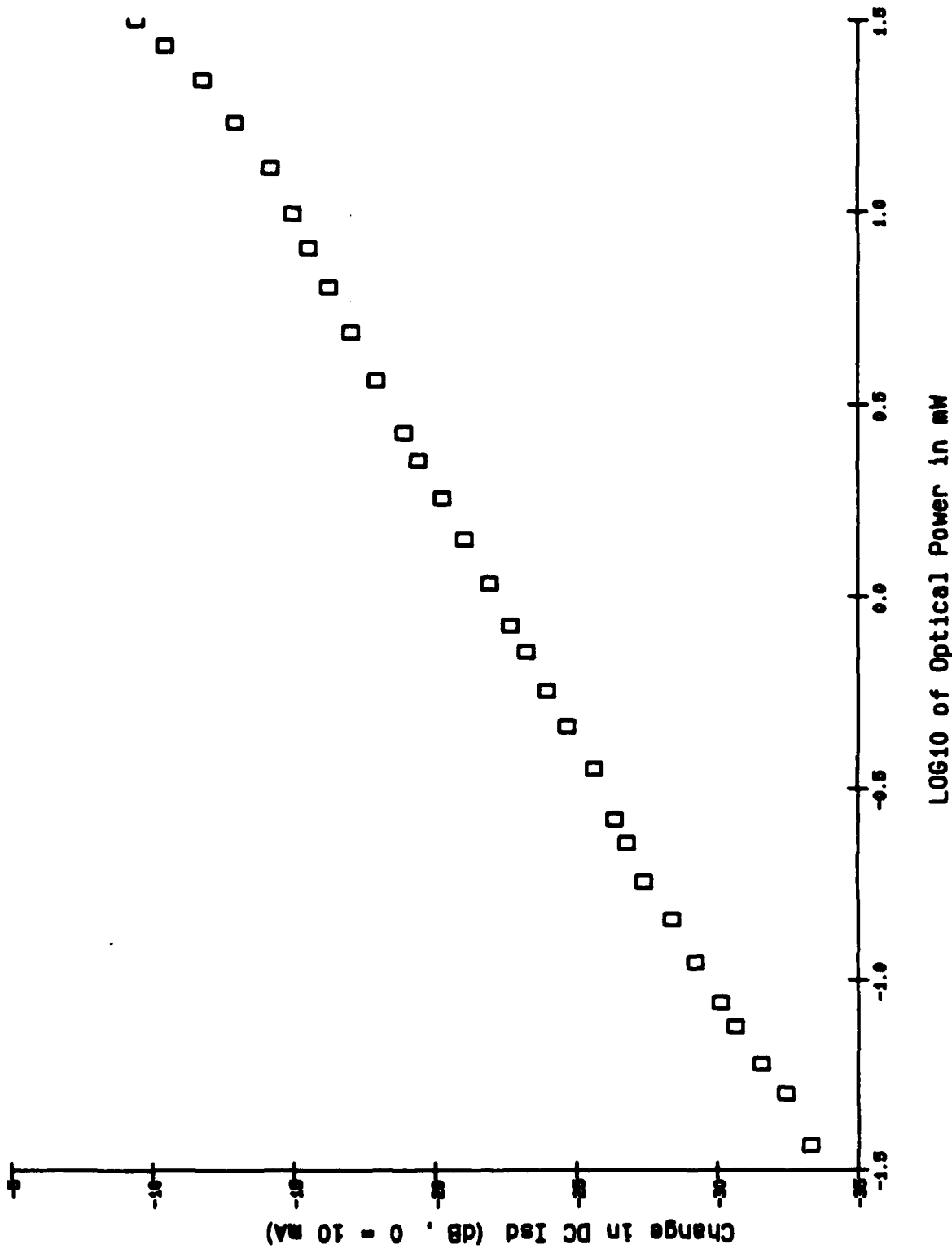


Fig. 5.6: Intensity dependence of the DC component of  $I_{sc}$ . Note the very gradual falloff with intensity. The gate is loaded with  $50 \Omega$ .  $V_{sd} = .75 \text{ V}$

The intensity dependences then give us clues as to the physical mechanism behind them. The nearly proportional nature of the AC effect to the optical power (or power squared, depending on the region), leads to the conclusion that the beam is directly contributing to the drain current by charge injection or photoconductivity. The DC effect, however, is more likely attributable to the backgating of the device through deep traps with long time constants. This hypothesis is confirmed by the elimination, upon optical excitation, of the "looping" in curve-tracer I-V plots that is typically associated with trap filling and emptying. Since the drain current is proportional to the gate voltage in the normal operating regime, the filling of traps that then results in quasi-Fermi level shifts will give a  $I_{sd}$  vs.  $P_{optical}$  dependence that is logarithmic. The changeover to two-photon absorption, together with the relation of the number of traps to the amount of generated charge will alter the simple relationship.

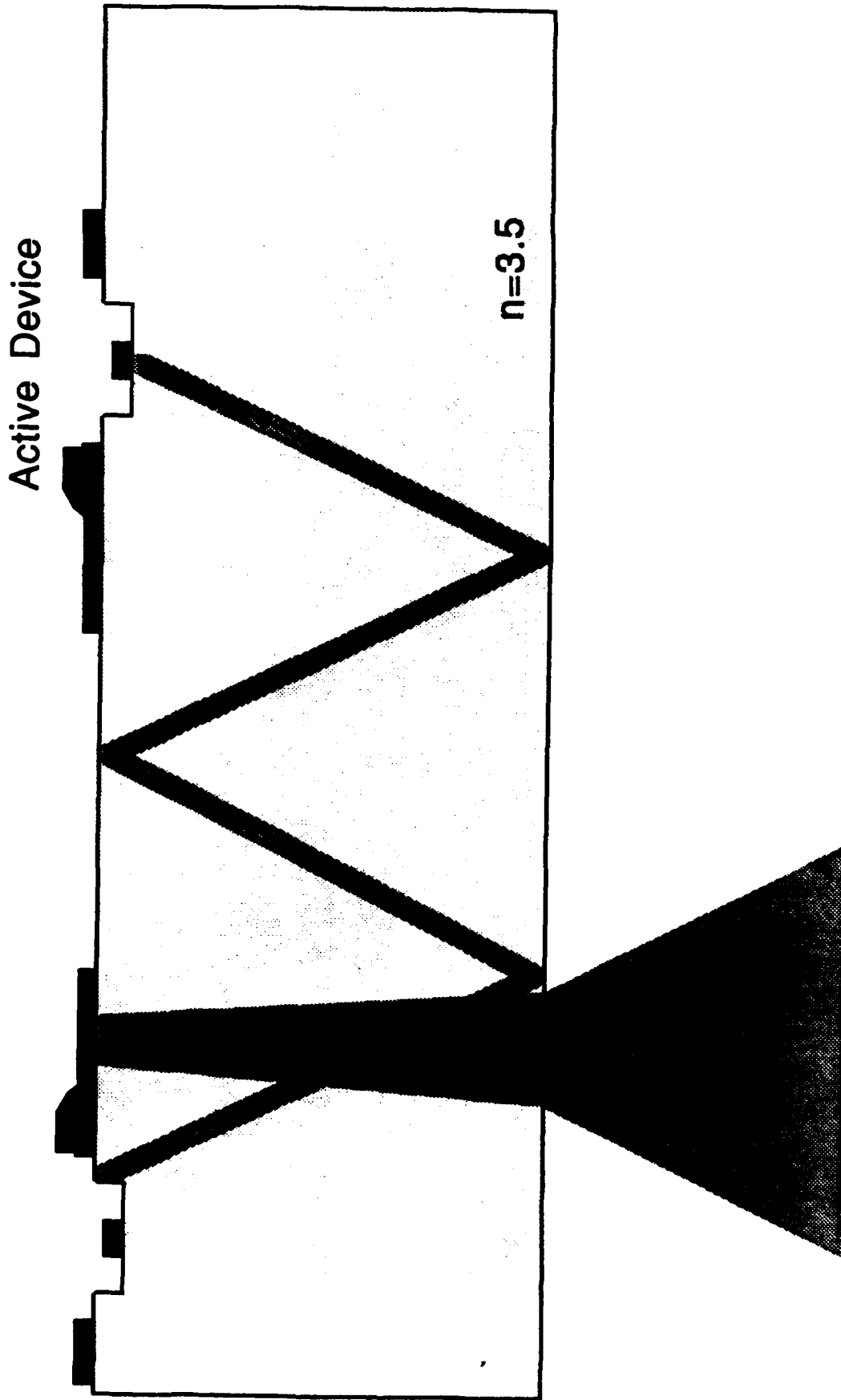
We conclude that changes to MESFET's caused by electrooptic probing will be largely DC in nature outside an active device. A slow variation with optical power frustrates attempts to significantly reduce invasiveness by lowering probe power. Since the effect is DC, however, it invites compensation by gate bias adjustment where possible. Finally, two-photon absorption dominates the charge generation at powers on the FET greater than several mW.

#### 5.4 Beam Propagation to an Active Device

If the falloff of the perturbation away from a device was solely determined by the distance of the beam from the gate, invasiveness could be significantly reduced by avoidance of the device under test. In actual probing, however, device perturbations can be observed that are quite strong, even when the beam is over a millimeter away. The explanation for this is described below.

Figure 5.7 illustrates the scattering of the optical beam from an active device. Although the beam itself is not within the device on the left, it presents significant content in its Gaussian tails. This tail content can then scatter from the surface roughness characteristic of an active device. Due to the large index of refraction of GaAs, total internal reflection will occur for any beam internally incident on an interface at an angle greater than  $16^\circ$ . Subsequently, this beam reflects from both front and back wafer surfaces, being waveguided throughout the die. This process results in light incident on an active device at levels much greater than expected from consideration of only the Gaussian tails.

# Propagation of optical beam from probe point to an active device



Optical Beam

Fig. 5.7: Mechanism for propagation of scattered radiation in the gaussian tails of the beam to the active region of a distant device. Total internal reflection occurs at the GaAs-air interfaces.



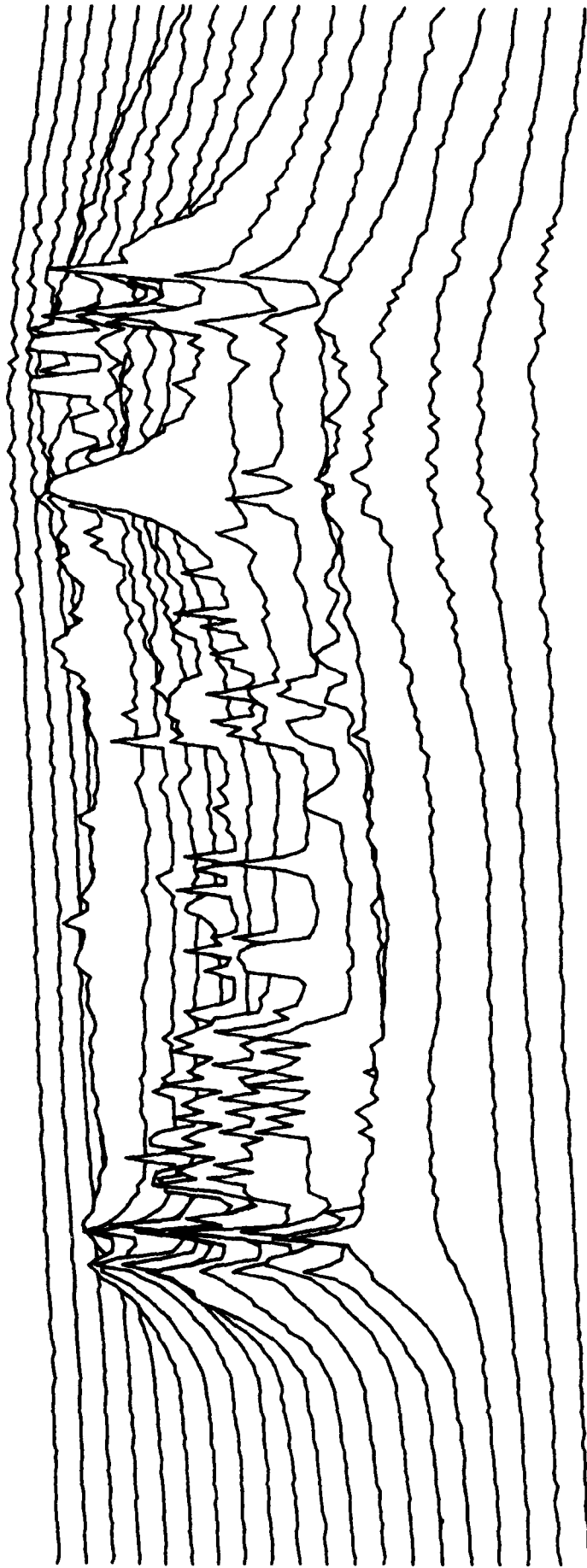


Fig. 5.8: 2D scan of the change in drain current of a MESFET as a function of beam position. The entire 5 mm chip is included in the scan. The MESFET being monitored is in the middle right.

Surface roughness which can scatter the probe occurs at several notable sites within a circuit: ohmic metal used for drain and source contacts and for diodes, and gate recesses. Roughened die edges, from edge chipping upon cleavage also contributes to scattering. Finally, the transversely varying reflection presented to a beam partially beneath a surface conductor can also mildly scatter light out of the return path of the beam. Figure 5.8 shows a 2-D scan of the perturbation to a FET's drain current as the beam is moved within the die. Note the large peaks well away from the device under test, located at the peak in the middle right. The largest distant perturbations can be attributed to active devices with gate recess.

Reduction of this scattering is a difficult problem. Total internal reflection cannot be eliminated by simple application of intervening layers of materials, though the interface of total reflection can be changed. It would be possible to make these intermediate layers of an absorbing material, but the probe then cannot properly enter the substrate. If a hole is made in the absorbing medium, probe positioning is impaired. The best solution to scattering seems to be a judicious choice of probe points well away from active devices.

## 5.5 Conclusion

Charge generation due to the 1.06  $\mu\text{m}$  probe beam is caused by two-photon absorption at optical powers on the FET above several milliwatts. Deep-level absorption is evident at lower power, and the threshold is determined by the concentration of EL2 in the material. MESFET's perturbed by the beam suffer an increase in drain current with both a fast component that decays before the next pulse and falls off quickly with optical power, and a DC component with a weak optical power dependence. Scattering from device surface roughness leads to waveguiding within the GaAs die, causing device perturbation far from the probe point. Low optical probe powers together with avoidance of active devices will minimize the invasive aspects. Cf. [5.12], Appendix V.

## References for Section 5

---

- 5.1 G.M. Martin, A. Mitonneau, and A. Mircea, *Electron. Lett.* **13**, 191 (1977).
- 5.2 S. Makram-Ebeid, P. Langlade, and G.M. Martin, in *Semi-insulating III-V Materials: Kah-Nee-Ta 1984*, edited by D.C. Look and J.S. Blakemore (Shiva, Nantwich, UK, 1984), p. 184.
- 5.3 See P. Dobrilla and J.S. Blakemore, *J. Appl. Phys.* **58**, 208 (1985) and references therein.

- 
- 5.4 G.M. Martin, in *Semi-Insulating III-V Materials: Nottingham 1980*, edited by G.J. Rees (Shiva, Nantwich, UK, 1980), p. 13.
- 5.5 J. Lagowski, M. Kaminska, J.M. Parsey, H.C. Gatos, and W. Walukiewicz, 10<sup>th</sup> Conference on GaAs and Related Compounds, 1982, Albuquerque, New Mexico.
- 5.6 L. Samuelson, P. Omling, H. Titze, and H.G. Grimmeis, *J. Cryst. Growth* **55**, 164 (1981); P.K. Battacharya, J.W. Ku, S.J.T. Owen, W. Aebi, C.B. Cooper, and R.L. Moon, *Appl. Phys. Lett.* **36**, 304 (1980); T. Matsumoto and P.K. Battacharya, *Appl. Phys. Lett.* **41**, 662 (1982).
- 5.7 S. Subramanian, B.M. Arora, and S. Guha, *Solid St. Electron.* **24**, 287 (1981).
- 5.8 G. Martinez, A.M. Hannel, W. Szuskiewicz, M. Balkanski, and B. Clerjaud, *Phys. Rev. B* **23**, 3920 (1981).
- 5.9 A. Saissy, A. Azema, J. Botineau, and F. Gires, *Appl. Phys.* **15**, 99 (1978).
- 5.10 E.W. Van Stryland, H. Vanherzeele, M.A. Woodall, M.J. Soileau, A.L. Smirl, S. Guha, and T.F. Boggess, *Optical Engr.* **24**, 613 (1985).
- 5.11 Courtesy of Majid Riaziat, Varian Associates.
- 5.12 K.J. Weingarten, "Gallium Arsenide Integrated Circuit Testing Using Electrooptic Sampling," Ph.D. Thesis, Stanford University, Stanford CA, 1987.  
Excerpts are reprinted in APPENDIX V of this report.

## 6. Electrooptic Sampler Measurement Modes

In the electrooptic sampling system, if first-order laser intensity noise is negligible, a signal processing scheme which translates the frequency of the measured signal to a spectral region above the  $1/f$  noise corner of the laser will allow near-shot-noise limited detection. The signal can be recovered in the presence of intensity noise in both the frequency and the time domain.

### 6.1. Vector Mode Measurements

Harmonic mixing is used for vector voltage measurements. The synthesizer driving the IC is set to an exact multiple of the laser repetition rate plus a frequency offset  $\Delta f$  (1 MHz typically) that is well above the background laser intensity noise. The synchronous detector, shown schematically in Fig. 6.1, consists of two sections in addition to the photodiode receiver; the frequency downconverter, and a commercial lock-in amplifier. The frequency downconverter is necessary because the lock-in amplifier's maximum frequency of operation, 100 kHz, is not quite sufficient to avoid low-frequency laser intensity noise. The lock-in amplifier provides precision measurement of the signal with a range of time constants for setting the integration time (or equivalently the receiver bandwidth) of the measurement.

Fig. 6.2 shows a block diagram of the frequency downconverter. The downconverter serves two purpose. First, it mixes the measured signal down to a frequency within the range of the lock-in amplifier, and second, it generates a synchronous reference signal for the lock-in amplifier. The frequency downconverter mixes the measured signal to a frequency (50 kHz typically) within the 100 kHz range of the lock-in, which measures and displays its magnitude and phase. To measure the response at different frequencies, the synthesizer frequency is stepped by an exact multiple of the laser repetition rate  $f_0$ .

#### 6.1.1. Harmonic Mixing

Harmonic mixing translates the detection frequency by simply setting the frequency offset  $\Delta f$  from (1.25) to a value above the  $1/f$  noise corner (typically 1-10 MHz). In this case the received signal corresponds to the intensity modulation given by (1.26)

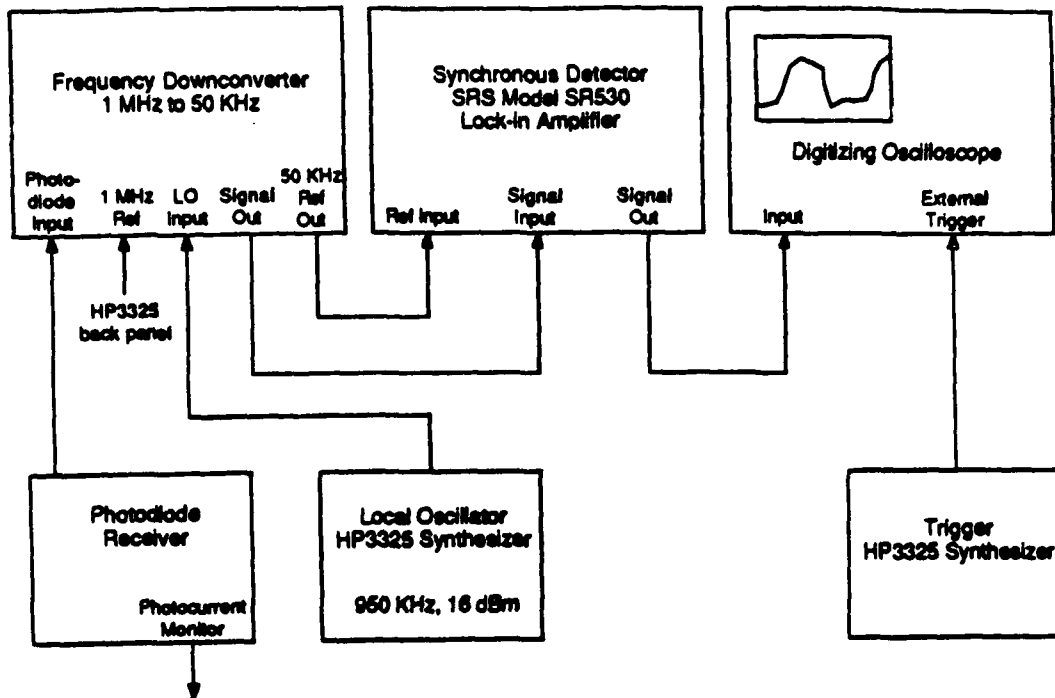


Fig.6.1. Receiver block diagram.

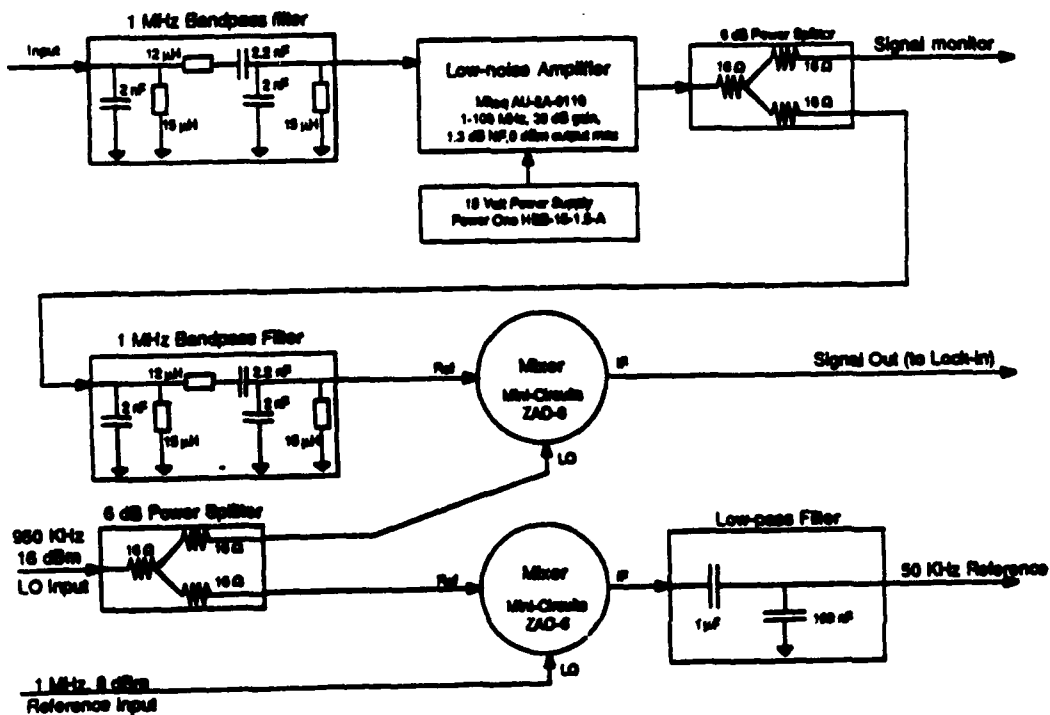


Fig.6.2. Frequency converter schematic.

$$i_{sig} = I_0 \frac{\pi}{V_{\pi}} v_s \quad (6.1)$$

and the noise-equivalent voltage is

$$v_{min} = \frac{V_{\pi}}{\pi} \sqrt{\frac{2q}{I_0}} \frac{V}{\sqrt{Hz}} \quad (6.2)$$

as in (3.3) for receiver bandwidth  $B = 1$  Hz. The acquisition time  $T_{acq} = 1/B$ , a 1 second measurement acquisition time for a 1 Hz receiver bandwidth. For a given noise voltage,

$$T_{acq} = \left( \frac{V_{\pi}}{\pi v_{min}} \right)^2 \frac{2q}{I_0} \quad (6.3)$$

### 6.1.2. Traveling-Wave Measurement

Harmonic mixing measures the vector voltage but not the electrical current, preventing a direct measure of two-port circuit parameters. At microwave and millimeter-wave frequencies, where conductor lengths and circuit element sizes often become large with respect to the electrical wavelength, direct measurements of conductor voltages and currents are difficult with conventional instruments. Microwave test instruments use directional couplers and directional bridges to separate the incident and reflected voltage traveling waves at the ports of a microwave device or network. The relationship between these waves, known as the *scattering parameters* [6.1], is a measure of a circuit's two-port parameters.

The optical probe measures the voltage on a conductor due to the sum of the incident and reflected traveling waves. Measuring the voltage as a function of position [6.2], similar to a slotted-line measurement, allows calculation of the incident and reflected waves on transmission lines connected to devices or circuits. The vector voltage due to the sum of the incident and reflected traveling waves on a lossless transmission line conductor is

$$V(z) = V^+ \exp(-j\beta z) + V^- \exp(+j\beta z) \quad (6.4)$$

where  $V^+$  and  $V^-$  are the forward and reverse traveling wave coefficients,  $\beta$  is the wavenumber  $2\pi/\lambda$ , and  $z$  is the position. The traveling-wave coefficients are calculated by measuring this vector voltage as a function of position along a conductor using the optical probe, then solving for these coefficients using a linear projection algorithm (see Appendix IV). From this information the network scattering parameters can then be determined.

### 6.1.3. Two-port S-parameter Measurements

Extending the one-port measurement to calculate the incident and reflected waves on the input and output ports of a network allows for calculation of the S-parameters with a reference plane on the integrated circuit. Fig. 6.3 shows a general test structure for S-parameter measurement, consisting of a device with transmission lines connected to its input and output. The  $a$ 's represent traveling waves propagating toward the DUT and the  $b$ 's represent traveling waves propagating away from the DUT. Applying an input signal, the electrooptic probe is scanned along the input and output transmission lines and the traveling wave coefficients are determined. With an ideal test structure, the transmission line characteristic impedance  $Z_0$  equals the load impedance  $Z_L$  and the S-parameters can be calculated directly from the measured traveling waves.

$$\begin{aligned}
 S_{11} &= \left. \frac{b_1}{a_1} \right|_{a_2=0} & S_{21} &= \left. \frac{b_2}{a_1} \right|_{a_2=0} \\
 S_{12} &= \left. \frac{b_1}{a_2} \right|_{a_1=0} & S_{22} &= \left. \frac{b_2}{a_2} \right|_{a_1=0}
 \end{aligned}
 \tag{6.5}$$

For example, with a drive signal applied to the input, any traveling wave  $b_2$  transmitted by the DUT is absorbed by the load, assuring  $a_2=0$ . However, in a practical test structure, the load impedance is determined by wafer probes with cabling or some other test fixture, and will not exactly match  $Z_0$ , resulting in a reflected wave  $a_2$ . The measured traveling waves must be corrected for this error term.

Fig. 6.4 is an error model for the source and load mismatch of the test setup. With the drive signal applied to the input of the device, the actual S-parameters (designated by the  $a$  subscript) are

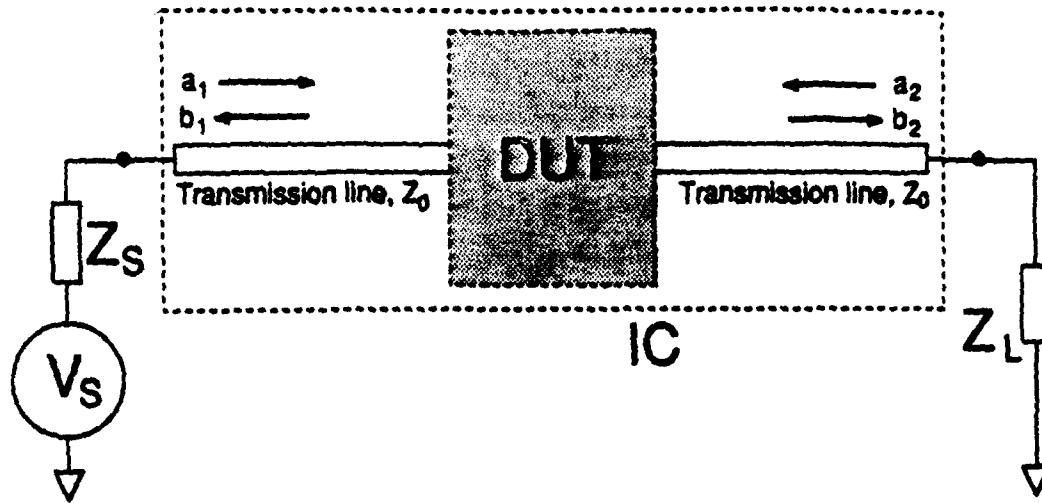


Fig. 6.3. Integrated circuit S-parameter test structure for the electrooptic probe.

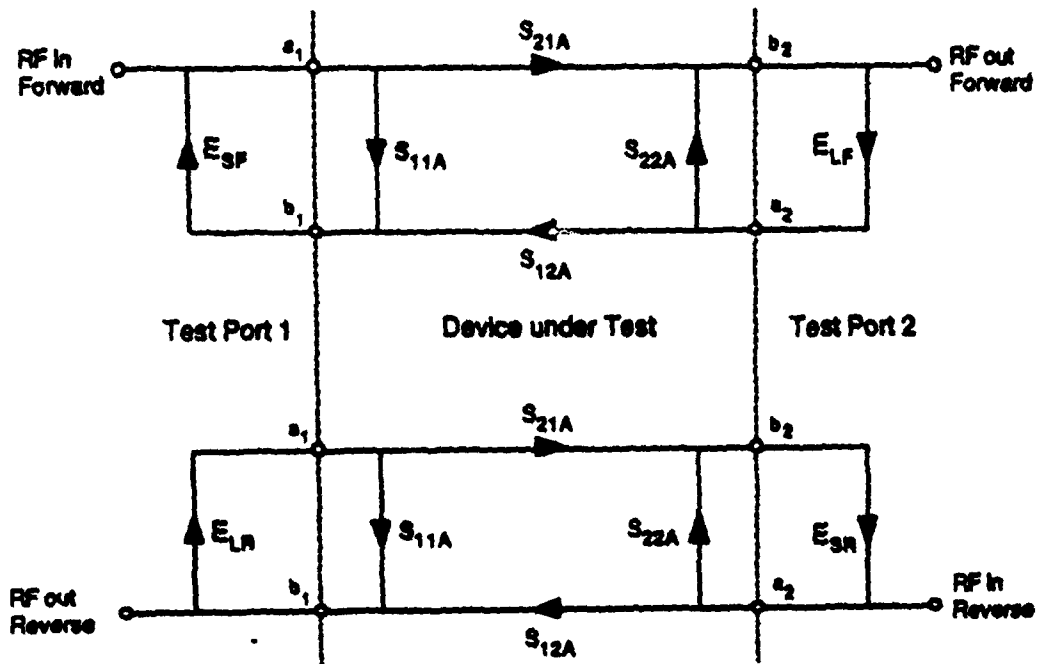


Fig. 6.4. Error model for the S-parameter test structure of Fig. 4.14. Only the forward and reverse load match, corrected for as shown in (4.5), contributes errors to the measurement.



$$S_{11a} = \frac{b_{1f} - S_{12a} a_{2f}}{a_{1f}} \quad (6.6)$$

$$S_{21a} = \frac{b_{2f} - S_{22a} a_{2f}}{a_{1f}}$$

where the  $f$  subscript indicates the drive signal is applied to the forward or input side of the DUT. Similarly, with the drive signal applied to the reverse (output) side of the DUT,

$$S_{22a} = \frac{b_{2r} - S_{21a} a_{1r}}{a_{2r}} \quad (6.7)$$

$$S_{12a} = \frac{b_{1r} - S_{11a} a_{1r}}{a_{2r}}$$

Now, the equations for  $S_{11a}$  can be substituted into the equation for  $S_{12a}$ , and vice versa, and  $S_{22a}$  can be substituted into the equation for  $S_{21a}$ , and vice versa, to obtain equations for the actual S-parameters in terms of the measured  $a$  and  $b$  values. The following defined variables are then substituted for ratios of the  $a$ 's and  $b$ 's

$$S_{11m} = \frac{b_{1f}}{a_{1f}} \quad S_{12m} = \frac{b_{1r}}{a_{2r}}$$

$$S_{21m} = \frac{b_{2f}}{a_{1f}} \quad S_{22m} = \frac{b_{2r}}{a_{2r}} \quad (6.8)$$

$$E_{Lf} = \frac{a_{2f}}{b_{2f}} \quad E_{Lr} = \frac{a_{1r}}{b_{1r}}$$

where the  $m$  subscript represents the measured values of the S-parameters, with no error correction, and  $E_{Lf}$  and  $E_{Lr}$  are the forward and reverse load match, respectively. The resulting error equations for electrooptic probing are

$$S_{11a} = \frac{S_{11m} - E_{Lf} S_{21m} S_{12m}}{1 - E_{Lf} E_{Lr} S_{21m} S_{12m}}$$

$$S_{22a} = \frac{S_{22m} - E_{Lr} S_{21m} S_{12m}}{1 - E_{Lf} E_{Lr} S_{21m} S_{12m}}$$

(6.9)

$$S_{21a} = \frac{S_{21m} (1 - E_{Lf} S_{21m} S_{12m})}{1 - E_{Lf} E_{Lr} S_{21m} S_{12m}}$$

$$S_{12a} = \frac{S_{12m} (1 - E_{Lr} S_{21m} S_{12m})}{1 - E_{Lf} E_{Lr} S_{21m} S_{12m}}$$

This technique has several important features for S-parameter measurements. First, the measurement is on-chip, with the phase reference points determined by the probe beam position with respect to the DUT. Secondly, the technique requires no separate calibration standards, such as precision  $50 \Omega$  terminations, opens, and shorts required with conventional network analyzers. The calibration standard by which the S-parameters are defined is the characteristic impedance  $Z_0$  of the input and output transmission lines. The accuracy and repeatability these lines, integrated into the IC fabrication, can be precisely controlled. Finally, the optical system's bandwidth allows measurements into the millimeter-wave frequency range.

A disadvantage of this approach is the size of transmission lines required, which use valuable space on the IC. Roughly an eighth of a wavelength is required to make a reasonable measurement with the optical system's current level of (multiplicative) intensity noise. Also, the intensity noise sets an effective directivity slightly more than 20 dB. Stabilizing

the laser intensity noise will improve the S-parameter measurement performance and allow for measurements on shorter sections of transmission line.

## 6.2. Time Waveform Measurements

Equivalent-time sampling is used to view time waveforms. The synthesizer is set to an exact multiple of the laser repetition rate ( $\approx 82$  MHz), plus a frequency offset  $\Delta f$  (10-100 Hz) that sets the measurement scan rate. The modulation frequency  $f_m$  for pulse modulation or phase modulation is set to a value (1 MHz typically) well above the low frequency intensity noise. The measured signal has a component at  $f_m$  whose amplitude varies in proportion to the signal at the scan rate  $\Delta f$ . The frequency downconverter mixes this signal to a frequency in the range of the lock-in amplifier (50 kHz typically), which demodulates the signal to baseband and detects the in-phase component of the signal that varies in proportion to the measured signal at the scan rate  $\Delta f$ . The signal is displayed on an oscilloscope which is externally triggered from a low-frequency synthesizer locked to the source microwave synthesizer, providing a time reference for the measurement so that relative time delays between two signals can be determined. For phase modulation (Section 6.2.2), the displayed signal is proportional to the time derivative of the measured signal, and is recovered by integrating the displayed signal in software using a desktop computer [6.3].

### 6.2.1. Signal Chopping

Signal chopping is a convenient method to suppress background intensity noise for equivalent-time sampling, where the measured signal is a waveform, not a single sinusoid as in harmonic mixing. This method requires chopping of the drive signal to the circuit at an RF rate above the  $1/f$  noise corner of the laser so that the measured signal has a frequency component whose amplitude varies in proportion to the measured waveform in a spectral region free of background intensity noise.

Sinusoidal amplitude modulation (AM) is the simplest type of chopping. The chopped signal is then

$$v_c(t) = \frac{1}{2}v(t)[1 + \cos(2\pi f_m t)] \quad (6.10)$$

where  $f_m$  is the modulation frequency and  $v(t)$  is the unmodulated signal. In the frequency-domain

$$V_c(f) = \frac{1}{2}V(f) * \left[ \delta(f) + \frac{1}{2}\delta(f-f_m) + \frac{1}{2}\delta(f+f_m) \right] \quad (6.11)$$

The modulation frequency  $f_m$  is chosen to be greater than the low frequency laser noise (typically 1-10 MHz for the system described in chapter 1) and a receiver using synchronous detection recovers the signal component at  $\pm f_m$ . The resulting signal current from the receiver is

$$i_{sig} = \frac{1}{2}I_0 \frac{\pi}{V_\pi} v(t) \quad (6.12)$$

which is one-half the value or a 6 dB reduction from the harmonic mixing case and has a noise-equivalent voltage set by shot-noise of

$$v_{min} = \frac{2V_\pi}{\pi} \sqrt{\frac{2q}{I_0}} \frac{V}{\sqrt{Hz}} \quad (6.13)$$

For some applications square-wave chopping or pulse modulation (PM) may be required or desirable. In this case the time-domain signal is

$$v_c(t) = v(t) \left\{ \text{rect} \left[ \frac{(t-n)}{\frac{1}{2}T_m} \right] \right\} \quad (6.14)$$

and the frequency-domain signal is

$$V_c(f) = V(f) * \sum_n \frac{1}{2} \text{sinc} \left( \frac{n}{2} \right) \delta(f - nf_m) \quad (6.15)$$

where  $\text{sinc}(x) = \frac{\sin(\pi x)}{\pi x}$ . Only the signal at the chopping frequency is recovered, resulting in a signal current

$$i_{sig} = \left(\frac{2}{\pi}\right) I_0 \frac{\pi}{V_{\pi}} v(t) \quad (6.16)$$

which is reduced by a factor of -3.9 dB from the harmonic mixing case and has a noise-equivalent voltage set by shot-noise of

$$v_{min} = \frac{V_{\pi}}{2} \sqrt{\frac{2q}{I_0}} \frac{V}{\sqrt{Hz}} \quad (6.17)$$

A further consideration is that signal chopping is typically used for waveform recovery with equivalent sampling. The signal then is a sum for harmonically-related sinusoids as given by (1.35), and results in an output intensity at the chopping frequency

$$P_{BB} = P_0 \frac{\pi}{V_{\pi}} \sum_{-n_{max}}^{n_{max}} \left[ \tilde{v}_n \delta(f - f_m - n\Delta f) \right] \quad (6.18)$$

To recover the full time waveform, the receiver bandwidth must include all the signal harmonics, i.e.  $B \geq n_{max}\Delta f$ . This puts a constraint on either the scan rate  $\Delta f$  or the noise-equivalent voltage  $v_{min}$ . The measurement acquisition time in this case is  $T_{acq} = 1/\Delta f \approx n_{max}/B$ . Related to the noise voltage, the acquisition time is

$$T_{acq} = \frac{2q}{I_0} \left( \frac{V_{\pi}}{2v_{min}} \right)^2 n_{max} \quad (6.19)$$

which is increased by  $(\pi/2)^2 n_{max}$  compared to harmonic mixing with the same noise voltage.

### 6.2.2. Phase Modulation

When signal chopping is inappropriate, such as when testing the clock signal of a digital IC where the logic states depend on a continuous clock signal, phase modulation ( $\phi M$ ) or time-dithering of the drive signal is an alternative method for signal processing. This scheme has the advantage that the drive signal remains continuous but it has some disadvantages in sensitivity and ease of signal processing.

The periodic drive signal is phase modulated by a small amount  $\delta(t)$

$$v_c(t) = v[t + \delta(t)] \quad (6.20)$$

where

$$v(t) = \sum_{n=-n_{max}}^{n_{max}} \tilde{v}_n \exp(j2\pi n f_s t) \quad (6.21)$$

and  $\tilde{v}_n = \tilde{v}_n^*$ . If  $\delta(t)$  is small, the exponential term is expanded to first order in  $\delta$  and the phase modulated signal is

$$v_c(t) = \sum_{n=-n_{max}}^{n_{max}} \tilde{v}_n \exp(j2\pi n f_s t) [1 + j2\pi n f_s \delta(t)] \quad (6.22)$$

The Fourier transform of  $v_c(t)$  is

$$V_c(f) = \sum_{n=-n_{max}}^{n_{max}} [\tilde{v}_n \delta(f - n f_s)] j [\delta(f) + j2\pi n f_s \Delta(f)] \quad (6.23)$$

where  $\Delta(f)$  is the Fourier transform of  $\delta(t)$ .

For sinusoidal phase modulation

$$\delta(t) = A_m \cos(2\pi f_m t) \leftrightarrow \Delta(f) = \frac{A_m}{2} \delta(f - f_m) + \frac{A_m}{2} \delta(f + f_m) \quad (6.24)$$

and the modulated signal is

$$V_c(f) = \sum_{n=-n_{max}}^{n_{max}} \tilde{v}_n \left\{ \delta(f - n f_s) + j\pi n f_s A_m [\delta(f - n f_s - f_m) + \delta(f - n f_s + f_m)] \right\} \quad (6.25)$$

Then, as in equivalent-time sampling, the signal at frequency  $f_s = N f_0 + \Delta f$  is sampled down to baseband and detected at the modulation frequency  $f_m$  resulting in a signal current given by

$$I_{sig}(f) = I_0 \frac{\pi}{V\pi} \sum_{n=-n_{max}}^{n_{max}} \tilde{v}_n j 2\pi n f_s A_m [\delta(f - n \Delta f)] \quad (6.26)$$

$$I_{sig}(f) = I_0 \frac{\pi}{V_{\pi}} \sum_{-n_{max}}^{n_{max}} \tilde{v}_n j 2\pi n f_s A_m [\delta(f - n \Delta f)] \quad (6.26)$$

Each harmonic is multiplied by  $n f_s$ , and using the Fourier transform principle that

$$\frac{d}{dt}[v(t)] \leftrightarrow j 2\pi f V(f) \quad (6.27)$$

the signal current in the time domain is

$$i_{sig}(t) = I_0 A_m \frac{f_s}{\Delta f} \frac{\pi}{V_{\pi}} \frac{d}{dt} \left[ v \left( \frac{\Delta f}{f_s} t \right) \right] \quad (6.28)$$

The actual signal can be recovered by integration either in software or by passing through an integrating filter with the transfer function  $\Delta f / (j 2\pi f_s A_m f)$ . Then, the filtered signal current is

$$i_{sig}(t) = I_0 \frac{\pi}{V_{\pi}} v \left( \frac{\Delta f}{f_s} t \right) \quad (6.29)$$

The noise current is obtained by passing the shot noise within the receiver bandwidth through the same filter, and  $v_{min}$  is obtained by setting the above signal current equal to the noise current, giving

$$\begin{aligned} v_{min} &= \frac{V_{\pi}}{\pi} \sqrt{\frac{2q}{I_0}} \frac{\sqrt{n_{max}^2 - n_{max}}}{\beta} \frac{V}{\sqrt{\text{Hz}}} \\ &= \frac{V_{\pi}}{\pi} \sqrt{\frac{2q}{I_0}} \frac{n_{max}}{\beta} \frac{V}{\sqrt{\text{Hz}}} \text{ for } n_{max} \gg 1 \end{aligned} \quad (6.30)$$

where  $\beta = 2\pi f_s n_{max} A_m$  is the index of phase modulation. The acquisition time is then

$$T_{acq} = \frac{2q}{I_0} \left( \frac{V_{\pi} n_{max}}{\pi \beta} \right)^2 \quad (6.31)$$

which is increased by  $(n_{max} / \beta)^2$  from the harmonic mixing case.

### 6.2.3. Fast-Offset and Averaging

Fast-offset and averaging is a signal processing method to recover the signal with no modulation of the drive signal. This technique is identical to ideal equivalent-time sampling except the offset frequency is increased to a value greater than the  $1/f$  noise corner frequency. The signal is passed through a high pass filter to remove low frequency laser noise and then signal averaged to recover the signal with suitable sensitivity. Fig. 6.5 shows a block diagram of this signal processing system. With this scheme the frequency offset  $\Delta f$  is increased 400-500 kHz, well above the low-frequency laser noise. The signal is recovered by high-pass filtering to remove the low-frequency laser noise, then by signal averaging at the offset rate  $\Delta f$ . If the received signal is averaged at the scan rate, the sensitivity using fast averaging is the same as for simple synchronous sampling with the same measurement acquisition time. Commercial digitizing oscilloscopes have limited averaging rates; at scan rates of 500 kHz, the LeCroy 9400 averages a maximum of  $\approx 200$  scans per second, corresponding to a signal-to-noise reduction of 34 dB from averaging every scan. However, the signal-to-noise reduction, compensated for by increased measurement acquisition time, is justified for testing IC's that are sensitive to signal chopping.

The filtered baseband signal from the output intensity is

$$i_{sig} = I_0 \frac{\pi}{V_{\pi}} \sum_{n=1}^{n_{max}} \left[ \frac{\tilde{v}_n}{2} \delta(f - n\Delta f) + \frac{\tilde{v}_n^*}{2} \delta(f + n\Delta f) \right] \quad (6.32)$$

and the noise voltage is the same as given in (), except now  $\Delta f \approx 500$  kHz and  $\Delta f n_{max} \approx 5$  MHz are typical values (instead of  $\Delta f \approx 10$  Hz and  $\Delta f n_{max} \approx 100$  Hz typical of equivalent-time sampling with chopping). Then, in one signal sweep,  $v_{min} = 70$  mV with an acquisition time of  $1/\Delta f = 2 \mu s$ . To recover the signal with a reasonable noise level, say  $v_{min} = 1$  mV, the measured signal needs to be repetitively averaged  $N_{avg} = 70^2 \approx 5000$  times. The voltage sensitivity is given by

$$v_{min} = \frac{V_{\pi}}{\pi} \sqrt{\frac{2q\Delta f n_{max}}{I_0 N_{avg}}} \quad (6.33)$$

The acquisition time is probably limited by the rate the data can be averaged. In this case, the acquisition time is



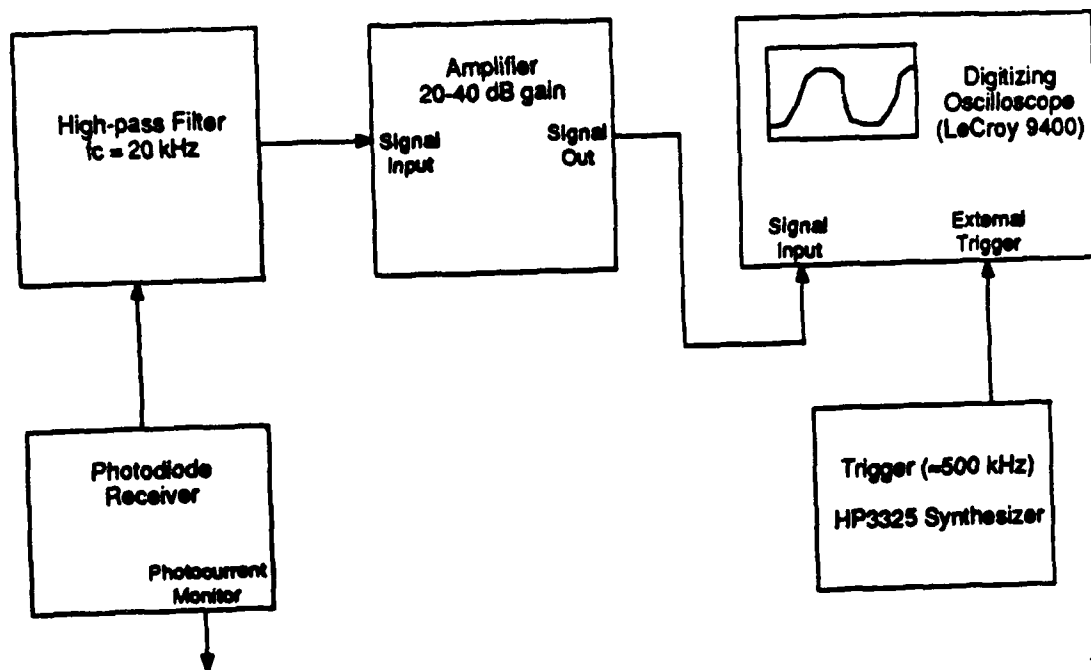


Fig.6.5. Fast scan rate signal processing block diagram.

# Fast Averager Block Diagram

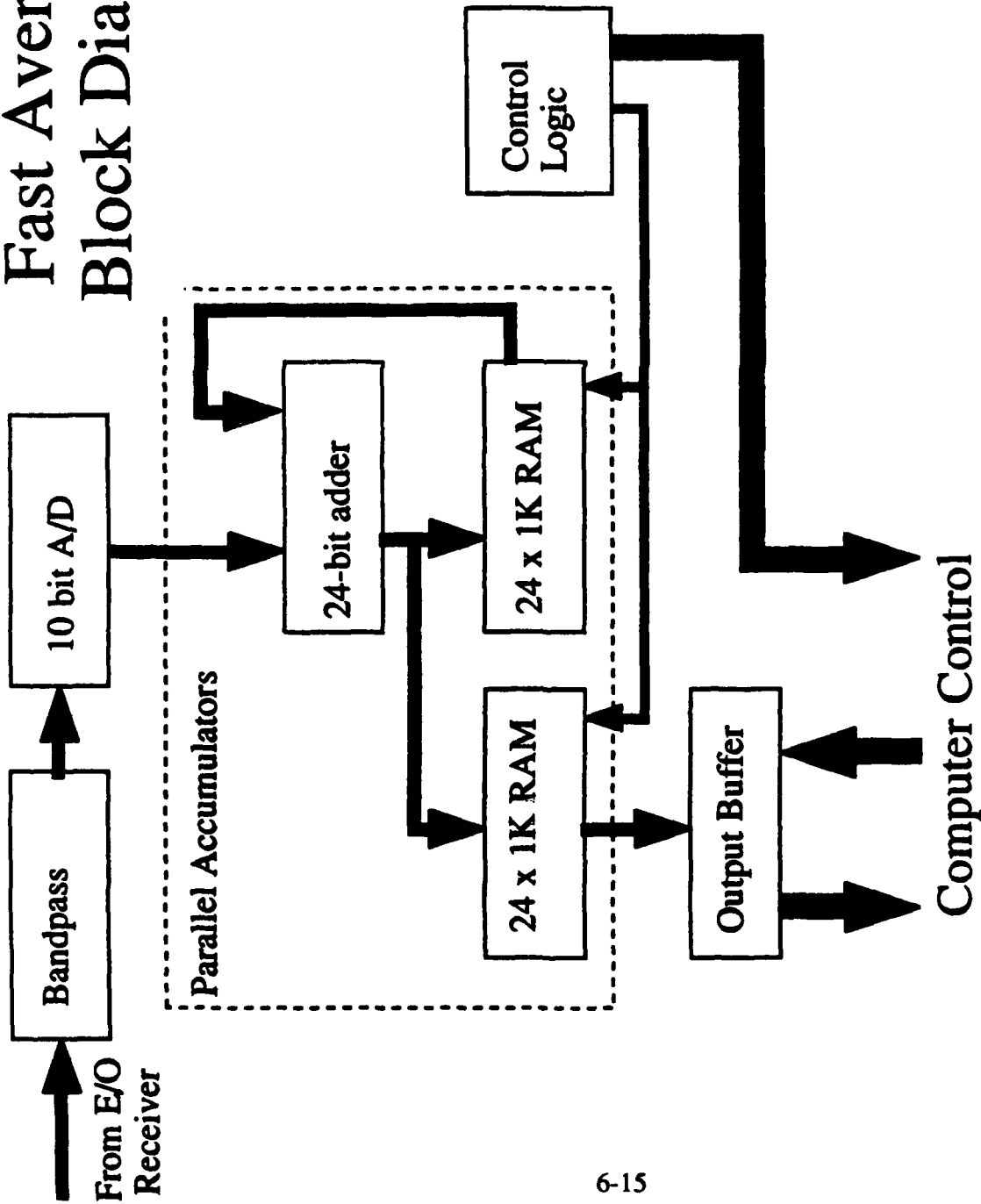


Fig. 6.6: Block diagram of the fast averager

$$T_{acq} = \frac{2q}{I_0} \left( \frac{V_\pi}{\pi v_{min}} \right)^2 \frac{\Delta f_a}{\Delta f} n_{max} \quad (6.34)$$

where  $\Delta f_a$  is the averaging scan rate set by the data processing hardware (and always  $\geq \Delta f$ ).

One difficulty with digital averaging oscilloscopes is the relatively small dynamic range. The large noise power requires operation on less sensitive scales, yielding a final signal that is a fraction of full-scale. Custom electronics have been designed to overcome this problem and to further increase the averaging rate for improved signal-to-noise. Fig. 6.6 shows the block diagram of such a fast averager. In this method, fast averaging involves offset of the device drive signal by 100 kHz from  $Nf_0$  yielding harmonics in the measured response every 100 kHz up to about 5 MHz. The effective detector bandwidth, then, should be 5 MHz. The large laser noise below 100 kHz may then be filtered along with noise above 5 MHz using a bandpass filter. Due to the large detected bandwidth the signal to noise at this stage is between about .1 and 10. The filtered output is then sampled by a 20 Megasamples/sec, 10 bit A/D converter (ADC) which is clocked synchronously with the 200th harmonic of the incoming signal repetition rate, which is equal to the offset  $Nf_0$ . For the 100 kHz fundamental, the ADC will sample 200 distinct positions in phase of the incoming signal. Each ADC sample output is then directed into one of 200 parallel accumulators, each of which adds 100 ksamples/sec and thus averages a single point on the incoming waveform by adding each successive repetition of that point as it is sampled by the ADC. The noise power contained in the detector bandwidth due to random processes is then reduced by a factor equal to the number of samples, or by  $10^5$  for each second of accumulation for the 100 kHz case. The output from the accumulators is sent over the IEEE-488 interface to a computer where the signal is displayed and further processed if desired. This system is capable of producing the same signal to noise ratio as a narrowband receiver, without the need for either AM or FM modulation of the device under test. It provides a significant advantage for the measurement of nonlinearities in quasi-linear circuits and highly non-linear circuits which are difficult to modulate.

### 6.3. Conclusion

The application of electrooptic sampling technique for vector voltage measurements at microwave frequencies has been described. The reflection coefficient of one port and S-

parameters of two port networks are obtained from these vector measurements. On chip S-parameter measurements at millimeter wave frequencies, without the need for separate calibration standards, are feasible due to large system bandwidth. Time waveform measurements with better than 2 ps resolution are similarly possible.

#### 6.4. References for Section 6

- 
- 6.1 R.E. Collins, *Foundations of Microwave Engineering*, New York: McGraw-Hill, 1966.
  - 6.2 K.J. Weingarten, M.J.W. Rodwell, J.L. Freeman, S.K. Diamond, and D.M. Bloom, "Electrooptic sampling of gallium arsenide integrated circuits," *Ultrafast Phenomena V*, ed. by G.R. Fleming and A.E. Siegman, Springer Ser. Chem. Phys., Vol. 46, New York:Springer-Verlag, 1986, pp. 98.
  - 6.3 M.J.W. Rodwell, K.J. Weingarten, J.L. Freeman, and D.M.Bloom, "Gate propagation delay and logic timing of GaAs integrated circuits measured by electro-optic sampling," *Elect. Lett.*, vol. 22, pp. 499-501, 1986.

## 7. Wafer Probe Station for Electrooptic Probing

### 7.1. Wafer Probe Station

For wafer-level testing of IC's, the drive signal is delivered with a microwave probe station (Cascade Microtech Model 42) modified to allow for backside electrooptic probing, as shown pictorially in Figs. 7.1 and 7.2, and schematically in Fig. 7.3. The transmission line probes used with this test station allow for launching a signal on the IC with repeatable, low reflection connections in a  $50\ \Omega$  environment to 40 GHz. The beam delivery system consists of two turning mirrors,  $90^\circ$  to each other, mounted on an X-Y stage controlled by automated positioners. The wafer chuck is modified so that the focusing objective is positioned under the wafer and accessed with either a hole in the top plate or a sapphire window. The window provides better heat conduction than an open hole for high power circuits. However, a small air gap may exist between the window and the wafer, causing the beam transmission to vary as a function of position due to interference. Index matching fluid (Cargille Series M) removes this problem, but it can evaporate leaving a rough salt residue that sticks to the window and the wafer. Use of a window that is anti-reflection coated on both sides removes the etaloning effect as well, without use of liquids; however, care must be exercised in placement and movement of the wafer to avoid damage of the AR layer.

Electrooptic sampling measurements on digital and microwave IC's have been made using this probe station. The interconnects and transmission lines on these IC's were in the uniplanar configuration, i.e. having signal and ground conductors on the front and no conductor on the backside of the wafer, thus allowing for backside electrooptic probing. A similar probe station with some additional modifications to further enhance the ease of wafer probing has been fabricated for Wright-Patterson Air Force Base and will be delivered as part of this contract.

Packaged circuits (mostly circuits using microstrip conductors and requiring frontside probing) are tested with a general purpose beam delivery system that allows for either frontside or backside probing. This arrangement requires either that the circuit package allow access to the IC from the frontside probing (roughly 8 mm working distance for a 10X objective) or that the package has a window under the portion of the circuit for beam access from the backside.

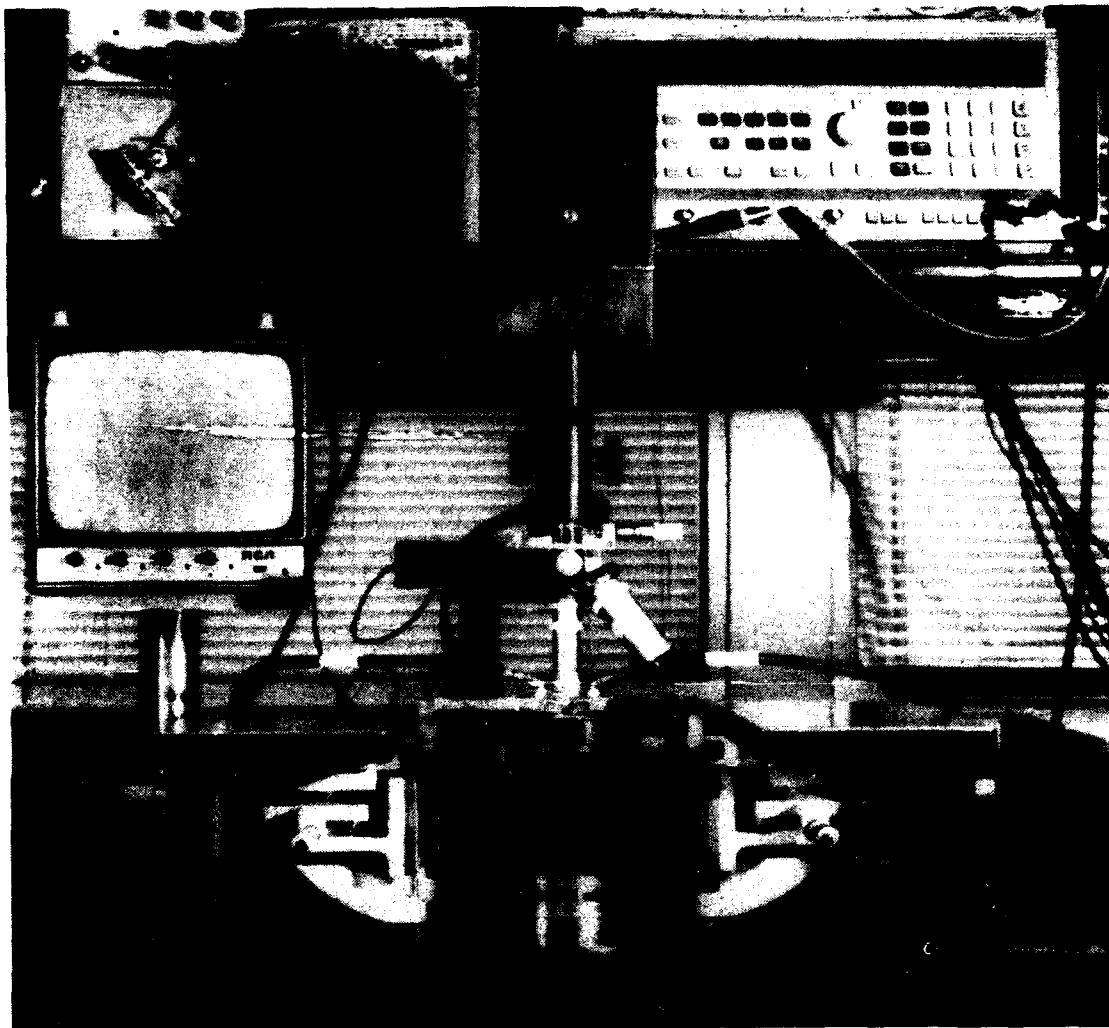


**Fig.7.1.** Front view of the Cascade microwave wafer probe station

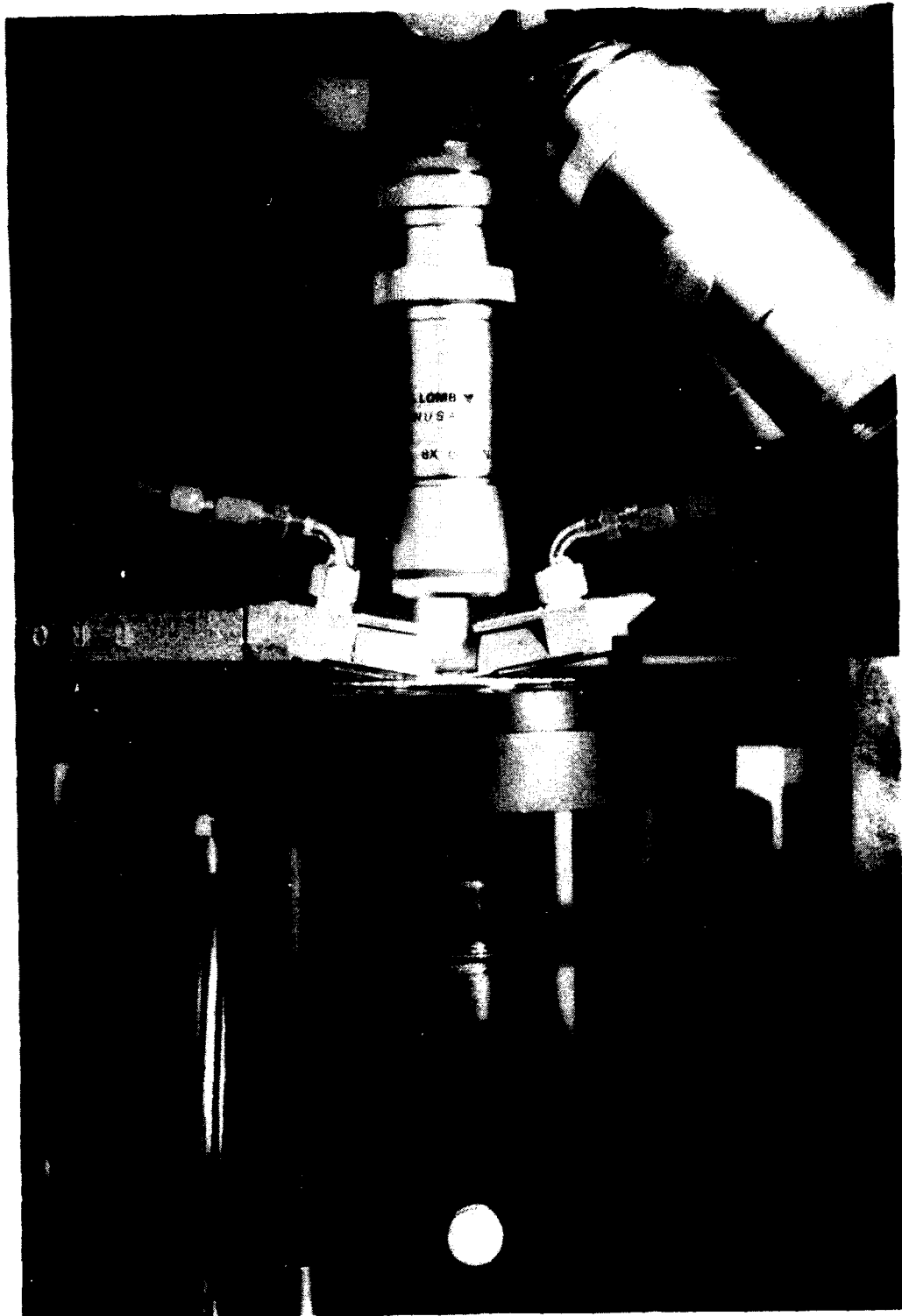


Fig.7.2. Front view close-up of the Cascade microwave wafer probe station showing the microscope objective below the wafer chuck, two CPW probes, and the long working-distance objectives used for the viewing system.

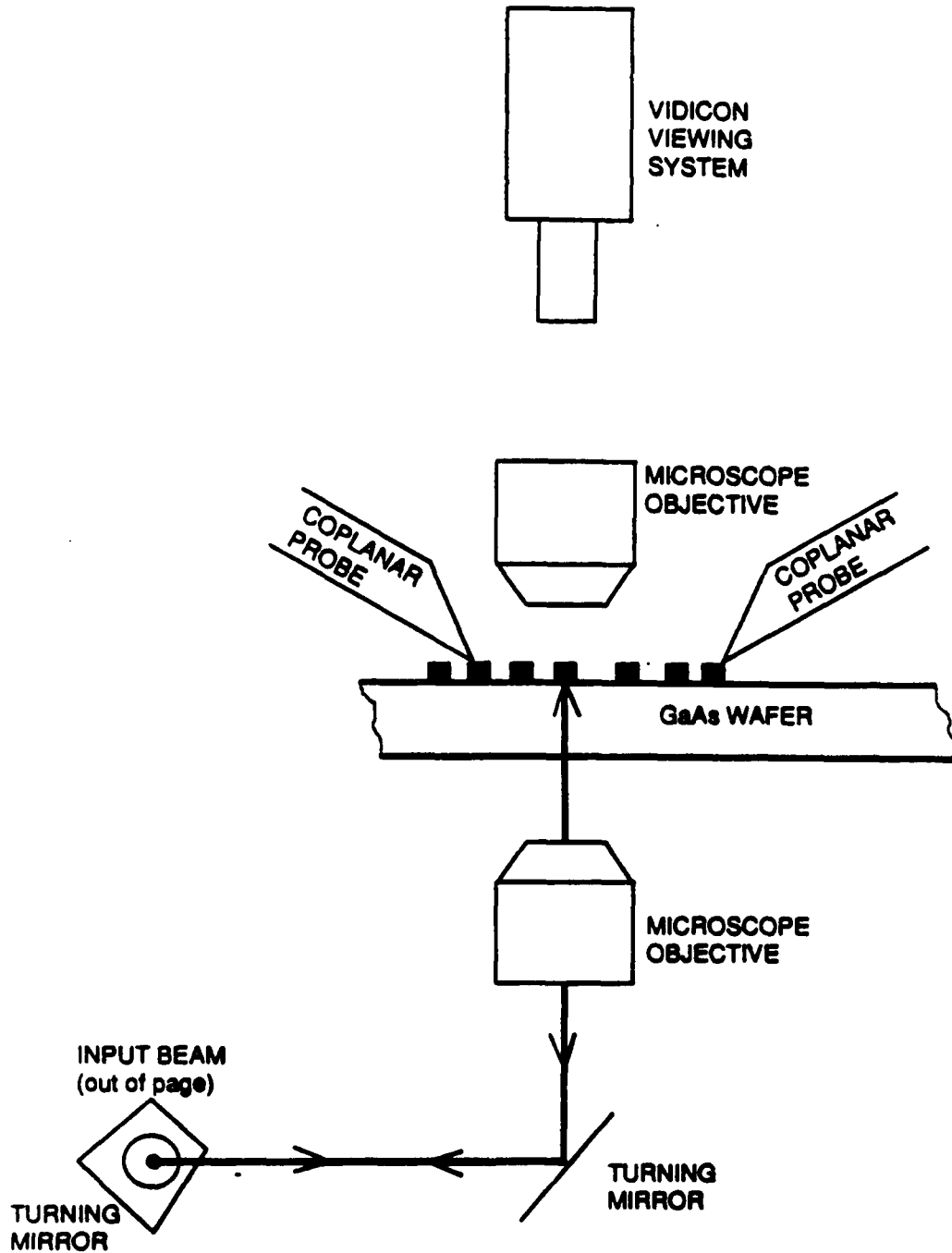


Fig.7.3 . Beam path through the Cascade microwave wafer probe station for backside probing. The turning mirrors and focusing objective are mounted on automated positioners to allow accurate positioning and scanning of the probe beam. The vidicon viewing system is sensitive to the infrared probe, allowing viewing of the probe position on the front surface of the test IC.



## 7.2. Microwave Circuit Measurements

At microwave and millimeter-wave frequencies, where conductor lengths and circuit element sizes often become large with respect to the electrical wavelength, direct measurements of conductor voltages and currents are difficult, particularly with conventional electrical test instrumentation. Directional couplers and directional bridges separate the forward and reverse traveling waves on a transmission line. Standard microwave test instruments use these devices to measure the incident and reflected waves at the ports of a microwave device or network. The relationship between these waves is expressed as the *scattering parameters* [7.1]. The electrooptic sampler directly measures voltages, but not currents, preventing a direct measure of two-port parameters. However, measuring the voltage as a function of position with the optical probe [7.2], similar to a slotted-line measurement, permits calculation of the incident and reverse waves on the transmission lines connected to devices (Section 6.1.2 and Appendix III). From this information the scattering parameters can then be determined.

### 7.2.1. One-Port Measurements

The traveling-wave coefficients on lossless transmission lines are measured as described in Section 6.1.2 and Appendix III. For a one-port transmission line the ratio of the traveling wave coefficients  $V^+$  and  $V^-$  is the reflection coefficient  $\Gamma$ , or  $S_{11}$ , the return loss. An example of such a measured vector standing wave and the calculated reflection coefficient for an unterminated slot line transmission line at a drive frequency of 22 GHz is shown in Fig. 7.4, and a similar measurement with an matched load terminating a CPW transmission line at 20 GHz is shown in Fig. 7.5.

### 7.2.2. Two-port S-parameter Measurements

Using the technique described in section 6.1.3, the S-parameters of simple microwave test structures have been measured. Fig. 7.6 shows the measured  $S_{11}$  for a test structure consisting of a section of 35  $\Omega$  CPW transmission line 1600  $\mu\text{m}$  in length with 2500  $\mu\text{m}$  length sections of 50  $\Omega$  CPW on its input and output. The drive signal is applied to the input side, the probe beam is scanned along the input and output sections of 50  $\Omega$  line, the traveling waves are calculated, and  $S_{11m}$ ,  $S_{21m}$ , and  $E_{Lf}$  are determined. Then, the drive signal is applied to the output side, the probe beam is scanned along the same sections of

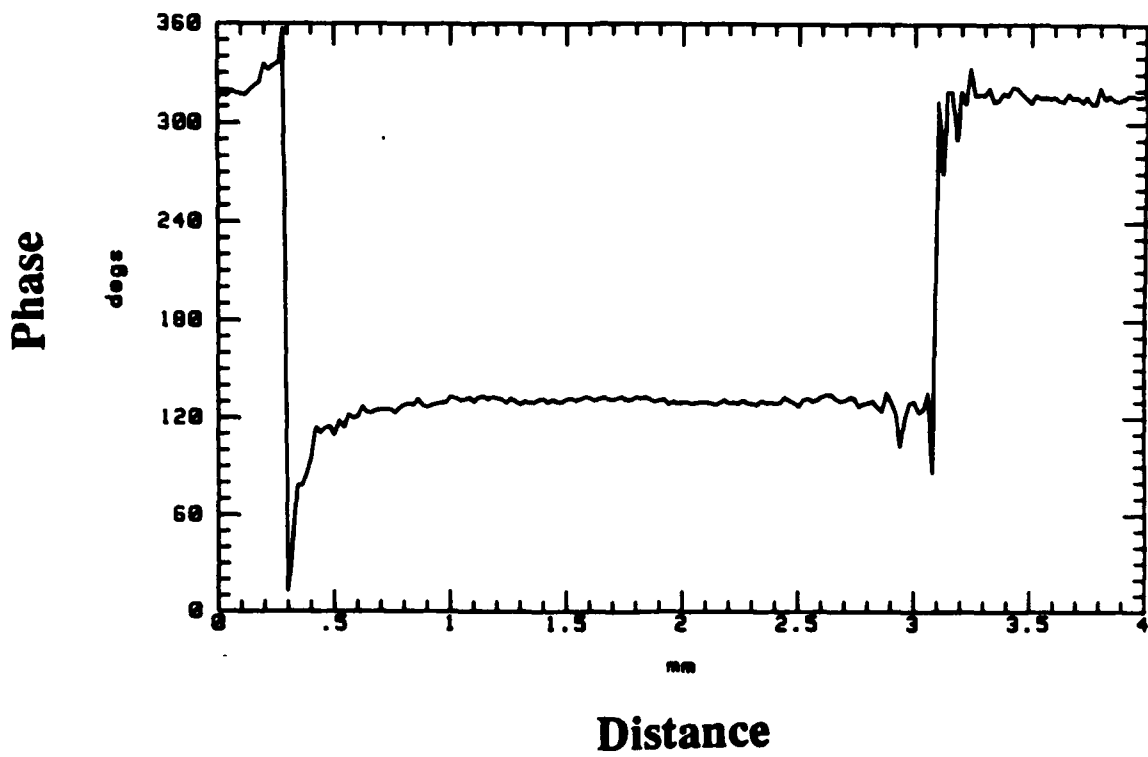
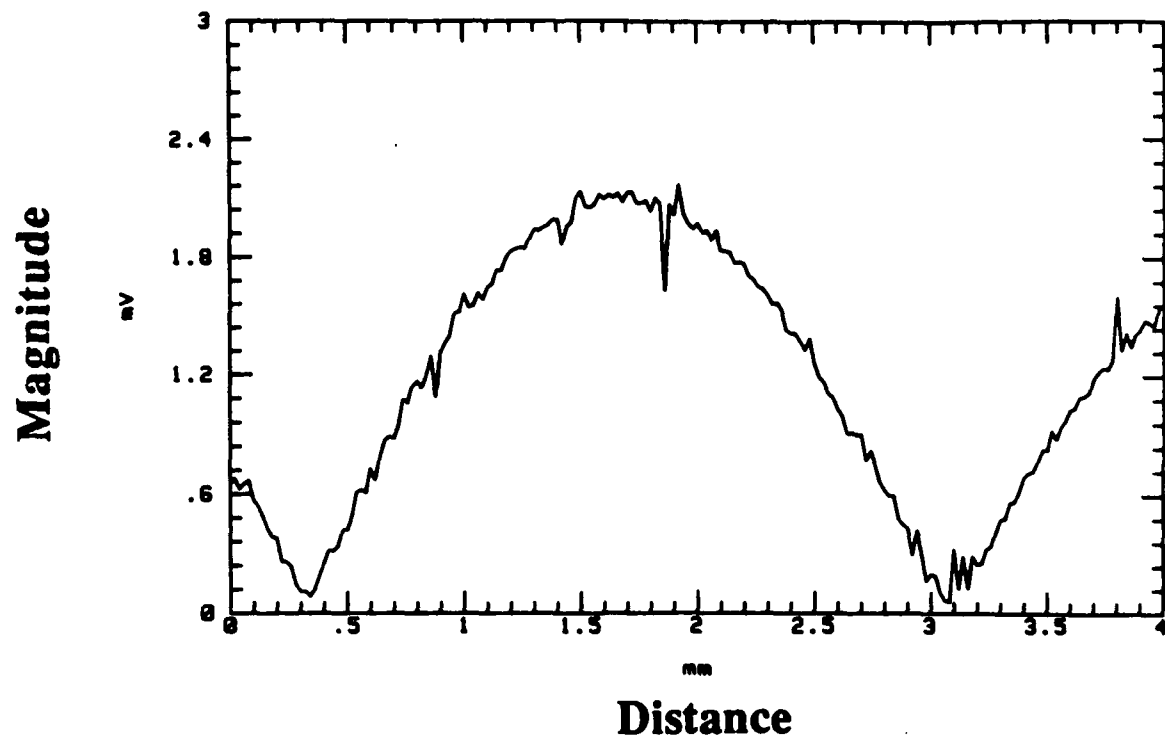


Fig. 7.4: Slot line standing wave at 22 GHz measured using electrooptic sampling

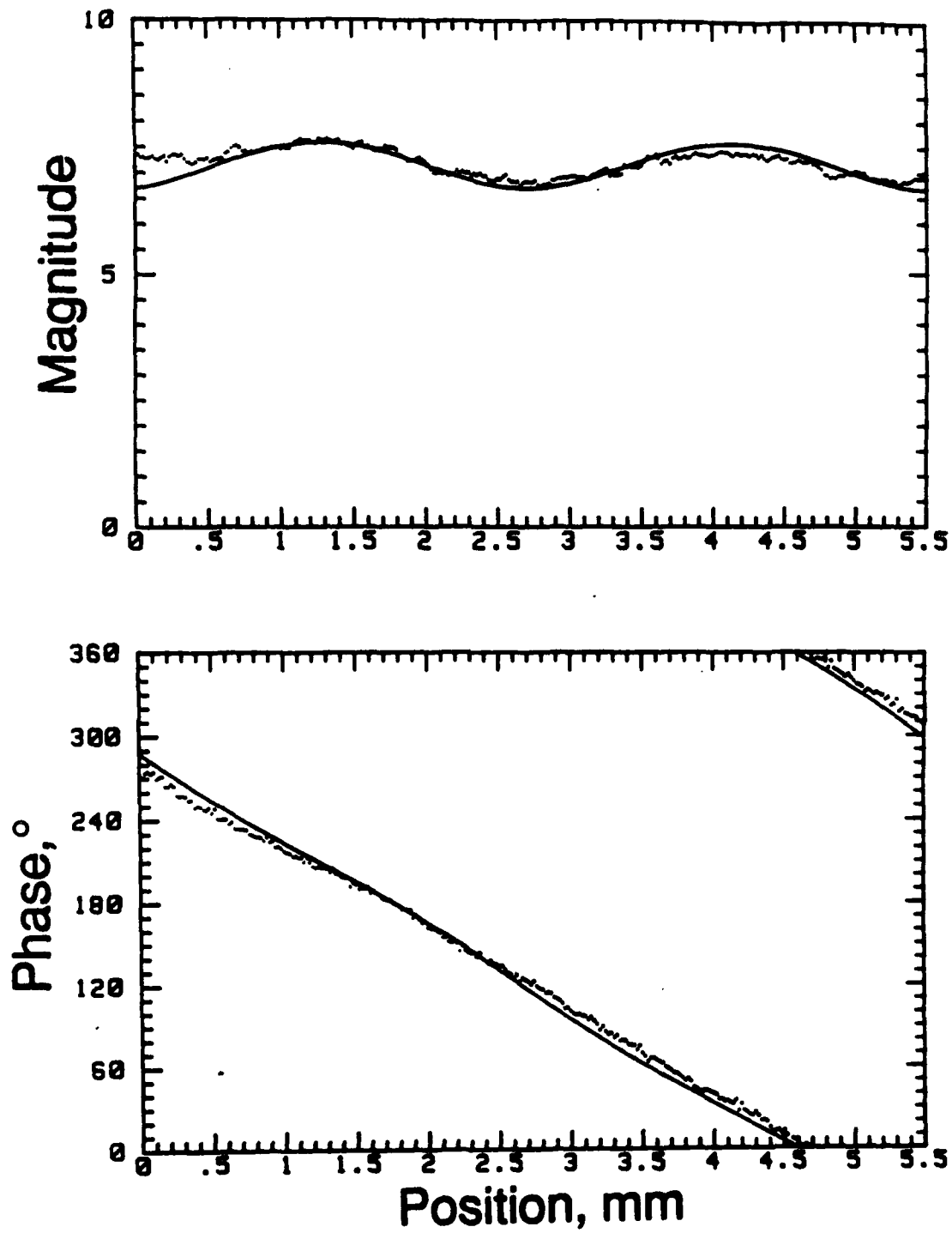


Fig.7.5. 20 GHz voltage standing wave on a GaAs coplanar waveguide transmission line terminated in 50  $\Omega$  (nominally), magnitude (top) and phase (bottom). The points are the data and the solid line is the fitted curve. From this measurement a reflection coefficient of 0.06 @  $-160^\circ$  is calculated.

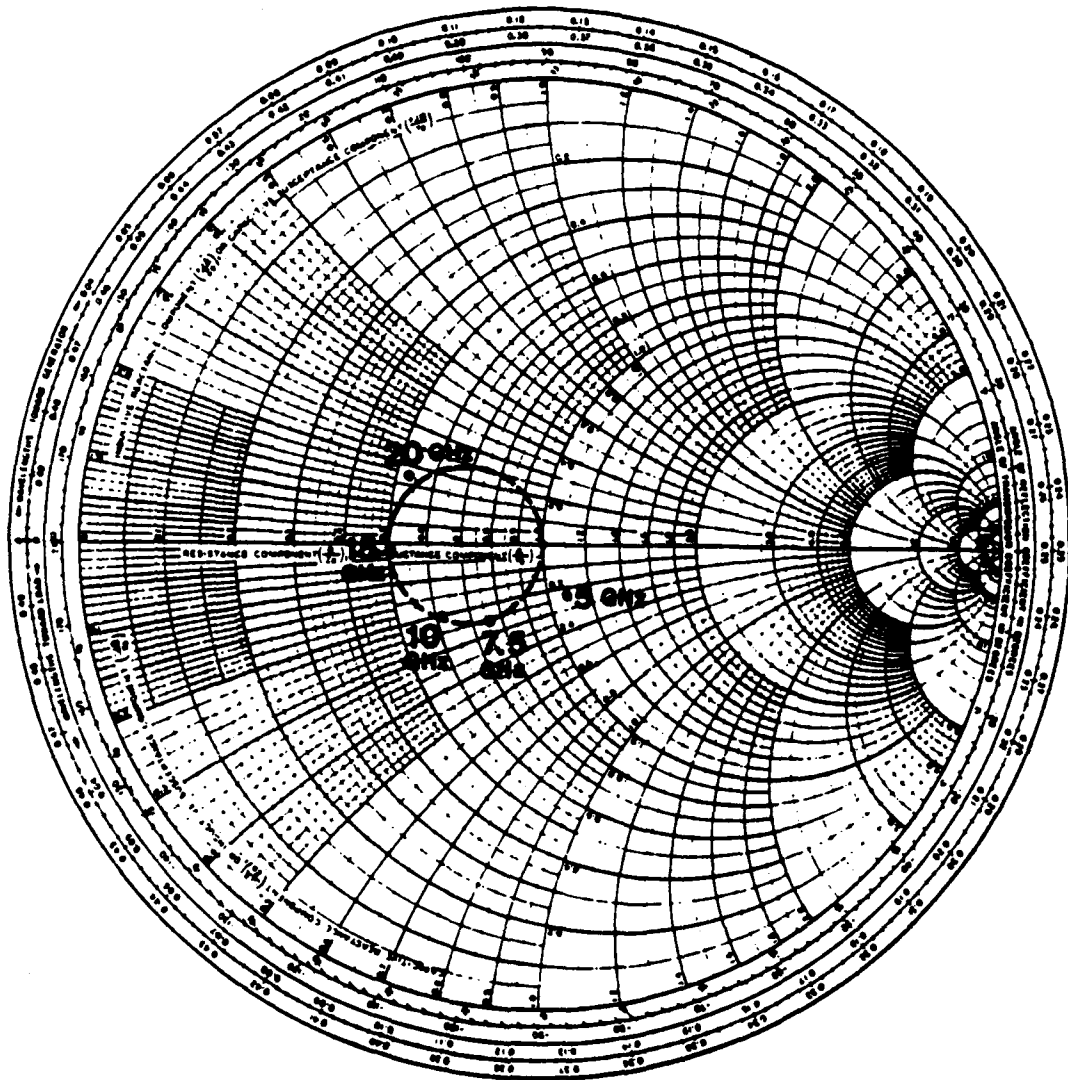


Fig.7.6. Measured  $S_{11}$  for a test structure consisting of a section of  $35 \Omega$  CPW transmission line  $1600 \mu\text{m}$  in length with  $2500 \mu\text{m}$  length sections of  $50 \Omega$  CPW on its input and output. The dashed-line circle is the theoretical  $S_{11}$  for a  $35 \Omega$  transmission line.

50  $\Omega$  line, the traveling waves are calculated, and  $S_{22m}$ ,  $S_{12m}$ , and  $E_{Lr}$  are determined. Finally, the corrected S-parameters are calculated using (6.9).

### 7.2.3 Potential Mapping for Circuit Modeling

The optical probe can be used to map the vector potential on and around IC conductors. For example, the magnitude and phase transverse to a microstrip transmission line in Fig. 7.7 shows the falloff from the conductor and a change in phase indicative of a non-TEM<sub>00</sub> mode. Fig. 7.8 shows the transverse scan of a slot line at 2 GHz. One proposal was recently published [7.4] for field mapping by varying the angle of incidence of the probe beam to obtain information allowing calculation of the three-dimensional field. The experimental feasibility of this technique, however, remains to be demonstrated.

### 7.2.4 Microwave Amplifiers

On GaAs microwave amplifiers and similar MMIC's, the propagation of microwave signals internal to the circuit can be measured. Fig. 7.9 is a monolithic 2-18 GHz MESFET distributed amplifier from Varian Research Labs [7.3,4] with coplanar-waveguide transmission line interconnects. In the distributed amplifier, a series of small transistors are connected between two high-impedance transmission lines. The high-impedance lines and the FET input and output capacitances together form a synthetic transmission lines of 50  $\Omega$  characteristic impedance. Series stubs are used in the drain circuit, equalizing the phase velocities of the two lines and providing some matching between the low impedance of the output line and the higher output impedances of the FET's at high frequencies, peaking the gain.

Measurements to better understand the circuit's operation include the relative drive levels to each FET as influenced by the loss and cutoff frequency of the synthetic gate line, the small-signal voltage at the drain of each FET, and identification of signal saturation leading to amplifier gain compression. Figure 7.10 shows the electrooptically measured small-signal gate voltages versus frequency for the CPW distributed amplifier. The rolloff beyond 18 GHz is due to the cutoff frequency of the periodically-loaded gate line, the slow rolloff with frequency is due to the gate line attenuation arising from the FET input conductance, and the ripples with frequency are due to standing waves resulting from mitermination of the gate line (the load resistance was not equal to the synthetic line's characteristic impedance due to a fabrication variance).

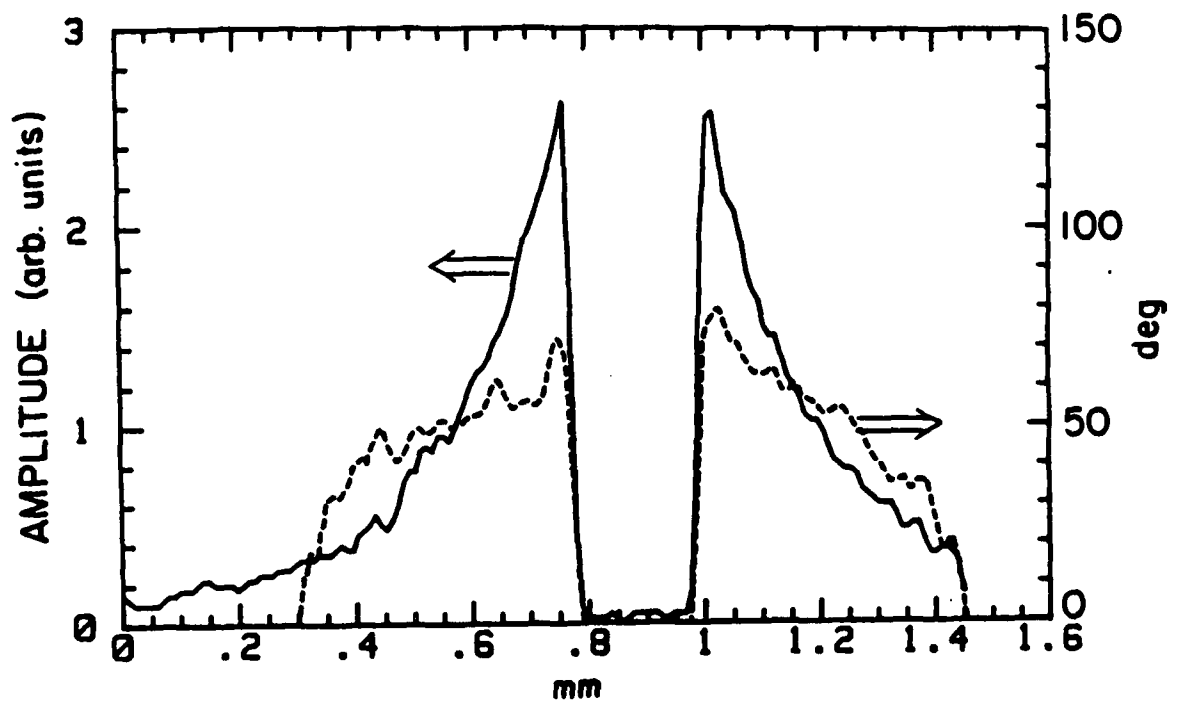


Fig.7.7. Transverse potential measured on a GaAs microstrip at a drive frequency of 30 GHz. The magnitude shows the falloff in the potential and the curvature to the phase is indicative of non-TEM mode propagation.

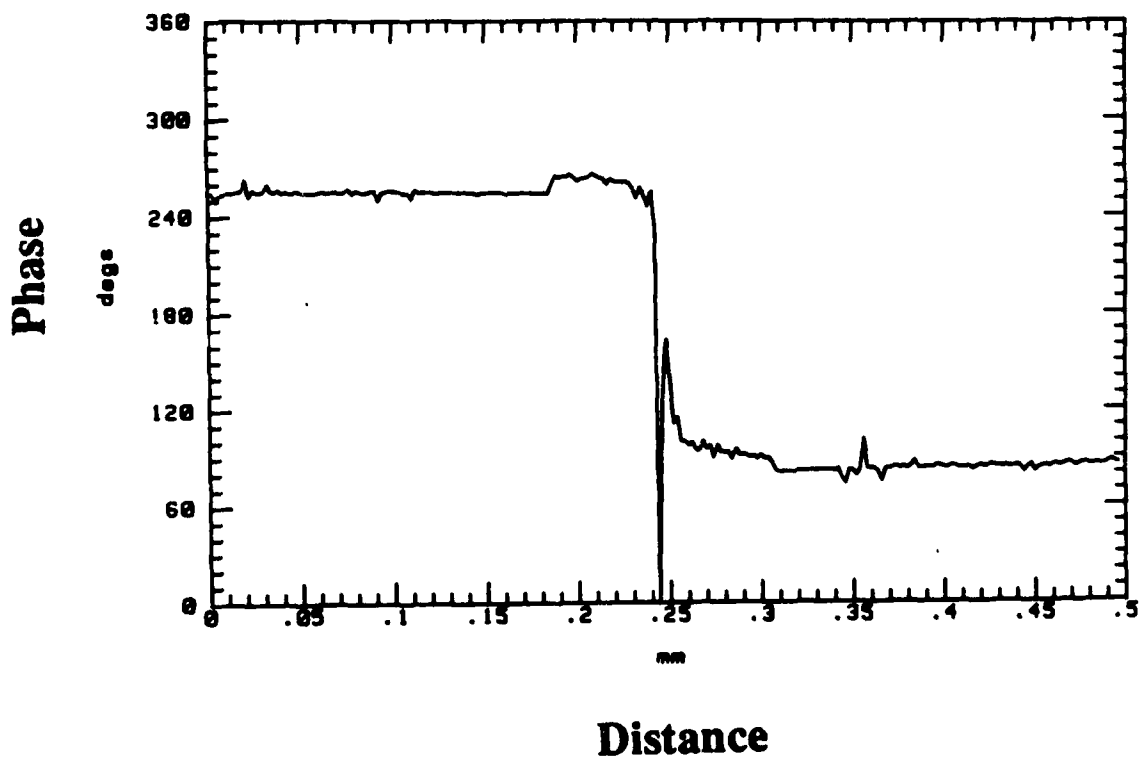
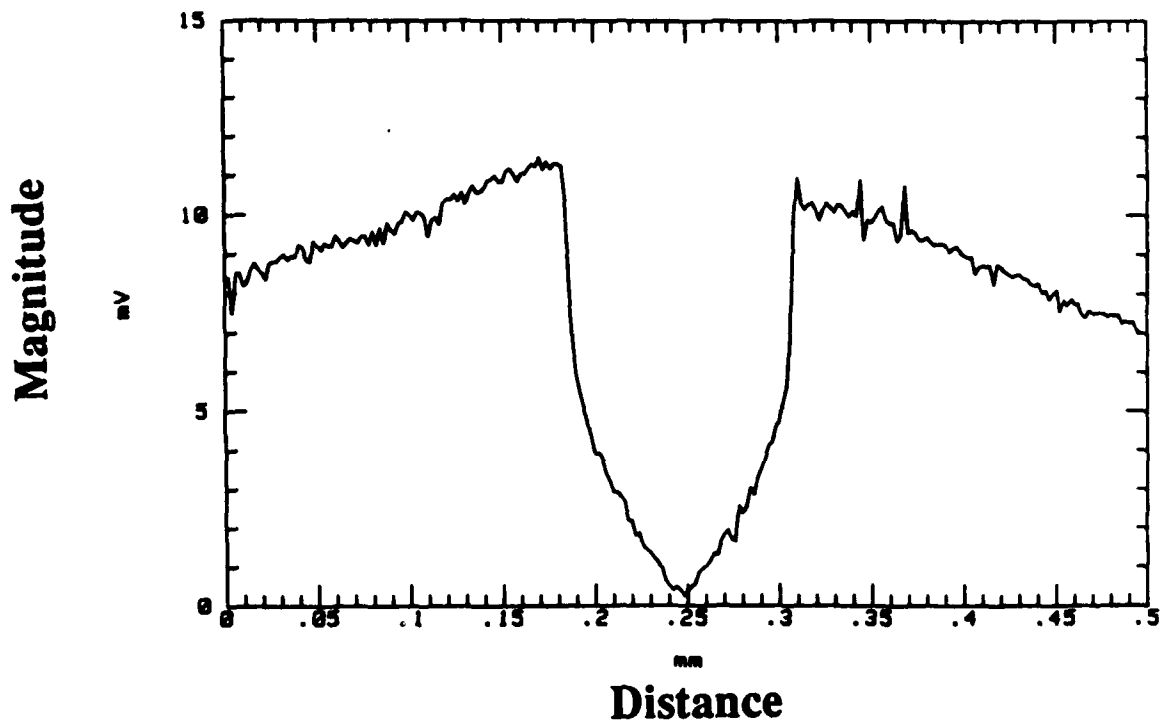


Fig. 7.8: Transverse potential distribution of slot line measured using electrooptic sampling

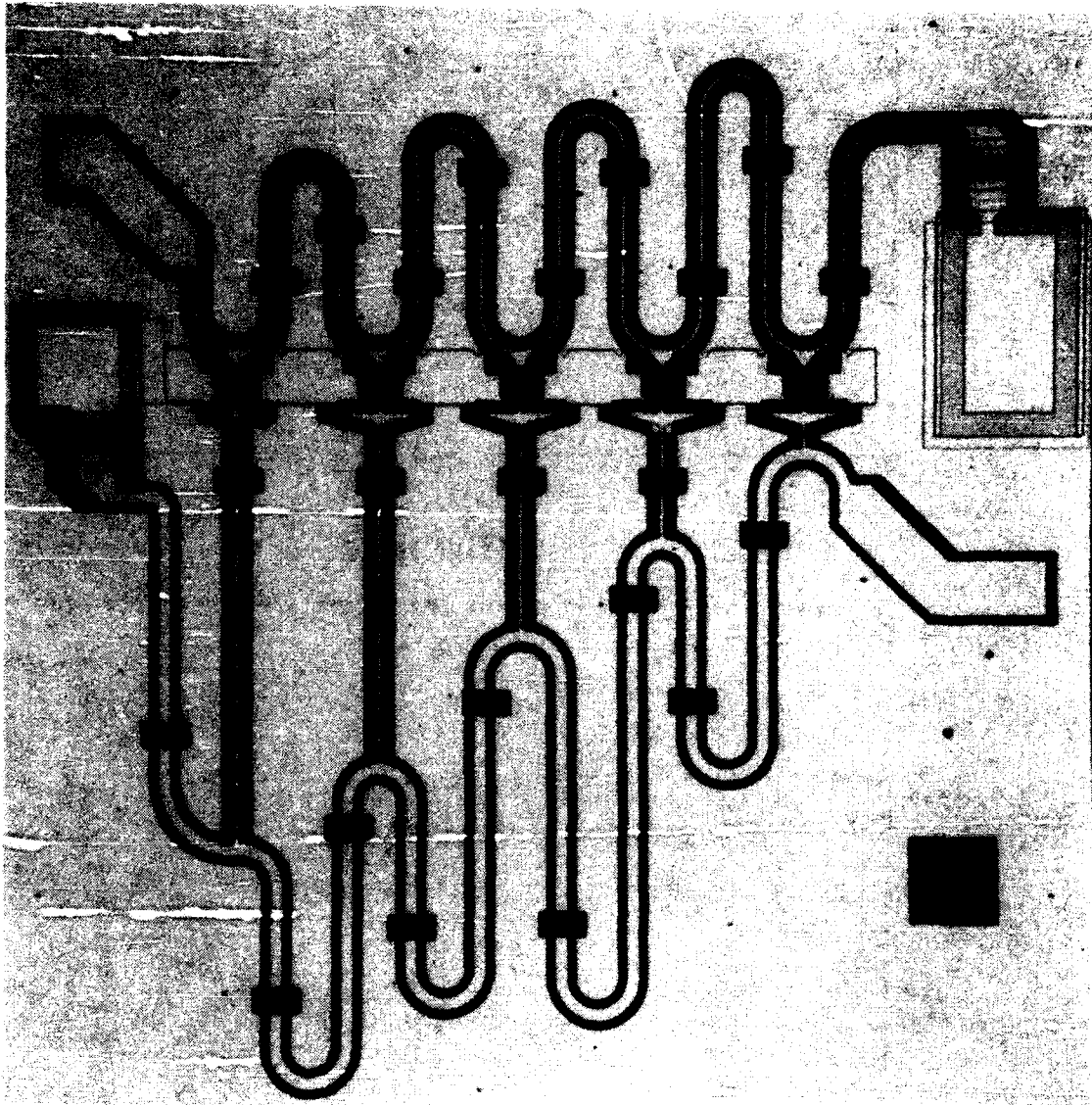


Fig. 7.9. Distributed amplifier using coplanar waveguide transmission line interconnects. Photo courtesy of M. Riazat, Varian Research Center.



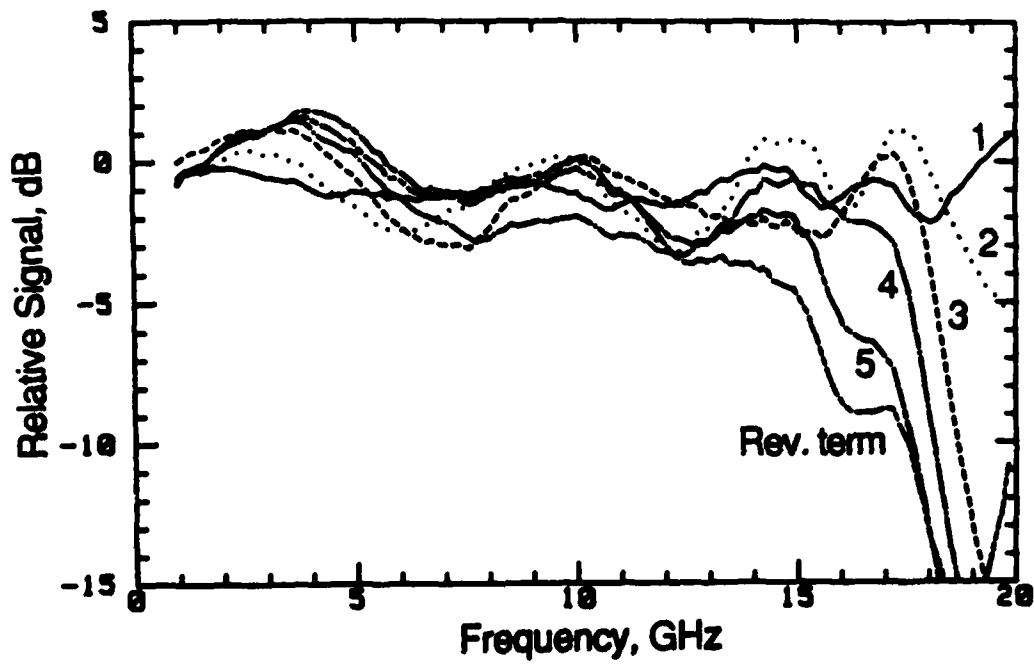


Fig. 7.10. Small-signal voltages on the coplanar 2-18 GHz distributed amplifier of Fig. 4.18, at the five gates and at the gate line termination resistor.

Fig. 7.11 shows the voltage waveforms at drains 4 and 5 of a microstrip distributed amplifier operated at 10 GHz and 7 dBm input power, the 1 dB gain compression point. For this amplifier at frequencies above 5 GHz, gain saturation is predominantly from drain saturation (i.e. reduction of  $V_{dg}$  the gate to drain voltage to the point where the drain end of the channel is no longer pinched off) of the fourth and fifth FET's. Saturation at drive frequencies as high as 21 GHz has been observed, as in Fig. 7.12.

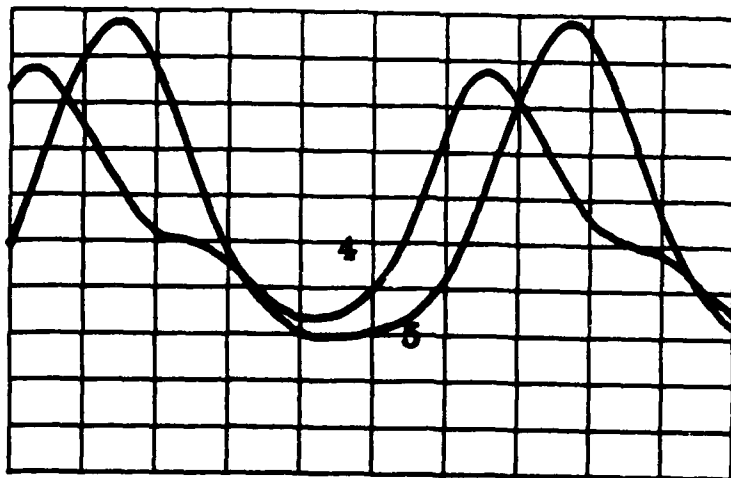
#### 7.2.5. Nonlinear Transmission Line

The capabilities of the electrooptic sampler are essential for measuring electrical signals with less than 10 ps transients, both because of its intrinsic time resolution and its on-chip probing, which avoids the difficult problem of propagating picosecond signals from the IC to coaxial connectors. In an ongoing research project in Ginzton Laboratories, GaAs IC structures are being fabricated to generate picosecond switching signals [7.5]. The structure consists of a transmission line periodically loaded with Schottky diodes from center conductor to ground. The nonlinear, voltage-dependent capacitance of the diodes creates a propagation velocity on the transmission line that depends on the signal voltage. With the diode polarity in the fabricated structures, more negative voltages travel at a slower speed, so that the falltime of a negative voltage swing decreases as the signal propagates down the line.

On the first such structure fabricated, consisting of 42 diodes uniformly separated by 160  $\mu\text{m}$  on a CPW transmission line and fabricated with 10  $\mu\text{m}$  design rules, signal falltimes of 7.8 ps were measured with the electrooptic sampler and a falltime compression factor of 3.7 was measured with two cascaded lines. The series resistance of the shunt diodes was found to be the limiting factor in the signal falltime, and a second design to reduce the diode resistance has generated falltimes of 3.5 ps (Figs. 7.13, 7.14). Further scaling of the structure should allow for signal falltimes approaching one picosecond.

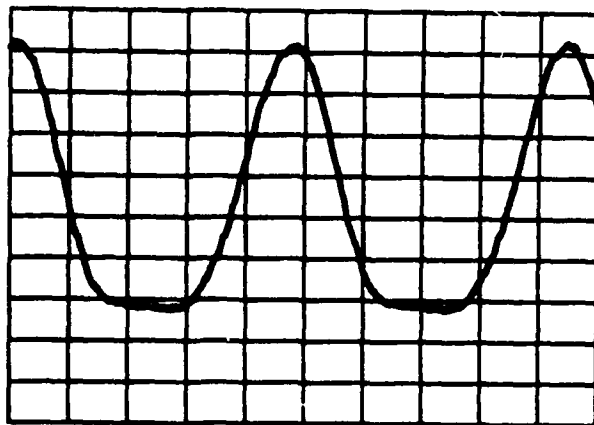
#### 7.2.6. Transmission line Mode Characterization

Electrooptic sampling also can be used to characterize different modes of a transmission line. The wavelength on a conductor can be directly measured, to obtain the guide wavelength for different modes of a guiding structure, such as the even and odd modes of CPW [7.6]. Below, the terms 'CPW' and 'coupled slot line' are used interchangeably, referring to the same physical structure.



16 ps/div.

Fig.7.11. Saturation at drains 4 and 5 of a microstrip distributed amplifier at a drive frequency of 10 GHz and 7 dBm input power, the amplifier's 1 dB compression point.



10 ps/div.

Fig.7.12. Saturation at drain 3 of a microstrip distributed amplifier at 21 GHz drive frequency.

### Shock-Wave Formation with Sinusoidal Input

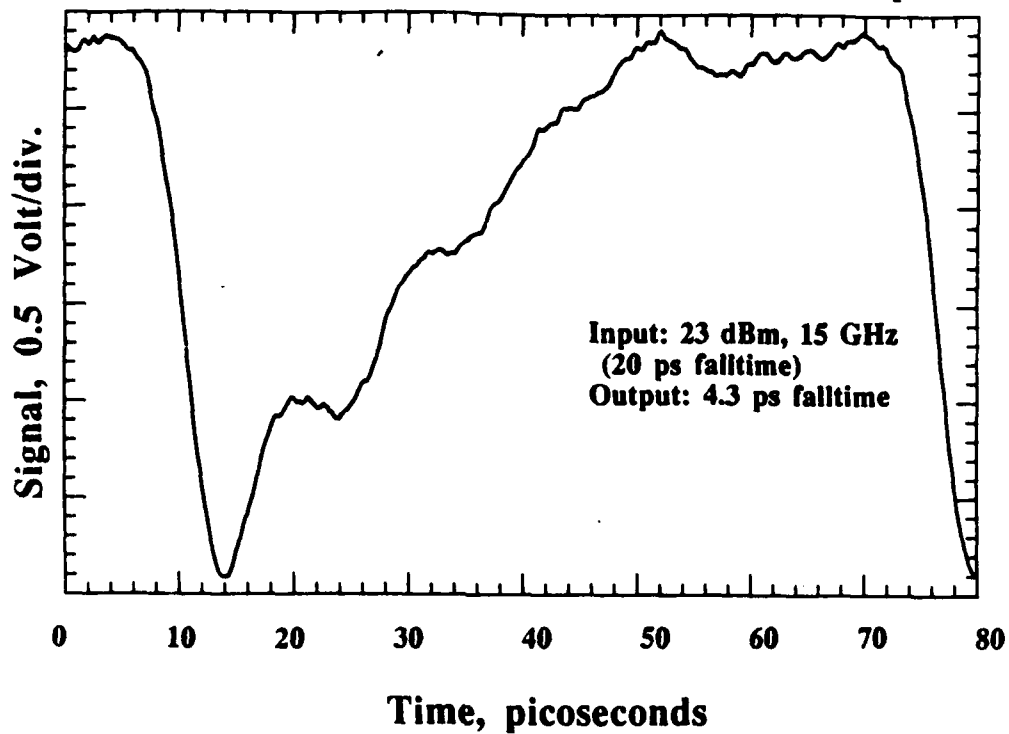


Fig.7.13. Shock-wave formation/falltime compression on the nonlinear transmission line with a sinusoidal input waveform.

### Falltime Compression with Two Cascaded Lines

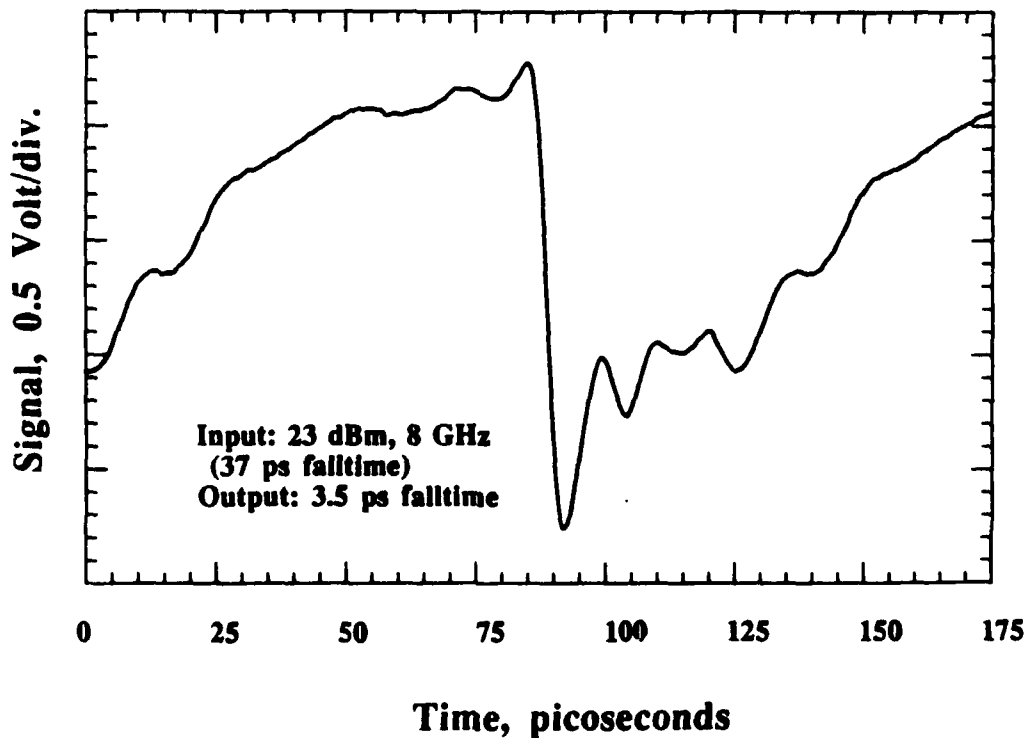


Fig.7.14. Shock-wave formation/falltime compression on two cascaded nonlinear transmission lines.

The CPW mode, which is the same as the odd mode of the coupled slot line, has electric fields of opposing polarity within the two slots. In contrast, the even mode of the coupled slot line has electric fields of the same polarity within the two slots. When the CPW mode is used, the even mode is suppressed by shorting the two outer conductors in Fig. 7.15 with an air bridge. However, discontinuities in the line can still result in the excitation of the unwanted even mode between the points shorted by the air bridges. In other applications of the coupled slot line structure, such as directional couplers and coupled line filters, both even and odd modes are required for the circuit operation. It is therefore important to characterize the mode conversion and propagation for designing CPW and coupled slot line circuits. In particular, understanding of the properties of the even and odd modes will provide information for the design of single mode CPW circuits at millimeter wave frequencies.

Electrooptic sampling was used to measure the velocities and field distributions of the even and odd modes of a  $50\ \Omega$  CPW terminated in an open circuit [7.6]. The CPW was fabricated on a  $500\ \mu\text{m}$  thick semi-insulating GaAs substrate with slot widths of  $50\ \mu\text{m}$  and the center conductor width of  $75\ \mu\text{m}$ . By scanning the electrooptic probe on the conductors along the direction of propagation (longitudinal) or over the cross section (transverse) of the guiding structure, the potential distribution in each direction can be measured. A two dimensional image of the potential distribution on the conductors of the guiding structure results. The potential distribution of the odd mode over the coplanar waveguide cross section, obtained by transverse scanning, is shown in Fig. 7.15. Standing wave, or longitudinal, measurements are obtained by scanning the probe along the direction of propagation. Figure 7.16 shows the magnitude and phase of the odd mode voltage standing wave on the center conductor. Similarly, even mode standing waves are shown in Fig. 7.17.

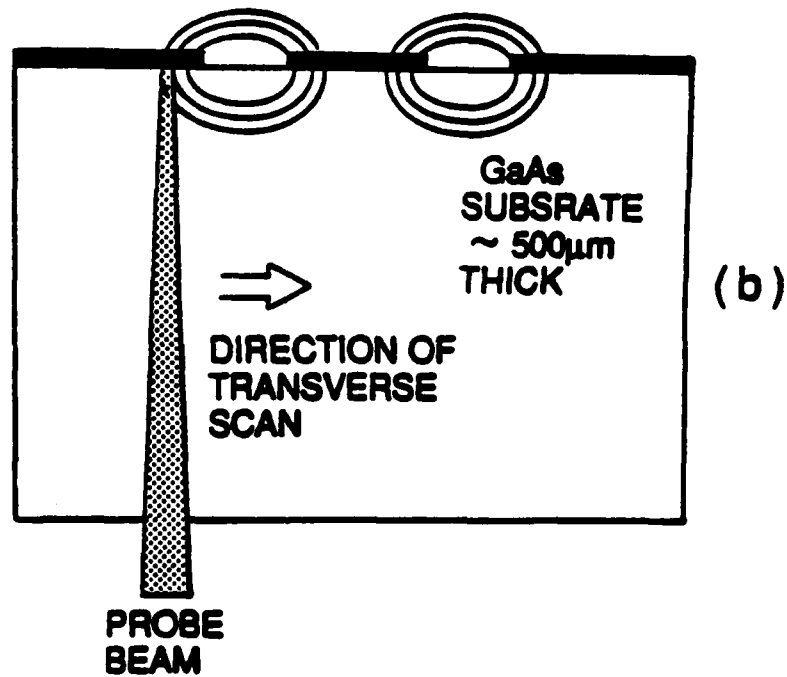
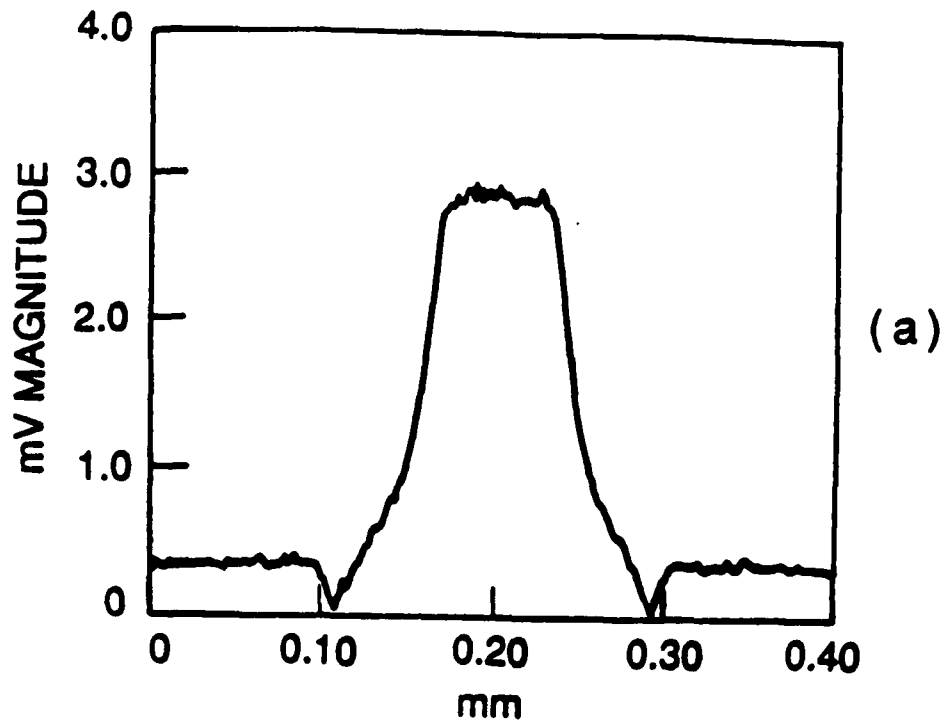


Fig.7.15. (a)- Magnitude of potential distribution of CPW (odd) mode over the cross section of the coplanar waveguide (obtained by transverse scanning)  
 (b)- Backside probing for coplanar waveguide

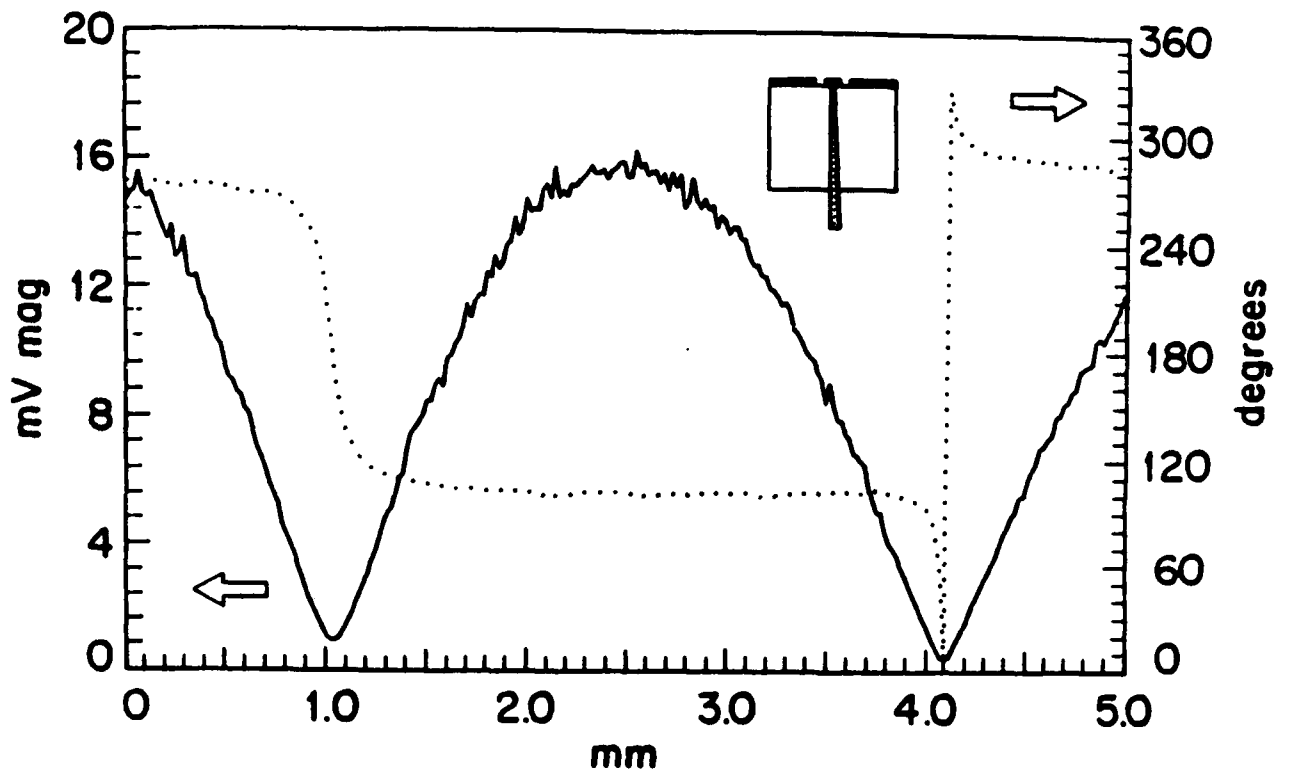


Fig.7.16. Magnitude and phase of the odd (CPW) mode standing wave on the center conductor

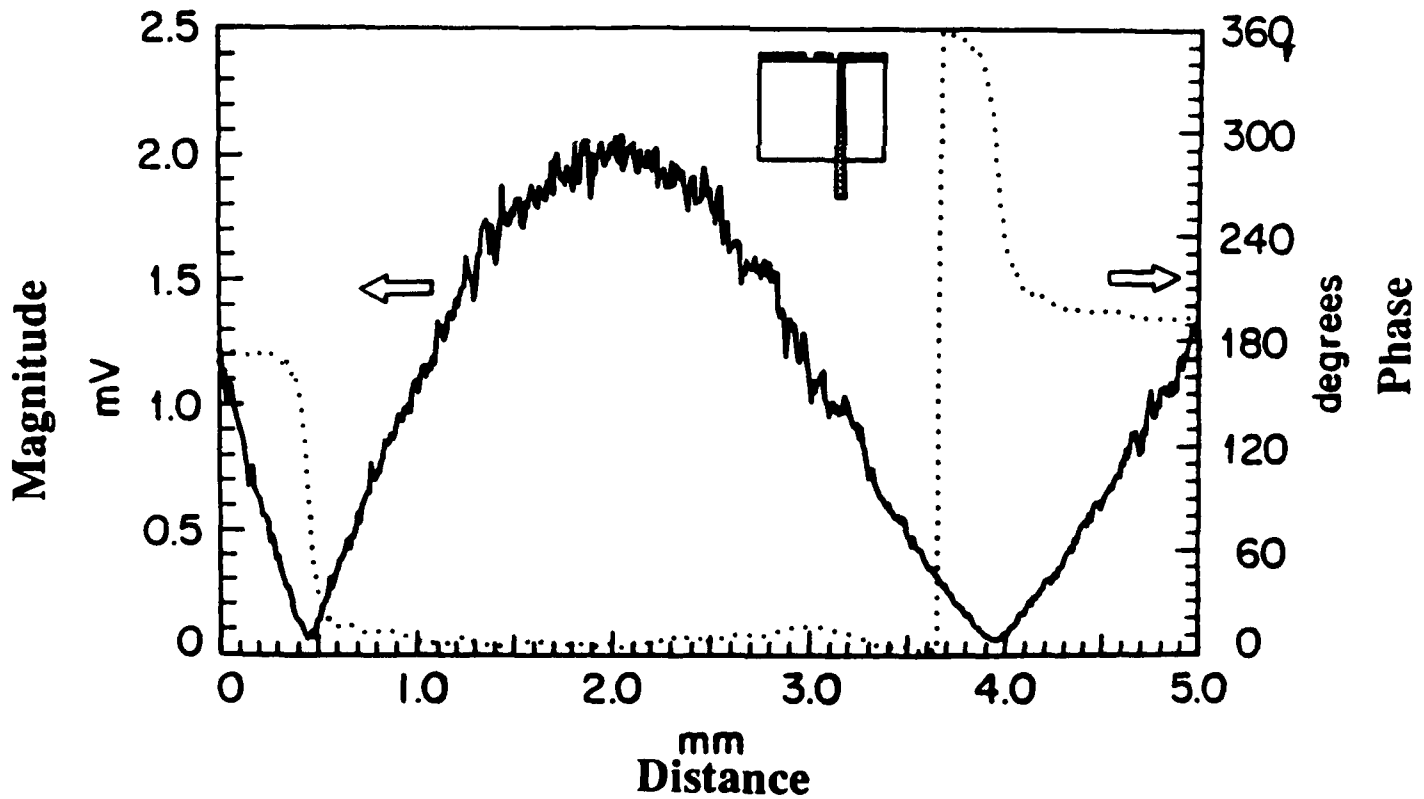
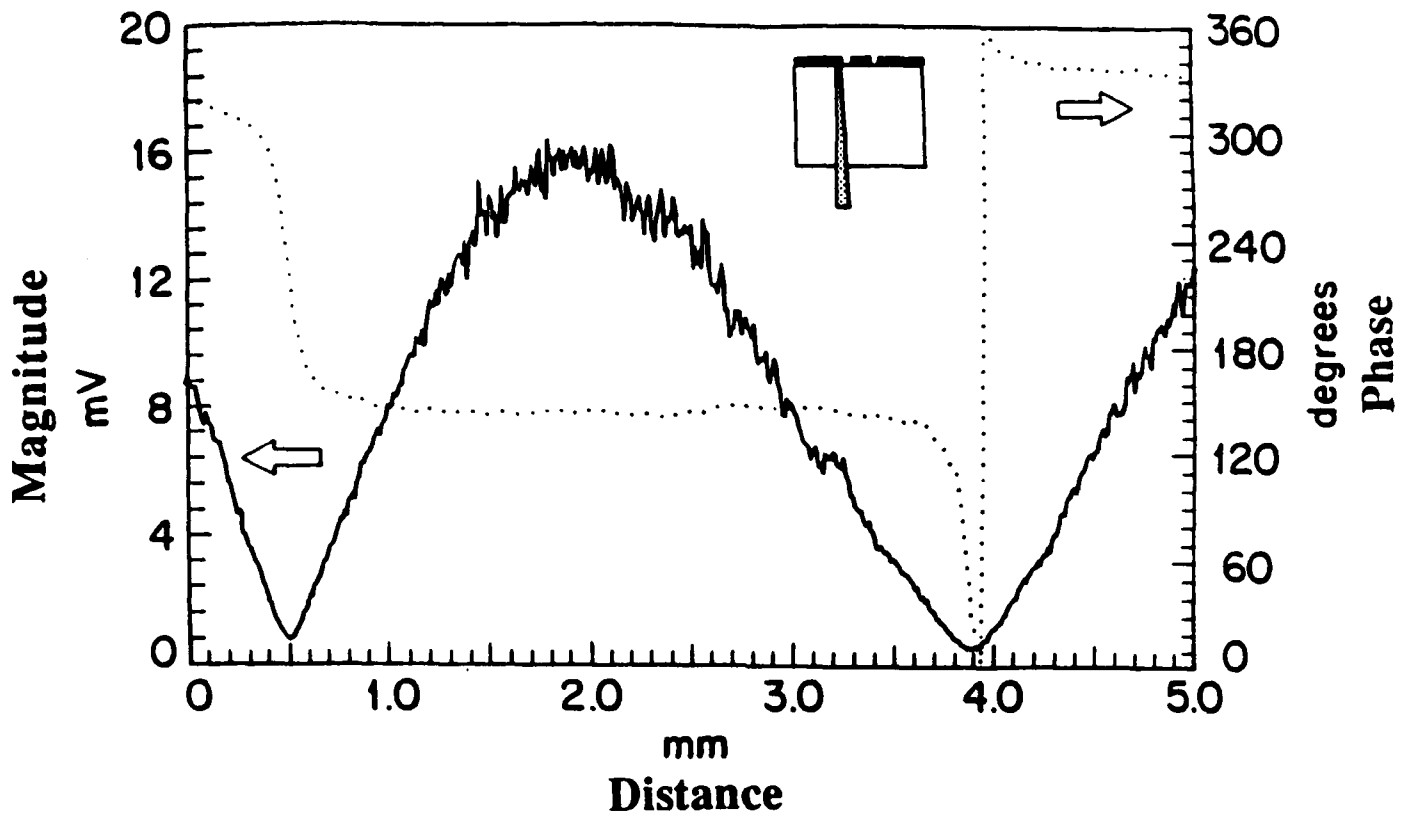


Fig. 7.17 (a)- Magnitude and phase of the even mode standing wave on the left conductor

(b)- Magnitude and phase of the even mode standing wave on the right conductor



## **7.3 Millimeter-Wave Wafer Probing: Active Probe Development**

Conventional millimeter wave sources have their output in waveguide configuration. Wafer testing of millimeter wave IC's, however requires a probe with planar configuration to contact the IC pads. Currently for low millimeter wave frequencies (up to 40 GHz) a frequency doubler (manufactured by Hewlett-Packard Co.) is added after the microwave sweep generator to extend the sampler capabilities. The waveguide output of this doubler is connected to a Cascade probe via a waveguide-K-connector adaptor which supplies the signal to the IC on the wafer. The millimeter wave circuit measurements up to 40 GHz described in Section 7.4. have been made using these added components. Recently Cascade probes with 2.4 mm coaxial connectors have been acquired which provide single coaxial up to 50 GHz. However, signal transfer from the source with waveguide output to the probe at frequencies as high as 100 GHz cannot be accomplished easily over broad bandwidth with low loss and single mode operation

An alternative approach is to generate the millimeter wave signal closer to the input of the IC on the wafer. For example, the signal could be generated directly on the wafer. This could be implemented by mixing two optical beams (separated in frequency by the desired millimeter wave frequency) in a nonlinear device on wafer. The disadvantage of two complex optical systems together with the need for an appropriate nonlinear device makes this approach unattractive for most users. Another approach is to generate the millimeter wave signal in the probe itself, where the probe incorporates a frequency multiplier and filter section. The latter approach for extending the sampler measurement capabilities to millimeter wave frequencies has been implemented. As a result of this development effort, electrooptic measurements of a 100 GHz standing wave has been made.

### **7.3.1 Active Probe Development**

#### **(a) Introduction**

Most millimeter wave sources use frequency multiplication by a diode IC together with a planar input circuit through which the microwave signal is transmitted, and finally a waveguide output from which the millimeter wave signal is extracted. If the output circuit is designed in a planar guide such as CPW and integrated with the input circuit on a single substrate the frequency multiplier can be mounted on a probe similar to the Cascade CPW probes. This scheme has the important advantage of using readily available high power microwave sources to provide the input signal to drive the nonlinear device. Interfacing

between the microwave source and the probe input is implemented over a broad bandwidth with a low-loss coaxial-to-CPW transition. The microwave signal is then multiplied to the appropriate millimeter wave frequency and the probe, contacted directly to the input pad of the DUT, supplies the test signal. Electrooptic sampling can then be used to measure input/output and internal node parameters of the GaAs IC on wafer.

Active probe fabrication requires a planar transmission medium. Microstrip and CPW are two of the more popular planar transmission lines used at millimeter wave frequencies. One of the major advantages of CPW over microstrip at millimeter wave frequencies is the existence of ground conductors on the same plane as the signal conductors. This class of transmission lines are referred to as "Uniplanar" guides. The shunt connection of passive and active circuit elements is thus realized with low dissipative and reactive parasitics and without the need for via holes. The characteristic impedance and guide wavelength of CPW are also less sensitive to substrate thickness compared to microstrip. These characteristics make CPW a better choice of transmission line for the millimeter wave active probe.

## **(b) CPW Circuit Design Considerations**

### **CPW Modes**

In designing CPW circuits, care must be taken to avoid excitation of undesired modes. To suppress the even mode in the CPW circuits of the active probe, gold bond wires were used instead of air bridges to reduce circuit fabrication complexity. A CPW low pass filter, described below, was used to evaluate the even mode-suppression of the bond wires. The circuit layout of this filter is shown in Fig. 7.18. The outer conductors were connected by 1.0 mil diameter gold bond wires for single mode operation. The insertion loss and return loss of the low pass filter with bond wires were measured using a HP 8510 network analyzer, as shown in Fig. 7.19. When the bond wires are removed, the presence of discontinuities results in mode conversion and the signal energy propagates in both even and the odd modes. Fig. 7.20 shows the resulting effect on insertion loss and return loss of the filter: the out-of-band rejection is significantly degraded by this mode conversion, the third harmonic rejection is reduced from a minimum of 15 dB to 5 dB, the fifth harmonic rejection is reduced from a minimum of 23.5 dB to 6 dB, and the pass band maximum insertion loss is increased to 1.0 dB.

The suppression of the even mode becomes even more difficult at higher frequencies due to the increasing impedance of the shorting bond wire. From the above evaluation of

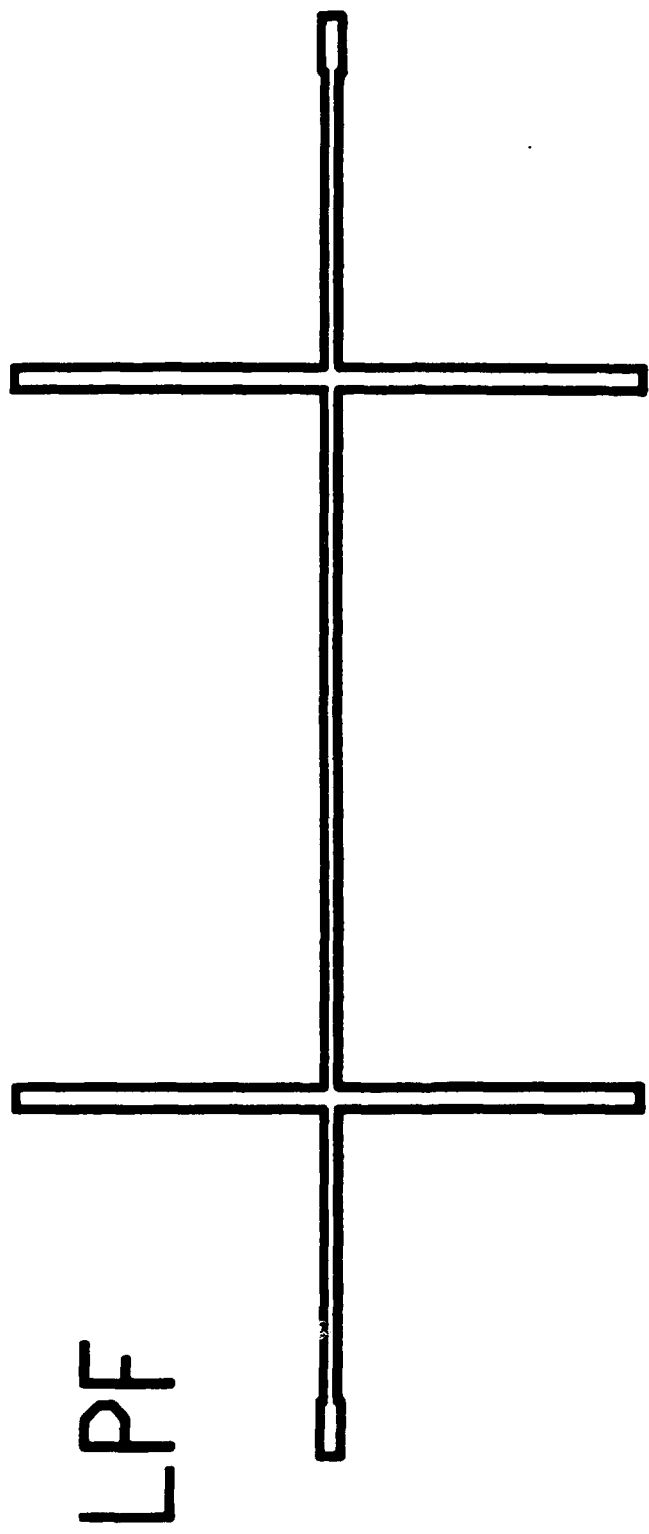


Fig. 7.18: CPW lowpass filter circuit layout

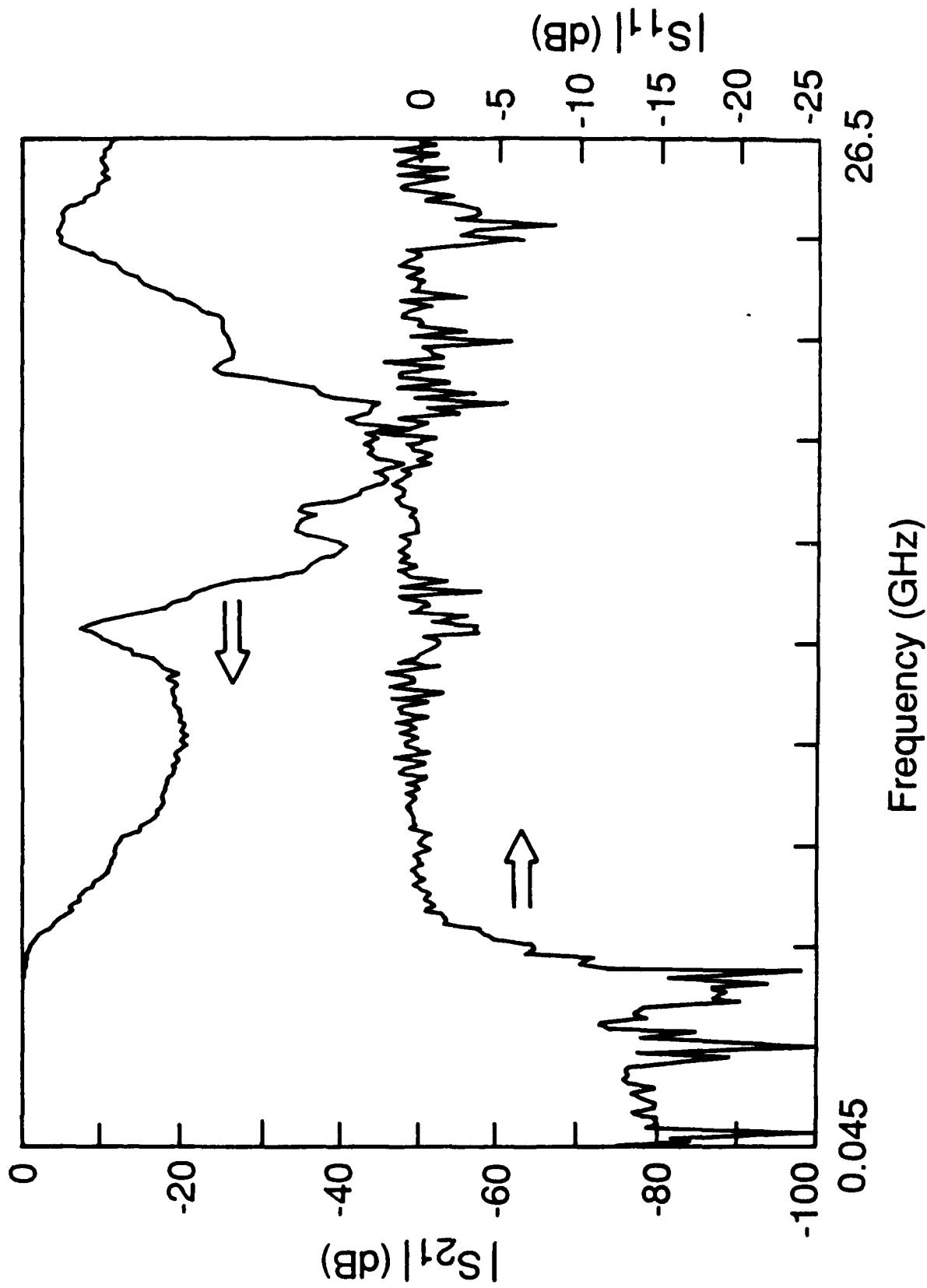


Fig. 7 19: CPW lowpass filter (with bond wires) measurement results

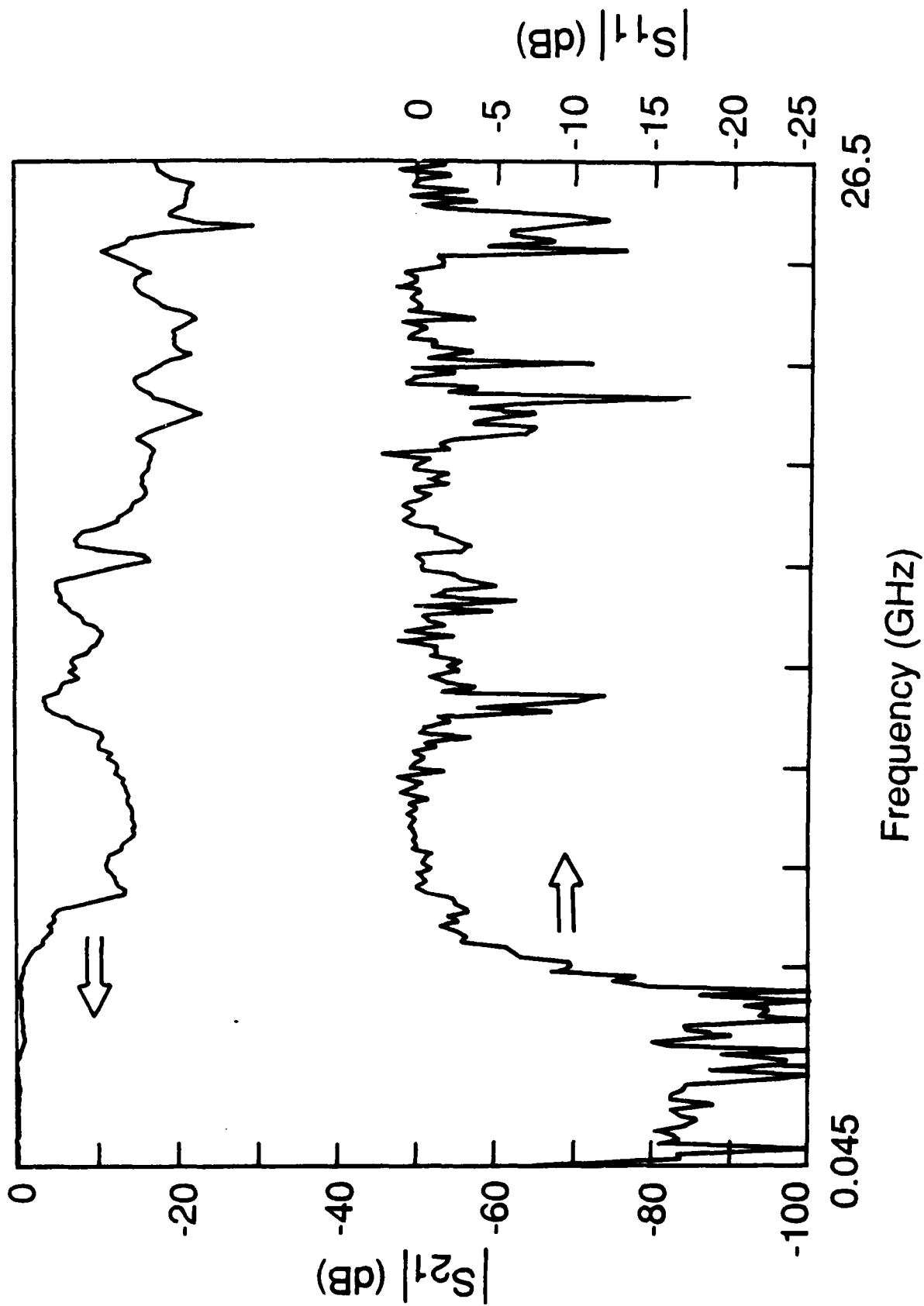


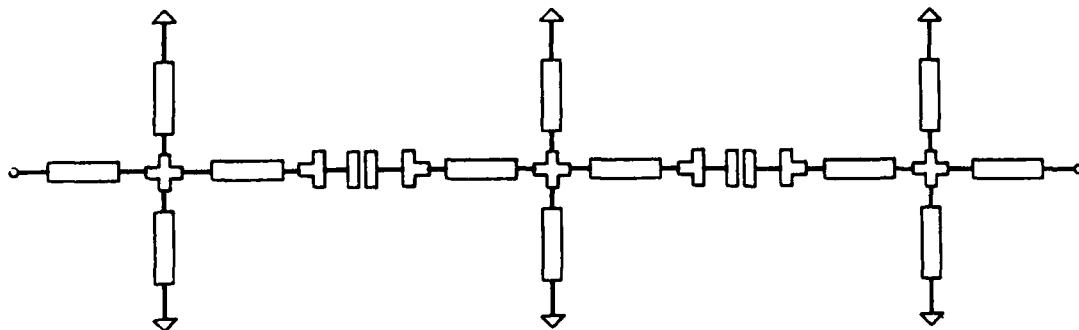
Fig. 7.20: CPW lowpass filter (without bond wires) measurement results

the scaled-model filter, however, we concluded that bond wires provide adequate suppression of the even mode.

### **CPW Discontinuities and Circuit Element Modelling**

Discontinuities in CPW involve an abrupt change in the dimensions of the center conductor or gap spacings. These changes give rise to changes in the electric and magnetic field distributions that can be represented by an equivalent capacitance and equivalent inductance, respectively. The discontinuity is then characterized by evaluating these capacitances and inductances. The types of CPW discontinuities present in the active probe circuits are: step in center conductor width, step in gap spacing, and cross-junction. Although at lower frequencies these discontinuities typically cause only very small perturbations to signal propagation, at millimeter wave frequencies, the effects are not negligible. Circuit models are therefore required for any discontinuities in the design and analysis of millimeter wave CPW circuits. Since models of CPW discontinuities currently are not available in the microwave circuit simulation programs, microstrip discontinuity models were used as an approximation in designing various parts of the active probe. Evaluation of the individual circuits, filters and matching networks, indicated that the errors due to these approximations were tolerably small.

Present models for CPW circuit elements are limited to purely uniform CPW sections. Other circuit elements, such as coupled CPW's and a series CPW gap, can be exploited to design more compact filters and matching networks with improved performance. Models for equivalent microstrip elements cannot be used as an approximation to these elements due to their generally higher Q, resulting in significant errors in predicting circuit performance. In an attempt to use the microstrip gap model in CPW filter design, the inaccuracy of the model in approximating a series CPW gap of same dimensions resulted in a significant discrepancy between the predicted and actual performance. Fig. 7.21 shows the schematic and predicted performance of a high pass CPW filter using uniform sections of lines and series CPW gaps as circuit elements, where the series microstrip gap model was used as an approximation. In this case, the use of the CPW gap allows realization of a more compact filter with improved performance. The actual performance of this filter is shown in Fig. 7.22. The significant discrepancy is due to the inaccuracy of the gap model used.



EEsof - Touchstone - Sun Jan 10 13:17:39 1988 - CPWBPF19

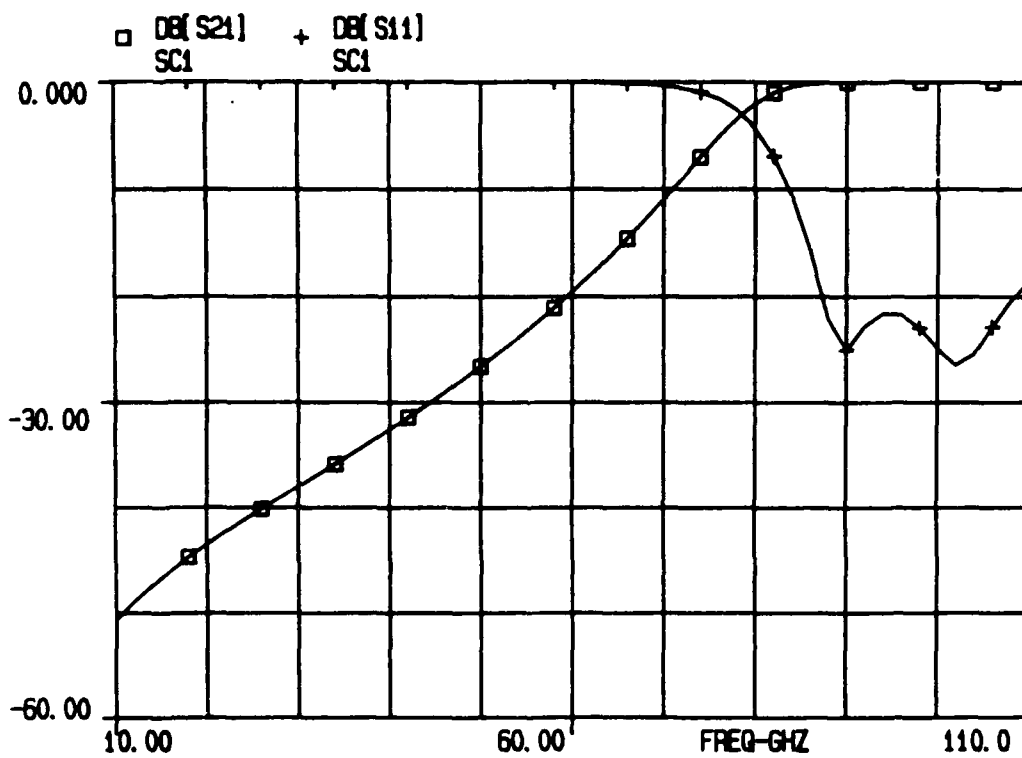


Fig. 7.21: Schematic and simulation results of CPW bandpass filter with series CPW gaps

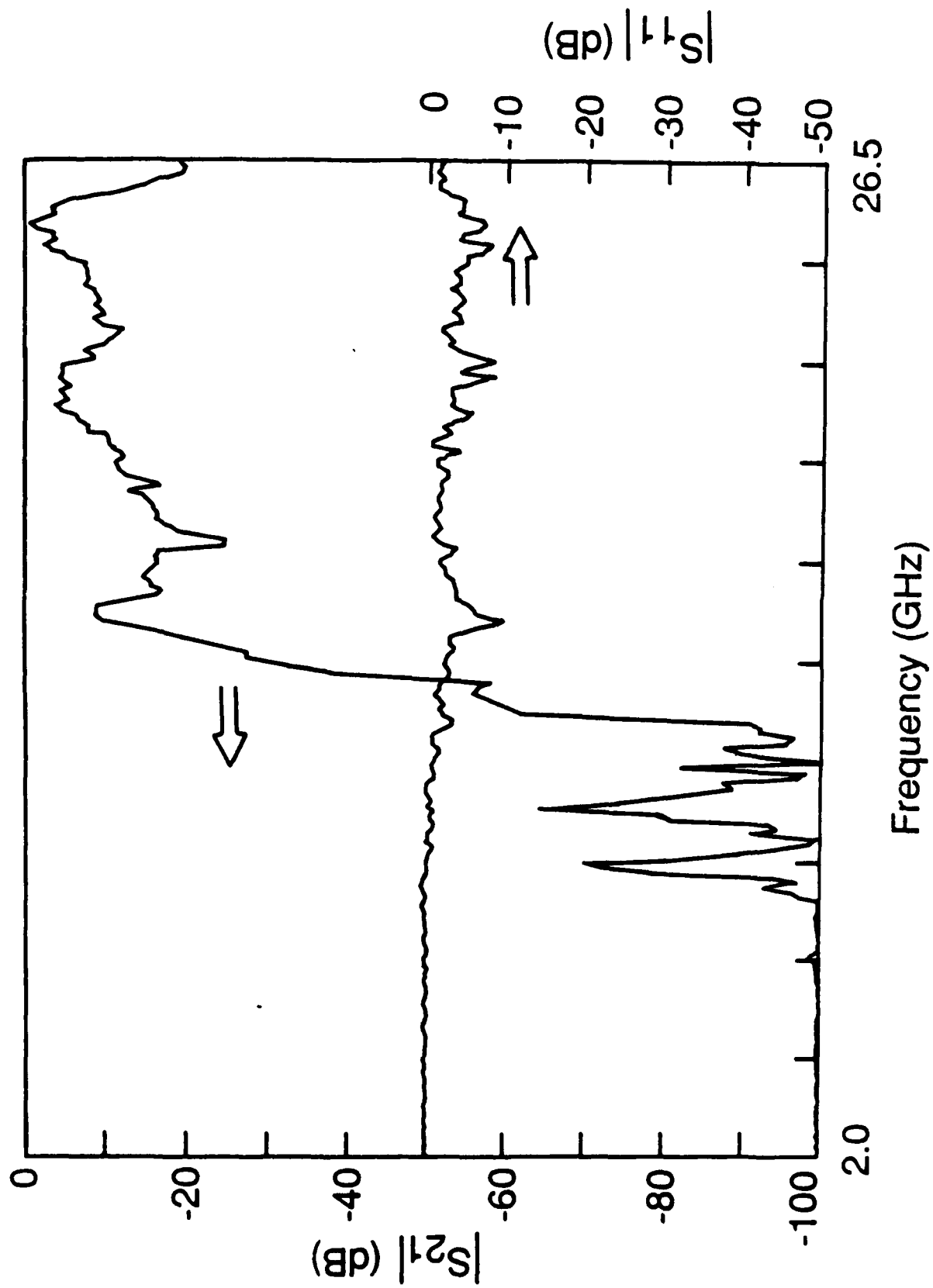


Fig. 7.22: Measurement results of CPW bandpass filter with series CPW gaps



### (c) Nonlinear Device Modelling

The device used as the nonlinear element in the frequency multiplier is a beam-lead antiparallel pair of double-stacked Schottky-barrier diodes fabricated on GaAs, manufactured by Hewlett-Packard Company. Each Schottky diode consists of two parallel fingers, each 10  $\mu\text{m}$  long. The equivalent circuit of the device is shown in Fig. 7.23. The parasitic elements in the nonlinear equivalent circuit model of the device are calculated from the geometry and process parameters of the chip together with the package dimensions. The primary nonlinear element used for the generation of higher order harmonics of the input signal is purely resistive.

Using the equivalent circuit model, the nonlinear simulation of this device was performed on MWSPICE™. The impedance of the device under large signal drive conditions is both time-varying and a function of the incident signal amplitude. The variation of the real and imaginary part of the diode impedance at the fundamental frequency as a function of input voltage when driven by a 20 GHz signal source is shown in Fig. 7.24. An estimate of the time-averaged impedance of the device at each frequency is obtained by taking the ratio of the Fourier component of the voltage and current at that frequency. In the case of the quintupler, these Fourier components are calculated at the fundamental and the fifth harmonic. The input impedance of the device for the input frequency band of 15-22 GHz is calculated under large signal drive by a signal of the same frequency. The output port of the device is assumed to be open circuit at the fundamental, which is a good approximation considering the relatively large out-of-band rejection of the output filter. The output impedance at 75-110 GHz (fifth harmonic) is calculated with an input signal at the fundamental frequency. Since the circuit is non-linear this impedance is a function of the load presented to the device at the fifth harmonic (output frequency). Consequently in the output impedance calculation this dependence has to be incorporated. The voltage and current waveforms under large signal drive by a +30 dBm, 25 GHz sinusoidal signal is shown in Fig. 7.25. The effect of the device nonlinearities on the input sinusoidal voltage waveform is seen in these waveforms. For comparison purposes and to see the drive dependence of the impedance the voltage and current waveforms of the device under a smaller (+10 dBm) drive signal are shown in Fig. 7.26. Since the device is in an antiparallel configuration the even order harmonics are suppressed, resulting in an nearly symmetrically distorted waveform.

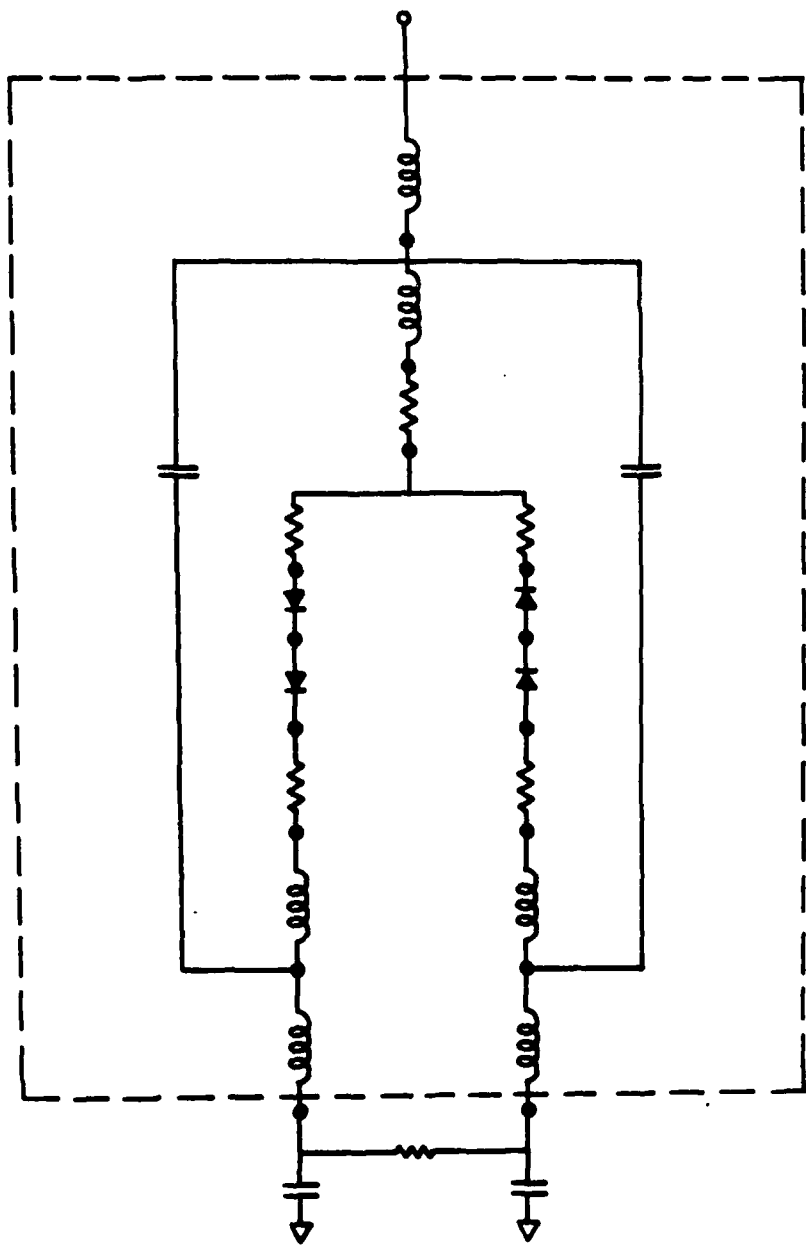


Fig. 7.23: Millimeter wave diode equivalent circuit

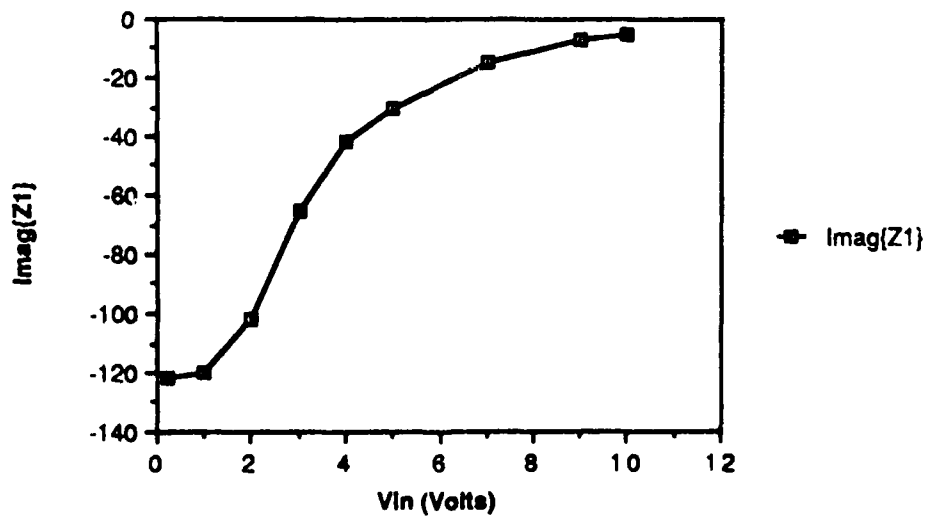
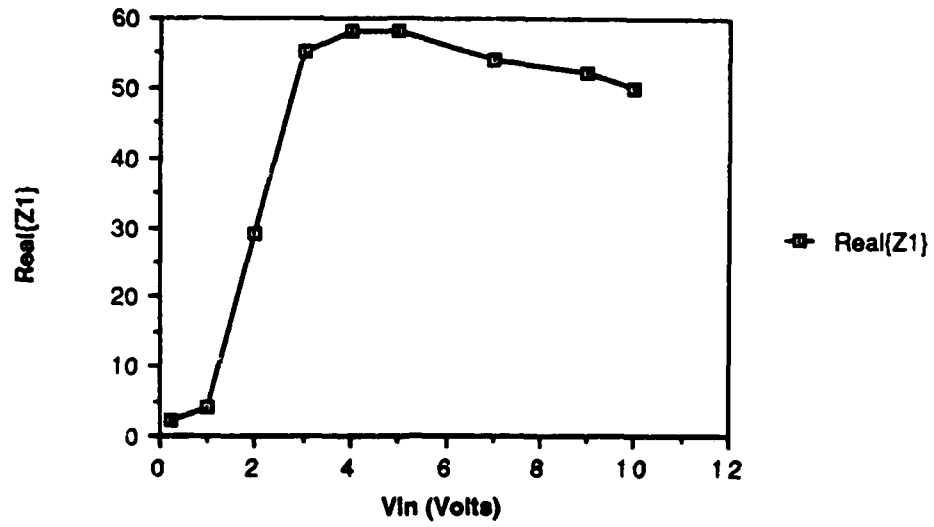


Fig. 7.24: Millimeter wave diode impedance vs. driving voltage

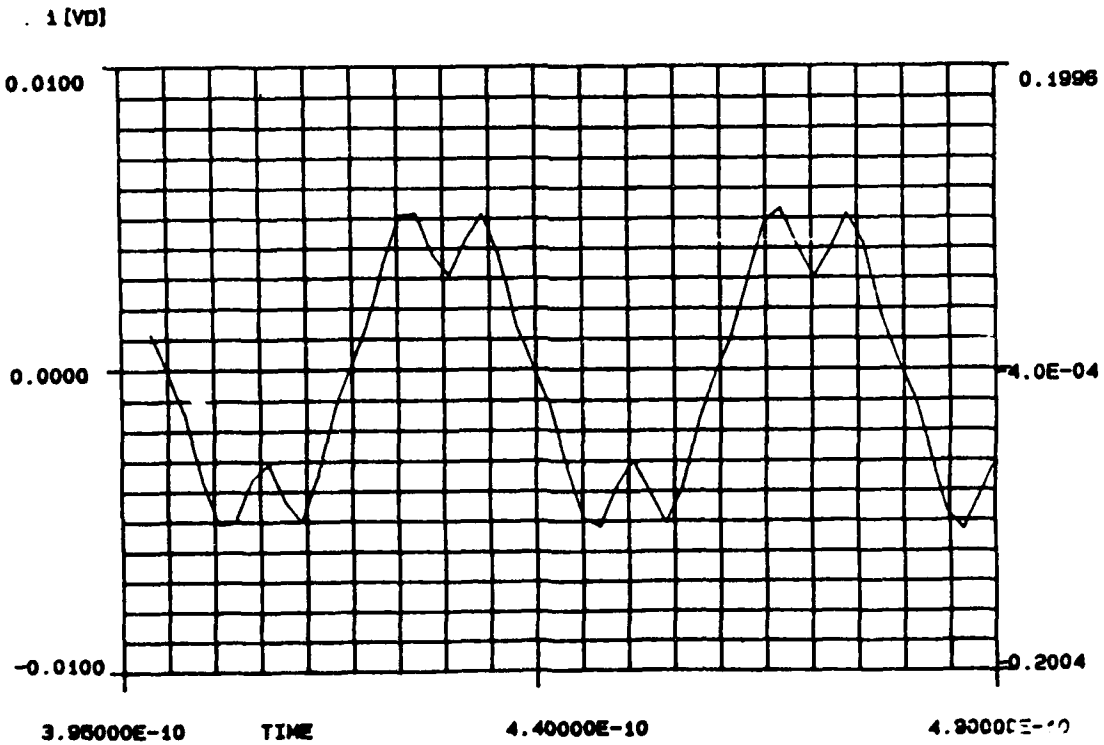
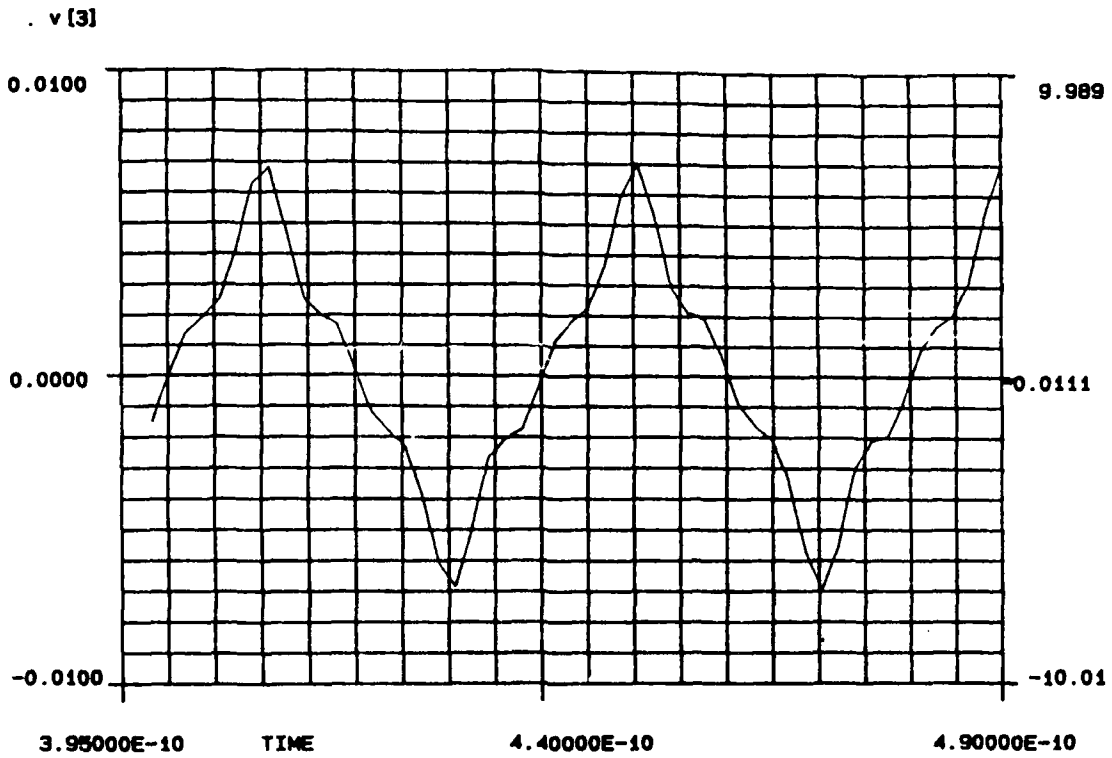
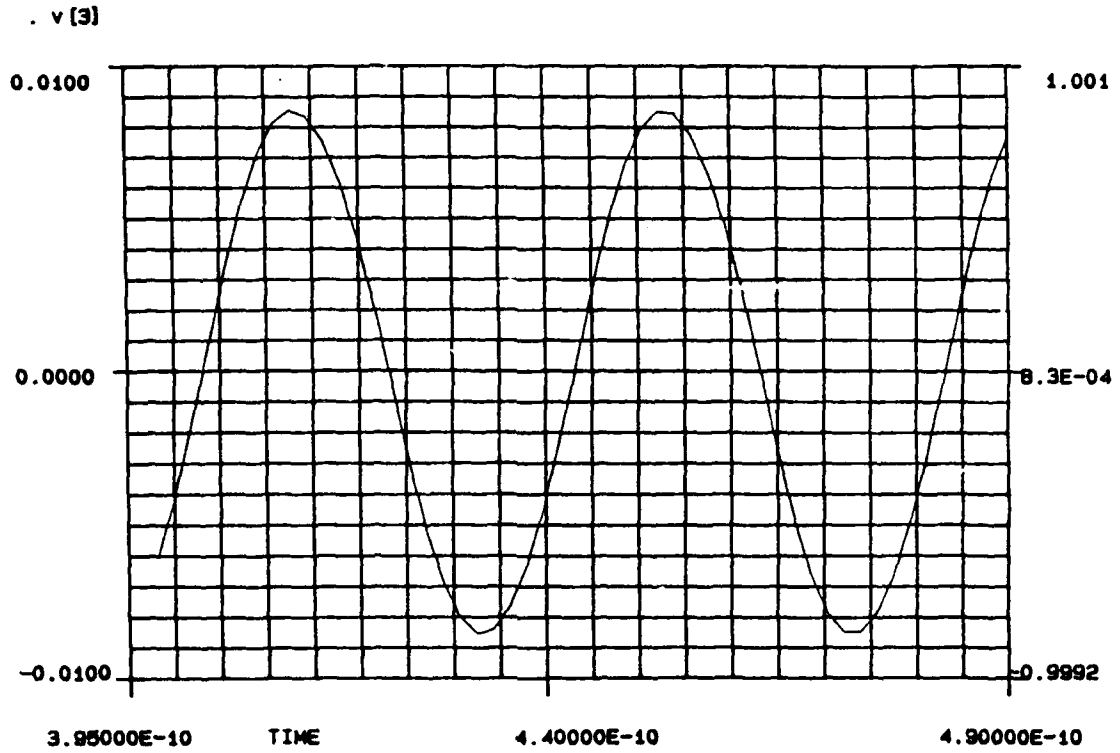


Fig. 7.25: Voltage and current waveforms at 25 GHz with +30 dBm input power

EEsof - mWSPICE - 10/12/87 - 19:18:43 - DTA  
NET



EEsof - mWSPICE - 10/12/87 - 19:18:43 - DTA  
NET

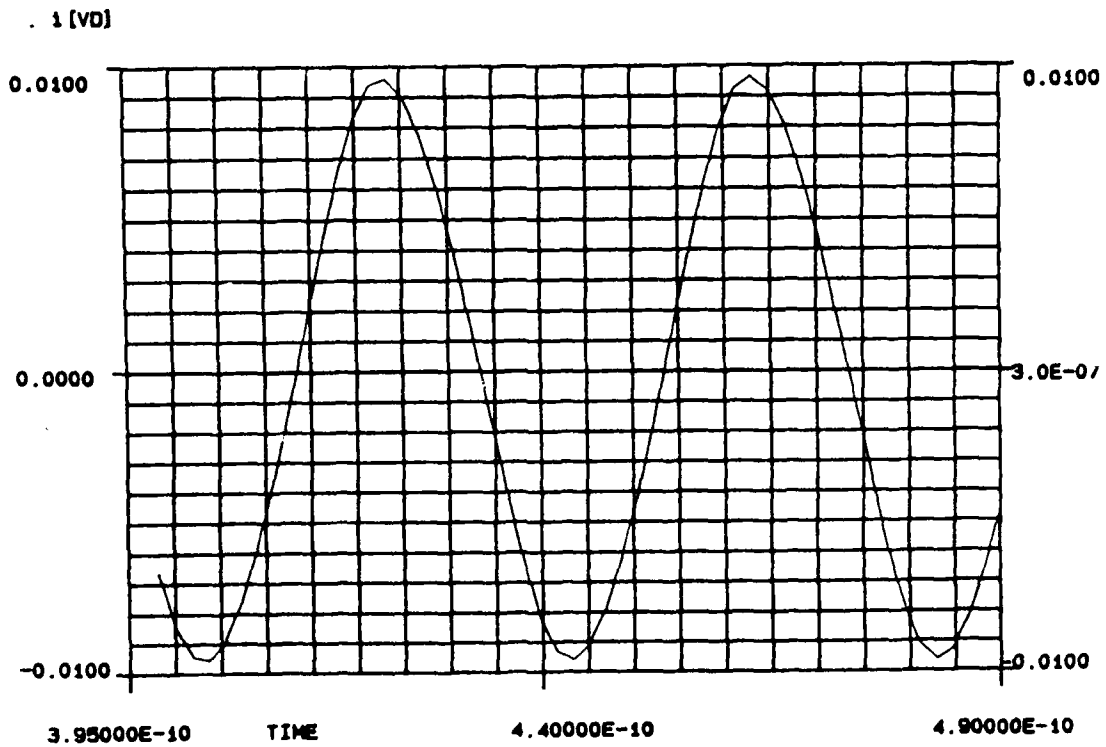


Fig. 7.26: Voltage and current waveforms at 25 GHz with +10 dBm input power

#### **(d) Scaled model frequency multiplier design**

At millimeter wave frequencies, discontinuities and parasitics have significant effects on circuit performance. To evaluate the circuit models and the design of the millimeter wave frequency multiplier, scaled models of the filters and matching networks of the active probe and an approximate scaled model quintupler were built for a scaling factor of 5:1. The scaled model has an input frequency range of 3.0-4.4 GHz and an output frequency range of 15.0-22.0 GHz. CPW on alumina, which has a relative dielectric constant of 9.9, was chosen as the transmission medium.

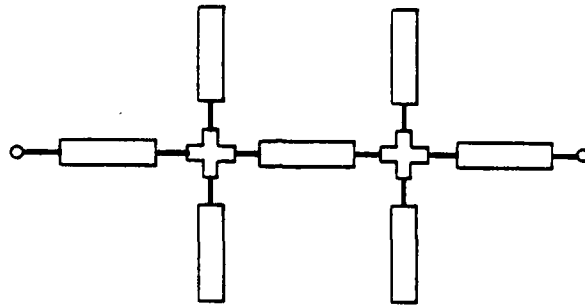
#### **Filter design**

Two filters were designed for the quintupler. A low pass filter at the input allows signal transmission at the fundamental frequency to the nonlinear element. The harmonics of the input signal frequency generated by the nonlinear element are rejected by this low pass filter to avoid transmission back to the input. A bandpass filter at the output of the nonlinear element allows the transmission of the fifth harmonic to the output of the quintupler, while rejecting all other harmonics.

The filters were designed based on doubly-terminated, lumped, low-pass prototype filters. The terminating impedance on both ports were chosen to be 50 ohms. The prototype filters were frequency and impedance scaled. Lowpass-to-bandpass transformation was performed for the output filter. The CPW filters were further optimized using TOUCHSTONE™.

The input filter was designed to provide low insertion loss for the pass band and to provide rejection of the odd harmonics of the pass band, in particular the fifth harmonic. Predicted results of the input low pass filter simulated on TOUCHSTONE™ and its schematic are shown in Fig. 7.27. The circuit was fabricated on 15 mil Alumina substrate using thin film deposition and liftoff of sputtered Ta-Au followed by additional Au plating to reduce skin effect losses. One mil diameter gold wire was used to connect the ground planes on the two sides of the center conductor on three of the circuits. Since the circuits were designed to be tested using CASCADE™ probes, substrate mounting on carriers was not required for circuit evaluation. The circuits were evaluated on a CASCADE model 42 probe station using HP8510A network analyzer.

The filters were evaluated from 45 MHz to 26.5 GHz. Fig. 7.20 shows the insertion loss and the return loss of the filter: the passband loss is less than .5 dB while the fifth



EEsof - Touchstone - Sun Jan 10 12:56:49 1988 - CPMLPF8

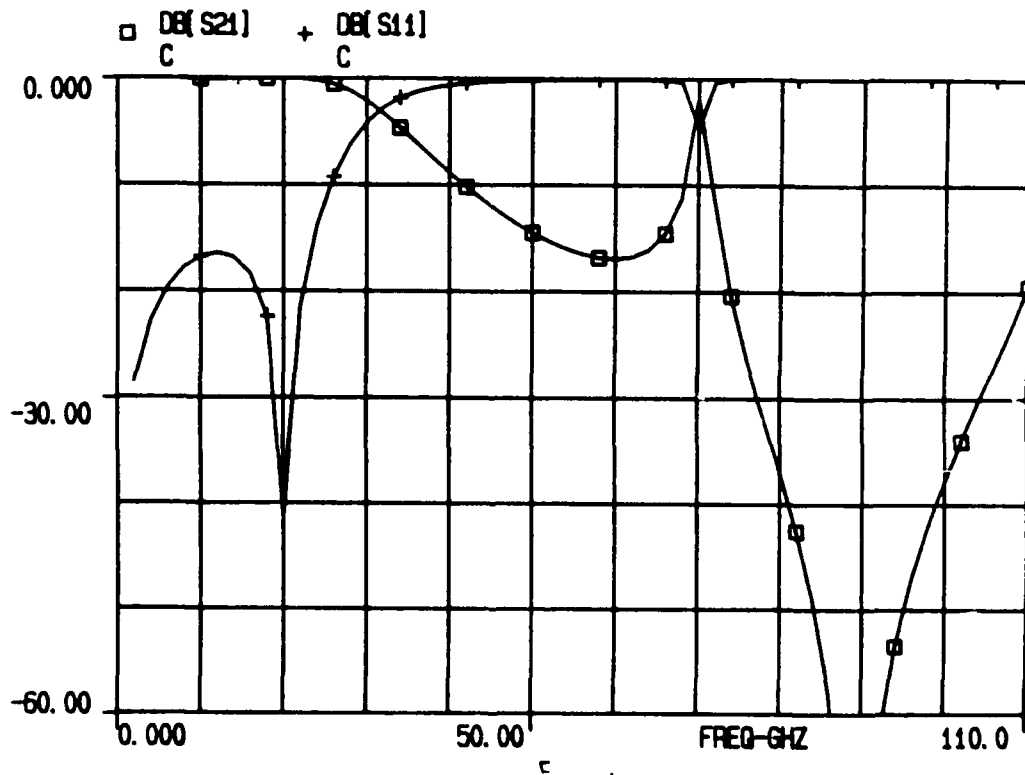


Fig. 7.27: Schematic and simulation results of CPW lowpass filter

harmonic (15.0 to 22.0 GHz) is rejected by a minimum of 23.5 dB. The third harmonic rejection (9.0-13.2 GHz) is more than 15.0 dB. There is very good agreement between the predicted and the measured results. The measured insertion loss at high frequencies was more than predicted due to the substrate dielectric losses and the conductor losses. The band-stop region was broadened due to the same effects resulting in a reduced Q. The measured match was better than 12 dB in the pass band.

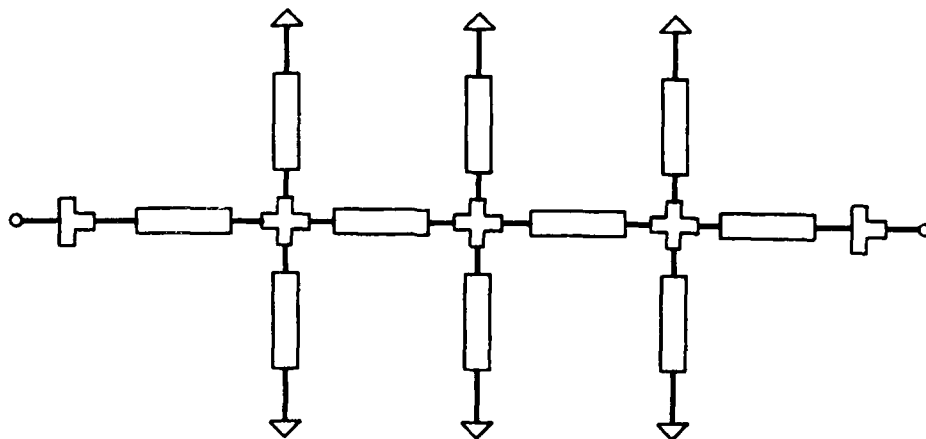
The first-iteration design of the output bandpass filter consisted of two versions. The pass band of this filter is 15.0 to 22.0 GHz. The evaluation results of these filters were not satisfactory. One major problem was the use of wide low impedance sections of CPW in these filters. The suppression of the even mode becomes increasingly more difficult as the width of the low impedance CPW's becomes larger due to the increase in the impedance of the bond wire shorting the outer conductors. At 20 GHz the impedance of the bond wire connecting the ground planes of the low impedance CPW sections in these filters was approximately 180 ohms. Thus mode conversion was partially a contributor to the discrepancy between the predicted and measured results. Transverse mode propagation was also a potential problem at the upper end of the passband where the width of the low impedance sections approached half-wavelength.

To eliminate some of the problems of CPW's with wide center conductors, the second iteration of this design employed a maximum center conductor width of 400 microns. The circuits were again fabricated on 15 mil Alumina with Ti-Au metallization. The schematic and predicted results of this filter are shown in Fig. 7.28. The measured insertion loss and return loss of band pass filter are shown in Figure 7.29. The passband insertion loss was less than 1.0 dB except at the low end of the band (15 GHz) where it rolled off to about 2.5 dB. The out-of-band rejection at 4.4 GHz (the fundamental frequency of the scaled model) was more than 40 dB, the return loss was better than 20:1 for most of the band, and the magnitude of the reflection coefficient was less than .25 at 20 GHz. The filter was best matched in the center of the band at 18.5 GHz where return loss is better than 25 dB.

### **Matching network design**

The time-averaged input and output impedances calculated from the nonlinear analysis are used to obtain equivalent lumped small-signal one-port circuits. The input impedance as a function of frequency from 15 to 22 GHz is plotted in Fig. 7.30 and the output impedance is shown in Fig. 7.31. from 75 to 110 GHz. A simple RLC network was used on TOUCHSTONE™ to match the model and the data for input and output separately. The model frequency responses are also shown in the same figures.





EEsof - Touchstone - Sun Jan 10 12:59:14 1988 - CPWBPF23

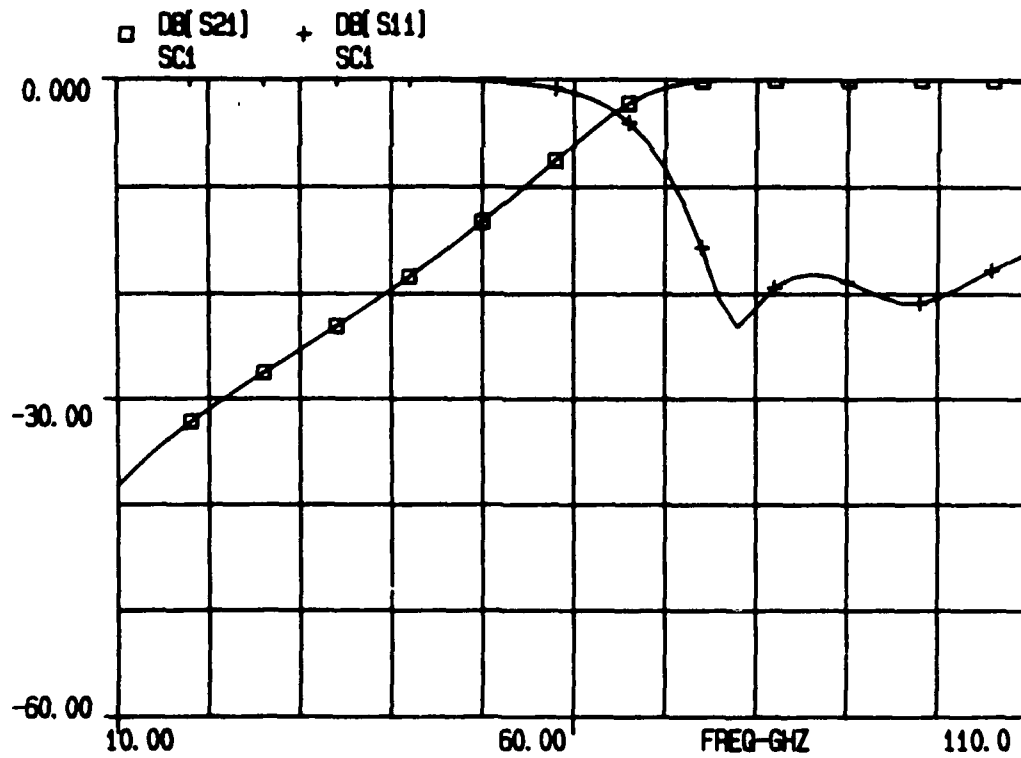


Fig. 7.28: Schematic and simulation results of CPW bandpass filter

CH1: A <sup>-M</sup> REF + 1.00 dB - 29.21 dB  
 5.0 dB/ REF + .00 dB

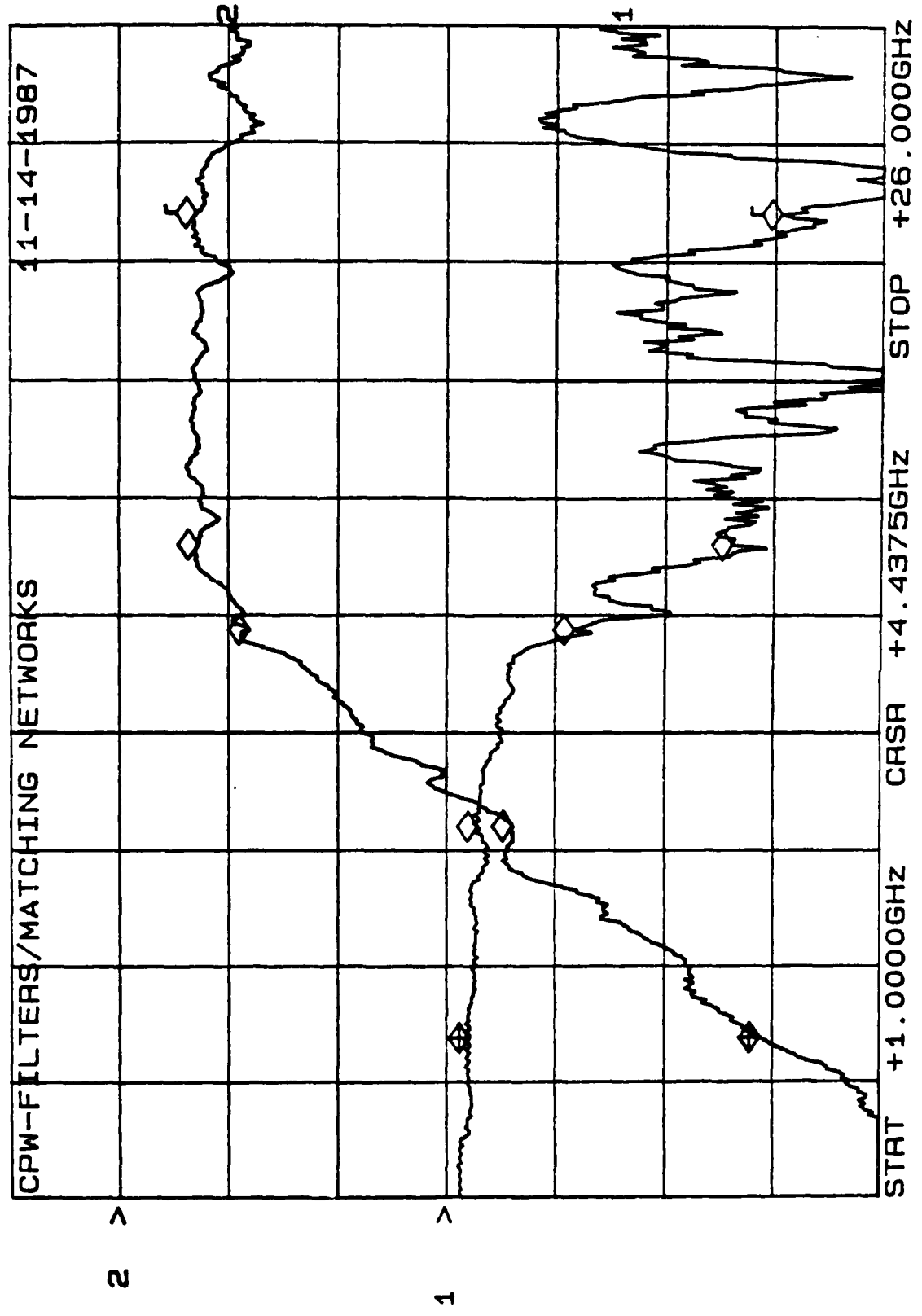


Fig. 7.29: Measurement results of CPW bandpass filter

.. ..

EEsof - Touchstone - Sun Jan 10 13:06:29 1988 - TC490MOD

□ S11  
A  
+ S11  
B

f1: 75.0000  
f2: 110.0000

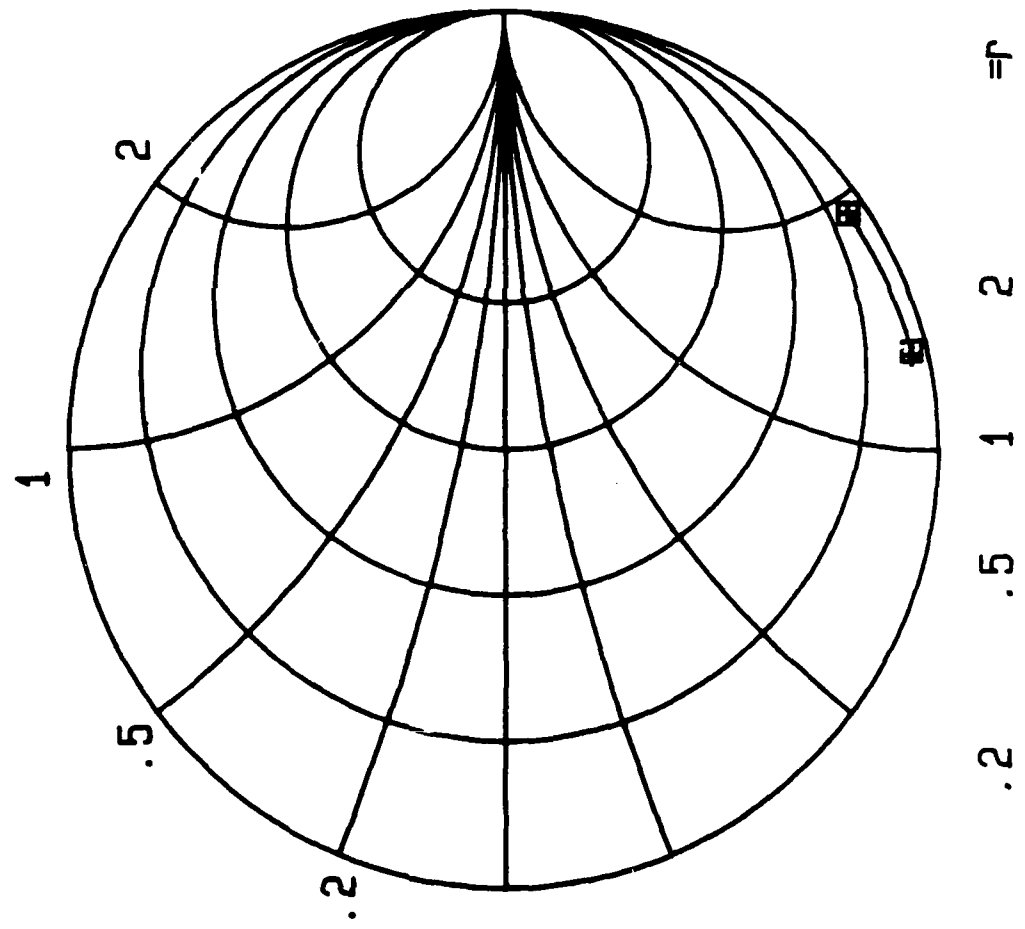


Fig. 7.30: Diode input impedance and the simplified model impedance vs. frequency

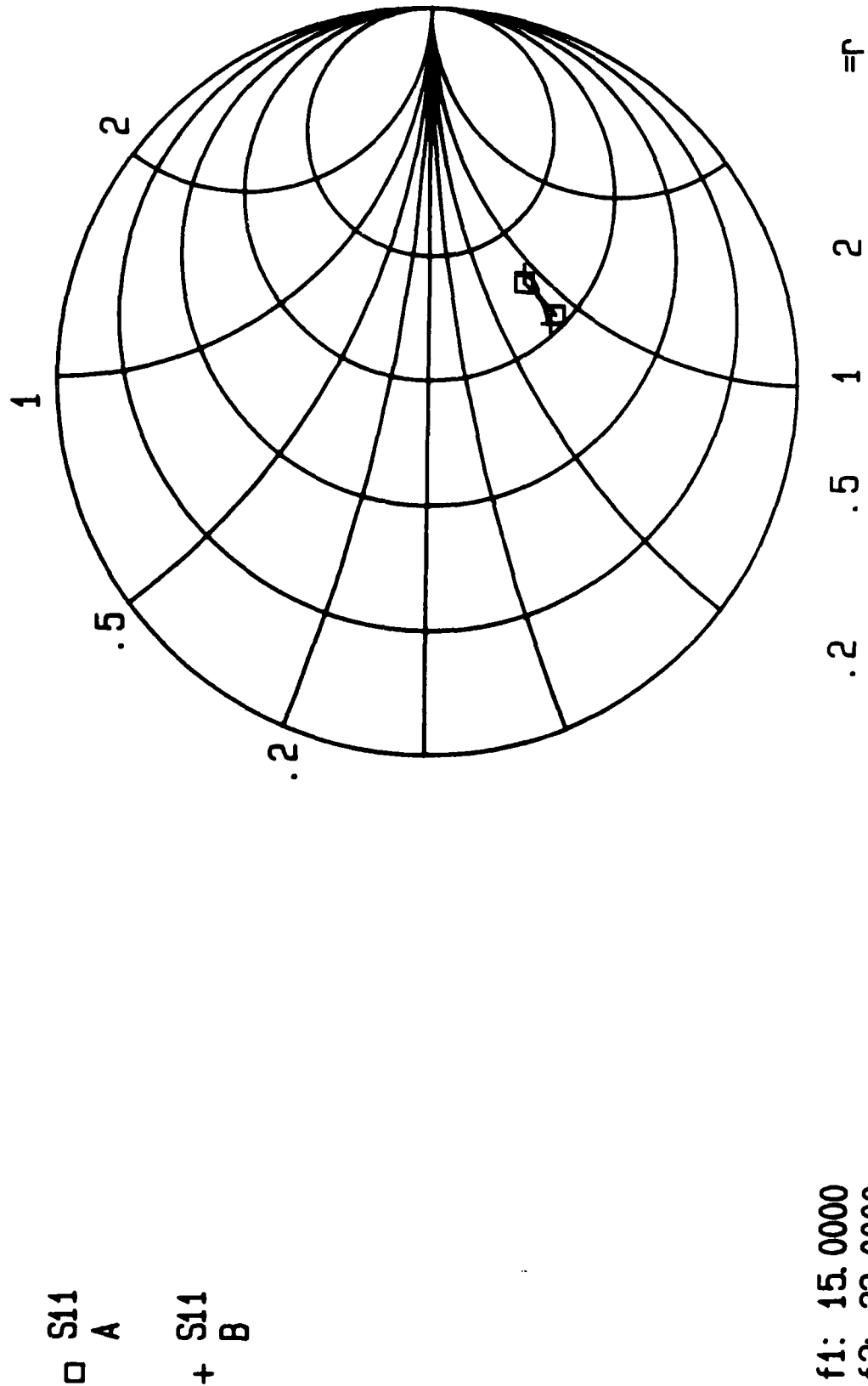


Fig. 7.31: Diode output impedance and the simplified model impedance vs. frequency

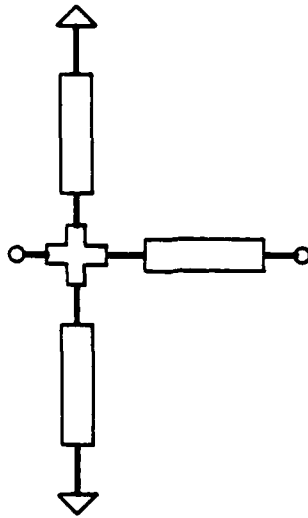
These lumped equivalent circuit models were used to design matching networks for the input and output. The input matching network consisted of a series transmission line and two shorted stubs in parallel. The schematic and predicted input reflection coefficient of the device with the input matching network is shown in Fig. 7.32. The output matching network is more complex due to the fact that the real part of the impedance at fifth harmonic is very low. The impedance transformation and the absorption of the imaginary part of the impedance as part of the matching network structure was done using the designed circuit topology. The schematic and predicted reflection coefficient of the device and the output matching network are shown in Fig. 7.33.

### **Scaled model quintupler**

A scaled model frequency multiplier was designed based on the scaling of the passive networks and approximate scaling of the nonlinear device. The scaling of the device was approximate due to the relatively complex equivalent circuit model of the actual millimeter wave diode. The complexity of the equivalent circuit is a direct result of the significant presence of the parasitic package capacitances and beam lead inductances at millimeter wave frequencies and also the diode itself. The junction capacitance and series resistance of the scaled device were calculated from the simplified equivalent circuit model of the millimeter wave diode. The scaled model device selected was a beam-lead medium-barrier silicon Schottky diode manufactured by Metelics Inc.

The scaled model frequency multiplier circuit was fabricated on 25 mil Alumina substrate. The metallization used was sputtered TiW-Au plated with 40 microinches of Au. Fig. 7.34. shows the circuit layout of the quintupler. The beam lead diodes, chip capacitors and chip resistors were then epoxied onto the substrate and bonded using gold wires. A test fixture was designed for the scaled model to facilitate RF testing and DC bias adjustments to the diodes. The scaled model frequency multiplier was tested using Cascade™ probes and a model 42 Cascade probe station.

The best performance was obtained at the low end of the band. Figure 7.35. shows the output signal of the frequency multiplier measured on a spectrum analyzer with an input signal at 3.0 GHZ. The results show up to the 7th harmonic present. The desired fifth harmonic signal is 24 dB above the fundamental and more than 25 dB above all other harmonics. The even order harmonics exist due to unbalance between the diodes. The maximum output power of -16.9 dBm obtained from this multiplier was at an output frequency of 15.56 GHZ. The suppression of the undesired harmonics decreases with increasing frequency. Fig.7.36. shows the results at an output frequency of 17.16 GHZ



EEsof - Touchstone - Sun Jan 10 13:01:53 1988 - H1M3

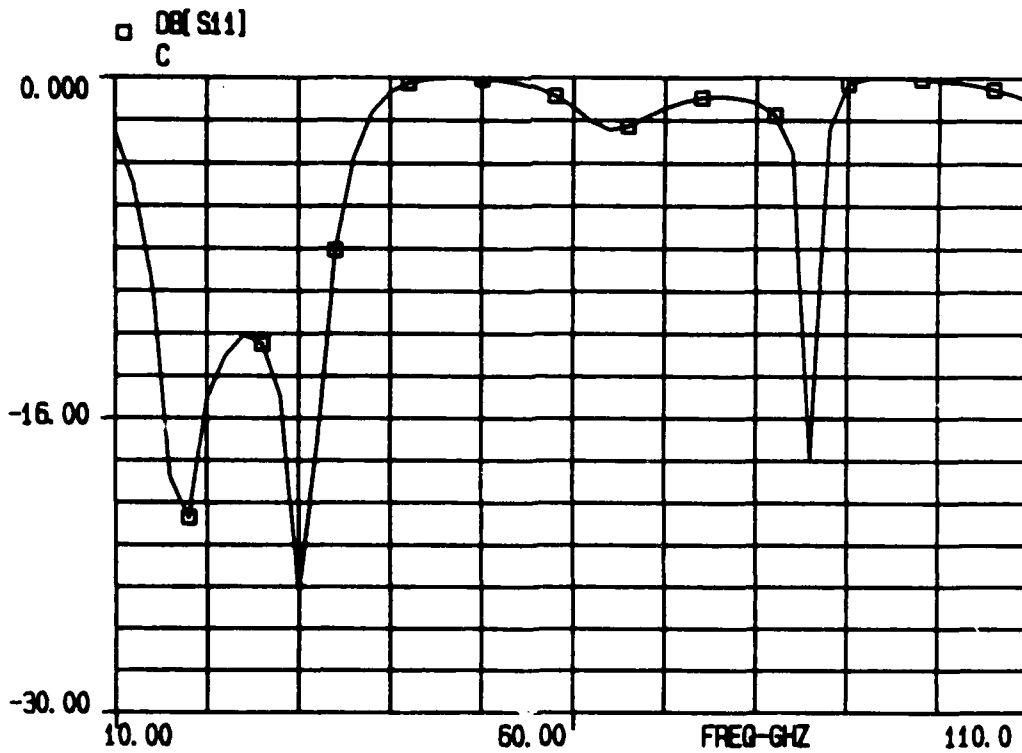
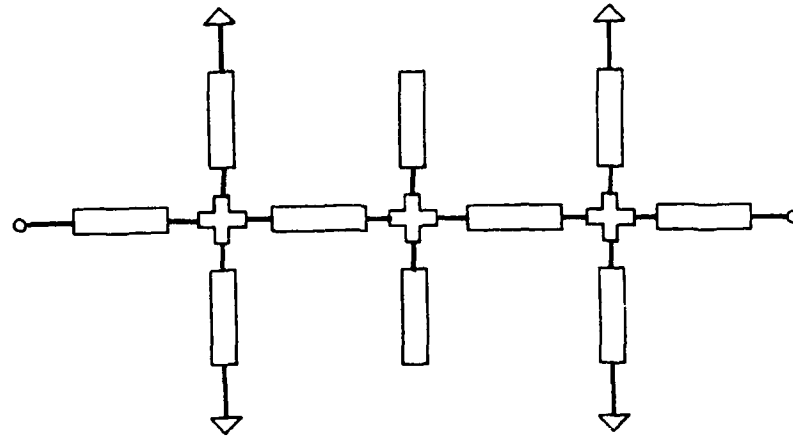


Fig. 7.32: Schematic and simulation results of input matching network



EEsof - Touchstone - Sun Jan 10 13:04:20 1988 - H5M16



Fig. 7.33: Schematic and simulation results of output matching network

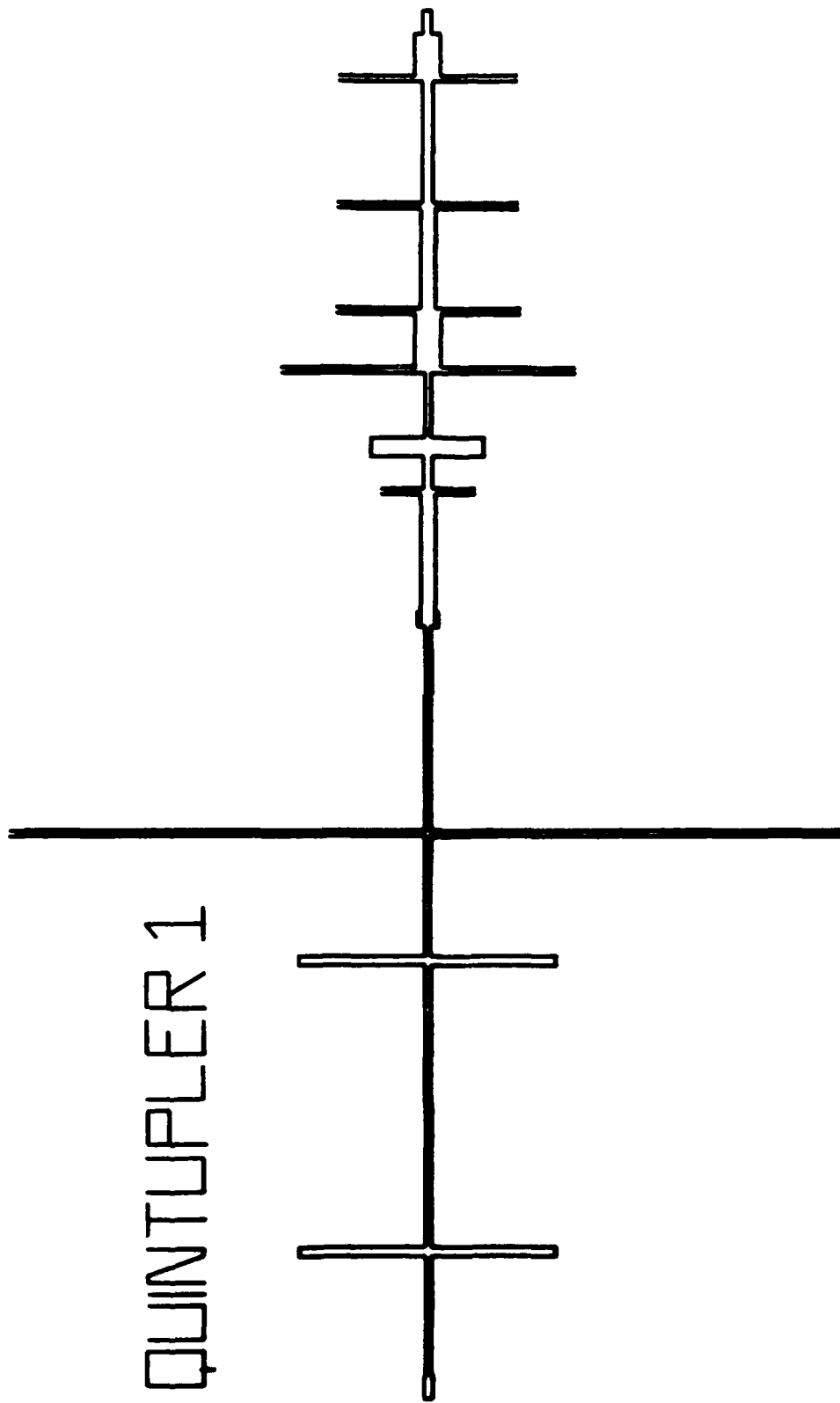


Fig. 7.34: Scaled model quintupler circuit layout



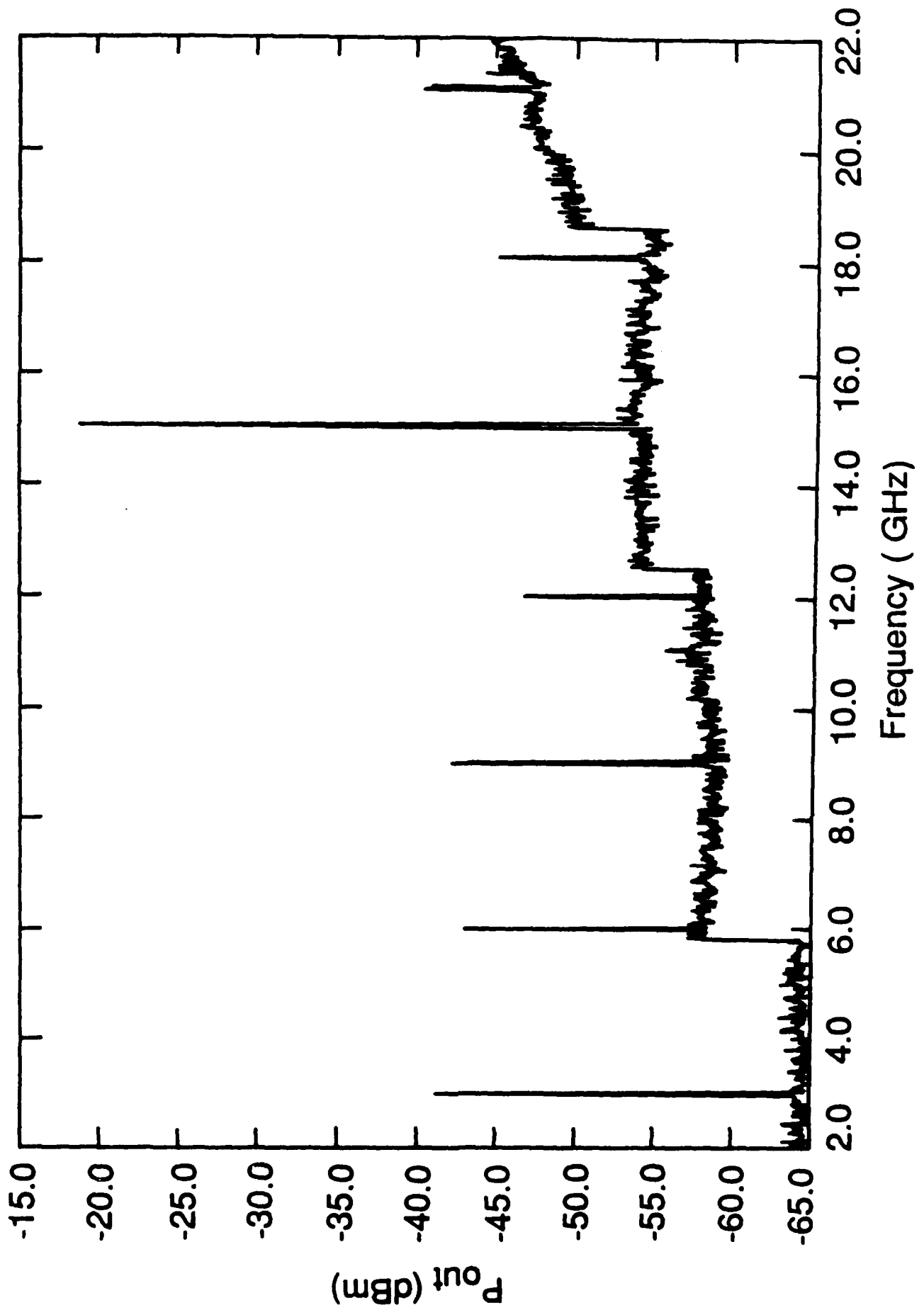


Fig. 7.35: Scaled model quintupler output with 3.0 GHz input

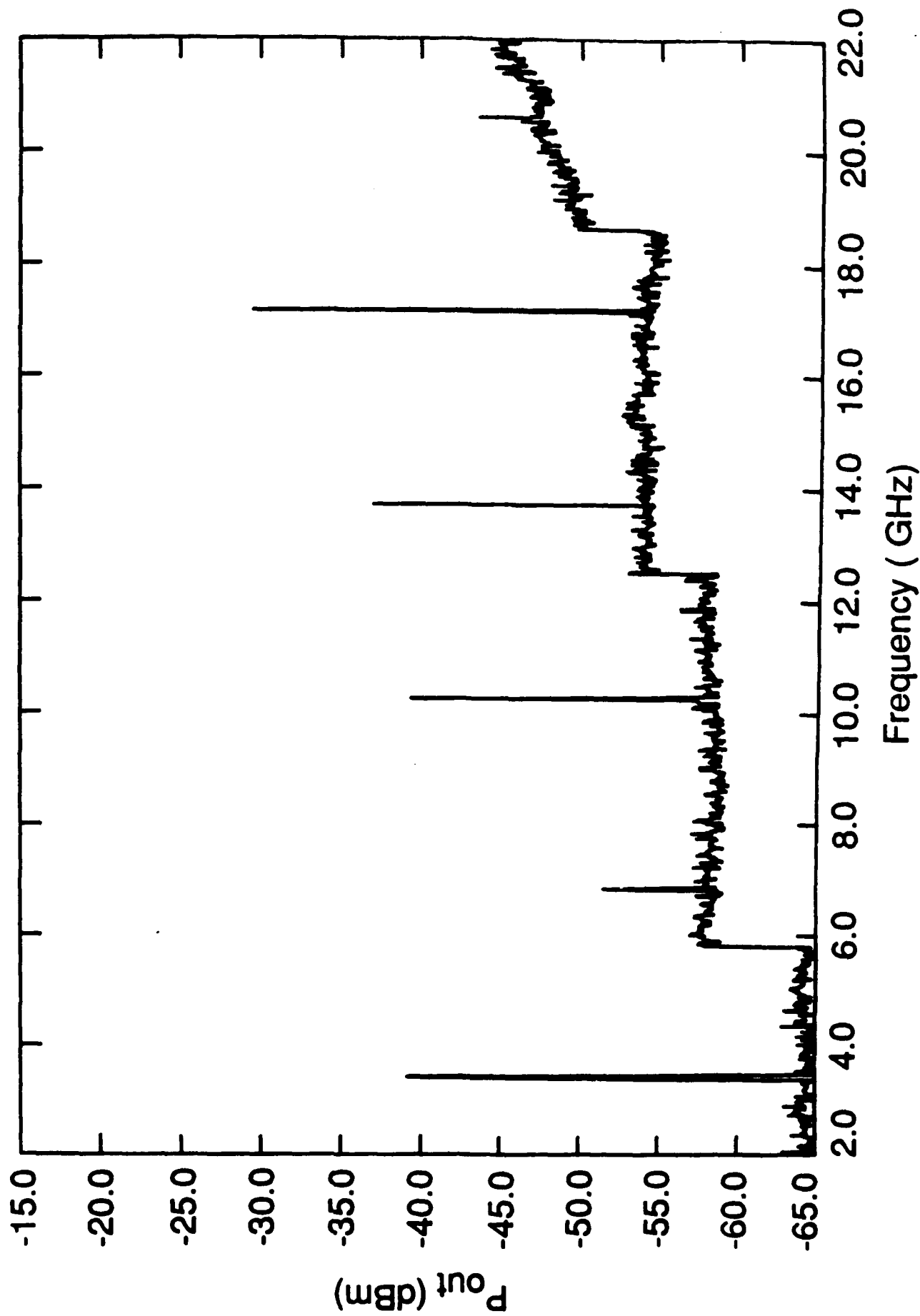


Fig. 7.36: Scaled model quintupler output with 3.432 GHz input

with the suppression reduced to 8 dB. The decrease in the conversion of the signal energy into its fifth harmonic resulted in a higher third harmonic at the high end of the band. Fig. 7.37 shows the results with an input frequency of 4.37 GHz. The third harmonic at 13.12 GHz is 1.0 dB higher than the desired fifth harmonic at 21.87 GHz and the fundamental is suppressed by less than 3.0 dB.

The degradation of the conversion efficiency of the scaled model frequency multiplier is due to several factors. The beam lead diode used is designed for doubler applications and becomes increasingly inefficient with higher order multiplications. In addition, the large signal input and output impedances of this device are different from the scaled impedance of the millimeter wave device. As a result, the input and output matching networks scaled from millimeter wave design do not provide an optimum match for the input driving signal and the output extracted signal. Since this is a nonlinear circuit, the matching network, or equivalently the source and load impedances to the nonlinear element, also change the diode large signal impedance from that under optimum matching condition.

The scaled model results, however, demonstrated the fifth harmonic generation with adequate suppression of undesired harmonics for part of the band. The scaled filters and matching networks on 25 mil Alumina were individually tested. The evaluation of these circuits indicated good correlation with the predicted results.

### **Probe Mechanical Design**

A probe holder was designed to be mounted on the wafer probe station. The input K-connector and DC feed-throughs are assembled on the probe body. The DC feed-throughs are glass-to-metal hermetic and have gold plated pins for connections to the substrate DC rails. DC biasing adjustments provide tuning capability to balance the currents through the antiparallel diode pairs. Two probe bodies were donated by Cascade Microtech Inc. which were modified for the active probe.

### **Millimeter wave active probe**

The W-band active probe circuit was designed incorporating the evaluation results of individual circuits, filters and matching networks, and the scaled model quintupler in the process. The circuit layout of the active probe, version 2, (AP5-2) is shown in Fig. 7.38. The ground plane at the probe tip is tapered to the typical ground pad size. The 50 ohm CPW line at the input is also tapered to match the diameter size of the inner conductor of the coaxial K-connector at the input. The DC bias lines on the substrate connect the DC feedthroughs assembled onto the probe body to the diodes.

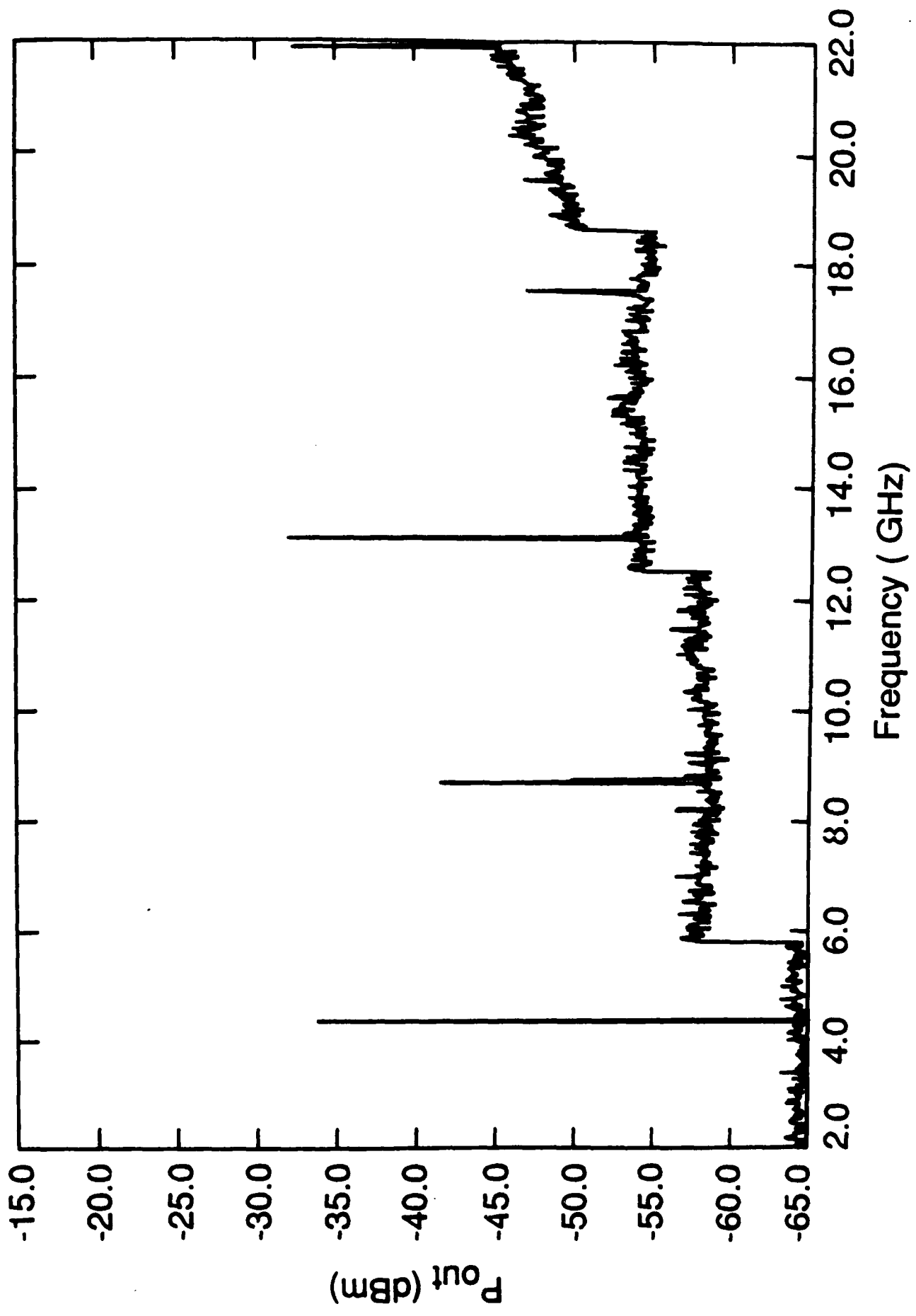


Fig. 7.37: Scaled model quintupler output with 4.374 GHz input

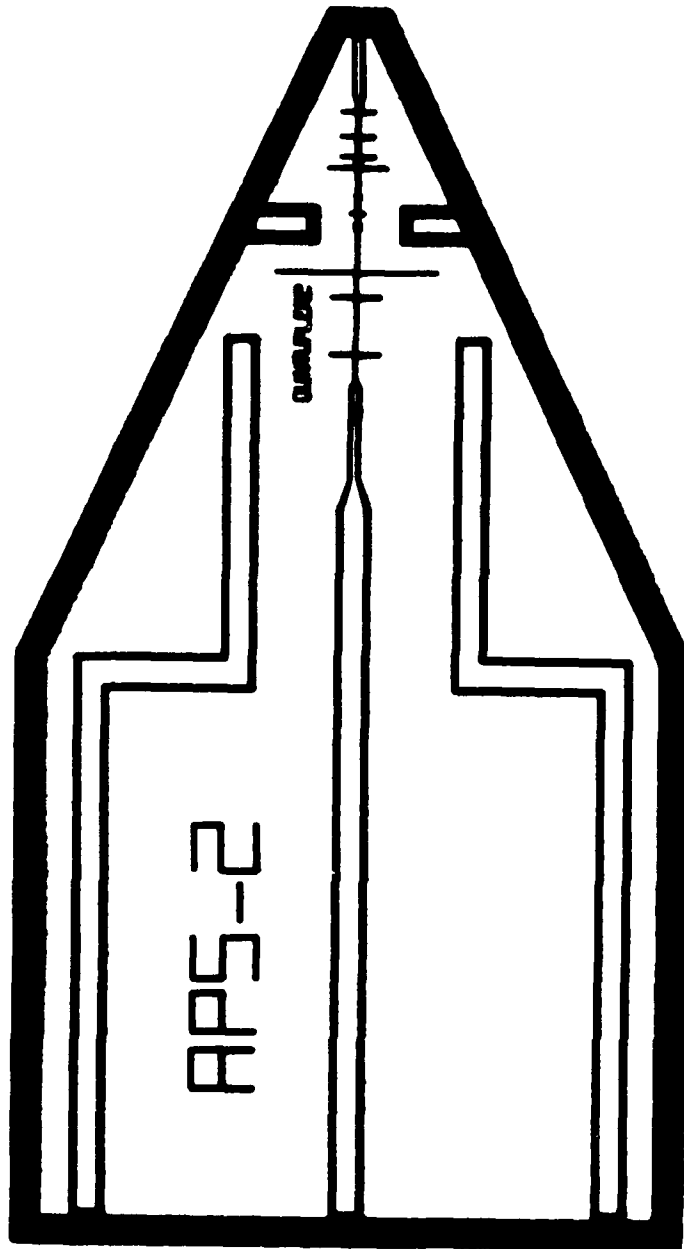
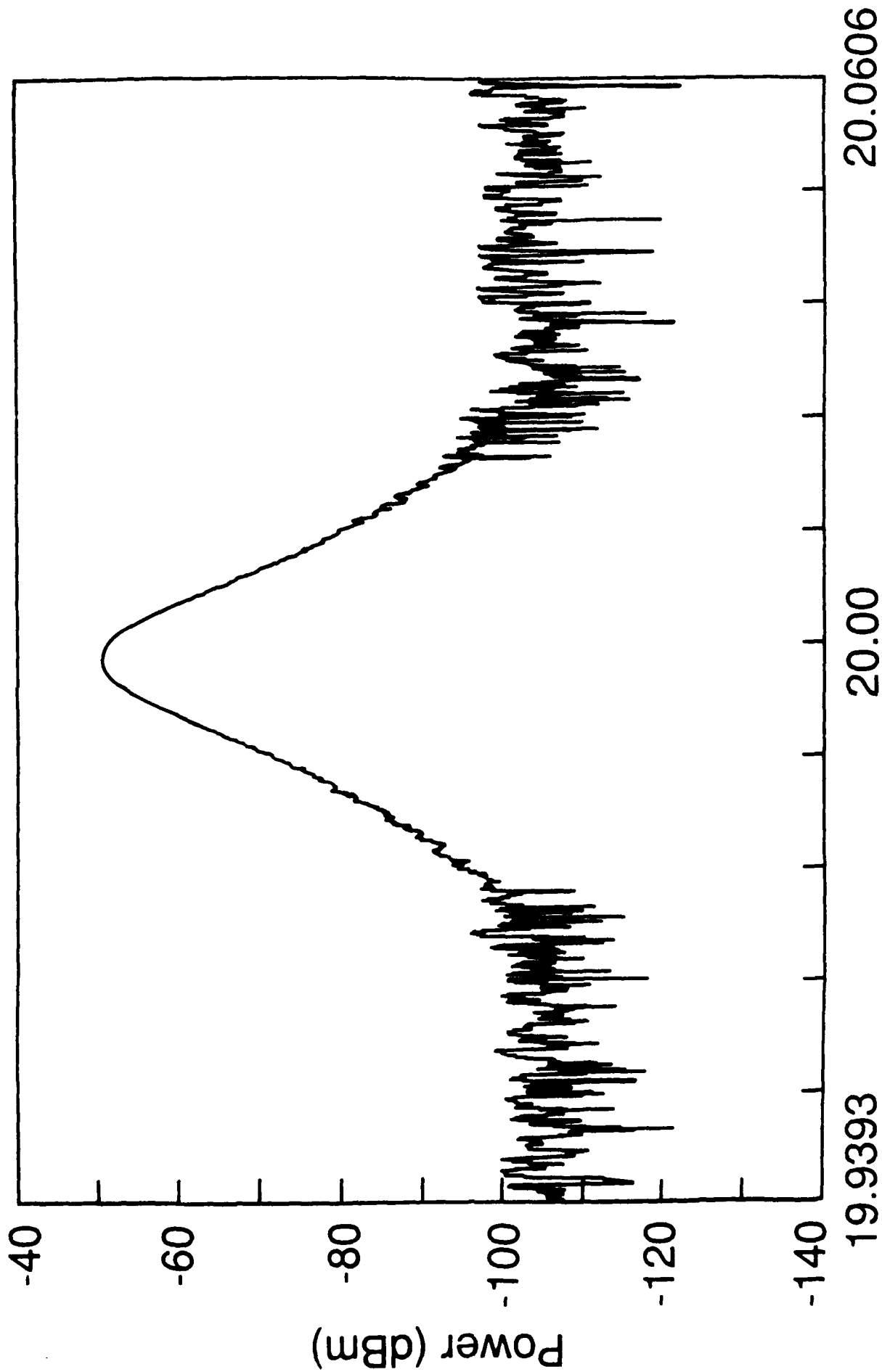


Fig. 7.38: Millimeter wave quintupler circuit layout

The probe circuits were fabricated on 5 mil thick Alumina using thin film techniques. The diodes, chip capacitors and chip resistors were then epoxied onto the substrate, gold bond wires were used to connect the ground planes and to make circuit connections, and the circuit was then epoxied onto the probe body. Gold ribbons were used to connect RF and DC feedthroughs to the circuit.

The same mask was also used to fabricate the circuits on GaAs. One quintupler was built, with same type of components used for the actual probe, on GaAs. The linear simulation of the filters and matching networks on a GaAs substrate indicated a slight decrease in the passband frequency due to the higher effective dielectric constant. The GaAs substrate permits diagnostic evaluation of the design through electrooptic sampling of the signal waveform and its harmonic content. The input microwave signal was supplied to the GaAs quintupler by a Cascade probe with the output of the circuit terminated in an open circuit. A spectrum analyzer was used to measure the voltage on the center conductor after electrooptic harmonic mixing. Fig. 7.39 shows the downconverted 20 GHz signal at the input of the quintupler, and Fig 7.40, the fifth harmonic (100 GHz) at the diode plane. The signal amplitude rapidly decreases as it propagates to the unterminated output. The testing of the GaAs quintupler as means of evaluating the W-band circuit is still continuing in conjunction with the evaluation of the W-band active probe.



### Frequency (GHz)

Fig. 7.39: GaAs quintupler input signal at 20GHz measured using electrooptic sampling and displayed on a spectrum analyzer (after frequency downconversion)

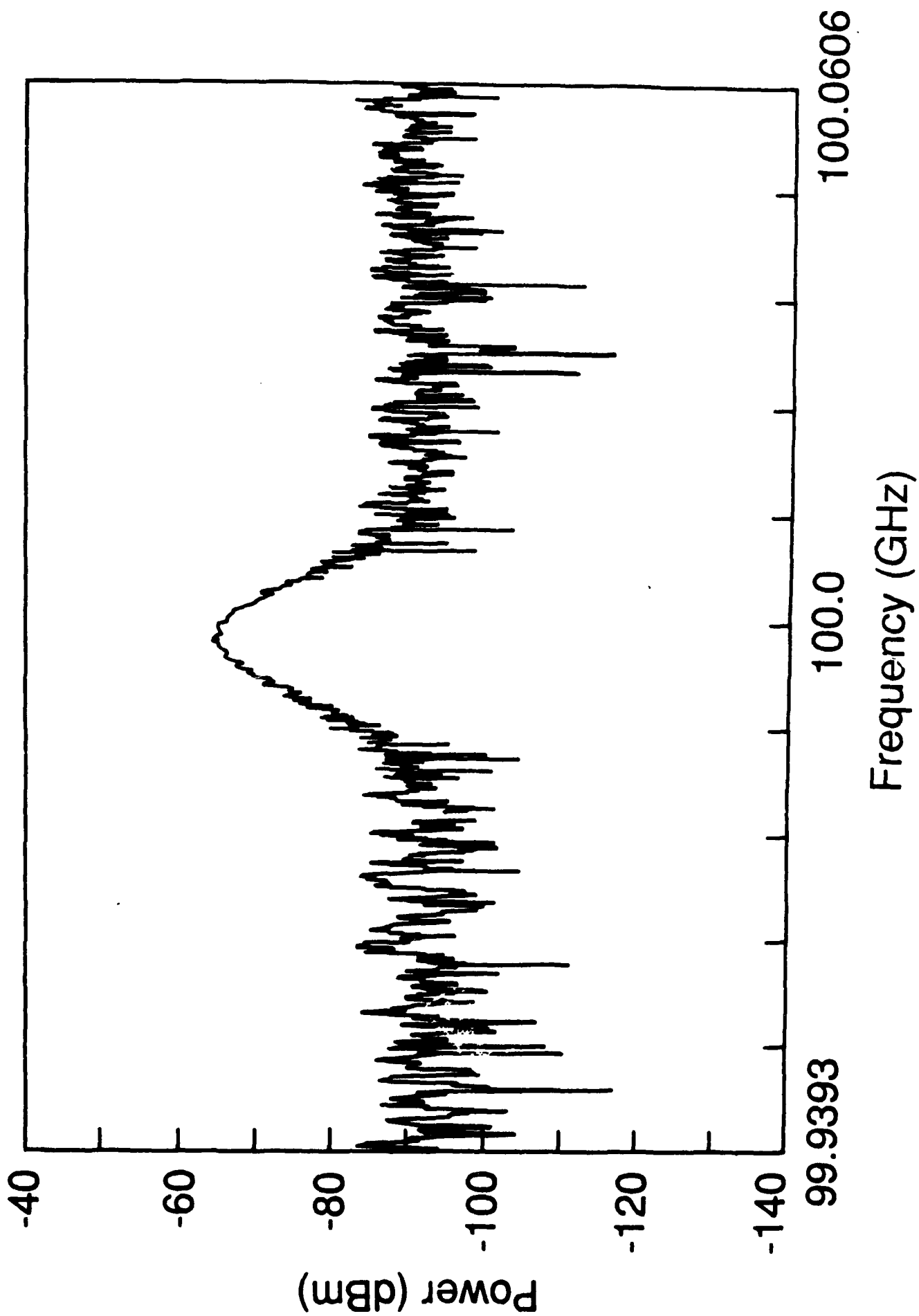


Fig. 7.40: GaAs quintupler output signal at 100 GHz measured using electrooptic sampling and displayed on a spectrum analyzer (after frequency downconversion)



## **7.4. Millimeter wave circuit measurements**

### **7.4.1. Standing wave measurements**

The 100 GHz signal generated in the GaAs quintupler described in section 7.3.2. was measured using electrooptic sampling. Fig. 7.41 shows the amplitude of the 100 GHz standing wave on the 50 ohm CPW of the GaAs quintupler. Since the signal amplitude is small, the amplitude fluctuations due to various noise mechanisms are significantly visible. The measured guide wavelength in GaAs was approximately 1.1 mm. This measurement demonstrated the feasibility of the application of the electrooptic sampler for millimeter wave circuit measurements at 100 GHz.

Standing waves have also been measured at 40 GHz where larger signals can be generated. These measurements used the standard Cascade probe, whose performance extends into the lower end of the millimeter wave band Fig. 7.42. shows the 40 GHz voltage standing wave on a CPW on GaAs terminated in open circuit. The calculated reflection coefficient, obtained as described in Section 6.1.2 and appendix III, is also shown.

### **7.4.2. CPW and Slot line Dispersion Characteristics**

The wavelength on a conductor can be directly measured, to characterize dispersion or measure the change in wavelength between different waveguide modes, such as the even and odd modes of CPW [7.6]. Since such information is critical to proper design of millimeter circuits like the active probe, the dispersion characteristics of slot line and even and odd modes of coplanar waveguide on semi-insulating GaAs substrate were investigated. The guide wavelength for each mode versus frequency was directly obtained from standing wave measurements by electrooptic sampling.

The guide wavelength of a 50 ohm CPW, with a center conductor width of 75 microns and gap spacings of 50 microns on a 500 microns thick GaAs substrate, was measured from 15 to 40 GHz in a single mode operation of the CPW, under odd and even mode excitations. The odd mode was excited by applying the signal to the center conductor and grounding the outer conductors with the results of Fig. 7.43. The same CPW was then excited in the even mode by applying two signals of equal amplitude and opposite phase to the outer conductors and grounding the center conductor with the results of Fig.7.44. Fig. 7.45 then shows the ratio of the free-space wavelength to guide wavelength versus

frequency for both modes. Note that the dispersion of the odd mode is significantly less than that of the even mode. Since the cutoff frequency of the lowest order quasi-slab model is 45 GHz, coupling to parasitic modes can be ignored in both cases. The standing wave measurements were repeated on a slot line of width 125 microns on a 500 microns thick GaAs substrate with the results of Fig. 7.46.

## 7.5. Summary

A wafer probe station suitable for electrooptic probing of microwave circuits has been developed and applied to the measurement of a variety of circuits. Extension of this probe station to the millimeter-wave region is possible through use of an on-probe frequency quintupler. Standing waves of the 100 GHz output of the quintupler and its harmonic content have been measured with the electrooptic sampling system. Further work is being pursued to complete the active probe.

## 7.6. References for Section 7

- 
- 7.1 R.E. Collins, *Foundations of Microwave Engineering*, New York: McGraw-Hill, 1966
  - 7.2 K.J. Weingarten, M.J.W. Rodwell, J.L. Freeman, S.K. Diamond, and D.M. Bloom, "Electrooptic sampling of gallium arsenide integrated circuits," *Ultrafast Phenomena V*, ed. by G.R. Fleming and A.E. Siegman, Springer Ser. Chem. Phys., Vol. 46, New York: Springer-Verlag, 1986, pp. 98
  - 7.3 M.J.W. Rodwell, M. Riazat, K.J. Weingarten, B.A. Auld, and D.M. Bloom, "Internal microwave propagation and distortion characteristics of travelling-wave amplifiers studied by electro-optic sampling," *IEEE Trans. Microwave Theory Tech.*, vol. MTT-34, pp. 1356-1362, 1986
  - 7.4 G. Zdasiuk, M. Riazat, R. LaRue, C. Yuen, and S. Bandy, "Enhanced performance ultrabroadband distributed amplifiers," *Picosecond Electronics and Optoelectronics*, New York: Springer-Verlag, 1987
  - 7.5 M.J.W. Rodwell, "Picosecond electrical wavefront generation and picosecond optoelectronic instrumentation," *Ph.D. Thesis*, Stanford University, Stanford, CA, 1987.
  - 7.6 R. Majidi-Ahy, K.J. Weingarten, M. Riazat, B.A. Auld, and D.M. Bloom, "Electrooptic sampling measurement of coplanar waveguide (coupled slot line) modes," *Elect. Lett.*, vol. 23, 1987

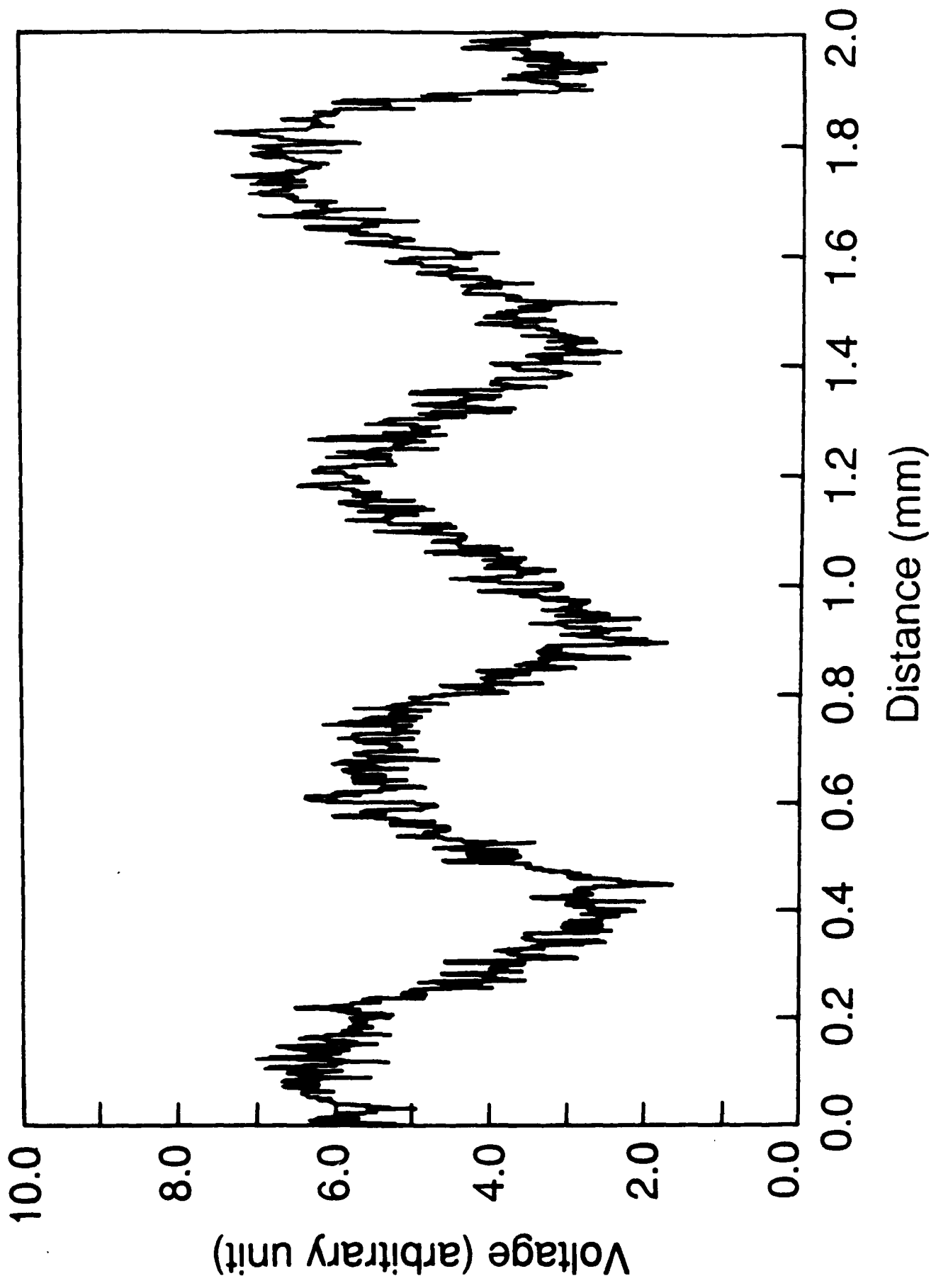


Fig. 7.41: 100 GHz standing wave measured using electrooptic sampling

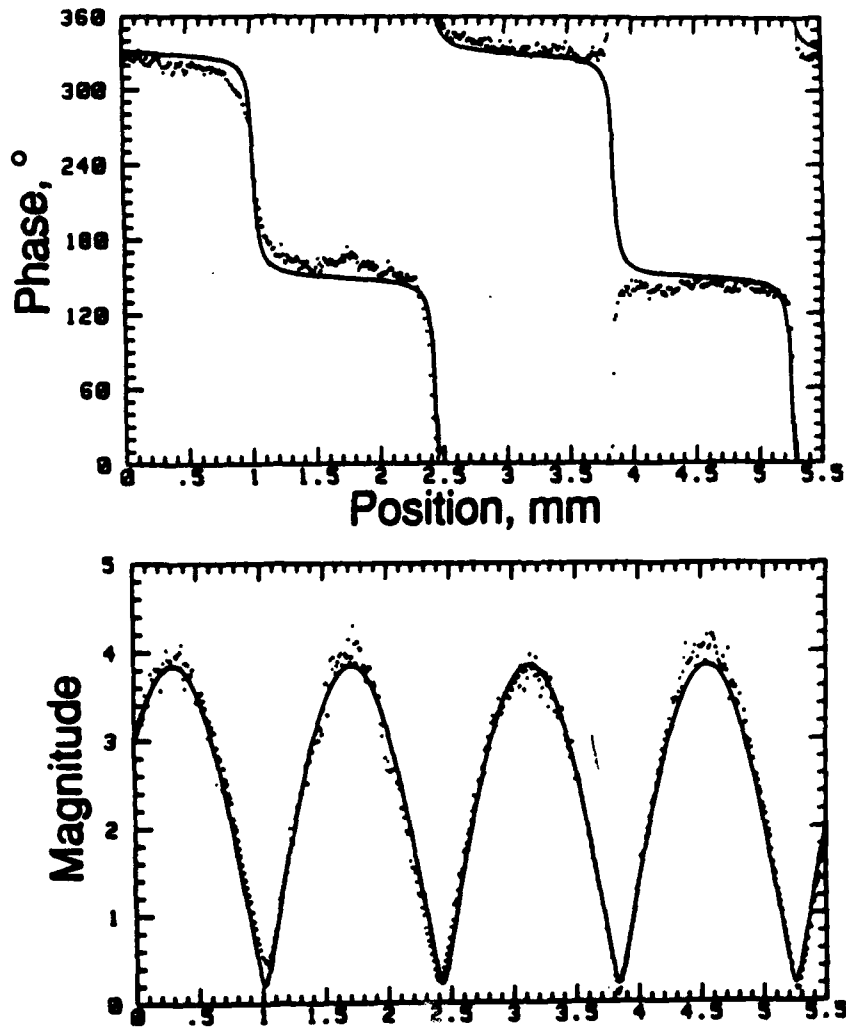


Fig.7.42. 40 GHz voltage standing wave on an open-terminated GaAs coplanar waveguide transmission line, magnitude (top) and phase (bottom). The points are the data and the solid line is the fitted curve. From this measurement a reflection coefficient of  $0.90 \angle -80^\circ$  is calculated. Note that each division of  $10^\circ$  in phase equals 0.7 ps in time.

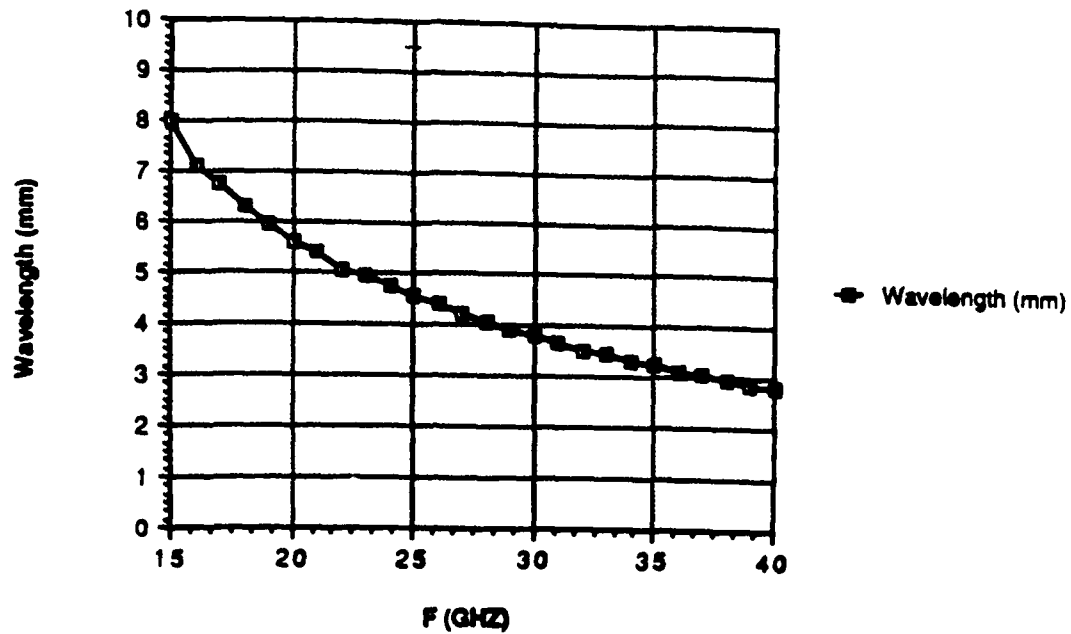


Fig.7.43. CPW odd mode dispersion characteristics

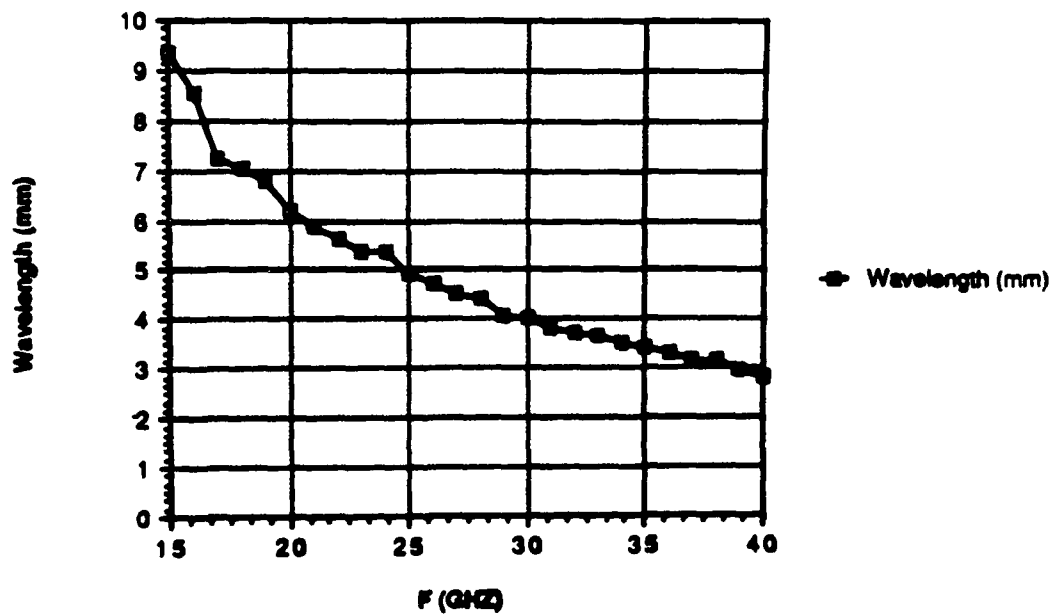


Fig.7.44. CPW even mode dispersion characteristics

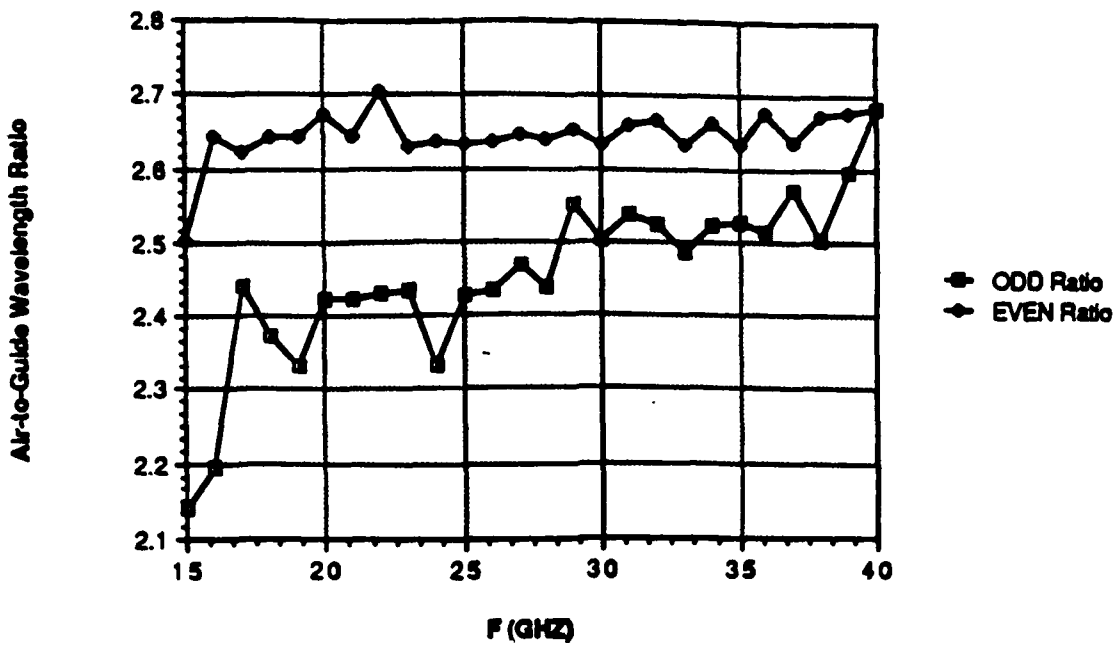


Fig.7.45. Free space-to-guide wavelength ratio vs. frequency for CPW even and odd mode

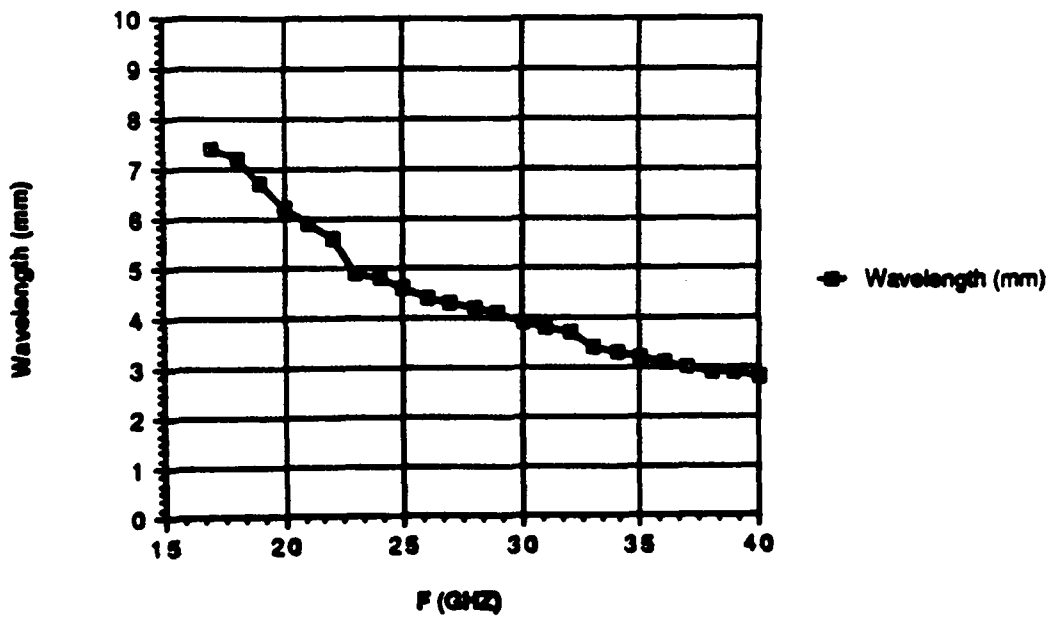


Fig.7.46. Slot line dispersion characteristics

## 8. Conclusion

The electrooptic sampler system has been both improved and evaluated. Below are summarized the work performed on each designated task, and the conclusion from this work.

### **Increase of Electrooptic Measurement Bandwidth**

Insertion of first one, and then a second new mode-locker has resulted in pulse with a full-width half-maximum of 1.25 ps, and a -3 dB point in the spectral domain of nearly 200 GHz. Short-term laser timing jitter has been reduced to below 250 femtoseconds through a refined timing stabilizer. Since the new mode-lockers yield significantly greater spectral spread in the pulse compressor that is not yet being fully recompressed, significantly shorter pulses are expected.

### **Improvements to Noise Performance**

Addition of the new mode-lockers together with insertion of a Faraday Isolator has dramatically reduced the laser amplitude noise. Since polarization-preserving fiber is very expensive, and of uncertain additional value, reduction of fiber noise has been pursued by active fiber temperature stabilization. Optical biasing through waveplate rotations is also used to reduce noise effects. Measurement repeatability with this system is good enough in testing of digital and microwave ICs that incorporation of differential and ratio detection has not yet been pursued.

### **Evaluation of Signal Crosstalk, Spatial Resolution**

Theoretical and experimental results indicate that the limiting factor in spatially resolving individual signals is the finite backplane potential. Spot-size and focused Gaussian beam effects are small in all but the most extreme cases. Ground to signal spacing is the dominant determinant of such backplane crosstalk, giving rise to error terms 20 to 30 dB down (10 % to 3%). Use of a conductive backside coating offers significant crosstalk reduction in structures where the impedance of surface transmission lines is not critical.

### **Voltage Calibration**

The excellent long-term and short-term amplitude stability of the laser system permits accurate comparisons of spatially distinct signals. A reference point is required for absolute signal calibration. Use of a backside conducting layer enhances calibration capability by

reducing error terms and by providing a baseline error beneath ground planes for subtraction.

### **Evaluation of the Invasiveness of Electrooptic Sampling**

The 1.06  $\mu\text{m}$  beam induces charge in the substrate predominantly by two-photon absorption above several milliwatts of optical power. The perturbation to MESFETs can be modeled as a negative gate bias that results in an increase in drain current. A DC component to this perturbation has a slow intensity falloff attributed to backgating through deep traps. Scattering of probe radiation from the tails of the Gaussian due to surface roughness at active devices then waveguides to distant devices through total internal reflection. Reduction of invasiveness except by lower optical powers and judicious choices of probe positioning has not yet been achieved.

### **Electrooptic Vector Measurements**

Electrooptic sampling may be accomplished in both vector and time modes. 1 or 2-port S-parameters may be derived from multi-position measurements of standing waves. Alternative modes for time measurements without signal chopping are being pursued.

### **Millimeter-wave Wafer Probing**

A microwave probe station donated by Cascade Microtech has been modified to accommodate backside electrooptic probing, and a second one similarly modified for Wright-Patterson Air Force Base. Extension of this station to millimeter-wave is still underway through completion of an on-probe frequency quintupler. This development has already resulted in generation of 100 GHz signals and measurement of standing waves at this frequency.



# Appendix I

## Laser Timing Stabilization System Design Considerations

Mode-locked laser systems, in conjunction with optical pulse compressors generate extremely short optical pulses, making these instruments attractive not only for electrooptic sampling, but also for time-resolved measurements of a variety of fast phenomena, including time-resolved carrier dynamics and electromagnetic transient measurements in semiconductors [A1.1,2], measurement of optical waveforms by optical sampling [A1.3], and time-resolved spectroscopy [A1.4]. In these experiments, the system under test is pumped (excited) by the pulsed laser and subsequently probe by a delayed portion of the same optical pulse; pulse timing fluctuations are therefore unimportant.

In electrooptic sampling, realistic test requirements for electronic circuits demand external electronic sources for circuit stimulation, and pump-probe techniques are inappropriate. In many experiments, laser pulse excitation of the system under test is either inconvenient or is an unrepresentative experimental condition. In electrooptic sampling, the integrated circuit under test is best excited by microwave sinusoids or digital data sequences (as appropriate) from external electronic oscillators. The timing fluctuations of the laser degrade the time resolution and introduce noise. For some stimulus-response laser experiments, it may be most desirable to excite the tested system with a pulse from one laser, and probe with a second laser having a different wavelength. Unless the two wavelengths are in an integer ratio (permitting synchronized pulse generation by optical harmonic generation) the two optical pulse trains must be generated by two separate laser systems. Again, the relative timing fluctuations of the two lasers will both degrade the time resolution and introduce noise.

The performance of a variety of vacuum electron devices, including free electron lasers and laser-excited klystrons, is improved by increasing the cathode electron flux. Increased electron fluxes can be attained by replacement of the thermionic cathode with a photosensitive cathode excited by intense optical pulses from a pulsed laser system. If so excited, the frequency stability of these vacuum devices will be degraded by the timing fluctuations of the laser photoexcitation source. In particular, stringent phase stability constraints [A1.5] must be placed upon the laser-excited klystrons now being developed for particle accelerators. Other potential applications appear to exist—initial publication of preliminary results of laser timing stabilization brought a number of reprint requests from researchers in the area of molecular and cellular biology.

### A1.1 Spectral Description of Amplitude and Timing Fluctuations

Fluctuations in mode-locked lasers include variations in both pulse intensity and pulse timing. These are random processes whose statistics are described by their power spectral densities. Before embarking on a description of the spectra of these random signals, first consider a single-frequency signal which is both amplitude-modulated and phase-modulated by small deterministic sinusoidal functions.

$$v_{am/pm}(t) = \left( 1 + N_c \cos \omega_m t + N_s \sin \omega_m t \right) \exp \left( j \left( \omega_l t + \theta_c \cos \omega_m t + \theta_s \sin \omega_m t \right) \right). \quad (A1.1)$$

If the modulations  $N_c$ ,  $N_s$ ,  $\theta_c$  and  $\theta_s$  are small, the Fourier transform  $V_{am/pm}(\omega)$  of  $v_{am/pm}(t)$  is then given by

$$V_{am/pm}(\omega) = 2\pi \left( \delta(\omega - \omega_l) + (C_a + C_p) \delta(\omega - \omega_l - \omega_m) + (C_a^* - C_p^*) \delta(\omega - \omega_l + \omega_m) \right), \quad (A1.2)$$

where

$$C_a = N_c/2 - jN_s/2 \quad C_p = \theta_s/2 + j\theta_c/2. \quad (A1.3)$$

The amplitude-modulation and phase-modulation of a signal can thus be determined from the Fourier spectrum. If the spectrum of a signal is given by

$$V_{am/pm}(\omega) = 2\pi \left( \delta(\omega - \omega_l) + C_u \delta(\omega - \omega_l - \omega_m) + C_l \delta(\omega - \omega_l + \omega_m) \right), \quad (A1.4)$$

where  $C_u, C_l \ll 1$ , then the time-domain signal has small amplitude and phase modulations, and is described by Eq. (A1.1). The amplitude and phase modulation indices are then given by

$$\begin{aligned} N_c &= \Re(C_u + C_l^*) & N_s &= \Im(C_u + C_l^*) \\ \theta_c &= \Im(C_u - C_l^*) & \theta_s &= \Re(C_u - C_l^*). \end{aligned} \quad (A1.5)$$

The symbols  $\Re(C)$  and  $\Im(C)$  denote the real and imaginary parts of a complex number  $C$ . Thus, the upper and lower sidebands  $C_u$  and  $C_l$  can be decomposed into phase and amplitude noise sidebands  $C_p$  and  $C_a$  by the relationships

$$C_a = \frac{C_u + C_l^*}{2} \quad C_p = \frac{C_u - C_l^*}{2}. \quad (A1.6)$$

These relationships will be used later to determine the magnitude of phase measurement errors occurring within a timing stabilization system.

The laser produces a train of pulses, not a single frequency, and the amplitude and phase modulations are random. The laser pulse train is approximated as a series of Gaussian pulses with timing and amplitude fluctuations as given by

$$P(t) = \bar{P}T \left(1 + N(t)\right) \times \sum_{n=-\infty}^{n=+\infty} \frac{1}{\sqrt{2\pi} \sigma_t} \exp\left(-\left(t - T_0 - nT_l - J(t)\right)^2 / 2\sigma_t^2\right), \quad (A1.7)$$

where  $P(t)$  is the laser intensity,  $\bar{P}$  is the beam's average intensity,  $T_l$  is the pulse repetition period,  $\sigma_t$  is the rms pulse duration,  $N(t)$  is the normalized pulse-intensity variation,  $J(t)$  is the timing fluctuation of the pulse train, and  $T_0$  is the static timing offset of the pulse train. The laser intensity then has a power spectral density  $S_P(\omega)$  approximated to second order in  $n\omega_l\sigma_J$  by

$$S_P(\omega) \simeq \bar{P}^2 e^{-\omega^2 \sigma_t^2} \sum_{n=-\infty}^{n=+\infty} \left( (1 - n^2 \omega_l^2 \sigma_J^2) 2\pi \delta(\omega - n\omega_l) \right. \\ \left. + (1 - n^2 \omega_l^2 \sigma_J^2) S_N(\omega - n\omega_l) \right. \\ \left. + n^2 \omega_l^2 S_J(\omega - n\omega_l) \right), \quad (A1.8)$$

where  $\sigma_J$  is the standard deviation of  $J(t)$  (i.e. the rms timing jitter),  $\omega_l = 2\pi/T_l$ ,  $S_N(\omega)$  is the power spectral density of  $N(t)$ , and  $S_J(\omega)$  is the power spectral density of  $J(t)$ .

Thus, the spectrum of the laser intensity is a series of lines at multiples of  $\omega_l$  plus spectra associated with timing and amplitude fluctuations, referred to as amplitude noise sidebands [ $S_N(\omega - n\omega_l)$ ] and phase noise sidebands [ $n^2 \omega_l^2 S_J(\omega - n\omega_l)$ ]. The jitter attenuates the pulse train's spectrum at high frequencies, as indicated by the  $(1 - n^2 \omega_l^2 \sigma_J^2)$  term, and degrades the rms time resolution  $\sigma_{\text{experiment}}$  of probing experiments:

$$\sigma_{\text{experiment}} = \sqrt{\sigma_t^2 + \sigma_J^2}. \quad (A1.9)$$

The phase-noise sidebands represent random fluctuations in the phase of the frequency components of the laser pulse train; in probing experiments using a pulsed laser imperfectly synchronized to a second source, the jitter introduces noise proportional to the time derivative of the experimental response. These phase-noise sidebands, having power proportional to  $n^2$ , predominate for harmonics of moderate order; at higher harmonics the expansion is inaccurate both because of higher-order terms in  $n\omega_l\sigma_J$  and because of spectral terms associated with pulse-width fluctuations. Monitoring the laser with a photodiode and a spectrum analyzer, and measuring the relative powers of the laser harmonic and its associated sidebands at some harmonic of moderate order,  $S_J(\omega)$  can be inferred. The total jitter can then be found:

$$\sigma_J = \sqrt{\frac{1}{2\pi} \int_{-\infty}^{+\infty} S_J(\omega) d\omega}. \quad (A1.10)$$

Spectrum analyzers display the spectra of random signals as the noise power integrated over the analyzer resolution bandwidth. Radio-frequency spectrum analyzers use mixers, filters, and envelope detectors to determine a signal's spectrum, and consequently show small differences in calibration between measurements of deterministic and random signals. Correction factors associated with the difference between spectral densities expressed as a function of Hertz, rather than as a function of radian frequency, resolution bandwidths expressed by half-power bandwidth rather than by equivalent noise bandwidth, and noise measurement by noise envelope detection rather than by noise power detection must be included [A1.6]. Characteristics and methods of measurement of phase noise are discussed in Robbins [A1.6] and in two application notes from Hewlett-Packard [A1.7,8].

The phase noise of several Nd:YAG lasers have been tested, and from this jitter (at rates of 50 Hz and above) in the range of 0.75-10 ps has been determined. Figures A1.1 and A1.2 show the measured phase noise on the 70<sup>th</sup> harmonic of the 70 MHz pulse repetition rate of a Coherent, co. mode-locked ND:YAG laser. The phase-noise measurements were not digitally stored (the figures are hand tracings of the original data) and the phase noise thus could not be numerically integrated to determine the jitter. A  $\sim$  0.75 ps rms timing jitter in the 50 Hz-5kHz frequency range is estimated.

## **A1.2 Timing Stabilization by Feedback**

The pulse-timing fluctuations of a mode-locked Nd:YAG laser can be reduced by a phase-lock-loop feedback system, as first demonstrated by Cotter [A1.9] (Fig. A1.3). A photodiode monitors the laser pulse train, and the phase of its fundamental component is compared to that of a very stable reference oscillator, generating a phase error signal. The signal driving the mode-locking acousto-optic (A-O) cell, whose frequency is half the laser pulse repetition frequency, is generated by frequency division from the reference oscillator; its timing (phase) is adjusted with a voltage-controlled phase shifter driven by the amplified and filtered (frequency-compensated) phase error signal. Given an error-free phase detector and a stable feedback loop with high loop transmission, the loop continuously adjusts the phase of the laser pulse train to equal the phase of the reference oscillator, suppressing the laser timing fluctuations. Jitter suppression is limited by spurious outputs from the phase detector, by the phase noise of the reference oscillator, and by the limited loop gain and limited loop bandwidth attainable in a stable, well-damped feedback control system.

Spurious outputs from the phase detector include both additive noise from the various electronic components in the feedback system, and inadvertent detection of amplitude noise by the phase detector. Because of the similarity of the latter problem to well-studied amplitude-noise sensitivity effects in phase-modulation and frequency-modulation radio systems [A1.10], amplitude noise sensitivity can be referred to as AM-PM conversion.

### **A1.2.1 AM-PM conversion by phase detector DC offset.**

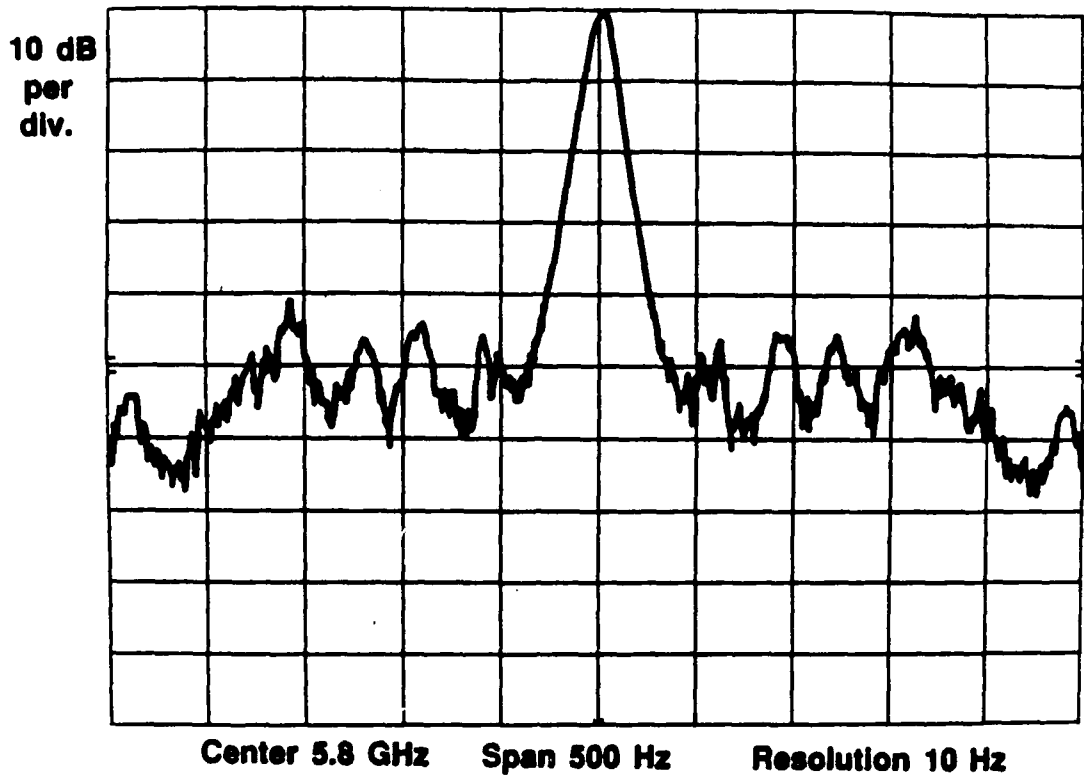
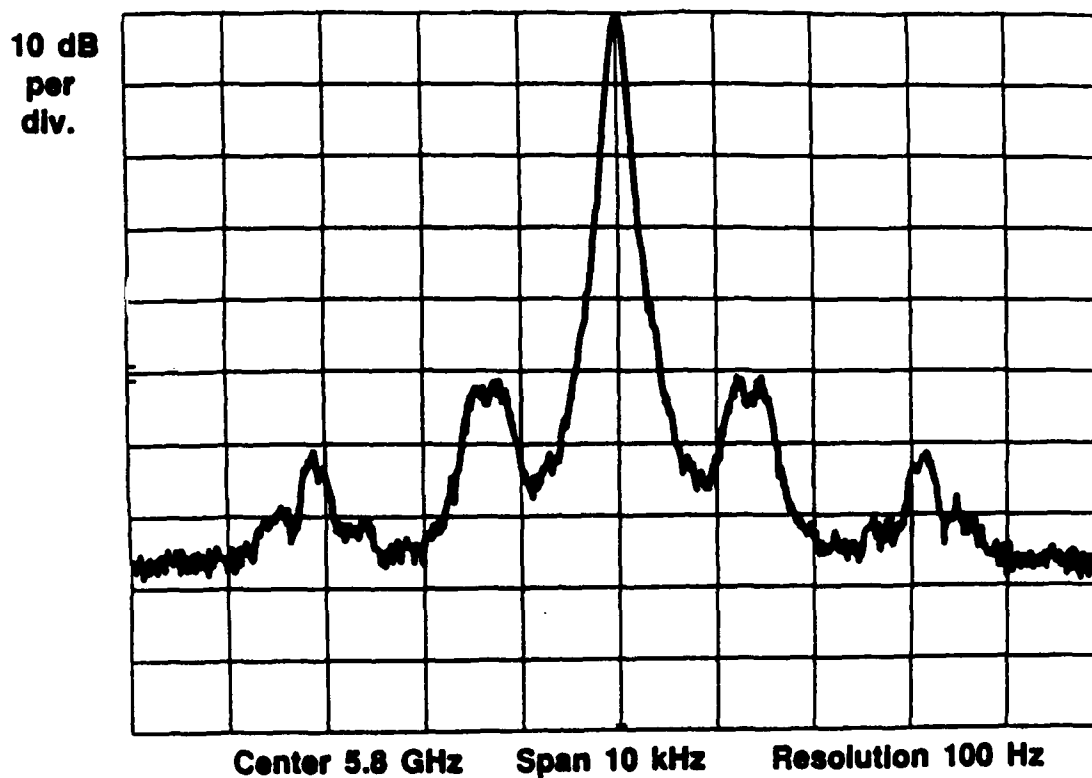


Figure A1.1: Phase noise sidebands, 50-250 Hz, on the 70<sup>th</sup> harmonic of the 70 MHz laser pulse repetition rate; Coherent Antares mode-locked Nd:YAG laser.



**Figure A1.2:** Phase noise sidebands, 500 Hz–5 kHz, on the 70<sup>th</sup> harmonic of the 70 MHz laser pulse repetition rate. Coherent Antares laser.

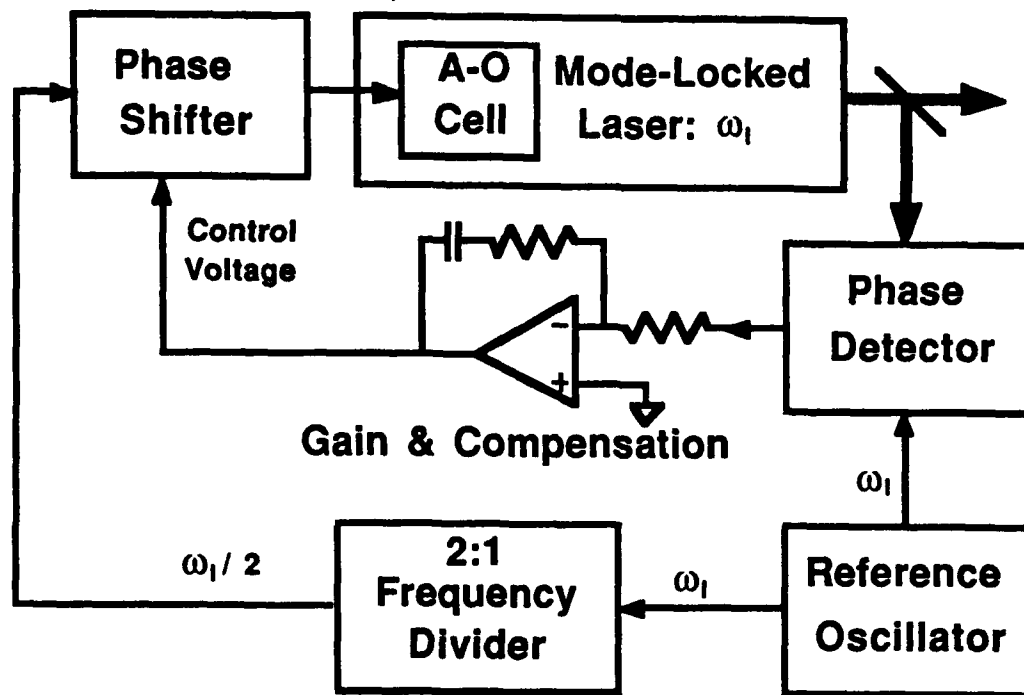


Figure A1.3: Phase-lock-loop laser timing stabilization.

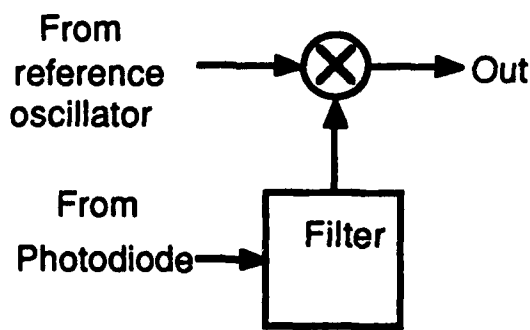


Figure A1.4: Simple phase detector using a double-balanced mixer. The filter passes only the fundamental component at  $\omega_1$  of the laser pulse train.

Radio-frequency phase detection is usually performed using a double-balanced mixer to form the product of the reference signal and the signal of unknown phase (Fig. A1.4). The multiplier output then contains terms both at DC and at twice the signal frequency; the latter terms are removed by loss-pass filtering. The output voltage of a multiplier (double balanced mixer) is then a function of both laser phase and amplitude,

$$V_{\text{detector}} = k_{\theta} \bar{P} [1 + N(t)] \sin(\theta) + V_{os} , \quad (\text{A1.11})$$

where  $\theta = 2\pi[T_0 + J(t)]/T$  is the phase difference (for convenience, a constant phase factor of  $\pi/2$  has been dropped) and  $V_{os}$  is the DC offset voltage of the phase detector arising from imbalances in the diodes and transformers [A1.11]. The phase detector slope coefficient can be related to the mixers' RF-IF conversion efficiency  $A_{M1}$  (here in units of Volts/Volt) by  $k_{\theta} \bar{P} = A_{M1} V_{in}$ . The peak voltage  $V_{in}$  of the sinusoidal input voltage is in turn given by  $V_{in} = A_{A1} \sqrt{2P_{\text{detector}} Z_0}$ , where  $A_{A1}$  is the voltage gain of amplifier A1 and  $P_{\text{detector}}$  is the power of the fundamental component of the photodiode output, as measured in a system with impedance  $Z_0$ . The impedance  $Z_0$  is usually 50  $\Omega$ . The quantity  $\sqrt{2P_{\text{detector}} Z_0}$  is the peak voltage of the sinusoidal fundamental component of the photodiode signal.

For small  $\theta$ , the detector output is approximately

$$V_{\text{detector}} \simeq k \bar{P} \left( [1 + N(t)] T_0 + J(t) \right) + V_{os} , \quad (\text{A1.12})$$

where  $k = 2\pi k_{\theta}/T$ . The terms in  $N(t)$  in the above equation result in sensitivity of the timing stabilization system to laser amplitude noise. To assess this effect, assume that we have an ideal (unrealizable) feedback loop having unbounded loop gain at all frequencies. The detector output is then forced to zero, and the laser timing becomes

$$\begin{aligned} T_0 &= -V_{os}/k\bar{P} \\ J(t) &= T_0 N(t) . \end{aligned} \quad (\text{A1.13})$$

Thus, in addition to causing timing drift with changes in mixer offset ( $T_0 = -V_{os}/k\bar{P}$ ), the DC offset results in first-order variation in the phase detector output with laser amplitude fluctuations, thus producing residual closed-loop timing jitter.

An improved phase detector (Fig. A1.5) suppresses the effect of the mixer offset by increasing the slope coefficient  $k$  of the detector. The technique is similar to that of chopper-stabilized DC amplifiers and synchronous ("lock-in") signal detectors. The reference oscillator output is multiplied in a double-balanced-mixer by a squarewave chopping signal whose frequency is  $\omega_{IF}$ . After narrowband filtration to remove spurious mixer outputs, the resulting reference signal is then a sinewave at the laser repetition frequency  $\omega_l$  whose phase is inverted  $+180^\circ / -0^\circ$  at the chopping rate  $\omega_{IF}$ . The fundamental component at  $\omega_l$  of the photodiode signal is passed to a second mixer, in which the laser phase is compared to that of the phase-modulated reference signal. The output of the second mixer is then a spurious DC offset voltage  $V_{os,2}$ , plus a squarewave at frequency  $\omega_{IF}$  whose amplitude varies as the phase difference of the photodiode and reference signals. The squarewave is bandpass filtered, removing both the spurious  $V_{os}$  and components at harmonics of  $\omega_l$ , and amplified by some large gain  $A_{A2}$  on the order of 20-40 dB. The phase error signal, now a sinewave, is synchronously detected by a third double-balanced mixer, producing an output voltage proportional to the laser phase. As with the simple phase detector, the chopper-stabilized detector has sensitivity to laser amplitude fluctuations and has a DC offset  $V'_{os}$  arising from the third mixer:



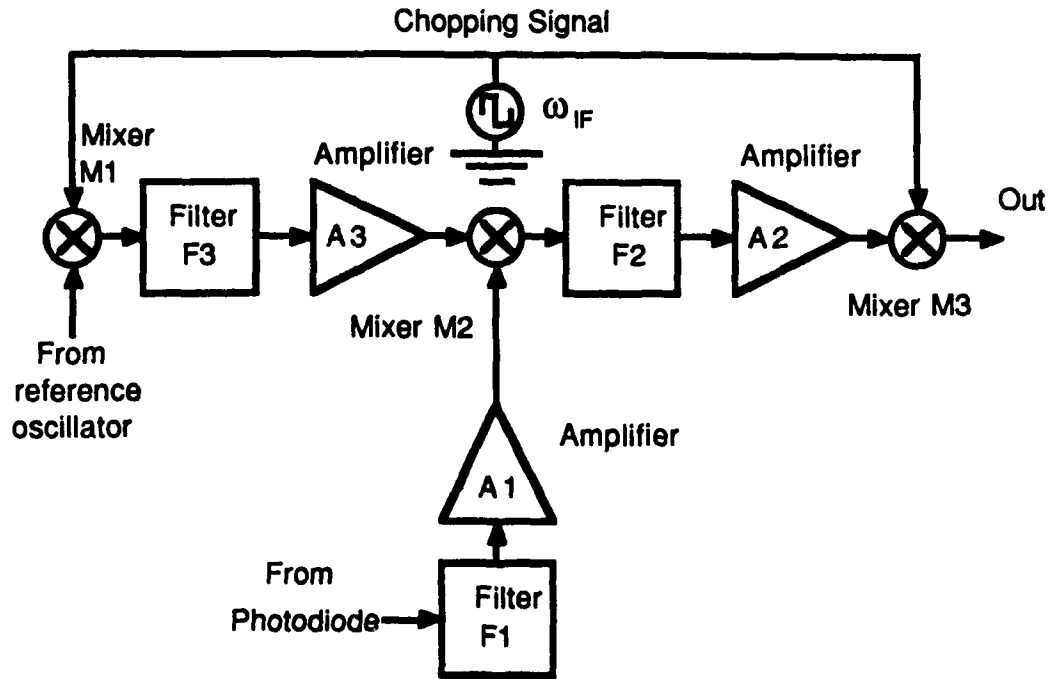


**Figure A1.5:** Chopper-stabilized phase detector. See text for description of operation. F3 is a filter with passband  $\sim \omega_l \pm 5\omega_{IF}$ , F1 is a filter with passband  $\sim \omega_l \pm \omega_l/2$ , and F2 is a filter with passband  $\sim \omega_{IF} \pm \omega_{IF}/2$ .

$$V'_{detector} \simeq k' \bar{P} \left( [1 + N(t)] T_0 + J(t) \right) + V'_{os} . \quad (A1.14)$$

In the chopper-stabilized detector, the phase-detector gain coefficient is given by

$$k' = \sqrt{2P_{detector} Z_0} A_{A1} (\omega_l) A_{M2} A_{A2} \left( \frac{8}{\pi^2} \right) A_{M2} , \quad (A1.15)$$

where  $A_{A2}$  is the voltage gain of amplifier A2 and  $A_{M2}$  is the RF-IF conversion loss (in units of Volts/Volts) of mixer M2. The factor of  $\omega_l$  results from the conversion from phase sensitivity coefficient to timing sensitivity coefficient, and the factor of  $8/\pi^2$  is a consequence of chopping with a square-wave signal but subsequently synchronously detecting only its sinusoidal fundamental component. With the chopper-stabilized phase detector, DC offset will result in timing offset and timing jitter given by

$$\begin{aligned} T'_0 &= -V_{os,M3}/k' \bar{P} \\ J(t) &= T'_0 N(t) , \end{aligned} \quad (A1.16)$$

where  $V_{os,M3}$  is the DC offset voltage of mixer M3. Amplitude-noise to phase noise conversion through nonlinear terms in the operation of mixer M2 place upper bounds

on  $\sqrt{2P_{\text{detector}}Z_0} A_{A1}$ , and thus the chopper-stabilized phase detector permits a phase-detector sensitivity  $k'$  several orders of magnitude larger than with a simple phase detector; the effect of DC offset is proportionately reduced.

With the continued assumption of infinite loop gain, the spectral density  $S_{J,os}(\omega)$  of spurious timing fluctuations resulting from detector DC offset will be

$$S_{J,os}(\omega) = T_0^2 S_N(\omega) . \quad (A1.17)$$

### A1.2.2 AM-PM conversion through device saturation

The simplest method of attaining large phase detector sensitivity is to provide large input signal levels to the detector. Problems with DC offsets are reduced, as are the effects of additive noise voltages and currents within the feedback loop. Above some power level, nonlinear effects within both the amplifiers processing the 82 MHz photodiode signal and the mixer used for phase detection will result in AM-PM conversion.

The response of a weakly nonlinear system can be described in the time domain by a Volterra series expansion [A1.10]:

$$\begin{aligned} v_{\text{out}}(t) &= \sum_{n=1}^{n=+\infty} \left( \int \int \cdots \int h_n(\tau_1, \tau_2, \dots, \tau_n) \prod_{i=1}^{i=n} v_{\text{in}}(t - \tau_i) d\tau_i \right) \\ &= \sum_{n=1}^{n=+\infty} v_{\text{out},n}(t) . \end{aligned} \quad (A1.18)$$

Denoting a series of n-dimensional Fourier transforms:

$$V_{\text{out}}(\omega) = \int v_{\text{out}}(t) e^{-j\omega t} dt ,$$

$$V_{\text{out},n}(\omega) = \int v_{\text{out},n}(t) e^{-j\omega t} dt ,$$

$$V_{\text{in}}(\omega) = \int v_{\text{in}}(t) e^{-j\omega t} dt ,$$

$$h_n(\tau_1, \tau_2, \dots, \tau_n) = \frac{1}{(2\pi)^n} \int \int \cdots \int H(\Omega_1, \Omega_2, \dots, \Omega_n) \left( \prod_{i=1}^{i=n} e^{j\Omega_i \tau_i} d\Omega_i \right) ,$$

the Fourier transform  $V_{\text{out}}(\omega)$  of the output voltage can be written as

$$V_{\text{out}}(\omega) = \sum_{n=1}^{n=+\infty} V_{\text{out},n}(\omega) \quad (A1.19)$$

where

$$\begin{aligned}
 V_{out,n}(\omega) = & \frac{1}{(2\pi)^{n-1}} \int \int \cdots \int H(\Omega_1, \Omega_2, \dots, \Omega_{n-1}, \omega - \sum_{i=1}^{i=n-1} \Omega_i) \\
 & V_{in}(\Omega_1) V_{in}(\Omega_2) \cdots V_{in}(\Omega_{n-1}) V_{in}(\omega - \sum_{i=1}^{i=n-1} \Omega_i) \\
 & d\Omega_1 d\Omega_2 \cdots d\Omega_{n-1} .
 \end{aligned} \tag{A1.20}$$

If  $v_{in}(t)$  is small (and this is required in order to have adequately small AM-PM conversion), the series can be truncated to third order with sufficient accuracy. Further, the second-order term results in nonlinear responses at DC and twice the input frequency; as these will be outside of the bandwidth of various filters within the system, their effect can be neglected. The nonlinear response of amplifiers and mixers within the timing stabilizer is then modeled in the frequency domain as

$$\begin{aligned}
 V_{out}(\omega) \simeq & H_1(\omega) V_{in}(\omega) \\
 & + \frac{1}{4\pi^2} \int \int_{-\infty}^{+\infty} H_3(\Omega_1, \Omega_2, \omega - \Omega_1 - \Omega_2) \\
 & V_{in}(\Omega_1) V_{in}(\Omega_2) V_{in}(\omega - \Omega_1 - \Omega_2) d\Omega_1 d\Omega_2 .
 \end{aligned} \tag{A1.21}$$

For a system with general third-order nonlinearities, the above equation cannot be further reduced. For the case of an input signal at  $\omega_l$  with narrowband amplitude modulation (i.e.  $\omega_m \ll \omega_l$ ) the terms  $H_1$  and  $H_3$  vary little over the frequency range from  $(\omega_l - \omega_m)$  to  $(\omega_l + \omega_m)$  and

$$H_1(\pm\omega_l \pm \omega_m) \simeq H_1(\pm\omega_l)$$

$$H_3(\pm\omega_l \pm \omega_m, \pm\omega_l \pm \omega_m, \pm\omega_l \pm \omega_m) \simeq H_3(\pm\omega_l, \pm\omega_l, \pm\omega_l) . \tag{A1.22}$$

Symmetries in its definition require that  $H_3(\alpha, \beta, \gamma)$  be invariant with permutations in the order of  $(\alpha, \beta, \gamma)$ ; we can thus denote:

$$H_3(\omega_l) = H_3(\omega_l, \omega_l, -\omega_l) \text{ and all permutations}$$

$$H_3(-\omega_l) = H_3(-\omega_l, -\omega_l, \omega_l) \text{ and all permutations}$$

Finally,  $H_3(-\omega_l) = H_3^*(\omega_l)$  and  $H_1(-\omega_l) = H_1^*(\omega_l)$  are required for systems with real response. For compactness, we will write  $H_3 = H_3(\omega_l)$  and  $H_1 = H_1(\omega_l)$ .

Consider the response of a third-order nonlinear system to an amplitude-modulated signal  $v_{in}(t)$

$$v_{in}(t) = v_0 (1 + N_C \cos \omega_m t) \cos \omega_l t \tag{A1.23}$$

The Fourier transform of  $v_{in}(t)$  is

$$\begin{aligned}
 V_{in}(\omega) = & \pi v_0 \left( \delta(\omega - \omega_l) + \delta(\omega + \omega_l) \right) \\
 & + \frac{\pi v_0 N_c}{2} \left( \delta(\omega - \omega_l - \omega_m) + \delta(\omega - \omega_l + \omega_m) \right) \\
 & + \frac{\pi v_0 N_c}{2} \left( \delta(\omega + \omega_l - \omega_m) + \delta(\omega + \omega_l + \omega_m) \right) .
 \end{aligned} \tag{A1.24}$$

Substitution of Eq. (A1.24) into (A1.21) and calculation of the resulting phase modulation from the phase of the spurious third-order products using Eq. (A1.5) shows that the output voltage  $v_{out}(t)$  is phase-modulated by  $\theta_c \cos \omega_m t$ , where

$$\frac{\theta_c}{N_c} = \frac{9}{4} v_0^2 \Im \left( \frac{H_3}{H_1} \right) . \tag{A1.25}$$

The AM-PM conversion factor  $\Im(H_3/H_1)$  is rarely specified for an electronic component. An upper bound can be found given knowledge of the commonly-specified (input-referred) two-tone third-order intercept power  $P_{3oi}$ . This is

$$P_{3oi} = \left\| \frac{H_1}{H_3} \right\| \frac{2}{3Z_0} , \tag{A1.26}$$

where  $Z_0$  is the system impedance, usually  $50\Omega$ . The spurious phase modulation can thus be bounded by

$$\left\| \frac{\theta_c}{N_c} \right\| \leq \frac{9v_0^2}{4} \left\| \frac{H_3}{H_1} \right\| = \frac{3v_0^2}{2P_{3oi}Z_0} . \tag{A1.27}$$

The spurious phase modulation occurring in any components processing the photodiode signal prior to phase detection will result in an erroneous phase error signal at the output of the phase detector. With the approximation of large loop gain, the output of the phase detector will be again forced to zero, and residual timing fluctuations will thus result from AM-PM conversion in the phase detector. If the power spectral density of the residual closed-loop timing jitter due to AM-PM conversion through 3<sup>rd</sup>-order nonlinearities is denoted as  $S_{J,3o}(\omega)$ , it is found that

$$S_{J,3o}(\omega) \leq \frac{9}{\omega_l^2} \left( \frac{P_{carrier}}{P_{3oi}} \right)^2 S_N(\omega) , \tag{A1.28}$$

where  $P_{carrier} = v_0^2/2Z_0$  is the signal power at the frequency  $\omega_l$  input to the device under consideration.

### A1.2.3 Additive noise in the phase detection system

For timing jitter below  $\sim 1$  ps with a laser whose repetition rate is  $\sim 100$  MHz, the phase noise sidebands will have very low power. For those components which process the

photodiode signal prior to phase detection, the component's additive noise will result in spurious signal sidebands. From the analysis of Section A1.1, these additive sidebands can be decomposed into spurious phase-noise and amplitude-noise sidebands of equal power; the additive noise for these components thus results in a spurious output at the phase detector. The equivalent input noise power of the components processing the pre-phase-detection photodiode signal (i.e. amplifier A1 and mixer M2) is

$$S_{RF}(\omega) = \frac{kT}{2} \left( F_{A1} + \frac{F_{M2} - 1}{A_{A1}^2} \right), \quad (A1.29)$$

where  $F_{A1}$  and  $F_{M2}$  are the noise figures of the amplifier and the mixer. The thermal noise spectral density is  $kT/2$  rather than  $kT$  because we are using two-sided spectral densities with frequency in the units of radians/second. With large loop transmission, these noise terms will result in a residual closed-loop timing jitter with spectral density

$$S_{J,RF}(\omega) = \frac{S_{RF}(\omega - \omega_I)}{\omega_I^2 P_{photodiode}}. \quad (A1.30)$$

Components with low noise figures must be used, and the signal levels should be as high as permitted by the limits imposed by third-order nonlinearities.

At the input to the amplifier chain following the phase-detector M2, the phase error signal is in the form of the amplitude of a sinewave at the chopping frequency:

$$v(t) = \sqrt{2Z_0} \alpha J(t) \sin \omega_{IF} t, \quad (A1.31)$$

where

$$\sqrt{2Z_0} \alpha = \sqrt{2P_{photodiode} Z_0} A_{A1} A_{M1} \omega_I \frac{4}{\pi}, \quad (A1.32)$$

and  $\omega_{IF}$  is the chopping (synchronous detection) frequency. The equivalent input noise power of the chopping-frequency (intermediate-frequency) components (amplifier A2 and mixer M3) is

$$S_{IF}(\omega) = \frac{kT}{2} \left( F_{A2} - 1 + \frac{F_{M3} - 1}{A_{A2}^2} \right). \quad (A1.33)$$

Noise of the intermediate-frequency components will result in residual closed-loop timing jitter with spectral density given by

$$S_{J,IF}(\omega) \simeq \frac{S_{IF}(\omega - \omega_{IF})}{\alpha^2}. \quad (A1.34)$$

Alternatively, the noise of the intermediate-frequency components can be combined with the noise of the radio-frequency components (i.e. the components processing the photodiode signal prior to phase detection by mixer M2). The equivalent input noise power of the RF and IF systems can then be expressed as

$$S_{RF/IF}(\omega) = \frac{kT}{2} \left( F_{A1} + \frac{F_{M2} - 1}{A_{A1}^2} + \frac{F_{A2} - 1}{A_{A1}^2 A_{M1}^2 (4/\pi)^2} + \frac{F_{M3} - 1}{A_{A1}^2 A_{M1}^2 (4/\pi)^2 A_{A2}^2} \right) \quad (A1.35)$$

$$= \frac{kT}{2} F_{equivalent}$$

where  $F_{equivalent}$  is an equivalent noise figure for the RF and IF systems. The residual closed-loop timing jitter due to additive noise in both the RF and IF sections is then

$$S_{J,RF}(\omega) + S_{J,IF}(\omega) = \frac{S_{RF/IF}(\omega - \omega_l)}{\omega_l^2 P_{photodiode}} \quad (A1.36)$$

Finally, the gain and compensation section has some equivalent input noise voltage with spectral density  $S_{amp}(\omega)$ , which will result in residual closed-loop jitter having a power spectral density

$$S_{J,amp}(\omega) = \frac{S_{amp}(\omega)}{k'^2} \quad (A1.37)$$

To suppress these last two residual noise terms, the signal levels (i.e. the gain factors  $\alpha$  and  $k'$ ) should be large, and the components should be selected for low equivalent input noise.

#### A1.2.4 Reference oscillator phase noise

A final error term in the phase detection system is the phase noise (timing jitter) of the reference oscillator itself; in an ideal timing stabilization system, the laser phase will track that of the reference oscillator. The phase noise of a free-running oscillator varies in proportion to the noise of the amplification device coupled to the oscillator's resonator, and the phase noise bandwidth is set by the bandwidth of the resonator and the degree of coupling between resonator and amplifier [A1.12]. The phase noise bandwidth is on the order of the resonator bandwidth. High-stability electronic oscillators use quartz crystal resonators whose quality factor  $Q$  is on the order of  $10^5$ . Moderate-cost quartz crystal oscillators at  $\omega \simeq 2\pi \times 100$  MHz are available with phase noise spectral densities ( $= \omega_l^2 S_J(\omega)$ ) on the order of -130 dBc (1 Hz) at  $\Delta f = 100$  Hz, -145 dBc (1 Hz) at  $\Delta f = 1$  kHz [A.13].

If the oscillation frequency must be tuned to accommodate variations in the laser cavity frequency  $\omega_l$ , then a simple crystal oscillator cannot be used. Frequency synthesizers, systems in which a broadband tunable oscillator is phase-locked to a precision fixed-frequency quartz oscillator, can then be used for the reference oscillator. Synthesizers having low phase-noise are expensive ( $\sim \$ 30,000$ ).

#### A1.2.5 Loop Bandwidth and Stability

Given a phase detector with negligible spurious outputs, the timing jitter suppression is set by the feedback loop transmission  $G(\omega)$ :

$$S_{closed\ loop}(\omega) = \left\| \frac{1}{1 + G(\omega)} \right\|^2 S_{open\ loop}(\omega), \quad (A1.38)$$

where the loop transmission is given by

$$G(\omega) = k' A_{comp}(\omega) k_s H_L(\omega). \quad (A1.39)$$

In the above equation,  $A_{comp}(\omega)$  is the transfer function of the amplifier providing loop gain and compensation,  $k_s$  is the slope coefficient of the voltage controlled phase shifter (i.e.  $d\tau/dV_{control}$ , where  $\tau$  is the delay and  $V_{control}$  is the control voltage), and  $H_L(\omega)$  is the phase transfer function of the laser.

The design of the loop gain and compensation  $A_{comp}(\omega)$  to attain the desired loop characteristics is the subject of classical (frequency-domain) control system theory, and is discussed extensively in D'Azzo and Houpis [A1.14]. Large  $G(\omega)$ , desirable at all frequencies at which  $S_{open\ loop}(\omega)$  has significant energy, is limited by stability constraints arising from  $H_L(\omega)$ . If the feedback loop is opened (this is achieved in practice by leaving the loop active but decreasing the loop bandwidth to  $\sim 1$  Hz) and the phase of the laser driving signal is perturbed by applying a step-function drive signal to the voltage-controlled phase shifter, then the output of the phase detector will show the transient behavior of the laser timing in response to a step-function phase shift. The result of this measurement on the Spectra-Physics Nd:YAG laser is shown in Fig. A1.6. This step response conforms well to  $h_l(t) = u(t)(1 - e^{-t/\tau_p})$ , with  $\tau_p = 50\mu s$ , and where  $u(t)$  denotes the unit step-function. The laser phase transfer function is therefore

$$H_L(\omega) \simeq \frac{1}{1 + j\omega/\omega_p}, \quad (A1.40)$$

where  $\omega_p = 1/\tau_p$ ; for our Spectra-Physics Nd:YAG laser,  $\omega_p \simeq 2\pi \times 3.2$  kHz.

As with any feedback loop, the loop bandwidth (the frequency at which  $\|G\| = 1$ ) must be constrained. The laser phase transient response may have additional poles in its transfer function at frequencies well above 3.2 kHz, whose influences on a time-domain measurement are masked by the response of the dominant pole, and other parasitic poles exist in the transfer functions of the phase shifter, phase detection system, and loop compensation section. Simple feedback systems commonly use an integration in the feedback loop. In this case,

$$A_{comp}(\omega) = \frac{\omega_c}{j\omega}, \quad (A1.41)$$

and the loop suppression is given by

$$R(\omega) \equiv \frac{1}{1 + G(\omega)} = \frac{1}{1 + j\omega(2\zeta/\omega_n) - \omega^2/\omega_n^2}, \quad (A1.42)$$

where the loop natural frequency  $\omega_n$  and the loop damping  $\zeta$  are given by

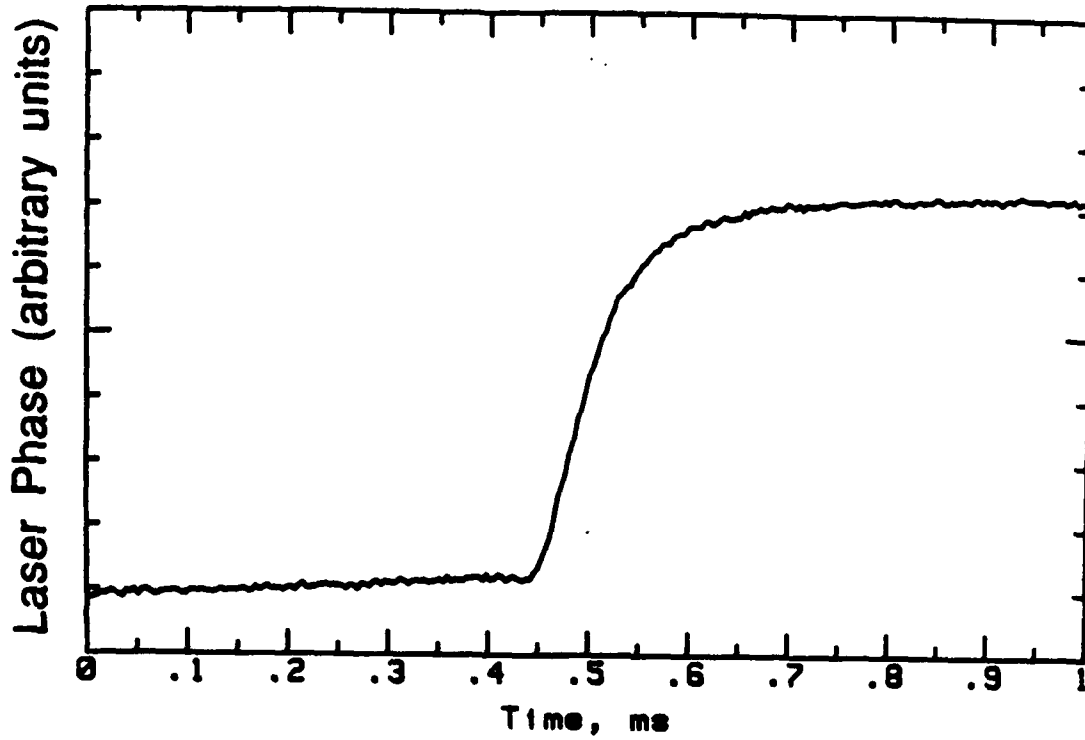


**Figure A1.6:** Transient response of the phase of a Spectra-Physics laser to a step change in the phase of the mode-locking drive signal. The response is that of a first-order dynamic system, and corresponds to a 3.2 kHz pole.



$$\omega_n^2 = k'k_s\omega_c\omega_p \quad \zeta = \frac{1}{2}\sqrt{\frac{\omega_p}{k'k_s\omega_c}} \quad (\text{A1.43})$$

If an attempt is made to attain large loop gain and large loop bandwidth by choosing a large gain coefficient  $k'k_s\omega_c$ , the loop damping factor  $\zeta$  will be degraded. For  $\zeta < 1/\sqrt{2}$ , the loop suppression will be greater than unity in the vicinity of  $\omega_n$ , and thus the spectral density  $S_J(\omega)$  of the timing jitter will be increased for  $\omega \approx \omega_n$ . For a well-damped control system without peaking of  $S_J(\omega)$  near  $\omega_n$ , the loop damping  $\zeta$  must be greater than  $1/\sqrt{2}$  and the loop natural frequency is then bounded:  $\omega_n \leq \omega_p/\sqrt{2}$ . Thus, in a simple control system using integrating feedback, the laser pole frequency limits the suppression of timing jitter to those frequency components below  $\omega_p/\sqrt{2}$ . Even within this bandwidth, the loop rejection is finite, and is given by the loop rejection Eq. (A1.42). Unfortunately,  $S_J(\omega)$  has significant energy at frequencies approaching the laser pole frequency  $\omega_p$ .

Well-damped control loops with larger loop bandwidth can be attained by a variety of compensation techniques, including lead compensators [A1.14] and observer-controller compensators [A1.15]. Given the variations in parameters found in experimental systems, the choice of compensator design is guided by the sensitivity of the system damping and system stability margin to changes in the loop parameters. In particular, it has been observed that the laser pole frequency increases as the laser pulse repetition rate is detuned from the laser cavity frequency. Simple lead compensation will permit a moderate increase in loop bandwidth. If a compensating zero is included in the transfer function of the gain and compensation,

$$A_{comp}(\omega) = \frac{\omega_c}{j\omega}(1 + j\omega/\omega_p) = \frac{\omega_c}{j\omega} + \frac{\omega_c}{\omega_p}, \quad (\text{A1.44})$$

then the loop suppression becomes

$$R(\omega) = \frac{j\omega/\omega_{loop}}{1 + j\omega/\omega_{loop}} \quad \text{where} \quad \omega_{loop} = k'k_s\omega_c. \quad (\text{A1.45})$$

The loop suppression is that of a first-order system, and is well-damped even for loop bandwidths  $\omega_{loop}$  exceeding  $\omega_p$ .

### A1.3 Experimental Results

The design guidelines outlined above have been used to implement a feedback system to reduce the timing jitter of a 82 MHz mode-locked Nd:YAG laser. The current design has evolved over the past three years, with early published results [A1.16] being a reduction from 2.9 ps unstabilized to 0.9 ps stabilized jitter; the current system reduces the laser timing fluctuations at rates greater than 50 Hz from  $\sim 1.25$  ps unstabilized to  $\sim 0.25$  ps stabilized. The decrease with time of the unstabilized jitter deserves some comment: in this period, the laser acousto-optic mode-locker and the end mirrors were replaced. These two changes should have resulted in both a narrower cavity bandwidth and stronger injection-locking, both of which reduce the phase noise; replacement of the two components resulted

in the open-loop jitter decreasing from  $\sim 2.9$  to  $\sim 1.25$  ps (for rates above 50 Hz). An unstabilized jitter of 10 ps was first measured by Brian Kolner [A1.17], while my first measurements on the same laser system were more consistent with 2.9 ps. As unstabilized jitter appears to increase with both laser misalignment and with deviations of the mode-locking frequency from the natural laser cavity frequency, perhaps the improvement was due to more careful laser operation as we became aware of its effect on jitter.

The laser stabilized is an 82 MHz Spectra-Physics Nd:YAG unit mode-locked by an acousto-optic cell. The amplitude noise sidebands are approximately -85 dB with respect to the carrier, at  $\sim 100$  Hz offset from the carrier, as measured in a 1 Hz resolution bandwidth, i.e.  $S_N \simeq -85$  dBc (1 Hz) at  $\Delta f = 100$  Hz. The unstabilized phase noise sidebands have significant spectral density up to a frequency of  $\sim 2$  kHz, and a loop bandwidth of  $\sim 5$  kHz is thus required for significant suppression of the strong phase-noise components at 1-2 kHz (Eq. A1.45). Given this estimate of the loop bandwidth, if timing fluctuations of  $\sim 100$ -200 fs are to be attained, phase noise spectral density must be on the order of -125 to -130 dBc (1 Hz) at frequencies within the  $\sim 5$  kHz loop bandwidth. The spurious phase-noise sidebands due to DC offset, 3<sup>rd</sup>-order nonlinearities, and additive noise must be well below the objective stabilized phase noise sidebands; the system is designed so that each spurious effect results in sidebands with power less than -135 dBc (1 Hz).

The timing stabilization system has been implemented following the general design guidelines outlined in the previous sections. The phase detection system is chopper-stabilized as in Section A1.2.1, with chopping at 1 MHz; the phase detector slope  $k'$  is 1 Volt/ns, and the mixer offset is less than 0.5 mV, resulting in a static timing offset  $T_o$  of less than 5 ps. The resulting AM-PM conversion due to DC offset is less than -50 dB; thus the laser's -85 dBc (1 Hz) amplitude noise results in less than -135 dBc (1 Hz) spurious closed-loop phase noise through AM-PM conversion by detector DC offset.

With amplitude noise sidebands some 50 dB more powerful than the objective phase noise sidebands, AM-PM conversion through third-order nonlinearities must be suppressed by at least 50 dB; using Eq. (A1.25), the input power levels to the amplifier A1 and to the phase detector (mixer) M2 must be at least 30 dB below the third-order intercept points of each component. In the current implementation, the input power levels are greater than 35 dB below the 3<sup>rd</sup>-order intercept power, and the suppression of AM-PM conversion is at least 60 dB, resulting in less than -145 dBc (1 Hz) spurious closed-loop phase noise through AM-PM conversion by 3<sup>rd</sup>-order products.

The photodiode power  $P_{\text{photodiode}}$  at the laser repetition frequency  $\omega_l$  is -24 dBm, while the equivalent noise figure  $F_{\text{equivalent}}$  of the RF and IF systems is 9 dB, and  $kT$  is -173 dBm (1 Hz). By Eq. A1.36, the additive noise of these subsystems thus will result in a spurious phase noise spectral density of -140 dBc (1 Hz).

Finally, the reference oscillator for the timing stabilization system is a Hewlett-Packard model 8662A low phase-noise signal generator. No phase-noise specification is available for this synthesizer operating at 82 MHz, but over the 320-640 MHz range, the phase noise specification is -104 dBc (1 Hz) at 100 Hz offset, -121 dBc (1 Hz) at 1 kHz offset, and -131 dBc (1 Hz) at 10 kHz offset. Extrapolation to 82 MHz is uncertain, but it is likely that the oscillator's timing deviations are relatively independent of oscillation frequency, in which case phase noise will scale as the square of oscillation frequency. The phase noise of the

HP8662A at 82 MHz is then estimated as -116 dBc (1 Hz) at 100 Hz offset, -133 dBc (1 Hz) at 1 kHz offset, and -143 dBc (1 Hz) at 10 kHz offset. Given both the small difference between the estimated reference phase noise and the objective stabilized laser phase noise, and the uncertainty of our estimate, this data will have to be verified if the laser phase noise is to be further reduced.

The control loop bandwidth is set at approximately 6 kHz; the control loop is lead compensated, with a compensating zero at 3.2 kHz cancelling the response of the 3.2 kHz laser pole. Due to variability in the laser pole frequency, with our laser the compensation does not consistently provide good loop damping if the loop bandwidth is increased much beyond 6 kHz. The bandwidth and damping of the control loop can be determined by measuring the suppression of a step-function error signal injected into the loop (Fig. A1.7). The response of the system to an injected error signal is a simple exponential decay, with no evidence of an underdamped second-order system response. In contrast, Fig. (A1.8) shows a similar measurement of an earlier laser timing stabilizer in which the lead compensation was incorrectly set; the response contains both an exponentially decaying response and a exponentially decaying oscillatory response, and is characteristic of an underdamped 3<sup>rd</sup>-order control system.

The suppression of phase noise by the feedback loop is shown as a series of three phase noise measurements (Figs. A1.9-A1.11). In the narrowband 500 Hz span (Fig. A1.9) 10-20 dB suppression is seen. Some sidebands at harmonics of the 60 Hz power line frequency are observed. The phase noise on the 82 MHz fundamental can be calculated from this; -113 dBc (1 Hz) at 100 Hz offset. In this bandwidth, the phase noise is very close to the estimate of the reference oscillator phase noise. Indeed, the measured phase noise may be that of the local oscillator in the spectrum analyzer used for these measurements, as the spectrum analyzer likely has a poorer local oscillator than the low-phase-noise oscillator from the same manufacturer. These points need to be investigated.

In the broader 10 kHz frequency span (Fig. A1.10), the phase noise is most likely that of the laser. Broad spectral peaks at 1.2 kHz are suppressed by approximately 16 dB, while some shoulders on the spectral density at 2 kHz are suppressed by 10 dB. These two spectral features might be ascribed to mechanical resonances within the laser mirror supports. The low-energy point of the sidebands is at  $\sim 2.5$  kHz; the phase noise spectral density at this point corresponds to -131 dBc (1 Hz) phase noise on the 82 MHz fundamental. It is likely that this corresponds to the combined spurious effects of reference oscillator phase noise, AM-PM conversion through DC offset, additive noise in the RF and IF systems, and additive noise ( $\sim 20$  dB noise figure) of the photodiode, amplifier, and spectrum analyzer used for these measurements. Of these effects, spectrum analyzer phase noise and additive photodiode, amplifier, and spectrum analyzer noise are not components of the laser phase noise, but are measurement error. For this reason, at offsets less than 2 kHz, we see strong suppression of the laser's open-loop phase noise sidebands consistent with a  $\sim 6-7$  kHz loop bandwidth  $\omega_{loop}$ , but see little phase-noise suppression at offsets from 2-5 kHz, consistent with a background phase noise floor of  $\sim -131$  dBc (1 Hz).

For completeness, the phase noise spectrum in a very broad 50 kHz span is also shown (Fig. A1.11). The stabilization system causes a slight increase in the spectrum at frequencies from  $\sim 6-10$  kHz, with little difference thereafter. The phase noise at 10 kHz

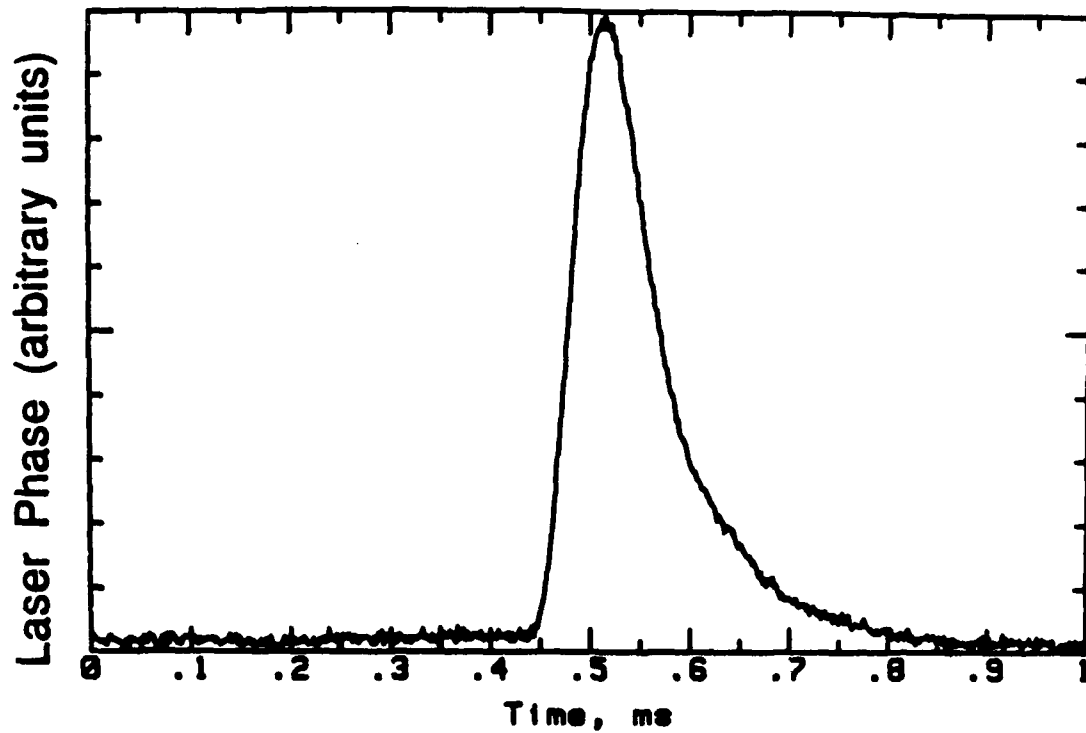


Figure A1.7: Suppression of a step-function error signal injected into the phase-lock loop. The exponentially decaying response is indicative of a stable control loop with large damping.

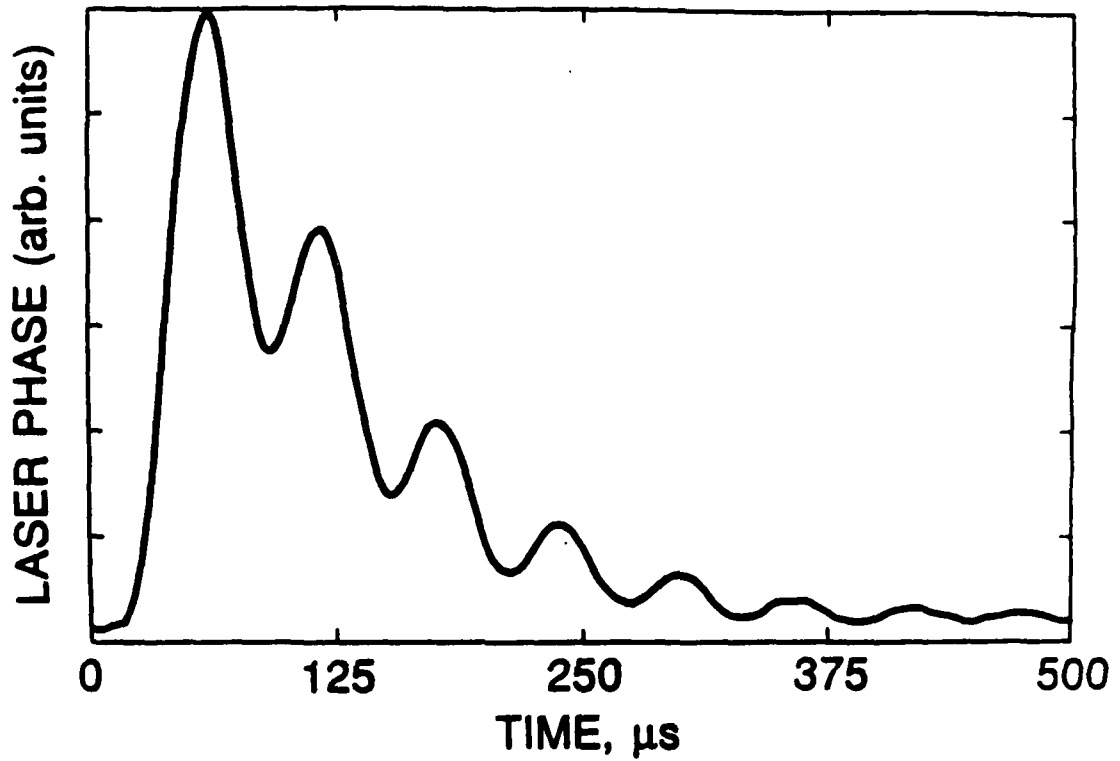
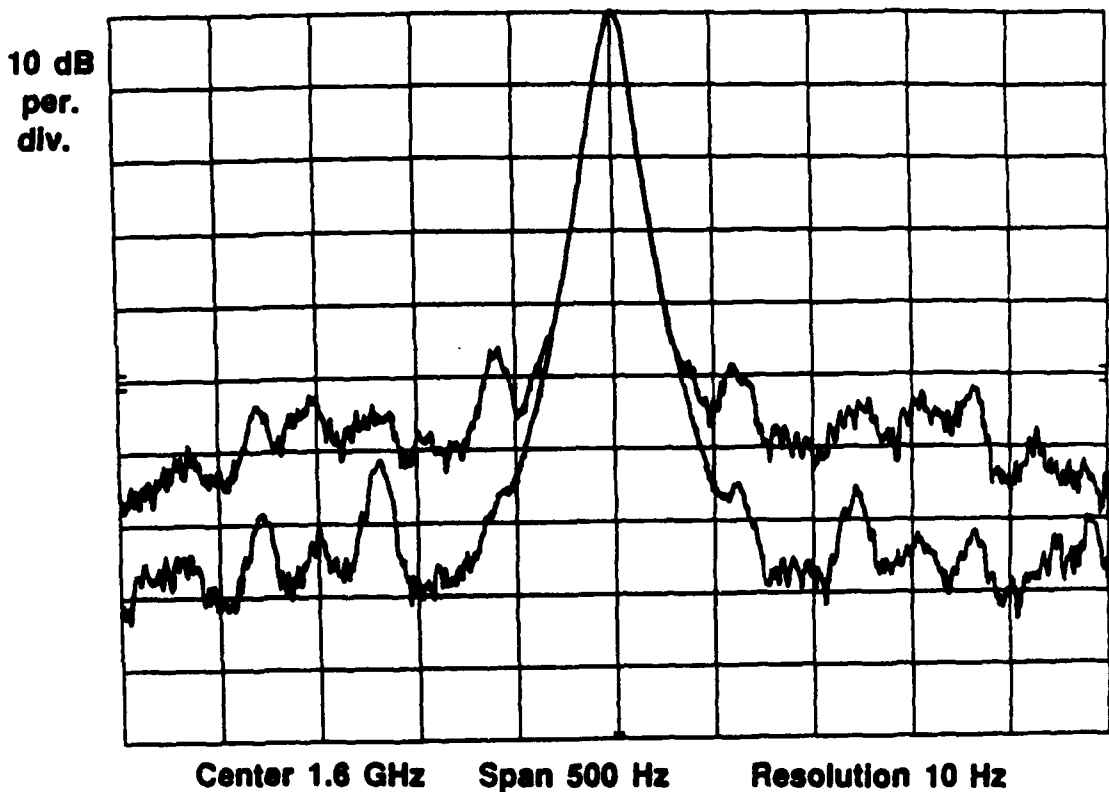
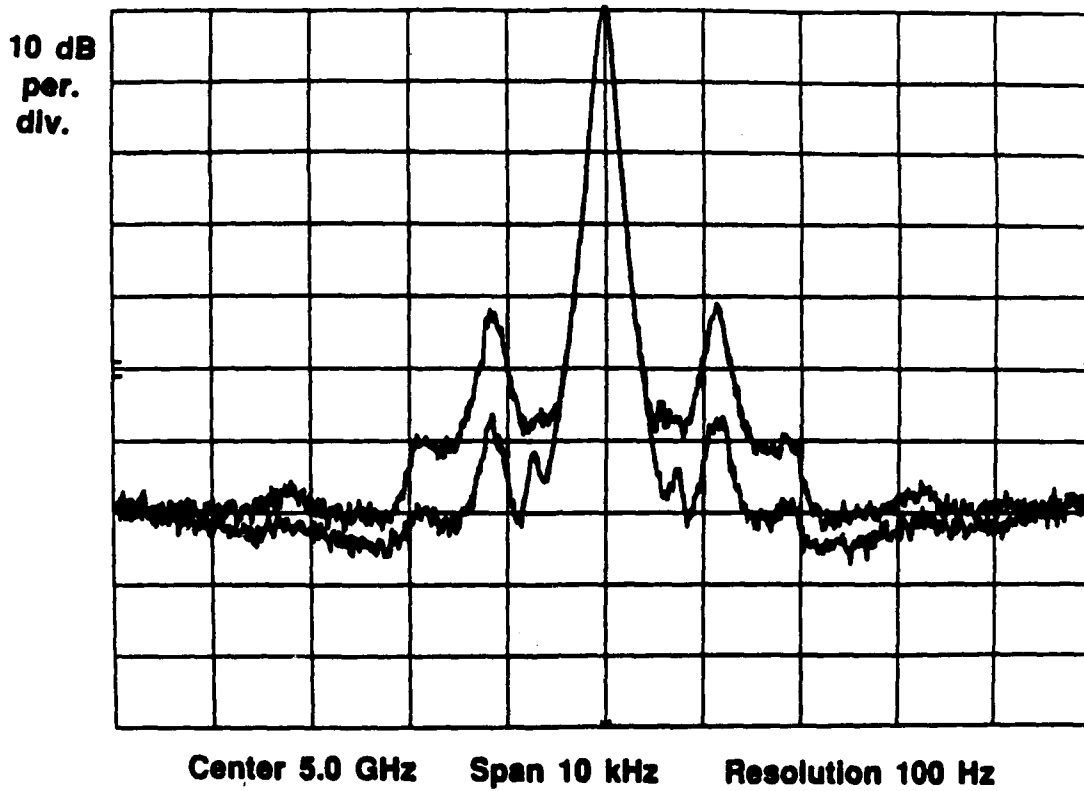


Figure A1.8: Suppression of an injected error signal by a previous implementation of the laser timing stabilizer, in which the lead compensation was incorrectly set. The system has 3<sup>rd</sup>-order dynamics, and the response contains both an exponentially decaying component and a damped oscillatory component. The stability margin of this system was small.



**Figure A1.9:** Suppression of the 50–250 Hz phase- noise sidebands of an 82 MHz Spectra-Physics mode-locked Nd:YAG laser, as measured by spectrum analysis of the 20<sup>th</sup> harmonic of the laser pulse repetition rate.



**Figure A1.10:** Suppression of the 500–5 kHz phase- noise sidebands of the Spectra-Physics laser, measured on the 60<sup>th</sup> harmonic of the laser pulse repetition rate.

offset corresponds to -131 dBc (1 Hz) on the 82 MHz fundamental. At offsets greater than 15 kHz the sidebands are below the additive noise of the instrumentation system, and the phase noise cannot be determined. Improved measurements will require an instrumentation system with improved noise figure in the  $\sim 2-6$  GHz microwave frequency range.

After integrating these phase noise spectral densities, the timing jitter of the laser is determined to be:

$$\sigma_J = \begin{cases} 1.2 \text{ ps,} & \text{open loop, 50 Hz-25 kHz;} \\ 0.24 \text{ ps,} & \text{closed loop, 50 Hz-25 kHz.} \end{cases}$$

The reduction in phase noise is 5:1 over the frequency range 50 Hz-25 kHz. Frequency components above 25 kHz should be measured, but the trend of Figs. (A1.9-A1.11) shows that the noise is rapidly decreasing above 5 kHz. The unstabilized phase noise components below 50 Hz have large energy, and should be measured; unfortunately, the resolution of the spectrum analyzer prohibits measurement of these components. Phase noise test sets can measure these very low-frequency components, but the instrument cost ( $\sim \$300,000$ ) is well beyond the laboratory resources. Further, the AM rejection of these instruments (the Hewlett-Packard 11729B carrier noise test set has a specified AM rejection of 20 dB) may be inadequate unless measurements are made at high harmonics of the laser pulse repetition rate. Observing the timing fluctuations of the laser pulses on a sampling oscilloscope, the unstabilized jitter appears to be on the order of 20 ps at low frequencies, while the the stabilized jitter is below the timing fluctuations ( $\sim 5$  ps) of the sampling oscilloscope. Phase noise components below 50 Hz clearly need further investigation.

#### A1.4 Conclusions

The (50 Hz-25 kHz) timing fluctuations of a mode-locked laser has been reduced by 5:1, attaining 0.24 ps jitter. These timing fluctuations are 2 parts in  $10^5$  of the laser pulse repetition period, while the amplitude fluctuations of the laser are approximately 5% of the average laser intensity. Stabilization of the timing to these levels requires a precise phase detector whose sensitivity to laser timing is at least a factor of  $10^4$  greater than its sensitivity to laser amplitude. The spectral density of the stabilized phase noise sidebands are on the order of -120 to -135 dB (1 Hz) with respect to the 82 MHz laser fundamental; as the thermal noise power power has spectral density  $kT = -173$  dBm (1 Hz), the radio-frequency signal levels must be selected so that the associated phase-noise sidebands have power well above  $kTF$ , where  $F$  is the noise figure of the phase detection system. The bandwidth of the unstabilized phase noise is significant in comparison with the bandwidth of the laser's dynamic phase response, and the feedback loop must be appropriately compensated if the loop is not to show instabilities or weakly damped resonances with associated peaking of the phase noise. With these results, the laser phase noise is now within an order of magnitude of the phase noise of high-stability radio-frequency sources. Further reduction of the jitter will require decreased offset, decreased noise figure, and decreased  $3^{rd}$ - order products in the phase detection system, increased loop bandwidth or more complex (lead-lag) compensation, and perhaps a reference source with further



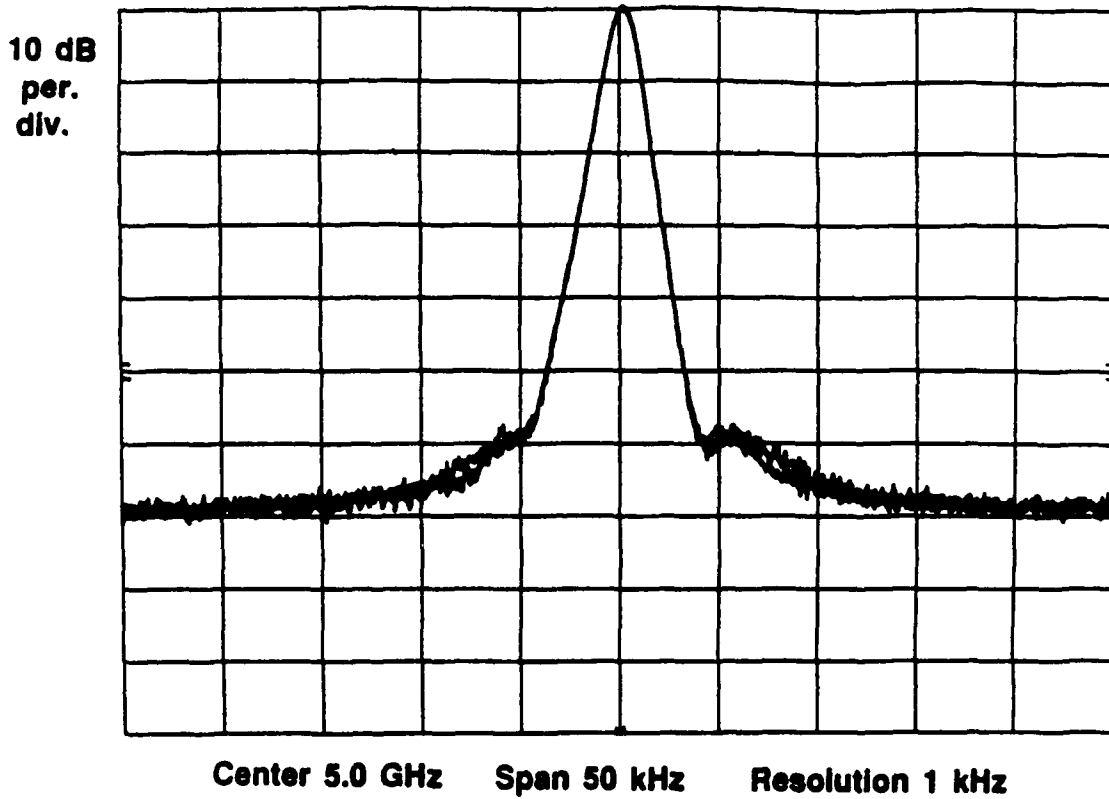


Figure A1.11: Suppression of the 5 kHz–25 kHz phase-noise sidebands of the Spectra-Physics laser, measured on the 60<sup>th</sup> harmonic of the laser pulse repetition rate.

improved stability (it is likely that only a fixed-frequency crystal oscillator will provide this).

Instrumentation is also a difficulty; the noise figure and the residual phase noise of the photodetector, amplifier, and spectrum analyzer measurement system are becoming a significant fraction of the measured sideband power. Precision carrier noise test sets may permit measurements with lower residual phase noise, and will permit measurements of phase noise at offsets below 50 Hz. Unfortunately, the cost of such systems is beyond the resources of most scientific laser laboratories, and their AM rejection is unestablished.

Despite these difficulties, no fundamental limits have been reached, and with continued refinement jitter below 0.1 ps is expected.

#### References.

- [A1.1] J. Bokor, R. Haight, J. Stark, R.H. Storz, R.R. Freeman, and P.H. Bucksbaum: "Picosecond Time-Resolved Photoemission Study of the InP (100) Surface", in *Picosecond Electronics and Optoelectronics*, G.A. Mourou, D.M. Bloom, and C.-H. Lee, eds., Springer-Verlag, New York, 1985.
- [A1.2] D.H. Auston, K.P. Cheung, J.A. Valdmanis, and D.A. Kleinman, *Phys. Rev. Lett.*, 53, 1555-1558 (1984).
- [A1.3] J.M. Weisenfeld, R.S. Tucker, P.M. Downey, and J.E. Bowers, *Electron Lett*, 22, 396-397, 1986.
- [A1.4] J.A. Kash, J.C. Tsang, and J.M. Hvam, "Subpicosecond Raman Spectroscopy of Electron-LO Phonon Dynamics in GaAs", in *Picosecond Electronics and Optoelectronics*, G.A. Mourou, D.M. Bloom, and C.-H. Lee, eds., Springer-Verlag, New York, 1985.
- [A1.5] J.D. Fox and H. Schwarz, in *Digest of the 1982 IEEE Symposium on Microwave Theory and Techniques*, pp. 334-336.
- [A1.6] W.P. Robbins, *Phase Noise in Signal Sources*, IEEE Telecommunications Series, No. 9, Peter Peregrinus, London, 1982.
- [A1.7] *Phase Noise Characterization of Microwave Oscillators, Phase Detector Method*, Product note 11729B-1, Hewlett-Packard Co., P.O. Box 10301, Palo Alto, CA. 94303-0890
- [A1.8] *Phase Noise Characterization of Microwave Oscillators, Frequency Discriminator Method*, Product note 11729C-2, Hewlett-Packard Co., P.O. Box 10301, Palo Alto, CA. 94303-0890
- [A1.9] D. Cotter: "Technique for Highly Stable Active Mode-Locking", in *Ultrafast Phenomena IV*, D. A. Auston and K. B. Eisenthal, eds., Springer-Verlag, New York, 1984.
- [A1.10] D. R. Jordan and P.L. Penny, eds.: *Transmission Systems for Communications, Fifth Edition*, Bell Laboratories, 1982. See especially Chapters 17 and 24.
- [A1.11] S.R. Kurtz: "Mixers as Phase Detectors" Watkins-Johnson Company Technical Notes, vol.5, no. 1, January/February 1978. Watkins-Johnson Company, Palo Alto,

CA.

- [A1.12] A. van der Ziel: *Noise in Solid State Devices and Circuits*, Wiley-Interscience, New York, 1986. See especially Chapter 10.
- [A1.13] Data on high-stability crystal oscillators are available from a number of manufacturers. One large supplier is Vectron Laboratories, Inc. 166 Glover Avenue, Norwalk, Connecticut 06850.
- [A1.14] J. J. D'Azzo and C. H. Houpis: *Linear control system analysis and design: conventional and modern*, McGraw-Hill, Inc. 1975.
- [A1.15] T.M. Kailath: *Linear Systems*, Prentice-Hall, 1980.
- [A1.16] M. J. W. Rodwell, K. J. Weingarten, D. M. Bloom, T. Baer, and B. H. Kolner: "Reduction of timing fluctuations in a mode-locked Nd:YAG laser by electronic feedback", *Optics Letters*, vol. 11, page 638, October 1986.
- [A1.17] B. H. Kolner and D. M. Bloom: "Electrooptic Sampling in GaAs Integrated Circuits", *IEEE J. Quant. Elect.*, vol. QE-22, 79-93, 1986.

## Appendix II

### Optical System Analysis using Jones-Vector Representation

The polarization states and intensity transfer function of the optical system shown in Fig. 1.8 can be calculated using the Jones-vector notation [AII.1,2]. Plane wave electric fields are expressed as complex amplitude vectors

$$\mathbf{D} = \begin{pmatrix} D_x e^{j\delta_x} \\ D_y e^{j\delta_y} \end{pmatrix} \quad (\text{AII.1})$$

The real  $x$  component of the electric field is obtained by the operation  $E_x(t) = \text{Re}[D_x e^{j\omega t}] = \text{Re}[D_x e^{j(\omega t + \delta_x)}]$ . Optical elements are represented by a four element matrix that operate on the complex vectors representing the applied optical fields.

$$\mathbf{D}_{out} = M \mathbf{D}_{in} \quad \text{or} \quad \begin{pmatrix} D_{x,out} \\ D_{y,out} \end{pmatrix} = \begin{pmatrix} M_{11} & M_{21} \\ M_{12} & M_{22} \end{pmatrix} \begin{pmatrix} D_{x,in} \\ D_{y,in} \end{pmatrix} \quad (\text{AII.2})$$

The following matrices represent the optical elements in this system.

$$\vec{x} \text{ polarizer: } M_x = \begin{pmatrix} 1 & 0 \\ 0 & 0 \end{pmatrix} \quad (\text{AII.3})$$

$$\vec{y} \text{ polarizer: } M_y = \begin{pmatrix} 0 & 0 \\ 0 & 1 \end{pmatrix} \quad (\text{AII.4})$$

$$\text{Rotation matrix: } R(\theta) = \begin{pmatrix} \cos\theta & \sin\theta \\ -\sin\theta & \cos\theta \end{pmatrix} \quad (\text{AII.5})$$

$$\frac{\lambda}{4} \text{ wave plate: } M_{\lambda/4} = \begin{pmatrix} 1 & 0 \\ 0 & j \end{pmatrix} \quad (\text{AII.6})$$

Rotated  $\frac{\lambda}{4}$  wave plate:

$$M_{\lambda/4}(\theta) = R^{-1}(\theta)M_{\lambda/4}^i R(\theta) = \begin{pmatrix} \cos^2\theta + j \sin^2\theta & (1-j)\sin\theta \cos\theta \\ (1-j)\sin\theta \cos\theta & \sin^2\theta + j \cos^2\theta \end{pmatrix} \quad (\text{AII.7})$$

$$\frac{\lambda}{2} \text{ wave plate: } M_{\lambda/2}^i = \begin{pmatrix} 1 & 0 \\ 0 & -1 \end{pmatrix} \quad (\text{AII.8})$$

$$\text{Rotated } \frac{\lambda}{2} \text{ wave plate: } M_{\lambda/2}(\phi) = R^{-1}(\phi)M_{\lambda/2}^i R(\phi) = \begin{pmatrix} \cos 2\phi & \sin 2\phi \\ \sin 2\phi & -\cos 2\phi \end{pmatrix} \quad (\text{AII.9})$$

$$\text{Gallium arsenide substrate: } M_{GaAs} = \begin{pmatrix} \exp(j\delta) & 0 \\ 0 & \exp(-j\delta) \end{pmatrix} \quad (\text{AII.10})$$

$$\text{where } \delta = \frac{\pi V}{2V_\pi}$$

Then,

$$D_{out,x} = M_x M_{\lambda/4} M_{\lambda/2} M_{GaAs} M_{\lambda/2} M_{\lambda/4} M_x D_{in} \quad (\text{AII.11})$$

is the component coaxial to the input beam and

$$D_{out,y} = M_y M_{\lambda/4} M_{\lambda/2} M_{GaAs} M_{\lambda/2} M_{\lambda/4} M_y D_{in} \quad (\text{AII.12})$$

is the component rejected by the polarizing beamsplitter. The input electric field  $D_{in}$  is  $x$ -polarized and of unity incident amplitude

$$D_{in} = \begin{pmatrix} 1 \\ 0 \end{pmatrix} \quad (\text{AII.13})$$

and then the resulting output electric fields are

$$D_{out,x} = \cos(2\theta)\cos(\delta) - \sin(\delta)\left[\sin 2(\theta)\sin(2\theta - 4\phi) - j\cos(2\theta - 4\phi)\right] \quad (\text{AII.14})$$

$$D_{out,y} = \sin(2\theta)\cos(\delta) + \sin(\delta)\cos(2\theta)\sin(2\theta - 4\phi)$$

The relative output intensity is the modulus squared of the D vector,  $I = |D|^2$ . Because  $V \ll V_\pi$ ,  $\delta \ll 1$ ,  $\cos(\delta) \approx 1$ ,  $\sin(\delta) \approx \delta$ , and terms of order  $\delta^2$  are negligible. Then,

$$I_x = |D_{out,x}|^2 = \cos^2(2\theta) - \delta\sin(4\theta)\sin(2\theta - 4\phi) \quad (\text{AII.15})$$

$$I_y = |D_{out,y}|^2 = \sin^2(2\theta) + \delta\sin(4\theta)\sin(2\theta - 4\phi)$$

With the wave plate angles are set to the values  $\theta = 22.5^\circ$ ,  $\phi = 33.75^\circ$ , then

$$I_x = \frac{1}{2}(1 + 2\delta) \quad (\text{AII.16})$$

$$I_y = \frac{1}{2}(1 - 2\delta)$$

which corresponds to the output intensity, normalized to  $I_0 = 1/2$ . This setting of the wave plate angles is the "quarter-wave" bias point of an electrooptic modulator.

## References for Appendix II

AII.1. A. Yariv and P. Yeh: *Optical Waves in Crystals*, New York: John Wiley & Sons, Inc., 1984, pp. 62-65 and Chapter 5, pp. 121-154

AII.2. R.C. Jones: "New calculus for the treatment of optical systems," *J. Opt. Soc. Am.*, vol. 31, pp. 488-493, 1941

## Appendix III

### Traveling wave coefficient calculation

The voltage on a transmission line at a specific drive frequency is due to the sum of forward and reverse traveling waves

$$v(z) = a \exp(-j\beta z) + b \exp(+j\beta z) \quad (\text{AIII.1})$$

where  $a$  and  $b$  are the forward and reverse traveling wave coefficients, respectively. In an actual measurement, the probe beam is scanned along the transmission line and the voltage is measured at discrete points spaced by  $\Delta z = nL$ . Then, the data is of the form

$$v_n = a \exp(-j\beta nL) + b \exp(+j\beta nL) \quad (\text{AIII.2})$$

The  $a$  and  $b$  coefficients can be solved for using a linear projection algorithm<sup>†</sup>. First, the following variables are defined

$$\begin{aligned} f &= \exp(-j\beta nL) \\ r &= \exp(+j\beta nL) \end{aligned} \quad (\text{AIII.3})$$

where  $f$  corresponds to a forward traveling-wave and  $r$  corresponds to a reverse traveling-wave. Then, two equations are formed from Eqn. (AIII.2) by multiplying first by  $f_n^*$  and by and summing over  $n$ , then multiplying by  $r_n^*$  and again summing over  $n$ .

$$\sum_n [v_n f_n^* = a f_n f_n^* + b r_n f_n^*] \quad (\text{AIII.4})$$

$$\sum_n [v_n r_n^* = a f_n r_n^* + b r_n r_n^*] \quad (\text{AIII.5})$$

This is expressed in vector form using the notation that

$$\langle x_n | y_n \rangle = \sum_n x_n y_n^* \quad (\text{AIII.6})$$

and then expressed in matrix form

$$\begin{pmatrix} \langle v_n | f \rangle \\ \langle v_n | r \rangle \end{pmatrix} = \begin{pmatrix} \langle f | f \rangle \langle r | f \rangle \\ \langle f | r \rangle \langle r | r \rangle \end{pmatrix} \begin{pmatrix} a \\ b \end{pmatrix} \quad (\text{AIII.7})$$

and solved for  $a$  and  $b$  using Cramer's rule

$$a = \frac{\langle v_n | f \rangle \langle r | r \rangle - \langle v_n | r \rangle \langle r | f \rangle}{\langle f | f \rangle \langle r | r \rangle - \langle f | r \rangle \langle r | f \rangle}$$

$$b = \frac{\langle v_n | r \rangle \langle f | f \rangle - \langle v_n | f \rangle \langle f | r \rangle}{\langle f | f \rangle \langle r | r \rangle - \langle f | r \rangle \langle r | f \rangle} \quad (\text{AIII.8})$$

Substituting for  $f$  and  $r$ , and noting that

$$\langle f | r \rangle = \langle r | f \rangle = \sum_{n=1}^N \exp(-j\beta n l) \exp(+j\beta n l) = N \quad (\text{AIII.9})$$

gives expressions for  $a$  and  $b$

$$a = \frac{N \sum_n v_n e^{+j\beta n L} - \sum_n v_n e^{-j\beta n L} \sum_n e^{+2j\beta n L}}{N^2 - \sum_n e^{+2j\beta n L} \sum_n e^{-2j\beta n L}} \quad (\text{AIII.10})$$

$$b = \frac{N \sum_n v_n e^{-j\beta n L} - \sum_n v_n e^{+j\beta n L} \sum_n e^{-2j\beta n L}}{N^2 - \sum_n e^{+2j\beta n L} \left( \sum_n e^{-2j\beta n L} \right)} \quad (\text{AIII.11})$$



# Appendix IV

•  
•  
•

•  
•

# Full-field modeling of the longitudinal electro-optic probe

J. L. Freeman, S. R. Jefferies, and B. A. Auld

Edward L. Ginzton Laboratory, Stanford University, Stanford, California 94305

Received March 13, 1987; accepted July 14, 1987

Optical polarization changes and mode coupling due to spatially varying anisotropic perturbations in  $\epsilon$  caused by electro-optic, acousto-optic, and other effects have been widely studied for both plane-wave and fiber mode propagation. A new optical  $S$ -parameter analysis of these effects, applicable to arbitrary optical field distributions, is presented. It is applied to evaluating the performance of the longitudinal electro-optic probe used for noninvasively examining GaAs integrated circuits. Error in probe measurements of circuit voltage distributions can be characterized by considering the probe as a scanned electro-optic spatial filter.

Direct electro-optic sampling of GaAs integrated-circuit voltages has recently seen widespread use in the characterization of ultrafast devices and circuits.<sup>1-4</sup> Although electro-optic probes using a transverse geometry or an external electro-optic material have also been developed,<sup>5,6</sup> the study of III-V integrated circuits is best pursued with a longitudinal approach, in which a near-infrared laser is focused through the GaAs substrate to a small spot on the top or bottom surface and the circuit voltage is measured by detecting the electro-optic polarization coupling (Fig. 1).<sup>7,8</sup> An earlier Letter described the several advantages of this particular geometry and showed the relation of the probe signals to the circuit voltages.<sup>9</sup> The analysis followed the plane-wave modulator approach used by Yariv<sup>10</sup> and others; it assumed a plane wave of infinitesimal transverse extent as well as a zero-potential substrate backplane. Although many instances of electro-optic interaction are adequately thus described, the interaction of a tightly focused probe beam with spatially varying anisotropic changes in  $\epsilon$  is difficult to evaluate in this way. To consider the nature and magnitude of possible inaccuracies in electro-optic probe measurements, we have developed a full-field analysis that treats a general optical field as well as an arbitrary electric-field distribution. In this Letter we summarize the essential features of the analysis and its application to the longitudinal electro-optic probe.

A general analytical model applicable to the electro-optic probe may be constructed by applying the electromagnetic reciprocity relation to the optical transfer function of the probing beam. It can be shown<sup>11,12</sup> that a change  $\Delta\epsilon = \epsilon' - \epsilon$  of the dielectric tensor in any two-port electromagnetic system induces a change

$$\Delta S_{21} = \frac{i\omega}{4} \int_V \mathbf{E}_2 \cdot \Delta\epsilon \cdot \mathbf{E}_1' dV \quad (1)$$

in the transfer  $S$  parameter between ports 1 and 2. In Eq. (1) the volume integral is performed over the region where the change in  $\epsilon$  occurs,  $\omega$  is the optical frequency, and  $\mathbf{E}_i$  is the electric field incident on port  $i$ . These fields are chosen to have unit incident power; the prime indicates fields excited when the dielectric tensor has its perturbed value  $\epsilon'$ . If, as in the electro-

optic probe, where the polarization coupling is very weak, the change in  $\epsilon$  is small, we may neglect the prime in  $\mathbf{E}_1'$  since only higher-order terms result. If large  $\Delta\epsilon$  are to be considered, first-order perturbation theory cannot be used and the primed value of the  $i = 1$  field in Eq. (1) must be retained.

Equation (1) is already widely employed in calculating changes in the transmission between radio antennas or changes in the  $S$  parameter of microwave circuits due to perturbations in the transmission medium.<sup>11,12</sup> Here, however, the application considers optical transmission changes due to anisotropic perturbations in the refractive index of the GaAs substrate due to applied microwave electric fields. Since Eq. (1) is exact and perfectly general it can also be applied, for example, to stress-induced polarization and mode coupling in optical fibers. Ports 1 and 2 are then at the input and output ends of the fiber, and fields 1 and 2 correspond to different fiber modes. Polarization effects in fibers are customarily treated by coupled-mode theory,<sup>13,14</sup> which allows for strong coupling but is sometimes applied in first-order approximation when  $\Delta\epsilon$  is very small. In this approximation the

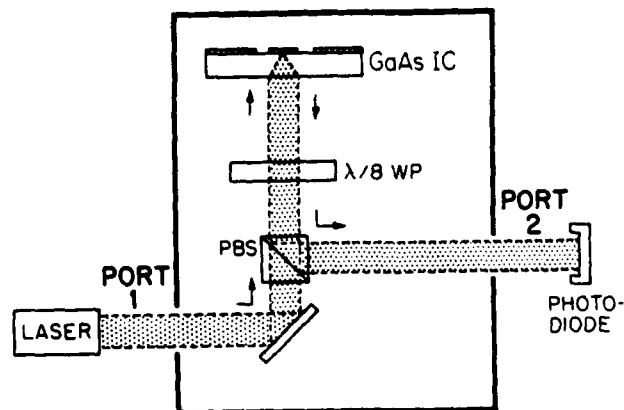


Fig. 1. Simplified diagram of the longitudinal electro-optic probing system and the port positions for the optical  $S$ -matrix calculation; the back-side geometry is shown here. The  $\lambda/8$  wave plate gives a net bias of  $\lambda/4$  after the double pass. PBS, polarizing beam splitter; IC, integrated circuit; WP, wave plate.

overall coupling can be obtained directly from Eq. (1) rather than by integrating the coupled-mode equations along the fiber. Note that Eq. (1) is a three-dimensional integral over three-dimensional field distributions, while the coupling constants in coupled-mode theory are expressed as two-dimensional integrals.

To apply Eq. (1) to the longitudinal electro-optic probe, we define a two-port system as in Fig. 1. Here  $E_1$  and  $E_2$  are the optical fields that would be excited by inputs at the laser and photodiode ports, respectively, and  $\Delta\epsilon$  is the electro-optically induced perturbation in  $\epsilon$  due to the microwave electric field of the integrated circuit on the top surface. Circuits fabricated on GaAs typically employ conductors on a (001) plane and along [110] or  $[\bar{1}10]$  directions. Thus, to be able to express simply the microwave fields that determine  $\Delta\epsilon$ , we choose a coordinate system with  $z$  normal to the substrate surface and  $x$  and  $y$  along [110] and  $[\bar{1}10]$ , then rotate the tensor for  $\Delta\epsilon$  in the crystallographic coordinates  $45^\circ$  about  $z$  to this system. If we then probe a long set of conductors running parallel to  $y$ , the  $y$  component of the microwave field may be neglected, and  $\Delta S_{21}$  becomes

$$\Delta S_{21} = \frac{-i\omega\epsilon_0\epsilon_r^2 r_{14}}{4} \int_{\text{GaAs}} [E_{1x}^{(o)} E_{1y}^{(o)} E_{1z}^{(o)}] \times \begin{bmatrix} E_z^{(m)} & 0 & E_x^{(m)} \\ 0 & -E_z^{(m)} & 0 \\ E_x^{(m)} & 0 & 0 \end{bmatrix} \begin{bmatrix} E_{2x}^{(o)} \\ E_{2y}^{(o)} \\ E_{2z}^{(o)} \end{bmatrix} dV, \quad (2)$$

where  $\epsilon_r$  is the relative dielectric constant,  $r_{14}$  is the electro-optic coefficient for this  $\bar{4}3m$  crystal, and  $E^{(o)}$  and  $E^{(m)}$  designate optical and microwave (or circuit) fields, respectively. It is assumed that the optical transit time is small compared with the microwave period.<sup>8</sup>

In the standard longitudinal probing configuration, the incident beam is polarized with equal components along the two dominant electro-optic axes, the relative phase shift along these axes is optically biased by  $\lambda/4$ , and the polarization orthogonal to the incident one is examined (Fig. 1).<sup>8</sup> These same considerations determine the system  $S_{21}$ , the transfer characteristic with no microwave field applied to the GaAs circuit. Since the photodiode measures an intensity proportional to  $|S_{21} + \Delta S_{21}|^2$ , the combination  $2 \operatorname{Re}(S_{21}\Delta S_{21}^*)$  will determine the component of the photodiode signal of interest.

Equation (2) is applicable to any GaAs circuit for which the microwave fields are known. In particular, it may be applied to circuits fabricated in either microstrip or coplanar geometries, where the quasi-static fields are derived from a Laplace potential. To simplify the evaluation and provide a physical interpretation of the result of Eq. (1), we express the solution to Laplace's equation,  $\phi(x, z)$ , as a sum over a discrete set of space harmonics<sup>15</sup> with frequencies  $\alpha_n = 2\pi n/L$ , where  $n$  is an integer and  $L$  is the period of the lowest nonzero spatial frequency and of amplitude  $\Phi(\alpha_n)$ . This gives

$$\phi(x, z) = \sum_n \Phi(\alpha_n) \exp(-\alpha_n z) \exp(i\alpha_n x) \quad (3)$$

for a substrate of infinite thickness. Each space harmonic penetrates to a depth that is proportional to the transverse period of the harmonic, as illustrated in Fig. 2. It can be seen that only those space harmonics with a large period will be probed by the converging portion of the optical beam.

From Eq. (3),  $\Delta S_{21}$  may then be calculated as an inverse transform of the product of a filter function  $H(\alpha_n)$ , resulting from the interaction of the probe beam and conductor fields, and  $\Phi(\alpha_n)$ , the Fourier coefficients of the potential. If the substrate is of thickness  $z_0$  and has a partially metalized back side with transformed potential  $\Phi_{\text{back}}(\alpha_n)$ , we use

$$\phi(x, z) = \sum_n \left\{ \Phi(\alpha_n) \frac{\sinh[\alpha_n(z_0 - z)]}{\sinh(\alpha_n z_0)} + \Phi_{\text{back}}(\alpha_n) \frac{\sinh(\alpha_n z)}{\sinh(\alpha_n z_0)} \right\}. \quad (4)$$

To calculate the  $\phi(x, z)$  for a variety of realistic conductor geometries, we have implemented a general finite-difference program that can take into account both the finite  $\epsilon_r$  and finite substrate thickness. From the resulting scalar potential on the substrate surface, the Fourier coefficients  $\Phi(\alpha_n)$  may be calculated.

The simplest application of Eq. (2) to the longitudinal electro-optic probe examines a focused optical beam of Gaussian profile, with minimum waist radius  $w_0$ , confocal parameter  $b = \pi w_0^2/\lambda$ , and propagation constant  $k = 2\pi/\lambda$  focused through the GaAs to the front surface (Fig. 2).<sup>16</sup> In this simple case, we neglect nonuniform reflection from the surface, multiple internal reflections, optical and electrical transit times, and higher-order Hermite-Gaussian modes, as well as the perturbation of Eq. (3) by the finite substrate thickness. After incorporating a net  $\lambda/4$  wave plate (in Fig. 1, a double pass through an effective  $\lambda/8$  wave plate), we find the filter function  $H(\alpha_n)$ :

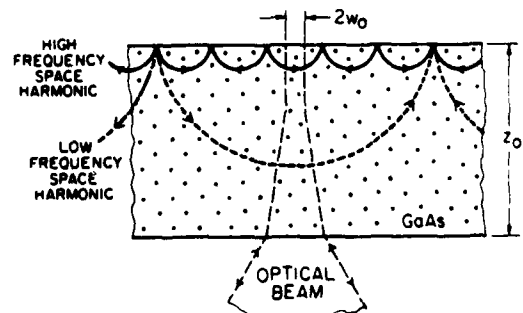


Fig. 2. Illustration of the interaction of the space-harmonic fields with a simple Gaussian beam that is incident from the back side of a GaAs integrated circuit, reflects from the front surface at the focus, and returns along the same path. High-frequency space harmonics are probed only by the waist of the beam; lower-frequency harmonics are also probed by the converging portion, where the optical field is nonplanar.

$$\begin{aligned}
 H(\alpha_n) = & -\frac{2\pi n_0^3 r_{14}}{\lambda_0} \alpha_n \exp(-\alpha_n^2 w_0^2/8) \\
 & \times \int_0^{z_0} \exp(-\alpha_n z) \exp(-\alpha_n^2 z^2/4kb) \\
 & \times \left(1 - \frac{\alpha_n z}{2kb}\right) dz, \quad (5)
 \end{aligned}$$

where  $n_0$  is the unperturbed index of refraction and  $\lambda_0$  is the free-space light wavelength. In Eq. (5), we may identify the term before the integral as describing the waist of the Gaussian at the surface; the exponential in the integrand as the falloff of an individual space harmonic; the Gaussian in the integrand as the changing width of the beam away from the focus; and the linear term as the contribution of the nonplanarity of the optical field. Clearly, a beam with confocal parameter large in comparison with the penetration of the field will possess a filter function  $H(\alpha_n)$  dominated by the simple Gaussian term before the integral in Eq. (5). Similarly, the low-frequency space harmonics, which decay slowly with  $z$ , will be more significantly affected by the finite substrate, the changing beam width, and the nonplanar optical field. This low-frequency filtering results in small distortions of the measured circuit voltage distribution similar to those reported in Ref. 17. In that paper the theory was based on the plane-wave electro-optic model; the full-wave theory presented here includes the effect of beam convergence and, when applied to the large structure in Ref. 17, shows that convergence angles up to the maximum permitted by refraction at the GaAs-air interface detract only slightly from the accuracy of the probe. Since a finite substrate thickness also contributes to the same low-frequency filtering, however, accurate characterization of circuit voltage distributions can be made only when surface conductor features are small in comparison with the substrate thickness.

The general form of Eq. (1) permits evaluation of a variety of problems. Any one of the Hermite-Gaussian modes<sup>16</sup> could be used for  $E^{(o)}$ . If  $E_1^{(o)}$  and  $E_2^{(o)}$  are different modes, Eq. (1) is a complete overlap integral for mode conversion in the presence of spatially varying anisotropic  $\epsilon$ . Materials or devices with highly localized perturbations in  $\epsilon$  may be probed by a submicrometer focused beam and the expected probe response found from Eq. (1). Similarly, devices that rely on  $\Delta\epsilon$  to impart information to a beam but that deviate from the expectations of a simple theory because of material or device defects may be examined in this way. Clearly, all types of electro-optic probes,<sup>5-9,17,18</sup> the recent charge-sensing system,<sup>19</sup> and the differential phase microscope used for index profile measurements<sup>20</sup> may also be analyzed. In particular, the effect of optical standing waves, higher-order optical modes, nonuniform surface reflection, and adjacent conductors on the performance of the longitudinal electro-optic probe can be studied.

In summary, we have described an optical S-parameter analysis that permits the evaluation of polarization changes in a focused optical beam due to a spatially varying anisotropic  $\Delta\epsilon$ . The analysis has applica-

tion to a variety of optical probing techniques as well as to the operation of optoelectronic devices. Using finite difference-field calculations, we have applied the analysis to a simplified form of the longitudinal electro-optic probing system and employed a space-harmonic approach to simplify the numerical evaluation. The characteristics of this, and other, probes under a variety of conditions can be examined. In particular, we have found that even tightly focused beams do not significantly detract from the accuracy of the longitudinal electro-optic probe.

The authors wish to thank D. M. Bloom for fruitful discussions on this work. J. L. Freeman also wishes to acknowledge the fellowship support of the IBM Corporation. This work was performed under U.S. Office of Naval Research contract N00014-85-H-0381 and Wright-Patterson Air Force Base contract F33615-86-C-1126.

## References

1. M. J. W. Rodwell, K. J. Weingarten, J. L. Freeman, and D. M. Bloom, *Electron. Lett.* **22**, 499 (1986).
2. M. J. W. Rodwell, M. Riazat, K. J. Weingarten, and D. M. Bloom, *IEEE Trans. Microwave Theory Tech.* **MTT-34**, 1356 (1986).
3. X.-C. Zhang and R. K. Jain, *Electron. Lett.* **22**, 264 (1986).
4. A. J. Taylor, R. S. Tucker, J. M. Wiesenfeld, C. A. Burrus, G. Eisenstein, J. R. Talman, and S. S. Pei, *Electron. Lett.* **22**, 1068 (1986).
5. J. A. Valdmanis, G. A. Mourou, and C. W. Gabel, *Appl. Phys. Lett.* **41**, 211 (1982).
6. J. A. Valdmanis and G. A. Mourou, *IEEE J. Quantum Electron.* **QE-22**, 69 (1986).
7. B. H. Kolner and D. M. Bloom, *Electron. Lett.* **20**, 818 (1984).
8. B. H. Kolner and D. M. Bloom, *IEEE J. Quantum Electron.* **QE-22**, 79 (1986).
9. J. L. Freeman, S. K. Diamond, H. Fong, and D. M. Bloom, *Appl. Phys. Lett.* **47**, 1083 (1985).
10. A. Yariv, *Introduction to Optical Electronics* (Holt, Rinehart and Winston, New York, 1976), pp. 256-259, 427-430.
11. G. D. Monteath, *Applications of the Electromagnetic Reciprocity Principle* (Pergamon, Oxford, 1973), pp. 57-62.
12. B. Lax and K. J. Button, *Microwave Ferrites and Ferromagnetics* (McGraw-Hill, New York, 1962), pp. 537-539.
13. R. Ulrich and A. Simon, *Appl. Opt.* **13**, 2241 (1979).
14. J.-I. Sakai and T. Kimura, *IEEE J. Quantum Electron.* **QE-17**, 1041 (1981).
15. H. Engan, *IEEE Trans. Electron Devices* **ED-16**, 1013 (1969).
16. H. A. Haus, *Waves and Fields in Optoelectronics* (Prentice-Hall, Englewood Cliffs, N.J., 1984), pp. 108-118.
17. Z. H. Zhu, J.-P. Weber, S. Y. Wang, and S. Wang, *Appl. Phys. Lett.* **49**, 434 (1986).
18. J. A. Valdmanis and S. S. Pei, in *Digest of Topical Meeting on Picosecond Electronics and Optoelectronics* (Optical Society of America, Washington, D.C., 1987), pp. 4-6.
19. H. K. Heinrich, D. M. Bloom, and B. R. Hemenway, *Appl. Phys. Lett.* **48**, 1066 (1986).
20. H. Chung, L. M. Walpita, and W. S. C. Chang, *Appl. Opt.* **25**, 3014 (1986).

## Appendix V

Excerpts of Ref. 1.47 and 5.12:

K.J. Weingarten, "Gallium Arsenide Integrated Circuit Testing Using Electrooptic Sampling," Ph.D. Thesis, Stanford University, Stanford CA, 1987.

- |  |           |
|--|-----------|
| (1) Accuracy, Crosstalk, and Spatial Resolution    | (2.1.2)   |
| (2) Linearity                                      | (2.1.3)   |
| (3) Invasiveness of the Electro-Optic Probing Beam | (2.1.4)   |
| (4) References for Chapter 2                       | (2.7)     |
| (5) The Electro-Optic Probing System               | (3.0-3.5) |
| (6) Integrated Circuit Measurements                | (4.1-4.5) |

Reprinted by Permission

GALLIUM ARSENIDE INTEGRATED  
CIRCUIT TESTING  
USING ELECTROOPTIC SAMPLING

by  
Kurt J. Weingarten

A Dissertation

Supported by  
AFOSR Contract # F49620-85-K-0016  
AFWAL Contract # F33615-86-C-1126

Ultrafast Electronics Laboratory  
Edward L. Ginzton Laboratory  
W.W. Hansen Laboratories  
Stanford University  
Stanford, California 94305

December 1987

## Abstract

Gallium arsenide (GaAs) integrated circuits (IC's) and other III-IV compound semiconductors have demonstrated operation speeds greater than the time resolution of conventional test instruments used for their characterization. In addition, digital GaAs IC's such as static frequency dividers have demonstrated clock rates greater than 20 GHz, frequencies where circuit models are poorly refined and influenced by layout-dependent parasitics. Conventional test instruments using contact probes are limited to monitoring input and output test points of these circuits. Probing at internal nodes, however, would greatly ease analysis of the circuit's operation.

To address these issues, an electrooptic sampling system has been developed at Stanford to measure internal-node signals in GaAs IC's with picosecond time resolution. Infrared light is focused through the GaAs IC substrate to detect voltages via the electrooptic effect, and a laser system generating ultrashort light pulses repetitively samples the signal to achieve picosecond time resolution. To obtain realistic testing conditions, a microwave synthesizer for providing excitation to the IC is synchronized to the repetition rate of the optical pulses, allowing equivalent-time sampling of the IC response.

The electrooptic sampling system and its performance characteristics for IC testing are described, and a number of test results are presented. The system has 2 picosecond time resolution or a corresponding bandwidth greater than 100 gigahertz, and a voltage sensitivity of 70 microvolts per root Hertz. On digital IC's, propagation delays and switching signals of digital test circuits such as inverter chains, frequency dividers, and multiplexers have been measured. On microwave IC's, small-signal and large-signal response of microwave amplifiers have been measured. A technique to measure S-parameters of a circuit using the optical probe has been developed, allowing the measurement reference plane to be positioned on the IC and eliminating the need for physical calibration standards.

### 2.1.2. Accuracy, Crosstalk, and Spatial Resolution

The accuracy of the electrooptic probe in Fig 2.4 depends on two key approximations. Is the plane-wave approximation appropriate for the optical probe (particularly when focusing tightly to probe interconnects whose width is near an optical wavelength) and does the substrate voltage at the probe position accurately equal the conductor voltage?

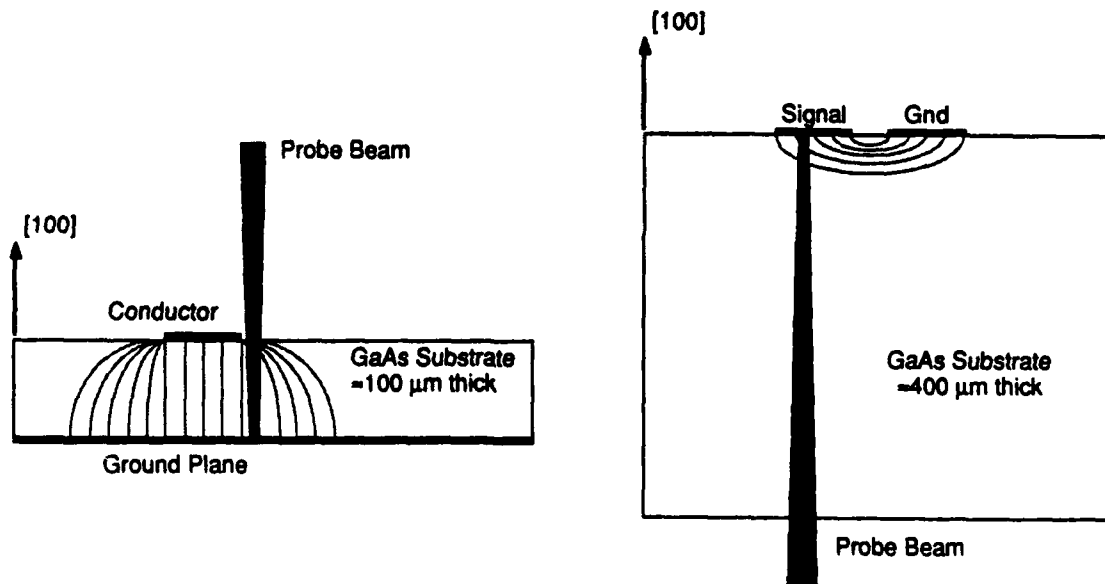


Fig. 2.3. Reflection probing geometries for IC's. Frontside probing is for circuits with microstrip transmission line, and the spot size is focused to 10-20  $\mu\text{m}$  typically. Backside probing is for circuits with planar transmission line such as coplanar waveguide, or circuits with standard metal interconnects. The spot size is typically 3-5  $\mu\text{m}$  in this case.



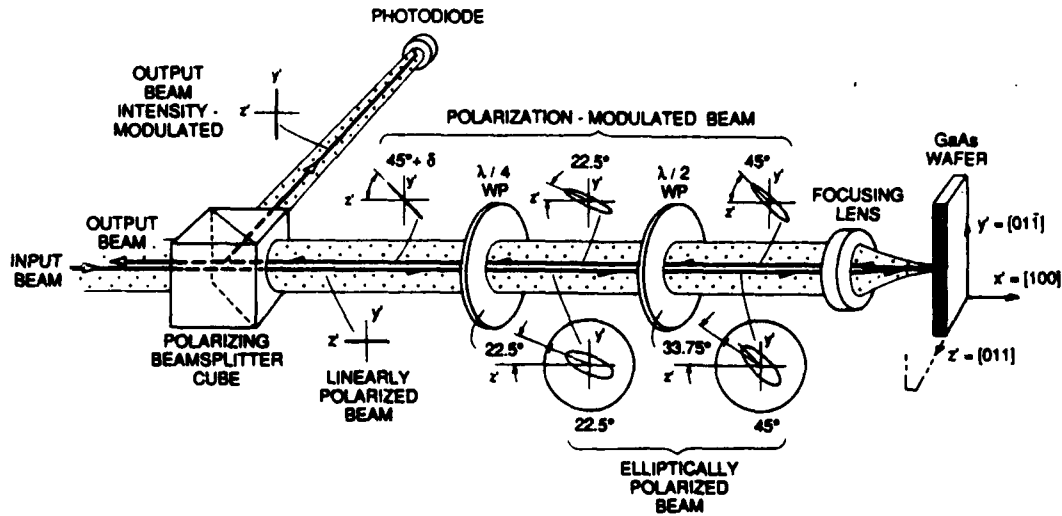


Fig. 2.4. Coaxial optical arrangement for separation of incident and reflected beams for the IC probing geometries of Fig. 2.3. The text gives a qualitative description of the polarization states and Appendix A gives a quantitative Jones-vector calculation description.

Corrections to the plane-wave approximation have been investigated with full field modeling of the optical probe [2.9] to take into account the focused beam and the field distribution for representative conductor geometries. The affect of a focused beam on the relative phase shifts through the GaAs was found to be negligible for backside probing when the spot size was greater than an optical wavelength, a condition met by typical experimental conditions. The substrate voltage, however, may not accurately reflect the signal voltage on planar conductors when the spacings between signal and ground conductors are a significant fraction of the substrate thickness.

To evaluate some limits on the accuracy of the optical probe, a simple model similar to Ref 2.9 is developed. Laplace's equation is solved for a structure consisting of a semi-infinite GaAs substrate with an arbitrary spatial voltage distribution on its frontside. A general solution to Laplace's equation for this structure is

$$\phi(x,z) = \int_{-\infty}^{\infty} \Phi(\alpha) \exp(-|\alpha|z) \exp(-j\alpha x) d\alpha \quad (2.11)$$

where  $\phi(x,z)$  is the two dimensional potential,  $\alpha$  is the spatial frequency, and

$$\Phi(\alpha) = \int_{-\infty}^{\infty} v(x) \exp(-j2\pi f\alpha x) dx \quad (2.12)$$

is the spatial Fourier transform of the voltage distribution on the frontside. Equation (2.11), the two-dimensional potential distribution, can be expressed as the Laplace transform of the Fourier transform of the frontside voltage spatial distribution.

$$\phi(s) = 2\mathcal{L} \{ \Phi(\alpha) \} = 2 \int_0^{\infty} \Phi(\alpha) \exp(-s\alpha) d\alpha \quad (2.13)$$

where  $\mathcal{L}$  is the one-sided Laplace transform and  $s = z + jx$ . Representative voltage distributions can be analytically solved if the Laplace transform of the spatial Fourier transform is known. Then, as a first approximation, the difference between the frontside potential and the backside potential at a distance  $L$ , as determined by  $\phi(s)$ , gives a limit to the accuracy with which the optical probe measures the conductor voltage.

Consider a rectangular voltage distribution, Fig. 2.5. The rectangle function is defined as [2.10]

$$\text{rect}(x) = \begin{cases} 1 & |x| < \frac{1}{2} \\ 0 & |x| > \frac{1}{2} \end{cases} \quad (2.14)$$

Then, the voltage distribution and its spatial Fourier transform are

$$v(x) = \text{rect}\left(\frac{x}{w}\right) \leftrightarrow V(\alpha) = w \text{sinc}(w\alpha) \quad (2.15)$$

where  $w$  is the width of the voltage profile and  $\text{sinc}(w\alpha) = \sin(\pi w\alpha)/(\pi w\alpha)$ . The Laplace transform of the sinc function is [2.11]

$$\phi(x,z) = 2\mathcal{L} \{ w \text{sinc}(w\alpha) \} = \frac{2}{\pi} \tan^{-1}\left(\frac{\pi w}{s}\right) \quad (2.16)$$

Evaluating this at the points  $(x,z) = (0,0)$  and  $(0,L)$ , the ratio of the substrate voltage to the conductor voltage is

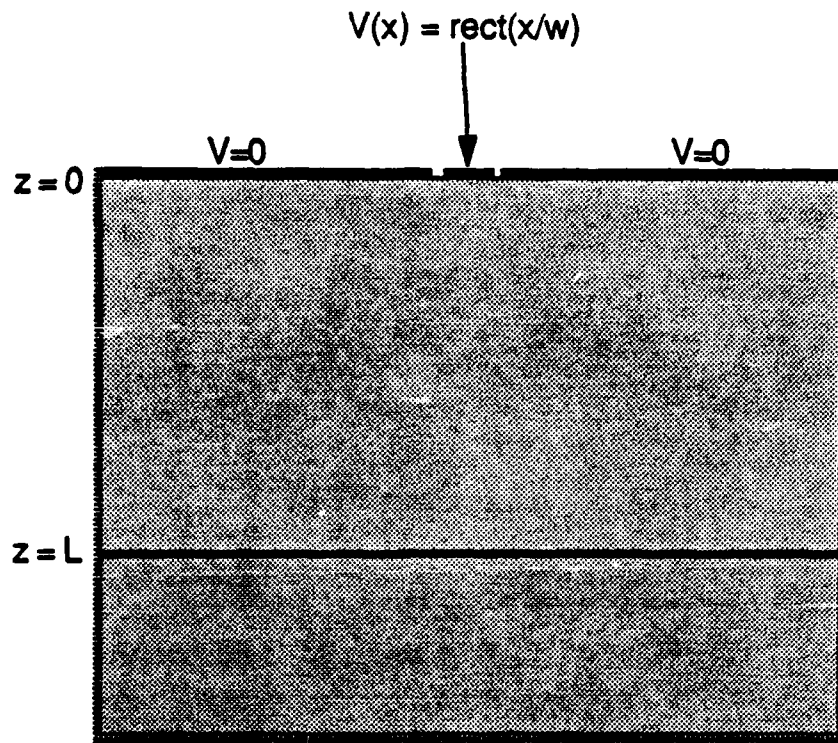


Fig. 2.5. Substrate voltage accuracy model. The top of the substrate has a rectangular voltage distribution of width  $x$  and the substrate thickness is semi-infinite in the  $z$  direction. The voltage the optical probe measures is approximated by calculating the voltage at a cut  $z=L$  through the substrate.

$$\begin{aligned}
 v_{front} - v_{back} &= \phi(0,0) - \phi(0,L) \\
 &= 1 - \frac{2}{\pi} \tan^{-1} \left( \frac{\pi w}{L} \right) \\
 &\approx 1 - 2 \frac{w}{L} \quad \text{for } \frac{w}{L} \lesssim 0.2
 \end{aligned}
 \tag{2.17}$$

The rectangle function can be used as an approximation to the voltage on a coplanar waveguide transmission line, for example, where  $w$  is the conductor width plus the gap width.

Crosstalk is the amount of signal optically detected from a nearby signal conductor when the probe beam is focused onto a conductor with no signal. This error is similar to accuracy errors due to the substrate voltage, i.e. a signal on a nearby conductor can change the backside potential underneath a conductor with no signal. A estimate for closely-spaced

conductors would be the same function as (2.16)) for  $w/L$  small, since only low-frequency spatial voltages affect the backside potential - it changes very little over the space of several conductor widths  $w$ . When the probe is on a conductor with no voltage, the measured substrate voltage is

$$v_{front} - v_{back} = \frac{2}{\pi} \tan^{-1} \left( \frac{\pi w}{L} \right) \quad (2.18)$$

$$= 2 \frac{w}{L} \quad \text{for } \frac{w}{L} \lesssim 0.2$$

due to crosstalk from the nearby signal conductor.

On circuits with conductor spacing large compared to the substrate thickness, spatial resolution on IC's could be set by required limits on the voltage accuracy and crosstalk. However, accuracy improves and crosstalk decreases due to substrate voltage effects as conductor spacings decrease, and well-designed microwave interconnects should have a spatial resolution set by the optical spot size. Diffraction-limited focusing of the  $1.06 \mu\text{m}$  wavelength probe has a minimum spot diameter (full-width half maximum) of

$$d_0 \equiv \frac{\lambda \sqrt{1 - NA^2}}{2NA} \quad (2.19)$$

where  $\lambda$  is the optical wavelength and  $NA$  is the numerical aperture of the focusing lens. With a high  $NA$  lens spot sizes approaching the optical wavelength are possible. Standard microscope objectives (focal length of 8 mm and  $NA$  of 0.4, for example) routinely achieve spot sizes of  $3 \mu\text{m}$ , suitable for probing most IC interconnects but not for probing very small features such as sub-micron gate lines. Since the GaAs substrate has a relatively large refractive index,  $n = 3.6$ , an "immersion"-type lens, indexed matched to the GaAs, would allow focusing to a diffraction limit set by the optical wavelength in the GaAs,  $\lambda = 0.3 \mu\text{m}$ .

### 2.1.3. Linearity

Because typical circuit voltages are small compared to the half-wave voltage  $V_{\pi}$ , the probe beam intensity modulation is small and very nearly linear with respect to the probed voltage. Kolner 2.4 has a full analysis of the linearity and dynamic range of the probe due to

the sinusoidal dependence of the probe intensity for different optical bias conditions. At the quarter-wave optical bias, the typical experimental setting and described by (2.8), the linearity range can be determined by including the linear and cubic terms in a Taylor series expansion of the sinusoid

$$\sin\left(\frac{\pi V_a}{V_\pi}\right) = \left(\frac{\pi V_a}{V_\pi}\right) + \frac{1}{6}\left(\frac{\pi V_a}{V_\pi}\right)^3 + \dots \quad (2.20)$$

The cubic term equals the minimum detectable voltage  $V_{min}$  due to shot noise for 1 mA photocurrent (Section 2.4.1) when the applied voltage  $V_a = 31$  volts, a dynamic range of 120 dB before *any* nonlinear response can be detected. For a linear response to within 1% for the signal voltage, the dynamic range is 140 dB above  $V_{min}$  under these conditions.

#### 2.1.4. Invasiveness

One important feature of optical probing of IC's is the non-contact, non-destructive nature of the technique. Compared to conventional electrical probes, the optical probe makes no mechanical contact to the IC (avoiding physical damage to the circuit), does not require the test point to drive a 50  $\Omega$  load impedance, and has no parasitic impedances. The lack of parasitic impedances is an important characteristic for measurement frequencies in the upper microwave and millimeter-wave region, where even the small parasitic impedances of well-designed electrical probes become significant.

However, the optical probe can perturb the circuit either by photogenerating carriers, which then change the substrate conductivity and generate photorefractive or photovoltaic potentials, or by the inverse electrooptic effect (optical rectification). Direct band-to-band absorption of the probe beam is avoided because the photon energy of the 1.06  $\mu\text{m}$  optical probe, 1.17 eV, is well below the bandgap energy, 1.42 eV, of GaAs. The presence of impurities in the GaAs results in deep levels (primarily the EL2 level), i.e. the presence of allowed electron states at energies near mid-bandgap, and these levels absorb some of the 1.06  $\mu\text{m}$  light in the GaAs and generate free carriers. Absorption can also occur if the probe beam is too intense. With tight beam focusing and short pulse duration, probe beams of average intensities of  $\approx 100$  mW have peak pulse intensities sufficient for two-photon band-to-band absorption.

The changes due to the optical beam are dominated by deep-level absorption. The signal generated by the probe beam has two parts. A fast response, consisting of a pulse  $\approx 25$  mV or less in amplitude with a risetime of  $\approx 100$  ps and a falltime of  $\approx 0.5$  ns

(corresponding to the carrier recombination time in the GaAs), dies away quickly enough (well before the next probe pulse) that its circuit perturbation is considered negligible. A typical slow, or DC, response is shown by Fig. 2.6. The data is well fit by a quadratic curve, and a simple equivalent circuit model can be derived for the probe (Fig. 2.7), based on this empirical data. For the test structure used, a CPW transmission line consisting of gold deposited directly on the GaAs, the probe has an open-circuit voltage of 175 mV, a short-circuit current of 1.1  $\mu$ A, and a nonlinear resistance varying from 220 k $\Omega$  (open-circuit load) to 100 k $\Omega$  (short-circuit load). The maximum electrical power delivered by the probe beam is about 40 nW (at a load resistance of 160 k $\Omega$ ), corresponding to a conversion efficiency with the 75 mW probe beam of  $\eta = 5 \times 10^{-5}\%$ . These specific values, based on the empirical data, will vary somewhat depending on the circuit metalization, layout, and substrate type, but the qualitative probe circuit model should apply. For example, shining the probe directly on a Schottky diode produces a curve similar to a photovoltaic cell where the open circuit voltage and short circuit current are a function of the optical power and the amount of light absorbed in the diode.

On circuits, small changes in the gain of microwave distributed amplifiers are observed when an intense 125 mW probe beam at 1.06  $\mu$ m wavelength is applied (Fig. 2.8). Focusing *directly* within the active FET channel causes significant changes in drain current. However, the probe is not focused within the device for circuit measurements, but on the adjacent metal interconnects. Circuit perturbation can be reduced further by reducing the probe beam intensity by as much as factor of ten without severe degradation of the system sensitivity (Section 2.4.1). Residual absorption of the probe also can be reduced by increasing the probe wavelength from 1.06  $\mu$ m to 1.3  $\mu$ m, where the absorption due to the EL2 deep level is reduced by a factor of 5 [2.12,2.13].

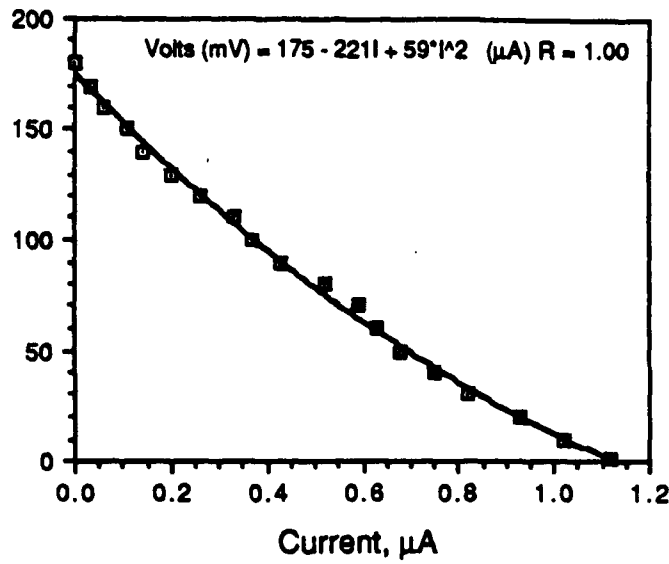


Fig. 2.6. Photogenerated DC signal for the optical probe on a CPW transmission line fabricated by depositing gold directly on the GaAs.

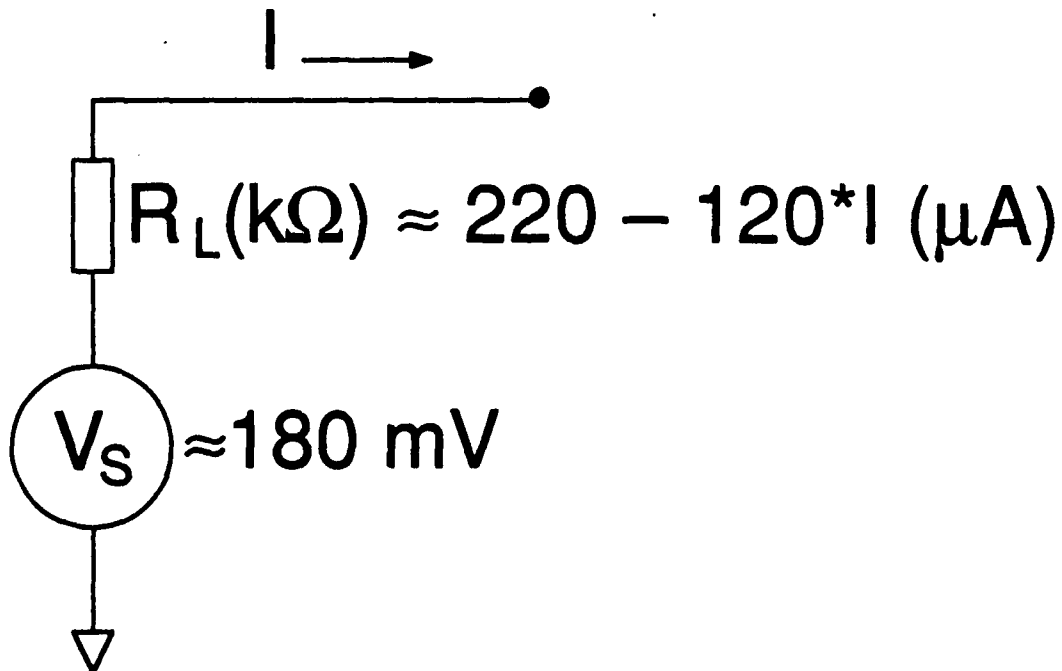


Fig. 2.7. Empirical circuit model for optical probe invasiveness based on the data of Fig. 2.6.

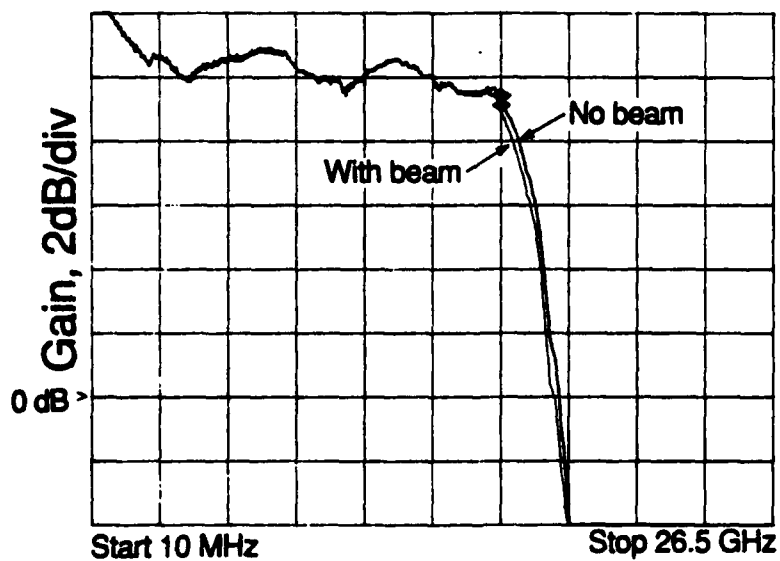
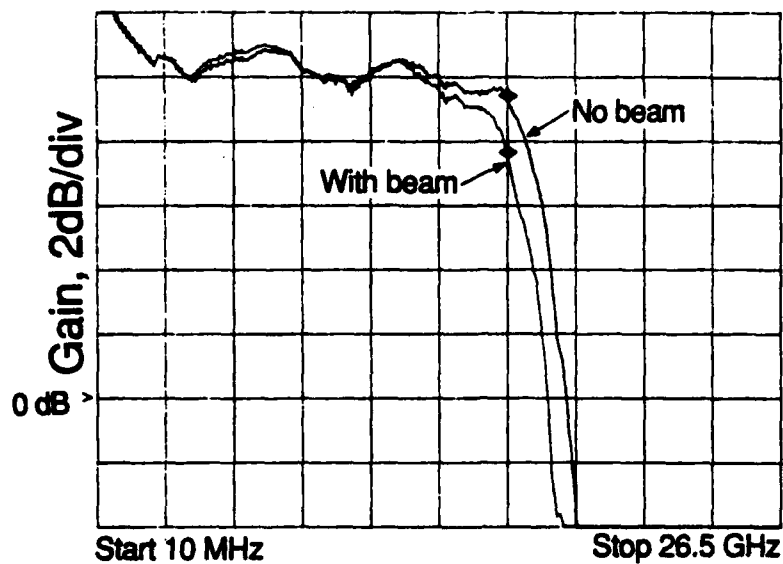


Fig. 2.8. Probe-induced perturbation of the gain of a microwave IC amplifier measured on a scalar network analyzer with and without a 125 mW probe beam. Top: Worst case perturbation with the probe beam focused on the gate of one of the amplifier FET's. Drain current of the amplifier varies from 167 mA (beam off) to 230 mA (beam on). Bottom: Typical case with the beam focused on the input pad. Drain current of the amplifier varies from 167 mA (beam off) to 187 mA (beam on).



## 2.7. References for Chapter 2

- 2.1 I.P. Kaminow, *An Introduction to Electro-Optic Devices*. New York: Academic Press, 1974.
- 2.2 I.P. Kaminow and E.H. Turner, "Electrooptic light modulators," *Proc. IEEE*, vol. 54, pp. 1374-1390, 1966.
- 2.3 B.H. Kolner and D.M. Bloom, "Direct electrooptic sampling of transmission-line signals propagating on a GaAs substrate," *Elect. Lett.*, vol. 20, pp. 818-819, 1984.
- 2.4 B.H. Kolner and D.M. Bloom, "Electrooptic sampling in GaAs integrated circuits," *IEEE J. Quant. Elect.*, vol. QE-22, pp. 79-93, 1986.
- 2.5 A. Yariv and P. Yeh, *Optical Waves in Crystals*, New York: New York: John Wiley & Sons, Inc, 1984, pp. 286-287.
- 2.6 *Ibid*, p. 230.
- 2.7 *Ibid*, pp. 241-243.
- 2.8 J.L. Freeman, S.K. Diamond, H. Fong, and D.M. Bloom, "Electrooptic sampling of planar digital integrated circuits," *Appl. Phys. Lett.*, vol. 47, pp. 1083-1084, 1985.
- 2.9 J.L. Freeman, S.R. Jeffries, and B.A. Auld, "Full field modeling of the longitudinal electrooptic probe," *Optics Letters*, vol. 12, pp. 795-797, 1987.
- 2.10 R.N. Bracewell, *The Fourier Transforms and its Applications*, New York: McGraw-Hill, 1978, p. 52.
- 2.11 Murray R. Spiegel, *Mathematical Handbook of Formulas and Tables*, Schaum's Outline Series in Mathematics, McGraw-Hill Book Company, New York, 1968, pp. 161-173.
- 2.12 G.M. Martin, "Optical assessment of the main electron trap in bulk-semi-insulating GaAs," *Appl. Phys. Lett.*, vol. 39, pp. 747-748, 1981.
- 2.13 P. Dobrilla and J.S. Blakemore, "Experimental requirements for quantitative mapping of midgap flaw concentration in semi-insulating GaAs wafers by measurement of near-infrared transmittance," *J. Appl. Phys.*, vol. 58, pp. 208-218, 1985.
- 2.14 W.H. Knox, R.L. Fork, M.C. Downer, R.H. Stolen, and C.V. Shank, "Optical pulse compression to 8 fs at a 5-kHz repetition rate," *Appl. Phys. Lett.*, vol. 46, pp. 1120-1121, 1985.
- 2.15 C.H. Brito-Cruz, R.L. Fork, and C.V. Shank, "Compression of optical pulses to 6 fs using cubic phase distortion compensation," *Technical Digest of the 1987 Conference on Lasers and Electrooptics*, pp. 12-13.

- 
- 2.16 A.S. Gouveia-Neto, A.S.L. Gomes, and J.R. Taylor, "Generation of 33-fsec pulses at 1.32  $\mu\text{m}$  through a high-order soliton effect in a single-mode optical fiber," *Optics Letters*, vol. 12, pp. 395-397, 1987.
- 2.17 B. Zysset, W. Hodel, P. Beaud, and H.P. Weber, "200-femtosecond pulses at 1.06  $\mu\text{m}$  generated with a double-stage pulse compressor," *Optics Letters*, vol. 11, pp. 156-158, 1986.
- 2.18 Bracewell, p. 110.
- 2.19 R.E. Collins, *Foundations of Microwave Engineering*, New York: McGraw-Hill, 1966.
- 2.20 K.J. Weingarten, M.J.W. Rodwell, J.L. Freeman, S.K. Diamond, and D.M. Bloom, "Electrooptic sampling of gallium arsenide integrated circuits," *Ultrafast Phenomena V*, ed. by G.R. Fleming and A.E. Siegman, Springer Ser. Chem. Phys., Vol. 46, New York: Springer-Verlag, 1986, pp. 98.
- 2.21 Bracewell, pp.115-116.
- 2.22 M.J.W. Rodwell, K.J. Weingarten, D.M. Bloom, T. Baer, and B.H. Kolner, "Reduction of timing fluctuations in a mode-locked Nd:YAG laser by electronic feedback," *Optics Letters*, vol. 11, pp. 638-640, 1986.

## Electrooptic Sampler System

The design of the experimental electrooptic sampling system described in this chapter has several goals: to non-invasively measure voltage signals within the IC with picosecond time resolution, to probe IC's under realistic test conditions, and to emulate conventional instruments to obtain easily interpretable data. To achieve these goals, the system uses direct electrooptic voltage probing of the substrate, synchronization of the laser pulse repetition rate to a microwave synthesizer to allow for repetitive sampling of the IC response, and a signal processing system that allows for emulation of either a vector voltmeter or a sampling oscilloscope.

The sampling system, shown schematically in Fig. 3.1, can be grouped into three sections; the laser system for optical pulse generation, the microwave instrumentation for driving the IC under test, and the receiver system for signal processing and data acquisition. These systems and their operating characteristics are described in the following sections.

Substrate electrooptic sampling has also been demonstrated using mode-locked or gain-switched InGaAsP diode lasers to generate sampling pulses of 10-20 ps pulsewidth [3.1,2]. This system uses two synthesizers, referenced to a master clock, one to drive the laser and one to supply a signal to the IC. The injection laser pulses have sub-picosecond timing jitter and the laser is a very compact and stable optical source with a continuously tunable pulse repetition rate. This system has been used to measure electrical signals in both GaAs and InP (indium phosphide) IC's [3.3].

### 3.1. The Laser System

The laser system consists of a mode-locked Nd:YAG laser, a fiber-grating pulse compressor, and a timing stabilizer feedback system. The Nd:YAG laser produces 1.06  $\mu\text{m}$ , 90 ps pulses at an 82 MHz rate with free-running pulse-to-pulse timing fluctuations of 4 ps rms. A wavelength in the near-infrared where GaAs has low absorption is required. A phase-lock-loop feedback system [3.4,5] synchronizes and stabilizes the laser pulse timing with respect to the microwave synthesizer, reducing the pulse-to-pulse jitter to less than 300 fs rms. The fiber-grating pulse compressor shortens the pulses to 1.5 ps [3.6]. The

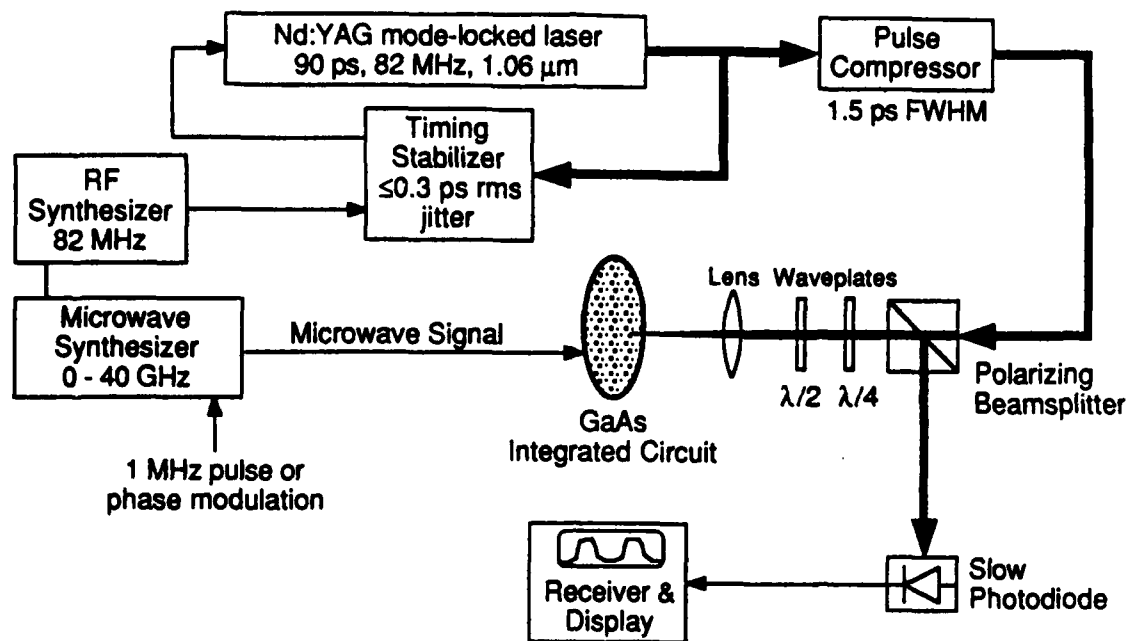


Fig. 3.1. Electrooptic sampler system schematic.

beam passes through a polarizing beamsplitter and two waveplates to adjust its polarization (Section 2.1.1.), then is focused through the IC substrate with a microscope objective to a  $3\ \mu\text{m}$  spot on the probed conductor (backside probing) or a  $10\ \mu\text{m}$  spot on the ground plane beneath and adjacent to the probed conductor (frontside probing). The reflected light is analyzed by the polarizing beamsplitter and detected by a photodiode connected to a photodiode receiver and synchronous detector.

### 3.1.1. Fiber-Grating Pulse Compressor

To reduce the pulsewidth, a fiber-grating pulse compressor is used [3.6,7]. This system is based on the Kerr effect or self-phase modulation (SPM) in a single-mode optical fiber. The laser output is launched into the fiber core, and through SPM, a frequency chirp is generated on each laser pulse as it propagates through the fiber. The light emerging from the fiber is red-shifted on its leading edge and blue-shifted on its the trailing edge, with the frequency variation (as a function of time) proportional to the derivative of the pulse intensity. For a Gaussian intensity pulseshape (characteristic of Nd:YAG mode-locked lasers) the frequency chirp is nearly linear over the center of the pulse. The new frequency components generated by SPM are recombined into a compressed pulse by passing the light through a grating pair, where the time-of-flight delay is proportional to the light's wavelength. The grating pair then acts as a dispersive delay line where the red-shifted leading frequency components are delayed with respect to the blue-shifted trailing frequencies. The

separation of the gratings is adjusted to match the frequency chirp of the light, so that all the spectral components of the pulse arrive together at the grating pair output, producing a compressed pulse.

Using a 1 km fiber length in the pulse compressor, the group velocity dispersion (GVD) enhances the region of linear frequency chirp [3.8], and the pulses from the mode-locked Nd:YAG laser are routinely compressed from 90 ps to 1.5 ps or less, a factor of 60:1. With two-stage optical compression, pulses as short as 200 fs at 1.06  $\mu\text{m}$  have been generated [3.9], and using other nonlinear fiber techniques, pulses as short as 19 fs have been generated [3.10,11] at infrared wavelengths.

A number of effects limit the amount of pulse compression available with this technique. Deviation from a linear frequency chirp on the pulse due to non-ideal input pulse-shapes can generate pedestals on an otherwise short compressed pulse, and stimulated Raman scattering limits the maximum optical power focused into the fiber core. Excess intensity noise can increase on the compressed pulsetrain due to stimulated Raman scattering and other nonlinear processes, degrading the signal-to-noise ratio for electrooptic measurements.

### **Non-ideal Pulseshape**

The compressed pulsewidth, measured with an optical intensity autocorrelator, deviates from the autocorrelation of an ideal Gaussian pulse as evidenced by slight "wings" or pedestals on the pulse due to the non-ideal frequency chirp of input pulse. Figure 3.2 shows a measured compressed pulse compared to an ideal 1.4 ps Gaussian pulse autocorrelation. The GVD of the 1 km fiber reduces the pulse pedestals compared to shorter fiber lengths [3.8], such as for the pulse compressed with a 100 m fiber length shown in Fig. 3.3. The reshaping of the pulse due to GVD is evident from Fig. 3.4, which shows the measured pulse from the output of the 1 km fiber (before compression by the grating pair) as a function of average pump power. As the pump power increases, the frequency chirp grows and broadens the pulse due to GVD spreading the chirped frequencies, approaching a flat top shape (within the  $\approx 60$  ps time resolution of the measurement) at  $P_{\text{out}} = 0.4$  W. Above this pump power, stimulated Raman scattering begins and the pump pulse becomes distorted.

The power spectrum of the compressed pulse is determined by numerically Fourier transforming the autocorrelation. A Gaussian pulse of 1.4 ps FWHM duration has spectral content extending past 200 GHz, while the spectral content of the compressed pulse deviates from an ideal Gaussian pulse, as shown in Fig. 3.5.

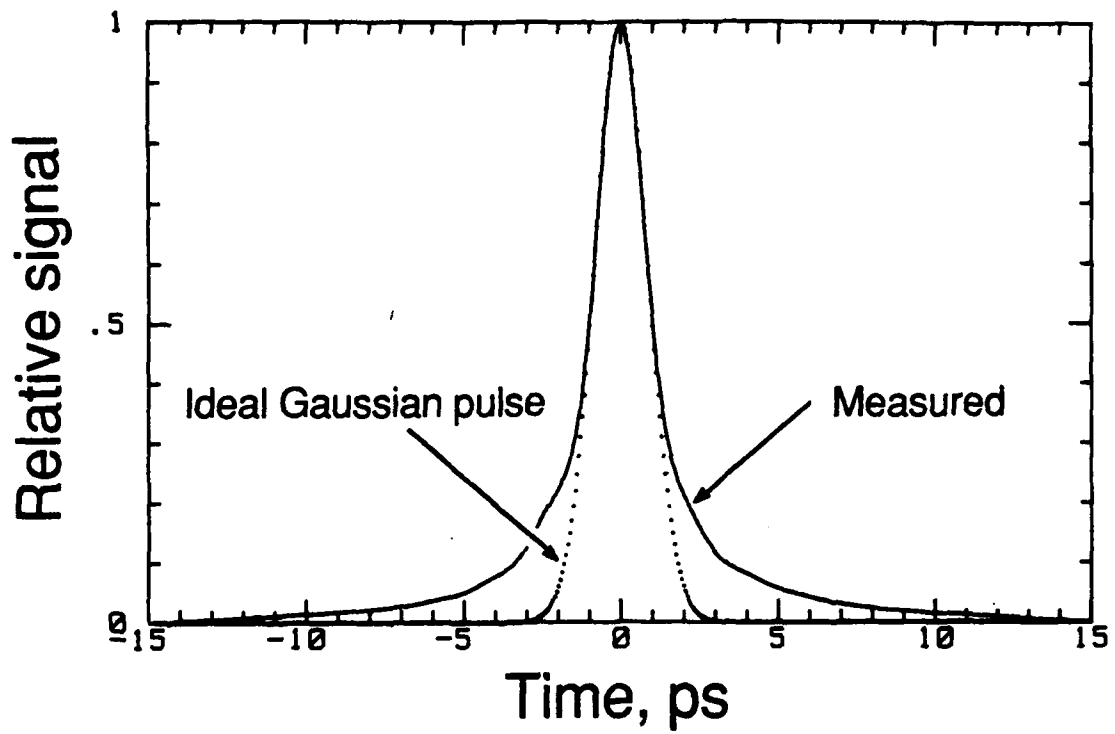


Fig. 3.2. Autocorrelation of compressed pulse using a 1 km fiber (solid line) compared to an ideal 1.4 ps FWHM Gaussian pulse (dashed line).

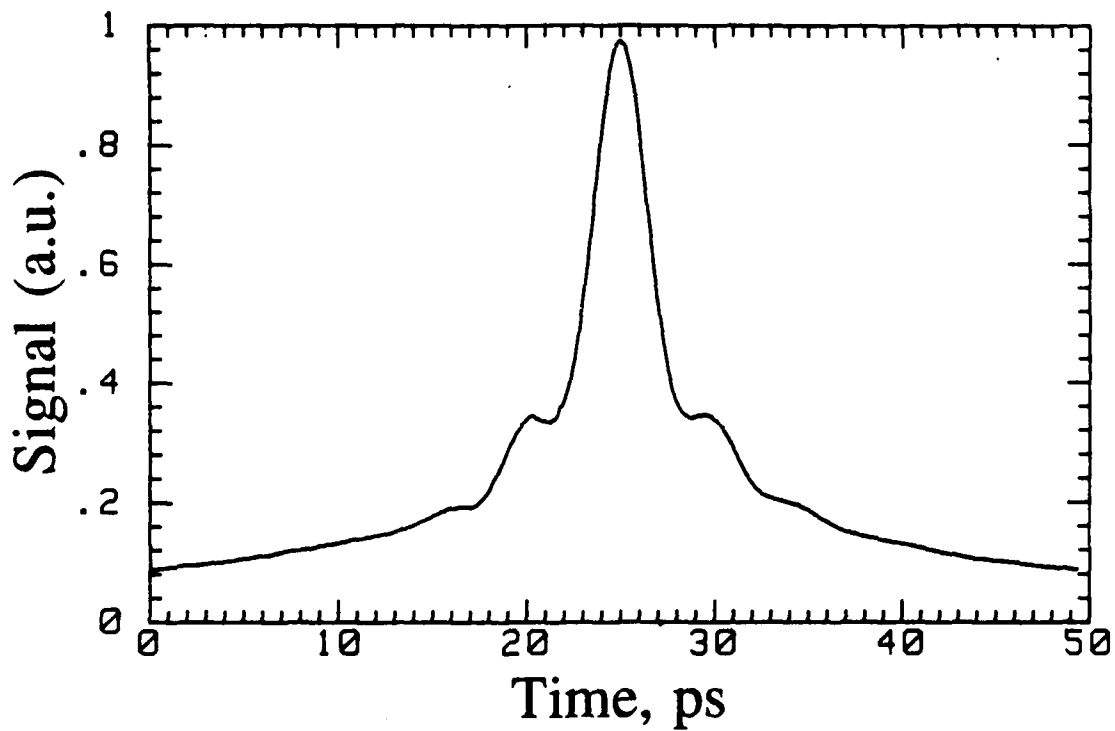


Fig. 3.3. Autocorrelation of a compressed pulse using a 100 meter fiber. The shorter fiber has negligible GVD resulting in larger wings on the pulse than with the 1 km fiber.

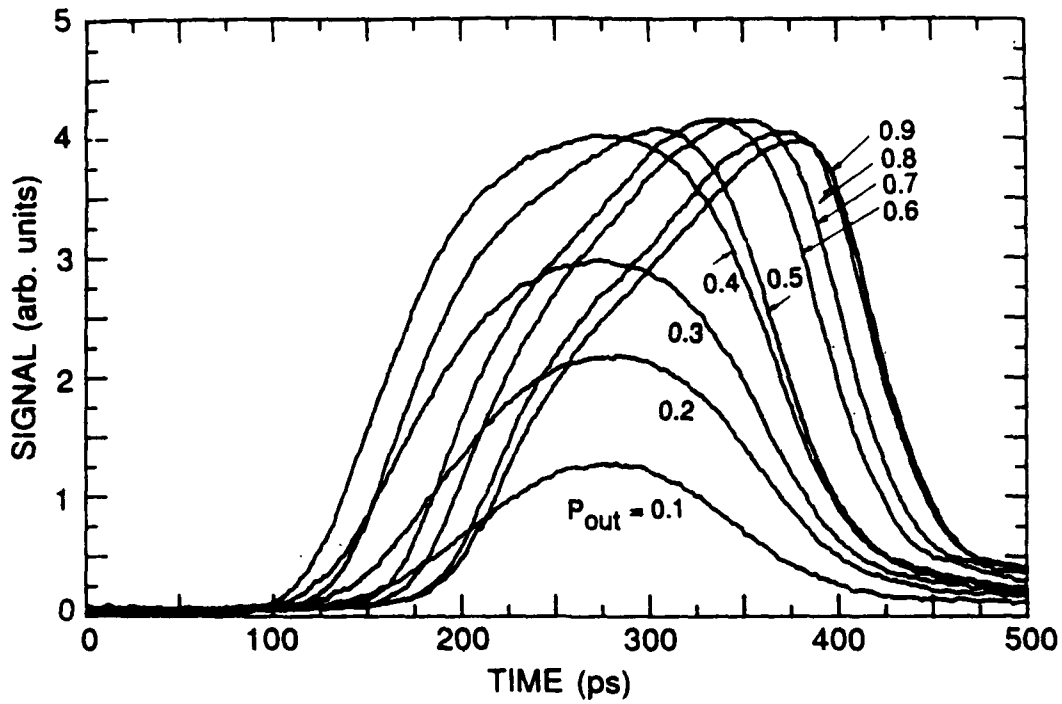


Fig. 3.4. Chirped pulse out of the fiber as a function of the average power  $P_{out}$  out of the fiber. The pulse is measured with a fast photodiode/sampling oscilloscope with an overall response time of  $<50$  ps.

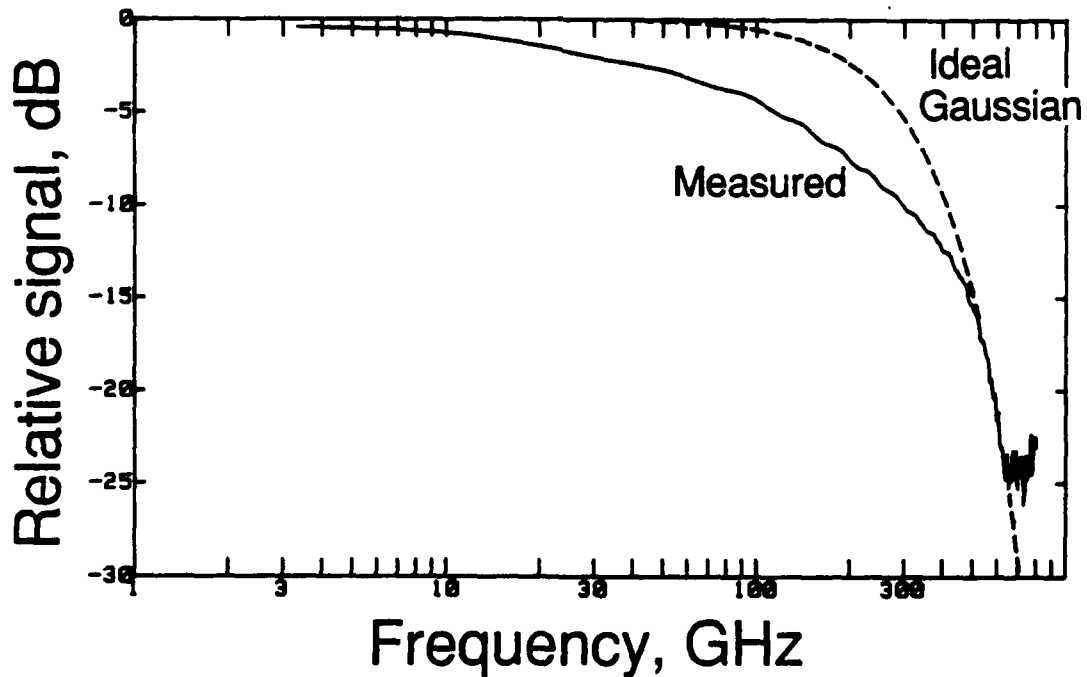


Fig. 3.5. Power spectral density of the compressed pulse of Fig. 3.2 (solid line) compared to a 1.4 ps ideal Gaussian pulse (dashed line).

The wings on the compressed pulse may be further reduced by "spectral windowing" [3.12] to remove part of the nonlinear frequency chirp, or polarization discrimination of the compressed pulse [3.13,14].

### Stimulated Raman Scattering

Stimulated Raman scattering (SRS) has gain proportional to the pump intensity and interaction length, setting an upper limit to the intensity in the fiber and an upper limit to pulse compression. SRS has frequency shift in glass is  $440 \text{ cm}^{-1}$ , a wavelength shift from  $1.06 \text{ }\mu\text{m}$  to  $1.12 \text{ }\mu\text{m}$ . The Raman threshold pump power is predicted to be [3.15]

$$P_{th} = \frac{30A}{GL} \quad (3.1)$$

where  $A$  is the effective core area of the fiber,  $G$  is the Raman gain  $9.2 \times 10^{-12}$ , and  $L$  is the effective interaction length in the fiber. The fiber has a core diameter of approximately  $7 \text{ }\mu\text{m}$ , dispersion of  $35 \text{ ps/nm}\cdot\text{km}$  at  $1.06 \text{ }\mu\text{m}$ , and an interaction length is set by dispersion-induced walkoff between the pump and Raman pulses. One advantage of the long  $1 \text{ km}$  fiber is that SPM occurs over the entire fiber length by SRS is limited by the dispersion-induced walkoff length. The interaction length could be estimated as the time for a Raman pulse to walk-off a pump pulse by one FWHM. However, this tends to underestimate the interaction length because the pump pulse broadens as it propagates through the fiber through SPM and the dispersion. A better way to determine the interaction length is to determine the temporal separation between the pump pulse and the Raman pulse at the output of the fiber. From this measurement, shown in Fig. 3.6, the walkoff length is calculated to be  $140 \text{ meters}$ , and the Raman threshold is  $P_{th} = 90 \text{ W}$ . For the pump pulses repeating at an  $82 \text{ MHz}$  rate, the average power resulting in this peak power

$$P_{avg} = \sqrt{\frac{\pi}{4 \ln 2}} T_{fwhm} f_0 P_{peak} \quad (3.2)$$

is  $P_{avg} = 700 \text{ mW}$ , where  $T_{fwhm}$  is the pulsewidth,  $f_0$  is the pulse repetition rate, and  $P_{peak}$  is the peak power.

In addition, a resonant effect in longer fibers can further reduce the Raman threshold. The high gain of the SRS and 4% Fresnel reflection at each end facet form a parasitic synchronously-pumped fiber-Raman laser [3.16]. Dispersion sets the pump walkoff length of



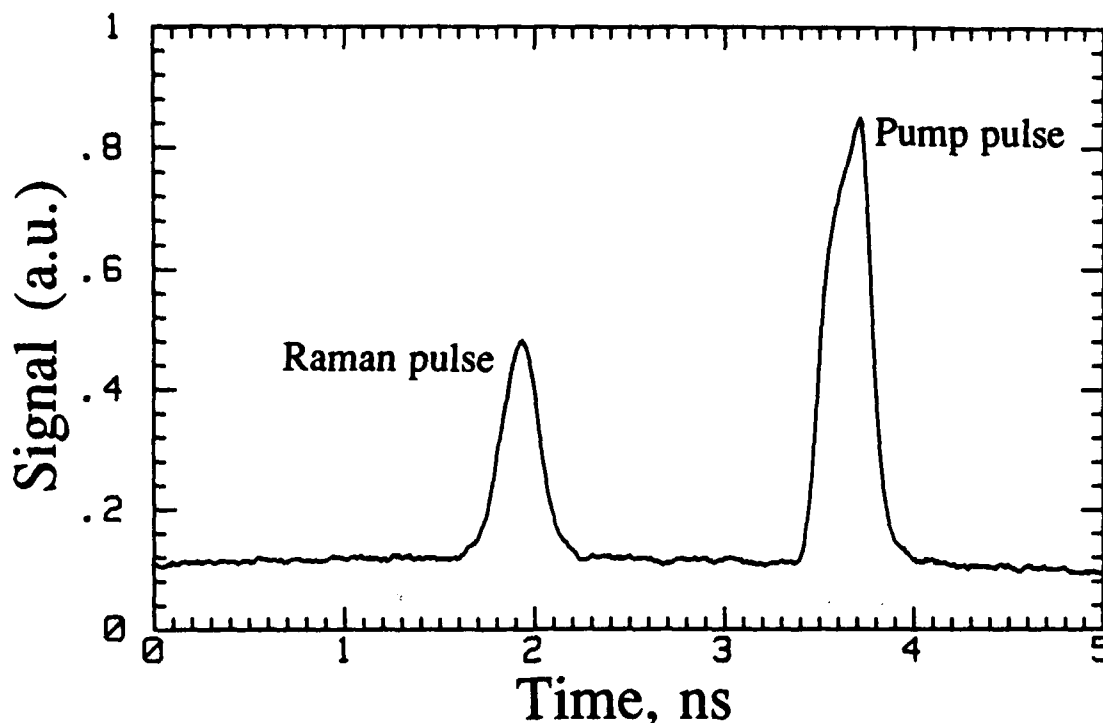


Fig. 3.6. Dispersion-induced walkoff between the pump pulse and the Raman pulse from the 1 km fiber, causing a 1.8 ns separation.

$\approx 140$  meters for SRS and also causes the  $1.06 \mu\text{m}$  pump and the  $1.12 \mu\text{m}$  Raman pulse to separate by 1.8 ns over the length of the 1 km fiber. The weakly reflected Raman pulse is further amplified if, after its first round trip through the fiber, it is synchronized to within 1.8 ns of a pump pulse. With this condition the Raman threshold with the 1 km fiber is 350-400 mW average fiber output power. Fig. 3.7 shows the Raman pulse buildup with pump power for this condition. Trimming the fiber length a few inches defeats this synchronism and increases the Raman threshold to about 700 mW. A compression ratio of 60X is then routinely obtained at  $\approx 400$  mW average power from the fiber output, well below the Raman threshold.

#### Excess Noise

The pulse compressor introduces excess intensity noise on the compressed pulsetrain due to a variety of causes. The excess intensity noise in general increases with increasing pulse compression from either increased fiber length or increased optical power launched into the

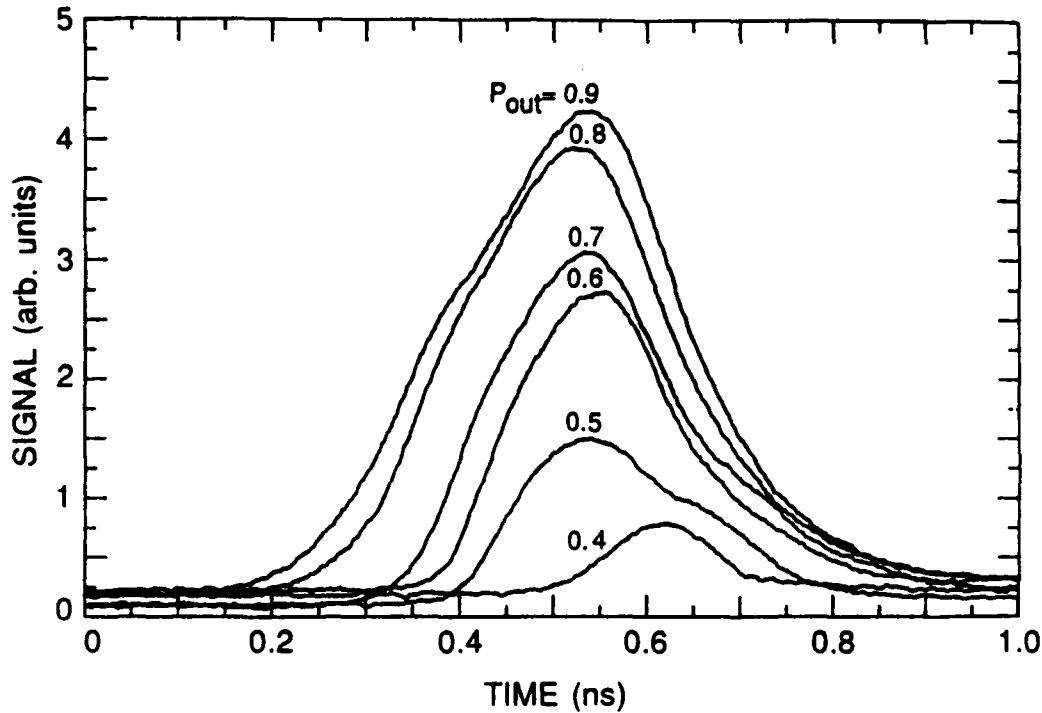


Fig. 3.7. Raman pulse build-up as a function of the average power from the fiber output  $P_{out}$  before trimming the fiber to defeat the parasitic fiber-Raman laser synchronism condition.

fiber. As the pump intensity approaches the SRS threshold, a substantial increase in intensity noise above the shot noise limit is observed, as shown in Fig. 3.8. The frequency period of the repetitive noise spectrum in this figure corresponds to the free spectral range of the 1 km fiber, indicative of the parasitic fiber-Raman laser.

In addition to SRS the fiber generates broadband polarization noise, possibly arising from guided acoustic wave Brillouin scattering [3.17] or some other nonlinear process in the fiber. The polarization noise is converted to amplitude noise after passing through the grating pair in the compressor, which has polarization dependent reflectivity. Adjusting the polarization from the fiber to maximize transmission through the grating path results in second-order intensity variations due to polarization fluctuations, reducing this excess noise to a level near the shot noise limit (Fig. 3.9). However, this excess noise typically adds 10-15 dB of broadband background noise above the shot noise limit.

Finally, temperature change of the fiber contributes to timing drift of the pulses, since the pulse compressor is "outside" the timing stabilizer feedback loop. The temperature coefficient of refractive of fused silica is  $11.8 \times 10^{-6}/^{\circ}\text{C}$  [3.18] resulting in an expected

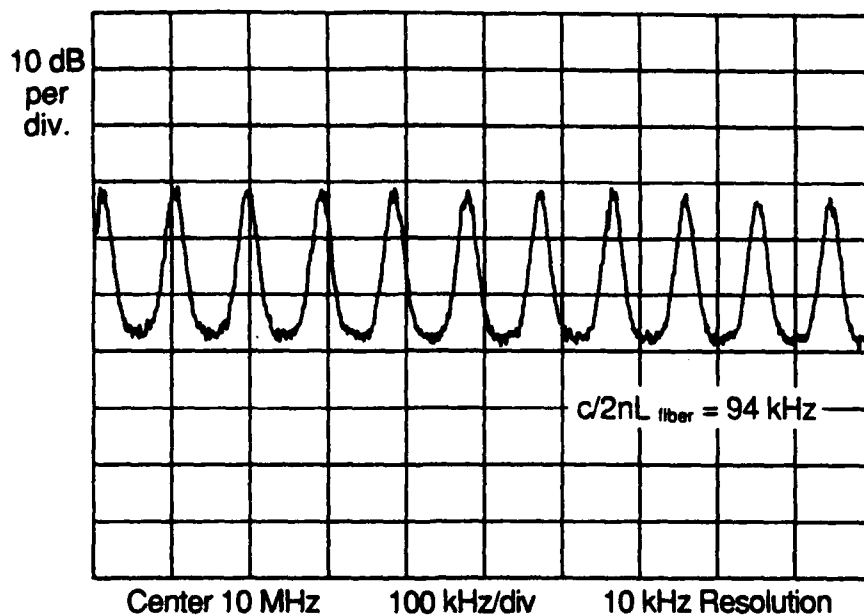


Fig. 3.8. Periodic noise spectrum from parasitic fiber-Raman laser when the pulse compressor is operated near the Raman threshold. The peaking at 95 kHz corresponds to the free spectral range of the 1 km fiber.

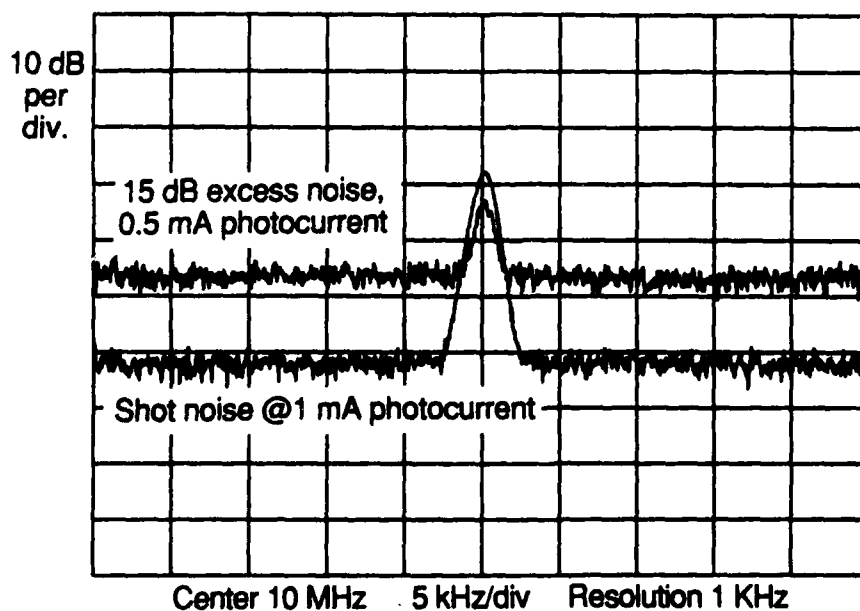


Fig. 3.9. Excess intensity noise due to misadjustment of the polarization from the output of the pulse compressor fiber.

timing drift ( $\Delta t = \Delta nL/c$ ) of 39 ps/°C for the 1 km fiber. To suppress polarization and timing drift, the non-polarization-preserving fiber is placed in an insulated container that is temperature-stabilized to  $\approx 0.1$  °C. However, temperature drift of the fiber probably accounts for most of the 2-4 ps per minute long-term timing drift observed with the system.

### 3.1.2. Timing Stabilizer

Figure 3.10 shows the block diagram of the timing stabilizer feedback system [3.5]. A photodiode monitors the 82 MHz laser pulse train, and the phase of the 82 MHz fundamental component is compared to the reference oscillator, generating a phase error signal. The 41 MHz signal required for driving the laser's acousto-optic (AO) cell is generated by frequency division from the 82 MHz standard, and its timing (phase) is adjusted with a voltage-controlled phase-shifter controlled by the amplified and frequency-compensated phase error signal. With an error-free phase detector, the laser timing fluctuations are suppressed in proportion to the loop gain of the feedback system.

The timing jitter calculated by measuring the phase noise of one of the laser harmonics—using a photodiode and a spectrum analyzer. The harmonic number is chosen to be great enough so that phase noise (which increases with the harmonic number) dominates the intensity noise (which is constant with harmonic number). Figure 3.11 shows the measured phase noise of the 20<sup>th</sup> harmonic of the laser with an HP 8662 low-phase noise synthesizer as the reference for the feedback system. From this measurement the timing jitter is calculated [3.19] from the relation

$$\Delta t_{rms} = \frac{T_0}{2\pi n} \sqrt{\frac{P_{SB}}{P_a}} \quad (3.3)$$

where

$$P_{SB} = 2 \int_{f_1}^{f_2} \frac{P_b(f)}{B} df \quad (3.4)$$

is the integrated phase noise power from a low frequency limit  $f_1$  to an upper frequency limit  $f_2$ ,  $P_a$  is the carrier power,  $P_b$  is the phase noise power at some frequency offset  $f$ ,  $T_0 = 1/f_0$  is the pulse period,  $n$  is the harmonic number, and  $B$  is the spectrum analyzer resolution. In practice, the calculation is done with the spectrum analyzer under control of a desktop computer [3.20]. From data similar to Fig. 3.11 the calculated timing jitter is

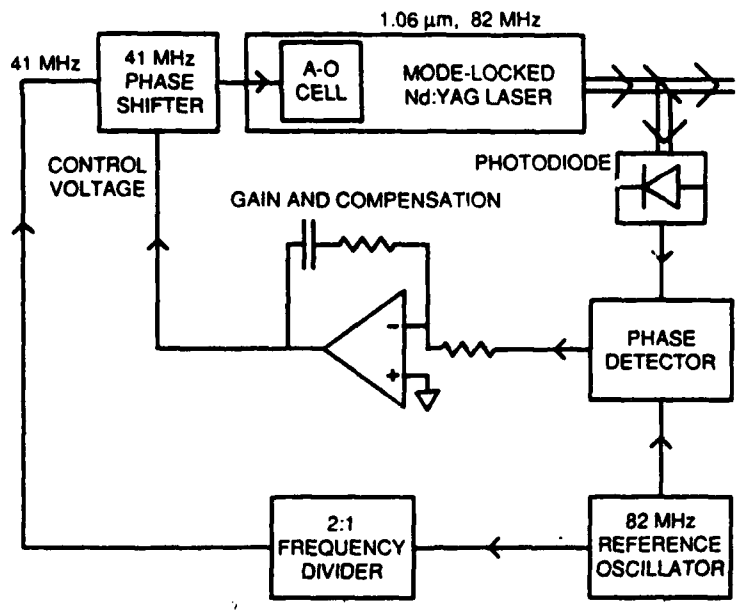


Fig. 3.10. Block diagram of phase-lock-loop timing stabilizer feedback system.

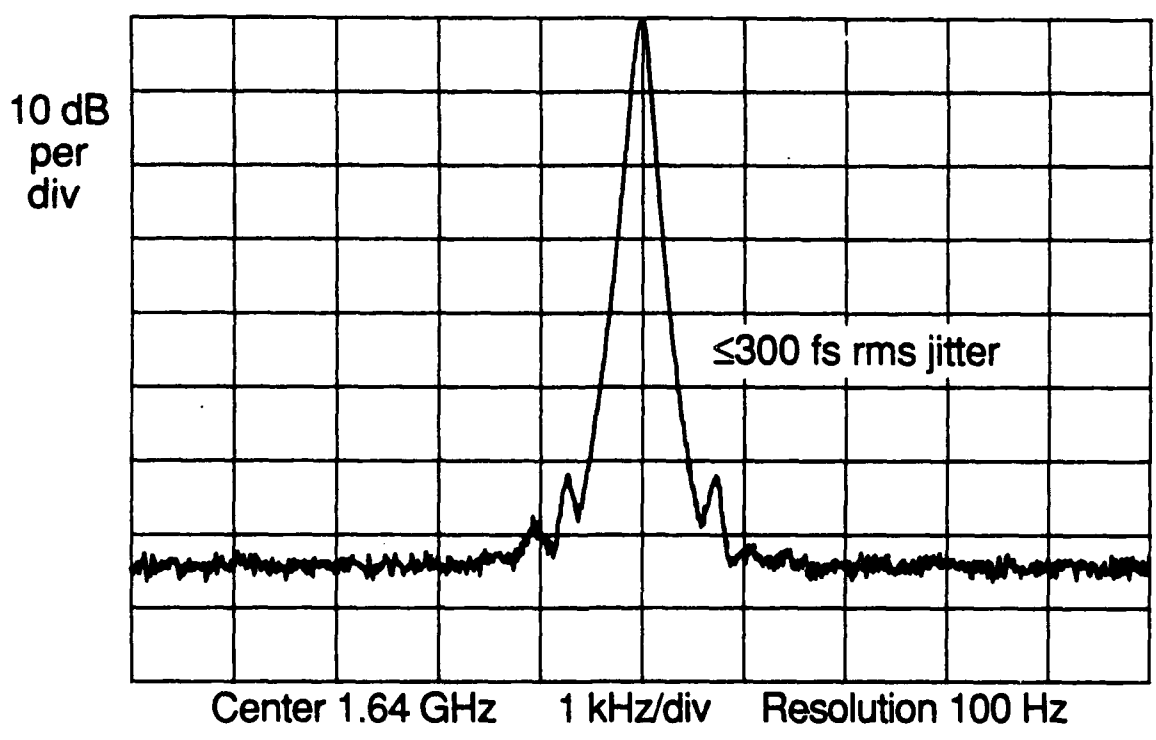


Fig. 3.11. Laser phase noise at the 20<sup>th</sup> harmonic of the pulse repetition rate, measured with a photodiode and a spectrum analyzer. The noise floor of this measurement is instrumentation limited. The overall calculated jitter is less than 250 fs rms at jitter rates between 50 Hz and 25 kHz.

250 fs rms (0.6 ps FWHM to express it on the same terms as the optical pulsewidth) from  $f_1 = 50$  Hz to  $f_2 = 25$  kHz. One limitation of an RF spectrum analyzer (Hewlett Packard 8566B) is a lower frequency limit of about 50 Hz, due to the 10 Hz minimum resolution bandwidth. Jitter components at rates less than 50 Hz cannot be measured in this fashion. Long term timing drift, on the order of seconds or minutes, can be monitored with the receiver system, measuring drift of the phase of a measured sinusoid.

## **3.2. Microwave Instrumentation**

### **3.2.1. Microwave Sources**

The electrooptic sampler relies on two key microwave instruments: the RF signal source driving the mode-locked laser and providing the reference for the timing stabilizer, and the microwave signal source for driving the IC. The RF signal source for driving the laser is a Hewlett-Packard 8662A, a precision low-phase noise synthesizer. The microwave signal source is a Hewlett-Packard 8340A or an 8341B. The microwave synthesizer generates either sinusoidal excitation for microwave circuits, or the clock/data signals for digital circuits from 10 MHz to 20 GHz, and diode multipliers can extend this range to 100 GHz.

The relative timing stability of the two synthesizers is critical for ensuring low timing jitter of the laser pulses with respect to the signal synthesizer. Because each synthesizer generates its signal with reference to the same stable, low-phase-noise crystal oscillator, the synthesizers have less than a picosecond of short-term relative timing jitter. If one of the synthesizers had poor timing stability, it would have to be included in the timing stabilizer feedback loop, severely increasing the difficulty of a practical feedback system.

### **3.2.2. Microwave Wafer Probe Station**

For wafer-level testing of IC's, the drive signal is delivered with a microwave probe station (Cascade Microtech Model 42) modified to allow for backside electrooptic probing, as shown pictorially in Figs. 3.12 and 3.13, and schematically in Fig. 3.14. The transmission line probes used with this test station allow for launching a signal on the IC with repeatable, low reflection connections in a 50  $\Omega$  environment to 40 GHz. The beam delivery system consists of two turning mirrors, 90° to each other, mounted on an X-Y stage controlled by automated positioners. The wafer chuck is modified so that the focusing objective is positioned under the wafer and accessed with either a hole in the top plate or a sapphire window. The window provides better heat conduction than an open hole for high power circuits. However, a small air gap may exist between the window and the wafer,

causing the beam transmission to vary as a function of position due to interference. Index matching fluid (Cargille Series M) removes this problem, but it can evaporate leaving a rough salt residue that sticks to the window and the wafer.

Packaged circuits (mostly circuits using microstrip conductors and requiring frontside probing) are tested with a general purpose beam delivery system that allows for either frontside or backside probing. This arrangement requires either that the circuit package allow access to the IC from the frontside probing (roughly 8 mm working distance for a 10X objective) or that the package has a window under the portion of the circuit for beam access from the backside.

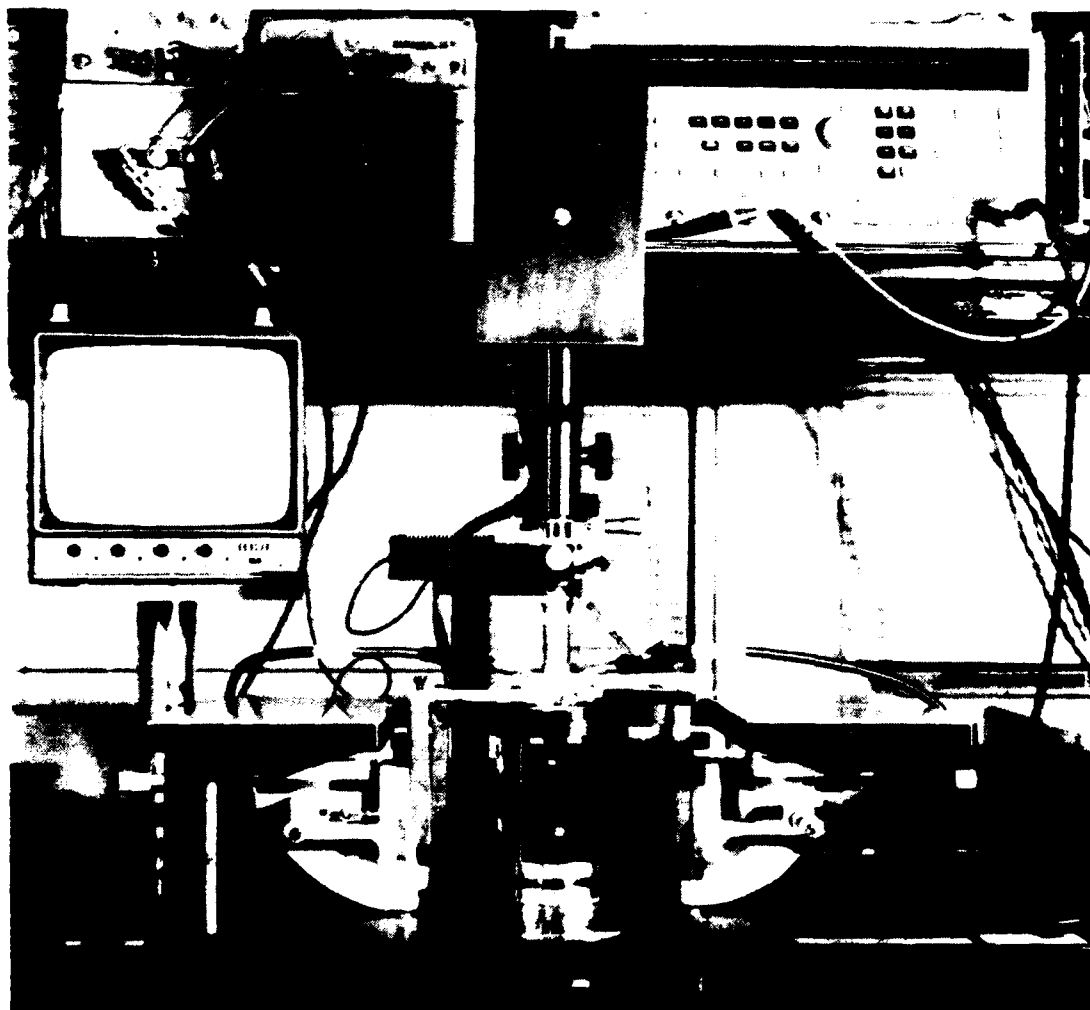


Fig. 3.12. Front view of the Cascade microwave wafer probe station

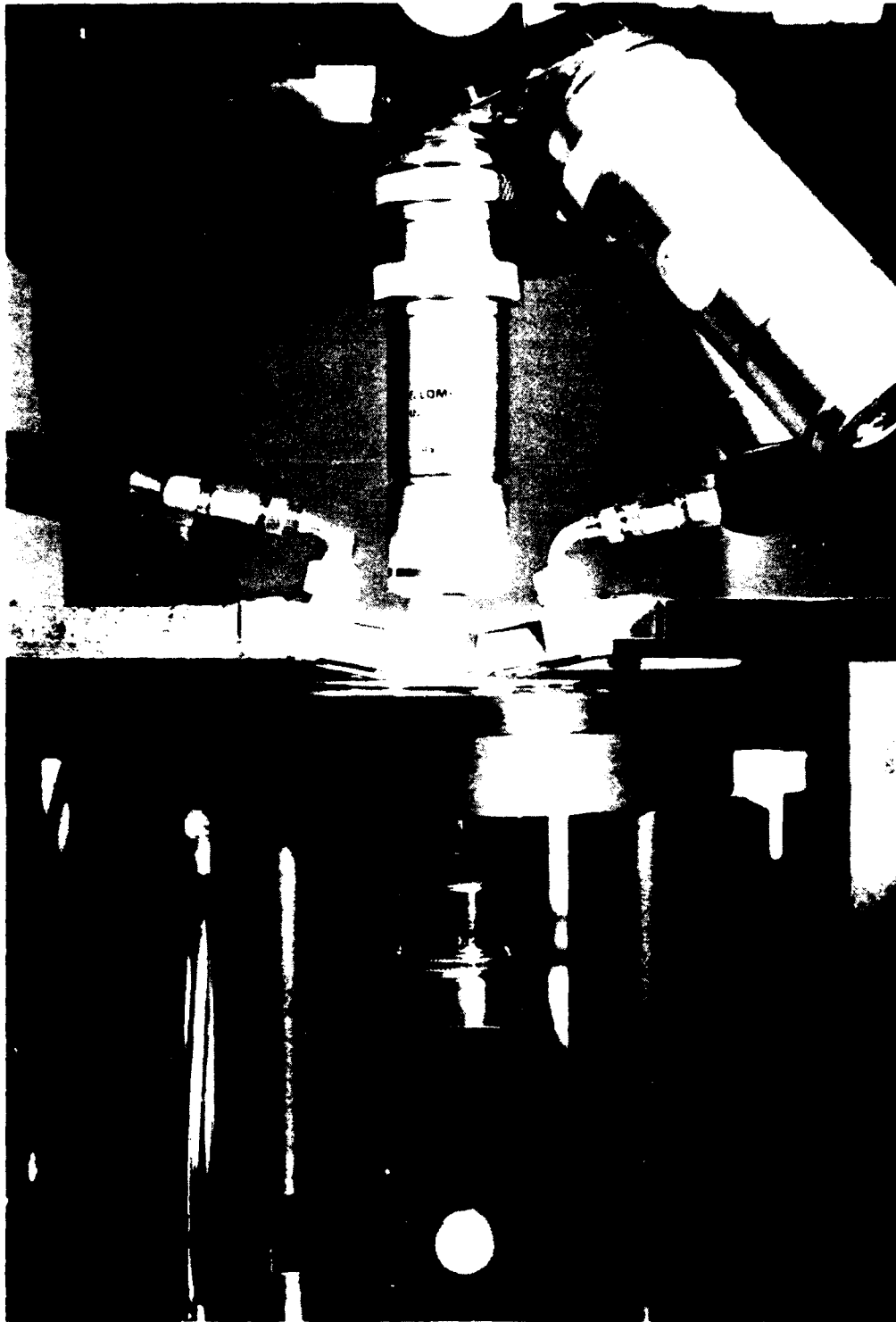


Fig. 3.13. Front view close-up of the Cascade microwave wafer probe station showing the microscope objective below the wafer chuck, two CPW probes, and the long working-distance objectives used for the viewing system.



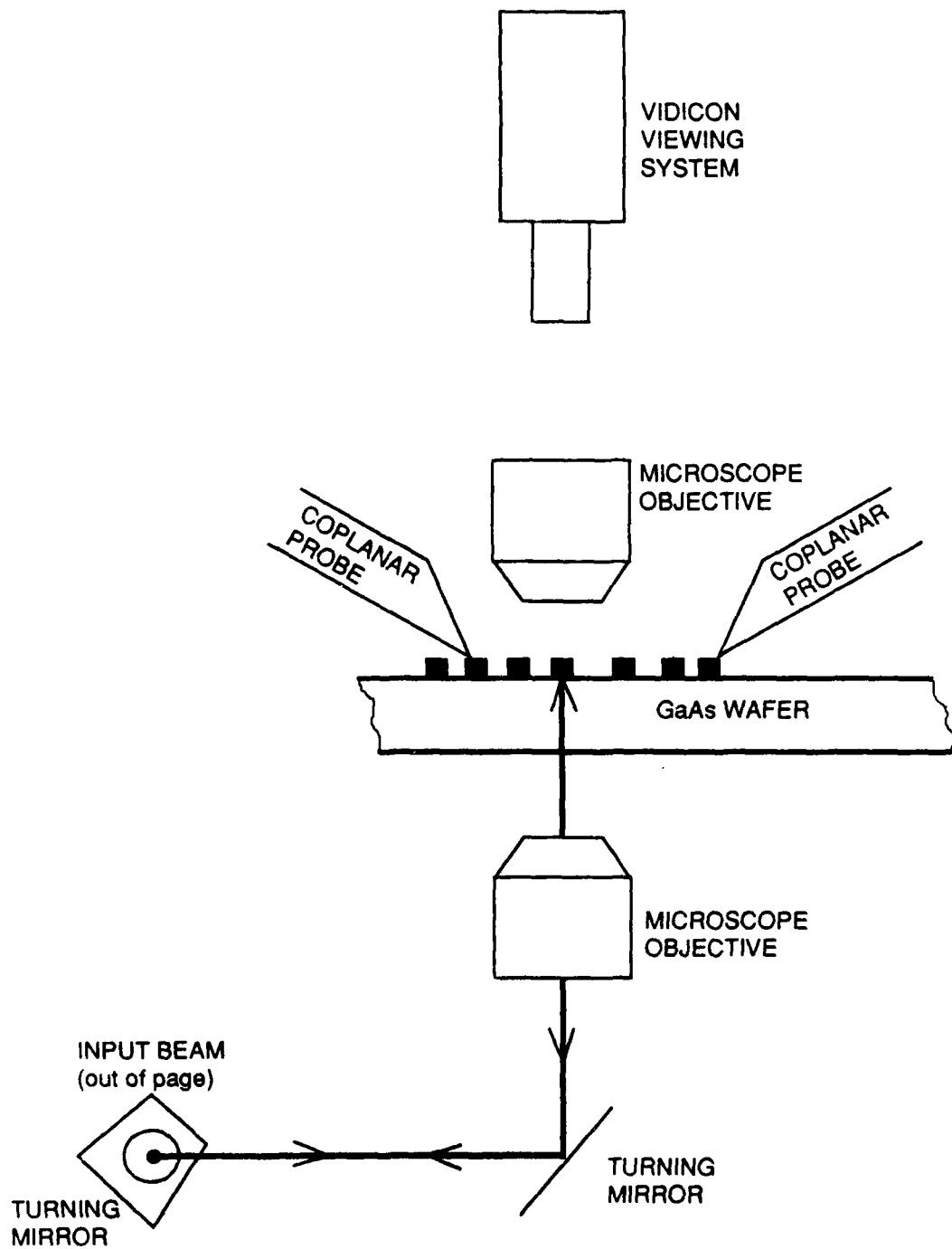


Fig. 3.14. Beam path through the Cascade microwave wafer probe station for backside probing. The turning mirrors and focusing objective are mounted on automated positioners to allow accurate positioning and scanning of the probe beam. The vidicon viewing system is sensitive to the infrared probe, allowing viewing of the probe position on the front surface of the test IC.

### 3.3. Signal Processing Systems

Signal processing as described in Section 2.5 is critical to achieve accurate, shot-noise limited measurements. The signal processing system consists of a photodiode receiver and synchronous detector which can be configured for either vector measurements (harmonic mixing) or time waveform measurements (equivalent-time sampling).

#### 3.3.1. Photodiode Receiver

The photodiode receiver is designed to achieve shot noise limited detection at a frequency above the  $1/f$  noise corner of the laser system. Figure 3.15 shows the photodiode receiver schematic. The photodiode produces a current proportional to the optical power, and the load resistor is chosen so the the shot noise from the DC photocurrent is greater than the Johnson noise of the resistor and the noise voltage of the buffer amplifier. The buffer amplifier then provides the current drive for the  $50 \Omega$  impedance of the synchronous detector section.

The mean-square shot noise current from the photodiode is

$$\overline{i_{SN}^2} = 2qI_0B \quad (3.5)$$

where  $q$  is the electronic charge,  $I_0$  is the average photocurrent, and  $B$  is the bandwidth. The mean-square Johnson noise current from the load resistor is

$$\overline{i_{JN}^2} = \frac{4kT}{R_L} \quad (3.6)$$

where  $k$  is Boltzmann's constant,  $T$  is the temperature in degrees Kelvin, and  $R_L$  is the load resistance. The minimum photocurrent  $I_0$  for shot noise limited detection occurs when the mean-square noise currents are equal. This sets a lower limit on the photocurrent of

$$I_{min} = \frac{2kT}{qR_L} \quad (3.7)$$

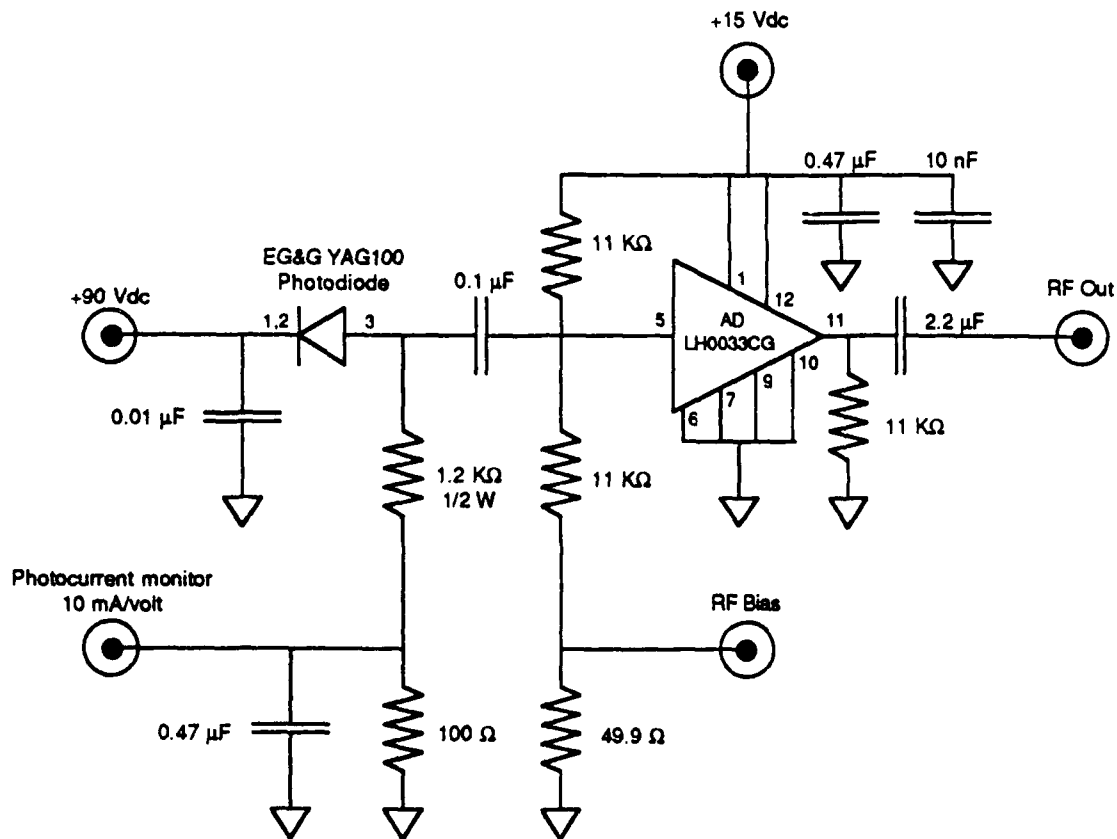


Fig. 3.15. Photodiode receiver schematic.

The shot noise current develops a noise voltage across the load resistor. The buffer amplifier has unity gain and transfers this voltage to its output, which has a load impedance of  $Z_0$  (typically  $50 \Omega$ ). Then, the noise power developed at its output is

$$P_{SN} = \frac{2qI_0BR_L^2}{Z_0} \quad (3.8)$$

In the photodiode receiver of Fig. 3.15,  $R_L = 1 \text{ k}\Omega$  ( $1.2 \text{ k}\Omega$  parallel the two  $11 \text{ k}\Omega$  bias resistors) and  $I_0 = 1 \text{ mA}$  typically. Then,  $I_{min} = 0.05 \text{ mA}$  indicating the shot noise is well above the Johnson noise, and  $P_{SN} = -141.9 \text{ dBm/Hz}$  for  $Z_0 = 50 \Omega$ .

For smaller photocurrents, the load resistor can be increased to maintain shot-noise-limited detection. However, increasing the load resistance increases the receiver time constant due to the photodiode capacitance and load resistance, decreasing its bandwidth. This may be an important constraint depending on the noise characteristics of the laser and the resulting signal processing scheme required.

### 3.3.2. Synchronous Detector

The synchronous detector, shown schematically in Fig. 3.16, consists of two sections in addition to the photodiode receiver; the frequency downconverter, and a commercial lock-in amplifier. The frequency downconverter is necessary because the lock-in amplifier's maximum frequency of operation, 100 kHz, is not quite sufficient to avoid low-frequency laser intensity noise. The lock-in amplifier provides precision measurement of the signal with a range of time constants for setting the integration time (or equivalently the receiver bandwidth) of the measurement.

Figure 3.17 shows a block diagram of the frequency downconverter. The downconverter serves two purposes. First, it mixes the measured signal down to a frequency within the range of the lock-in amplifier, and second, it generates a synchronous reference signal for the lock-in amplifier.

### 3.3.3. Vector Measurements

Harmonic mixing is used for vector voltage measurements. The synthesizer driving the IC is set to an exact multiple of the laser repetition rate plus a frequency offset  $\Delta f$  (1 MHz typically) that is well above the background laser intensity noise. The frequency downconverter mixes the measured signal to a frequency (50 kHz typically) within the 100 kHz range of the lock-in, which measures and displays its magnitude and phase. To measure the response at different frequencies, the synthesizer frequency is stepped by an exact multiple of the laser repetition rate  $f_0$ .

### 3.3.4. Time Waveform Measurements

Equivalent-time sampling is used to view time waveforms. The synthesizer is set to an exact multiple of the laser repetition rate ( $\approx 82$  MHz), plus a frequency offset  $\Delta f$  (10-100 Hz) that sets the measurement scan rate. The modulation frequency  $f_m$  for pulse modulation or phase modulation is set to a value (1 MHz typically) well above the low frequency intensity noise. The measured signal has a component at  $f_m$  whose amplitude varies in proportion to the signal at the scan rate  $\Delta f$ . The frequency downconverter mixes this signal to a frequency in the range of the lock-in amplifier (50 kHz typically), which demodulates the signal to baseband and detects the in-phase component of the signal that varies in proportion to the measured signal at the scan rate  $\Delta f$ . The signal is displayed on an oscilloscope which is

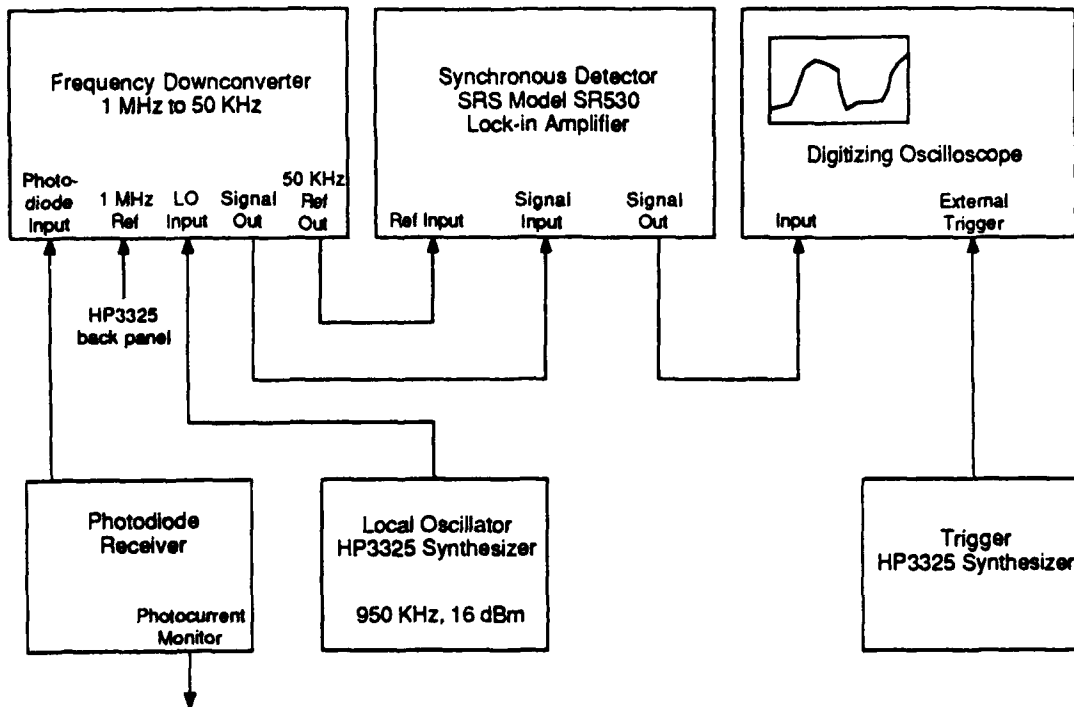


Fig. 3.16. Receiver block diagram.

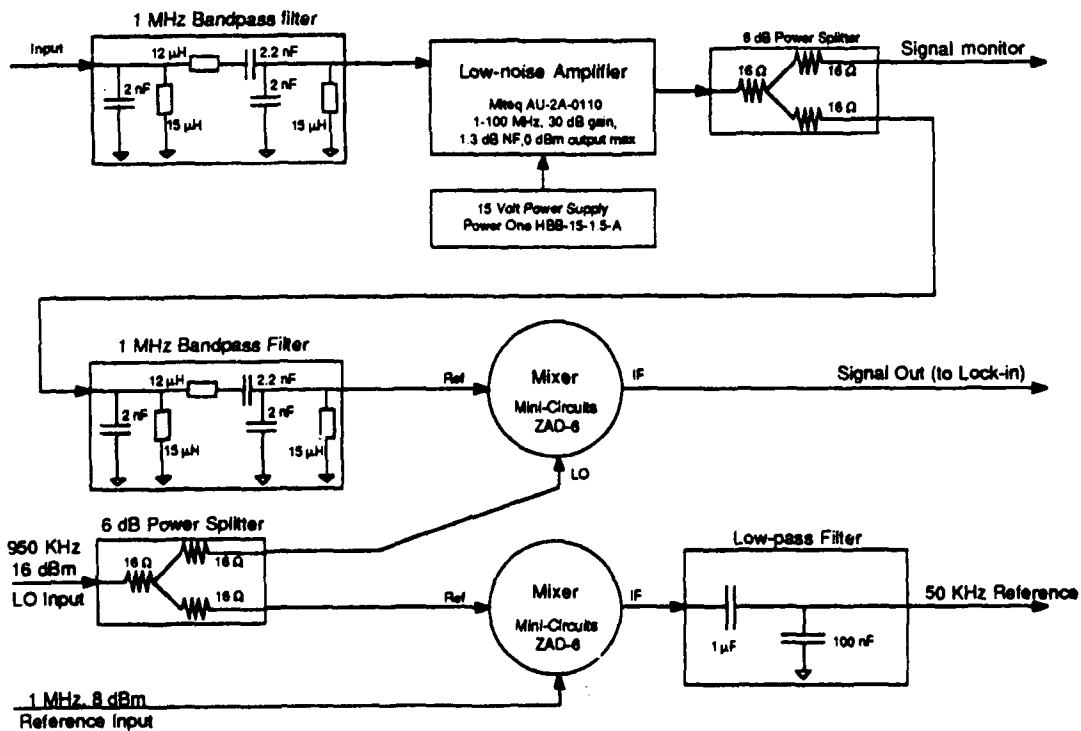


Fig. 3.17. Frequency converter schematic.

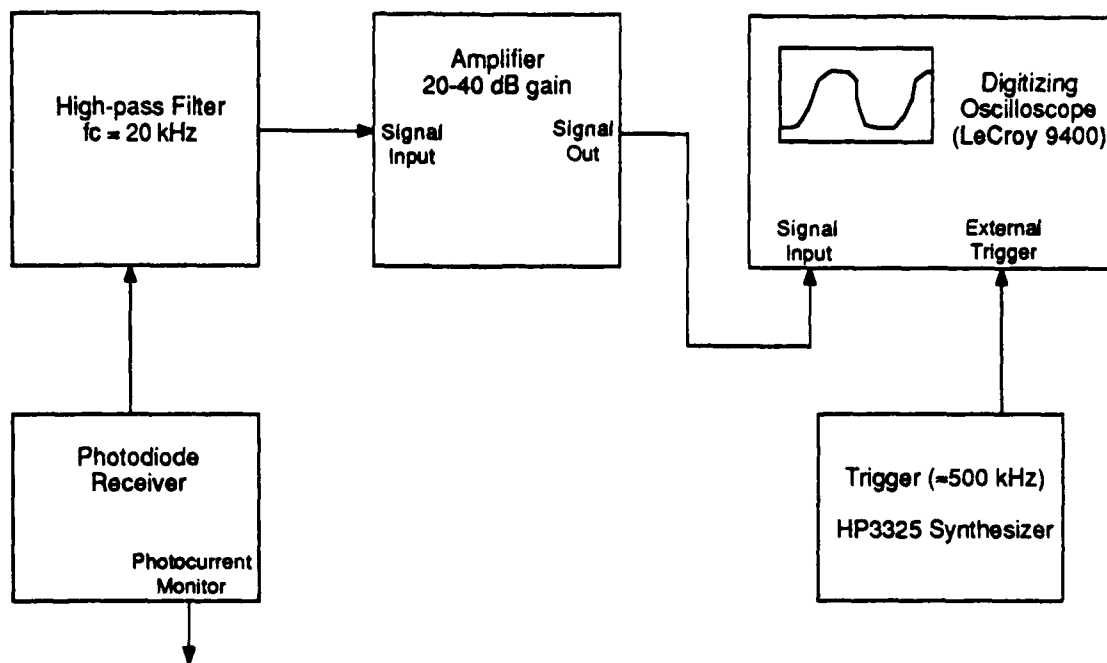


Fig. 3.18. Fast scan rate signal processing block diagram.

is externally triggered from a low-frequency synthesizer locked to the source microwave synthesizer, providing a time reference for the measurement so that relative time delays between two signals can be determined. For phase modulation (Section 2.5.3), the displayed signal is proportional to the time derivative of the measured signal, and is recovered by integrating the displayed signal in software using a desktop computer [3.21].

An alternative to chopping or phase modulation of the drive signal is fast offset and averaging (Section 2.5.4). Figure 3.18 shows a block diagram of this signal processing system. With this scheme the frequency offset  $\Delta f$  is increased 400-500 kHz, well above the low-frequency laser noise. The signal is recovered by high-pass filtering to remove the low-frequency laser noise, then by signal averaging at the offset rate  $\Delta f$ . If the received signal is averaged at the scan rate, the sensitivity using fast averaging is the same as for simple synchronous sampling with the same measurement acquisition time. Commercial digitizing oscilloscopes have limited averaging rates; at scan rates of 500 kHz, the LeCroy 9400 averages a maximum of  $\approx 200$  scans per second, corresponding to a signal-to-noise reduction of 34 dB from averaging every scan. However, the signal-to-noise reduction, compensated for by increased measurement acquisition time, is justified for testing IC's that are sensitive to signal chopping.

### 3.4. Summary

The system described in this chapter combines several sophisticated technologies: optical pulse compression, synthesized electronics, phase-lock-loop feedback for stabilizing laser pulse timing, and synchronous signal detection. The fiber-grating pulse compressor was optimized for short pulses with small wings by using the GVD of a 1 km fiber to enhance the linear frequency chirp. However, the longer fiber increases excess intensity noise, from stimulated Raman scattering, which can be eliminated, and from polarization noise, which adds 10-15 dB of excess broadband background intensity noise. The timing stabilizer feedback system effectively reduces the pulse-to-pulse timing jitter of the laser to a level less than the optical pulsewidth and allows synchronization of the microwave synthesizer used to drive the circuit under test. The receiver system uses synchronous signal detection to achieve near shot noise limited sensitivity, and is configured to emulate either a vector voltmeter (harmonic mixing) or a sampling oscilloscope (equivalent-time sampling).

Overall, the measurement system has a time resolution 2 ps due to its 1.5 ps FWHM optical pulsewidth and 0.6 ps FWHM (250 fs rms) timing jitter, a sensitivity of  $70 \mu\text{V}\sqrt{\text{Hz}}$ , and receiver system that measures either a vector signal for the small-signal frequency response, or time waveforms for the large-signal response. A modified microwave wafer probe station allows for backside optical probing with drive signals from either coplanar waveguide probes to frequencies of 40 GHz or from IC probe cards to frequencies of several GHz.

### 3.5. References for Chapter 3

- 3.1 A.J. Taylor, J.M. Wiesenfeld, G.Eisenstein, R.S. Tucker, J.R. Talman, and U. Koren, "Electrooptic sampling of fast electrical signals using an InGaAsP injection laser," *Elec. Lett.*, vol. 22, pp. 61-62, 1986.
- 3.2 A.J. Taylor, J.M. Wiesenfeld, R.S. Tucker, G.Eisenstein, J.R. Talman, and U. Koren, "Measurement of a very high-speed InGaAs photodiode using electrooptic sampling," *Elec. Lett.*, vol. 22, pp. 325-327, 1986.
- 3.3 J.M. Wiesenfeld, R.S. Tucker, A. Antreasyan, C.A. Burrus, and A.J. Taylor, "Electrooptic sampling measurements of high-speed InP integrated circuits," *Appl. Phys. Lett.*, vol. 50, pp. 1310-1312, 1987.
- 3.4 D. Cotter, "Technique for highly stable active mode-locking," *Ultrafast Phenomena IV*, D.A. ed. by Auston and K.B. Eisenthal, New York:Springer-Verlag, 1984, pp. 78-80.
- 3.5 M.J.W. Rodwell, K.J. Weingarten, D.M.Bloom, T. Baer, and B.H. Kolner, "Reduction of timing fluctuations in a mode-locked Nd:YAG laser by electronic feedback," *Optics Letters*, vol. 11, pp. 638-640, 1986.
- 3.6 J.D. Kafka, B.H. Kolner, T. Baer, and D.M. Bloom, "Compression of pulses from a continuous-wave mode-locked Nd:YAG laser," *Opt. Lett.*, vol. 9, pp. 505-506, 1984.
- 3.7 E.B. Treacy, "Optical pulse compression with diffraction gratings," *IEEE J. Quant. Elect.*, vol. QE-5, pp. 454-458, 1969.
- 3.8 D. Grischkowsky and A.C. Balant, "Optical pulse compression based on enhanced frequency chirping," *Appl. Phys. Lett.*, vol. 41, pp. 1-3, 1982.
- 3.9 B. Zysset, W. Hodel, P. Beaud, and H.P. Weber, "200-femtosecond pulses at 1.06  $\mu\text{m}$  generated with a double-stage pulse compressor," *Optics Letters*, vol. 11, pp. 156-158, 1986.
- 3.10 F.M. Mitschke and L.F. Mollenauer, "Ultrashort pulses from the soliton laser," *Optics Letters*, vol. 12, pp. 407-409, 1987.
- 3.11 A.S. Gouveia-Neto, A.S.L. Gomes, and J.R. Taylor, "Generation of 33-fsec pulses at 1.32  $\mu\text{m}$  through a high-order soliton effect in a single-mode optical fiber," *Optics Letters*, vol. 12, pp. 395-397, 1987.
- 3.12 J.P. Heritage, R.N. Thurston, W.J. Tomlinson, and A.M. Weiner, "Spectral windowing of frequency-modulated optical pulses in a grating compressor," *Appl. Phys. Lett.*, vol. 47, pp. 87-89, 1985.



- 
- 3.13 N.J. Halas and D. Grischkowsky, "Simultaneous optical pulse compression and wing reduction," *Appl. Phys. Lett.*, vol. 48, pp. 823-825, 1986.
- 3.14 B. Nikolaus, D. Grischkowsky, and A.C. Balant, "Optical pulse reshaping based on the nonlinear birefringence of single-mode optical fibers," *Opt. Lett.*, vol. 8, pp. 189-191, 1983.
- 3.15 P.M.W. French, A.S.L. Gomes, A.S. Gouveia-Neto, and J.R. Taylor, "Picosecond stimulated raman generation, pump pulse fragmentation, and fragment compression in single-mode optical fibers," *IEEE J. Quant. Elect.*, vol. QE-22, pp. 2230-2235.
- 3.16 M.N. Islam, L.F. Mollenauer, and R.H. Stolen, "Fiber raman amplification soliton laser (FRASL)," *Ultrafast Phenomena V*, ed. by G.R. Fleming and A.E. Siegman, Springer Ser. Chem. Phys., Vol. 46, New York:Springer-Verlag, 1986, pp. 46-50.
- 3.17 R.M. Shelby, M.D. Levenson, and P.W. Bayer, "Guided acoustic-wave Brillouin scattering," *Phys. Rev. B*, vol. 31, pp. 5244-5252, 1985.
- 3.18 *American Institute of Physics Handbook*, 3<sup>rd</sup> ed., D.E. Gray, ed., McGraw-Hill Book Company, New York, p. 6-29.
- 3.19 B.H. Kolner and D.M. Bloom, "Electrooptic sampling in GaAs integrated circuits," *IEEE J. Quant. Elect.*, vol. QE-22, 1986, pp. 79-93.
- 3.20 Program and calculation courtesy of B.K. Kolner, Hewlett-Packard Laboratories.
- 3.21 M.J.W. Rodwell, K.J. Weingarten, J.L. Freeman, and D.M. Bloom, "Gate propagation delay and logic timing of GaAs integrated circuits measured by electro-optic sampling," *Elect. Lett.*, vol. 22, pp. 499-501, 1986.

# Circuit Measurements

## 4.1. Realistic Circuit Testing Conditions

Optical probing, providing access to the high-impedance internal nodes of IC's with picosecond time resolution and micron spatial resolution, permits direct measurements of the performance of state-of-the-art microwave and digital GaAs circuits. However, these measurements must be made under realistic circuit operating conditions for meaningful measurements of a circuit's performance and for comparisons between competing circuit technologies. For example, the propagation delay of switching devices in simple test circuits is used to estimate the maximum clock frequency of these devices used in digital systems. Unless the test circuit provides representative switching voltages, interface impedances, and fan-outs, the measured delays will not correlate well with the maximum clock frequency of more complicated functional circuits such as shift registers, binary multipliers, and memory. For example, the response of a transistor driven by a low-impedance photoconductor and loaded by a low-impedance,  $50 \Omega$  transmission line is in general much faster than the response of a logic gate driven by the normal output impedance of a driving gate and loaded by the normal input capacitances of cascaded gates. Or if the test circuit is constructed in hybrid form with wire bonds between the tested device and the transmission lines, the interconnect parasitic impedances may dominate the circuit response.

For digital circuits, ring oscillators and inverter strings are the simplest test structures used as benchmarks of circuit speed. With gate loading (fan-in/fan-out) of unity, these circuits tend to show optimistically small propagation delays. Also, ring oscillators may operate with small-signals (without full logic-level swings), further decreasing their gate delay, while large-signal operation of inverter strings is easily controlled and verified. Better, more sophisticated test circuits are master-slave flip-flops, connected as binary frequency dividers, which operate with logic signal levels and fan-out of two gate loading.

For microwave/analog circuits such as distributed amplifiers, appropriate test signals are swept-frequency sinusoids to measure the small-signal transfer function, or single-frequency signals set to amplitudes to cause large-signal distortion for saturation measure-

ments. Signal sources and terminations should have  $50\ \Omega$  impedances to eliminate source and load reflections.

## 4.2. Digital Circuit Measurements

### 4.2.1. Inverter Chains and Ring Oscillators

Figure 4.1 shows a logic element schematic of a ring oscillator/inverter chain. Ring oscillators are free-running at an oscillation frequency set by the signal propagation time around an odd-numbered ring of inverters. These circuits provide a measure of a gate delay, where the repetition period corresponds to product of the average gate delay and the number of gates. These free-running circuits are not readily clocked with an external signal, making synchronization to the probe pulses for electrooptic sampling difficult. To measure ring oscillators with the optical probe, a drive signal is applied to injection lock the circuit, allowing the probe pulses to be synchronized for sampling. The ring oscillator typically must be "tweaked" by adjusting its power supply voltage to shift its oscillation frequency and allow injection locking, and measurements made in this manner tend to be unstable and hard to reproduce. Inverter chains, however, a series of cascaded inverting logic gates, are clocked with an external signal, permitting the synchronization of probe pulses for electrooptic measurements and assuring full logic-level switching of the gates. Typically, average gate delays are measured with sampling oscilloscopes; the propagation delay of the entire chain is measured and divided by the number of inverters to estimate the average delay of an individual inverter. For electrooptic testing the input inverter is switched with a microwave synthesizer, generating a square wave that ripples through the test structure. The first several inverters condition the input signal, sharpening the switching transients

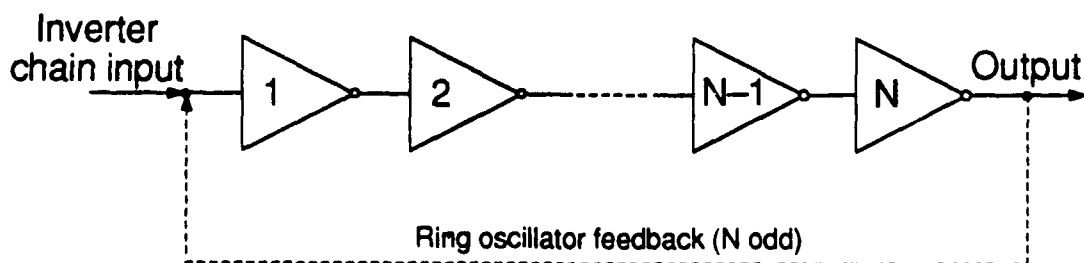


Fig. 4.1. Inverter chain/ring oscillator schematic. For a ring oscillator, the dashed line is connected providing feedback for a pulse propagating down the chain from the output to the input.

until the signal risetimes and falltimes reach a steady-state value. The optical probe is then positioned from node-to-node, measuring directly the propagation delays and signal risetimes at gate input and output nodes and at nodes internal to the gate.

Fig. 4.2 shows an electrooptically measured gate delay on an inverter chain from Lawrence Livermore National Labs [4.1,2], using  $1\mu\text{m}$  gate-length buffered-FET logic MESFETS. Figure 4.3 shows an SEM picture of one inverter of the 20 gate circuit loaded with a fan-out (FO) of unity. The delay between curves A and B of Fig. 4.2 is the propagation delay of the inverting common-source stage, 60 ps, while the delay between curves B and C is the delay of the source-follower buffer and diode level-shifter, 15 ps.

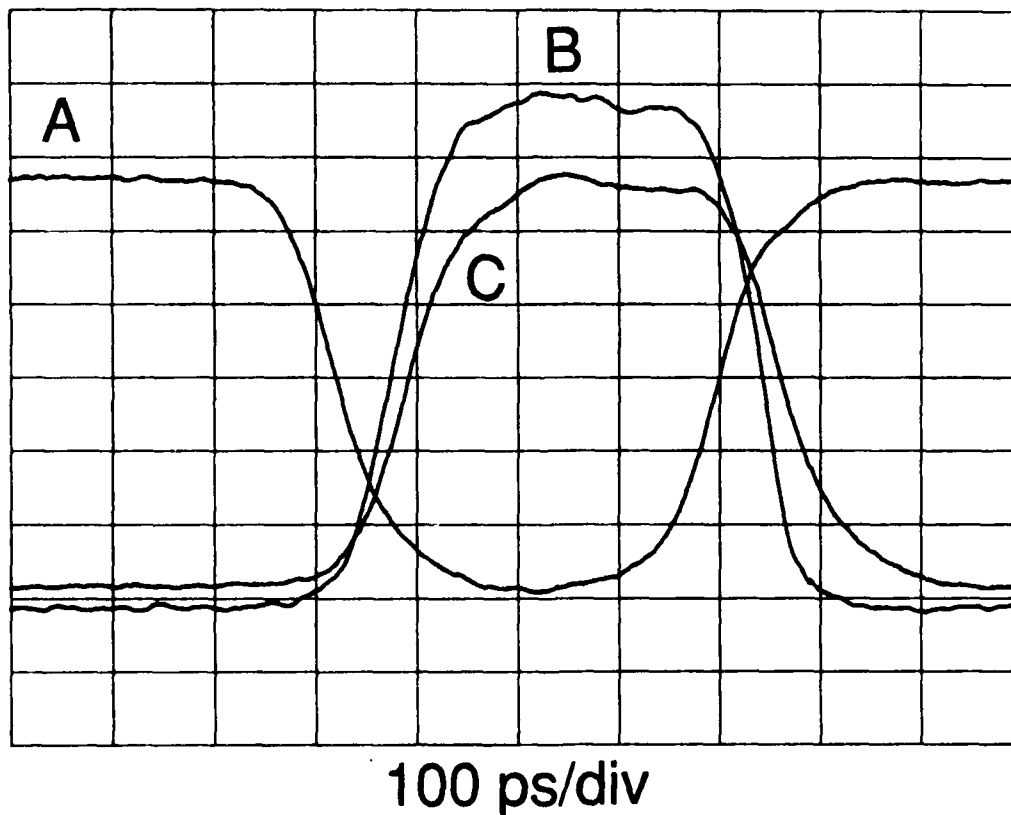


Fig. 4.2. Propagation delay through a GaAs buffered-FET logic inverter gate [4.2]. Voltage waveforms at the input (A), the source follower gate (B), and the output (C).

The timing of inverter chains has also been examined by Zhang, *et. al.* [4.3], optically triggering an inverter in the chain and using electrooptic sampling to measure the circuit response and gate propagation delays in a pump/probe configuration. A frequency-doubled portion of the probe beam (at  $\lambda=532\text{ nm}$ ) focused on the gate region of a FET generates

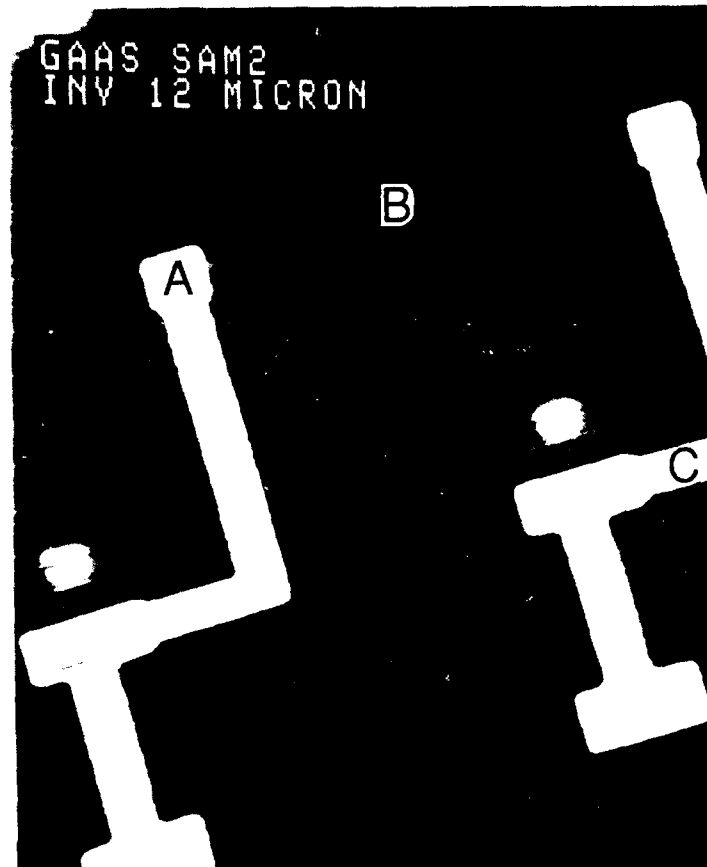


Fig. 4.3. SEM photo of a buffered-FET logic gate in the inverter chain [4.1]. The gate metal is  $1\ \mu\text{m}$  in width and the interconnect metal is about  $5\ \mu\text{m}$  in width. Photo courtesy of S. Swierkowski, Lawrence Livermore National Laboratories.

photocurrent, turning on the FET and generating a switching transient that propagates down the test structure. The probe beam, positioned at a node after the switched gate, is slowly delayed with respect to the switching pulse to map the transient waveform. This technique offers an all-optical approach, avoiding microwave connection to the IC, which is suitable for testing of simple IC test structures. However, optical triggering is an impractical method for generating the multiple clock and data signals required to drive large scale IC's.

A more complex inverter chain from Hewlett-Packard Laboratories, using  $1\ \mu\text{m}$  enhancement/depletion-mode logic and modulation-doped FET's (MODFET's), begins with a section of six inverters with  $FO=1$ . The last of these inverters drives the input to a section of 48 inverters with  $FO=3$  to simulate normal loading. Figure 4.4 shows the propagation delay measured electrooptically through two inverters of the input section. The propagation delay of  $60\ \text{ps}$  increases to  $150\ \text{ps}$  in the  $FO=3$  section and the signal risetime degrades, as shown in Fig. 4.5.

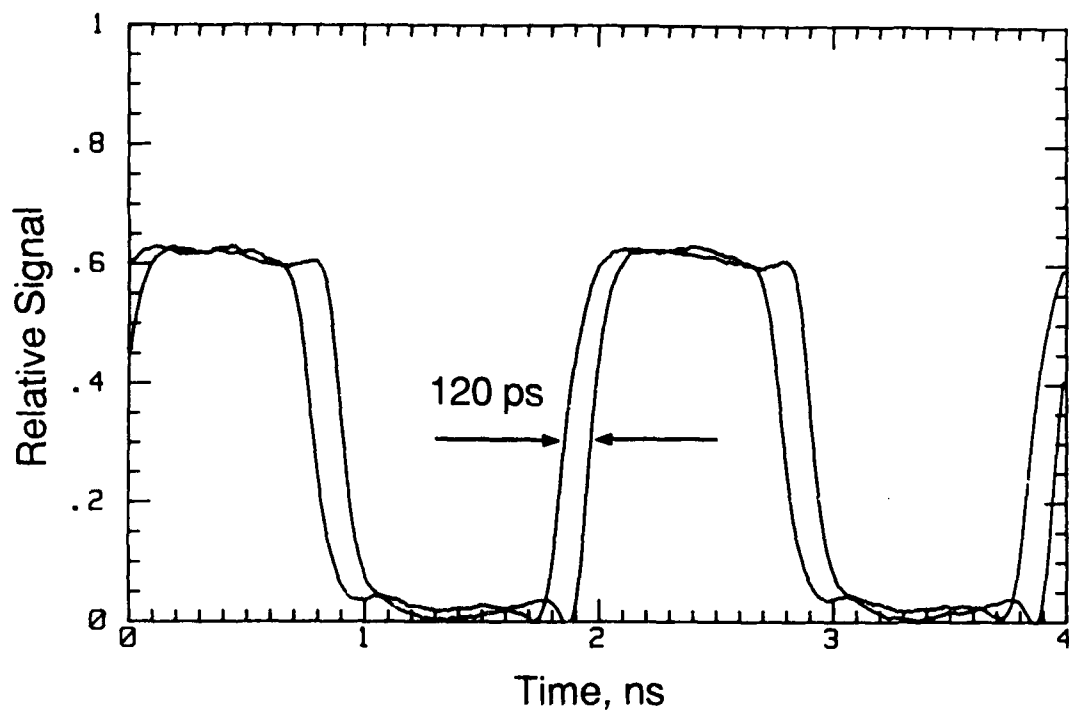


Fig. 4.4. Propagation delay through two inverters of an E/D MODFET inverter chain with a fan out loading of unity.

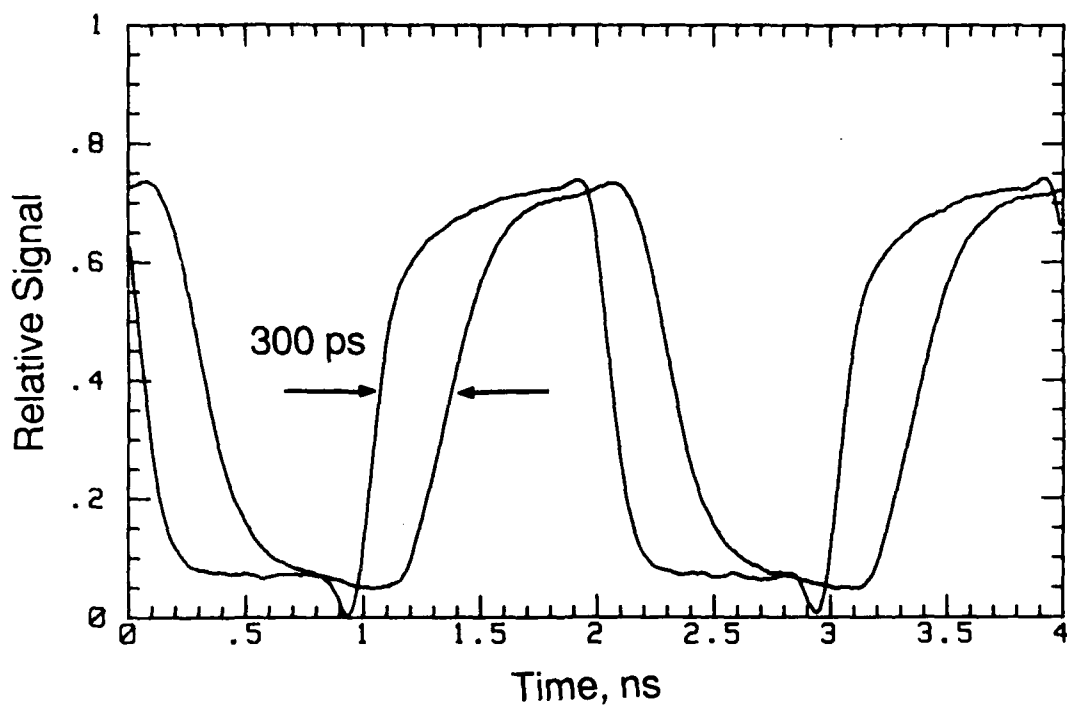


Fig. 4.5. Propagation delay through two inverters of an E/D MODFET inverter chain with the fan out loading increased to three.

#### 4.2.2. Frequency Dividers

A higher-level test circuit for IC performance is the static frequency divider, consisting of two flip-flops in a master-slave divide-by-two arrangement [4.4]. Testing this circuit is normally accomplished by increasing the clock rate of the divider until its divide-by-two output fails. The maximum clock frequency of the divider, set by the propagation delays through the master-slave feedback path, provide an indirect measure of the devices' speed.

Such a test circuit from Hughes Research Laboratories (Fig. 4.6), using  $0.2 \mu\text{m}$  e-beam written gates, molecular-beam epitaxy grown channels, air-bridge interconnects, and optimized feedback to achieve high frequency clock rates, was electrooptically tested. The dividers were implemented in two circuit families, buffered-FET logic (BFL), Fig. 4.7, and capacitively enhanced logic (CEL), Fig. 4.8. Conventional testing, using transmission line probes to drive the circuit and a spectrum analyzer to monitor its output, indicated correct circuit operation to 18 GHz. However, the spectrum analyzer data gives inconclusive evidence of correct divider operation, since it measures only the output frequency power and not its time waveform.

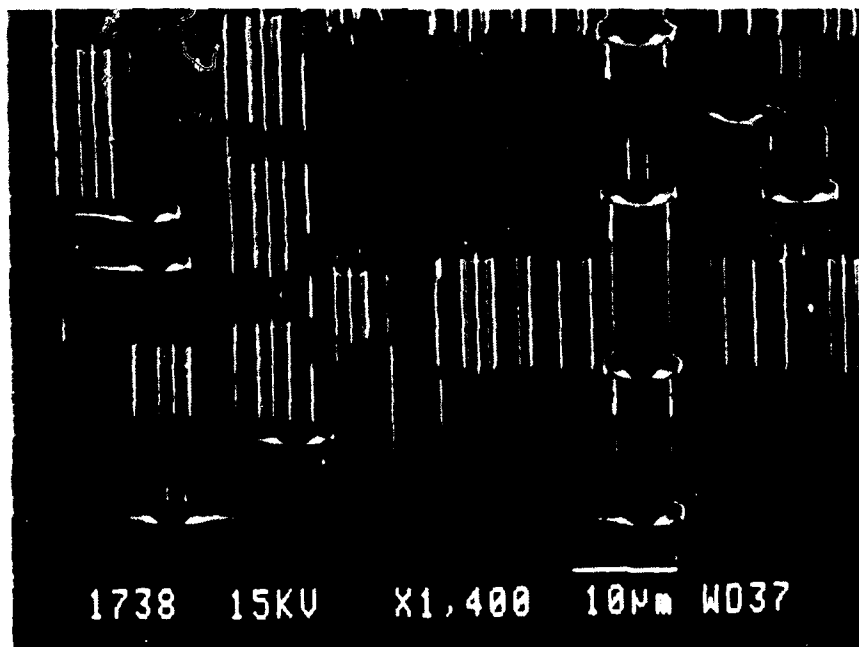


Fig. 4.6. SEM photo of a section of an 18 GHz static frequency divider, courtesy of J.F. Jensen, Hughes Research Laboratories [4.4]. The circuit uses  $0.2 \mu\text{m}$  electron-beam written gates, molecular-beam epitaxially-grown channels, air-bridge lines to reduce interconnect capacitance, and an optimized feedback to achieve high frequency clock rates.

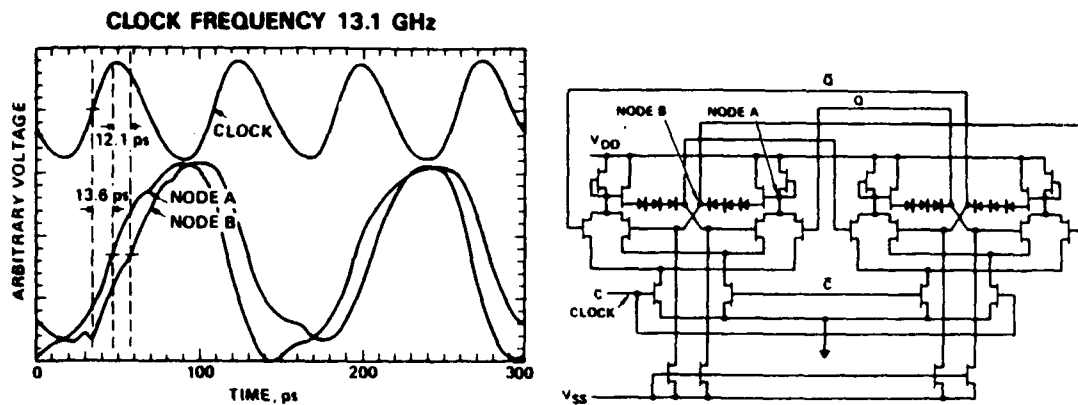


Fig. 4.7. Schematic diagram of a buffered-FET-logic static frequency divider showing the test points for the adjacent electrooptically measured data. The maximum frequency of operation, calculated as the inverse of twice the propagation delay through nodes A and B, is 19.4 GHz compared to 18.05 GHz measured with the spectrum analyzer.

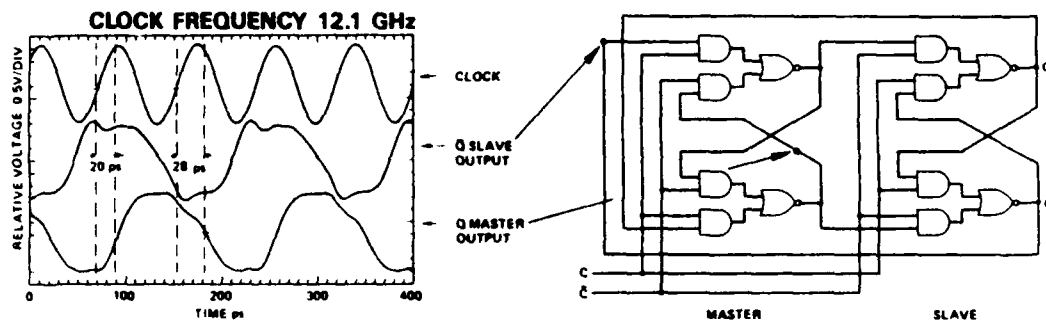


Fig. 4.8. Schematic diagram of a capacitively-enhanced-logic static frequency divider showing the test points for the adjacent electrooptically measured data. The maximum frequency of operation is calculated as 17.9 GHz from the measured propagation delays compared to 17.9 GHz measured with the spectrum analyzer.

By direct waveform measurements using electrooptic sampling, correct divide-by-two operation was verified, gate propagation delays of 20-30 ps were observed and correlated to maximum clock frequencies (Fig. 4.7 and 4.8), and the internal delays through the inverting and source-follower stages of individual BFL gates were identified [4.5]. Note that while the scaled 0.2  $\mu\text{m}$  gate-length FET's had significantly shorter delay through the inverting stage, the delay through the buffer stage was comparable to the 1  $\mu\text{m}$  PFL from LLNL. These data suggest the speed limitation through the buffer stage is no longer *tran-*



*sistor* limited but limited by the resistance-capacitance time constant of the level-shifting diode resistance and the input capacitance of the cascaded gates.

On dynamic dividers, a related type of test circuit, divide-by-two operation was electrooptically measured to a clock rate of 23 GHz (Fig. 4.9), and the timing of the propagation delays predicted the measured maximum frequency of operation [4.6].

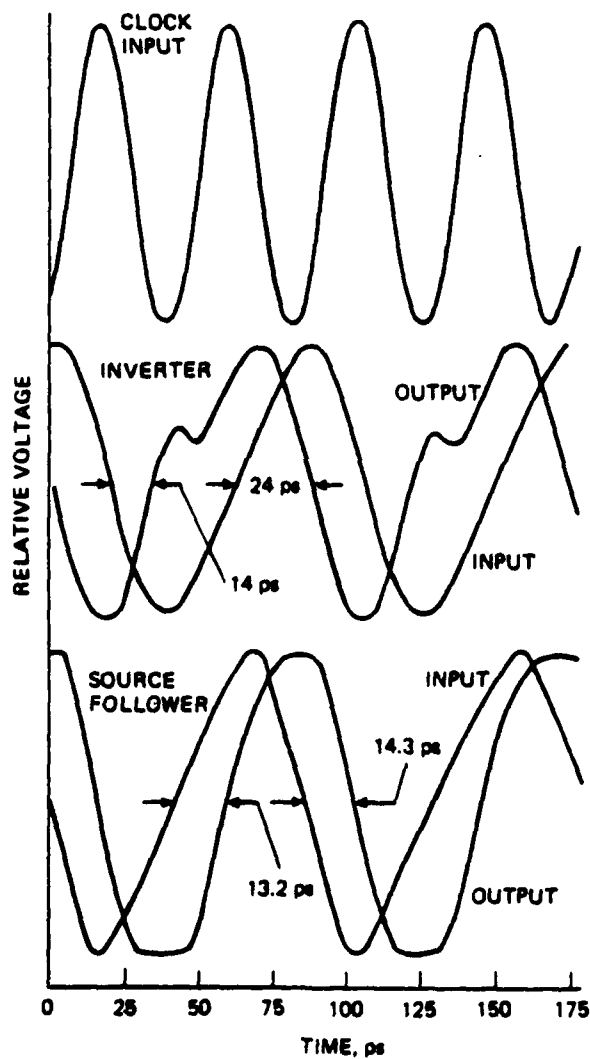


Fig. 4.9. Propagation delays through gates of a dynamic divider clocked at 23 GHz [4.6]. These propagation delays predict a maximum clock frequency of 26.1 GHz, compared to a measured maximum frequency of 26.58 GHz.

### 4.2.3. Other Digital IC's

The spatial resolution of the electrooptic sampler permits probing of MSI GaAs digital IC's to determine signal risetimes and timing. Figure 4.10 shows serial output waveform probed on a  $2\ \mu\text{m}$  width conductor internal to the output buffer in a 2.7 GHz 8-bit multiplexer/demultiplexer from Tri-Quint Semiconductor [4.7] and Fig. 4.11 shows the 8-phase clock waveforms probed on  $4\ \mu\text{m}$  width metal interconnects separated by  $6\ \mu\text{m}$ . Similar measurements have been made recently on gigahertz logic flip-flops and counters [4.8].

Preliminary electrooptic measurements have been made on voltage comparator circuits [4.9] implemented with heterojunction bipolar transistors (HBT's), to determine switching waveforms and signal levels. Applications of this type of circuit are in precision high-speed analog-to-digital converters and frequency dividers [4.10].

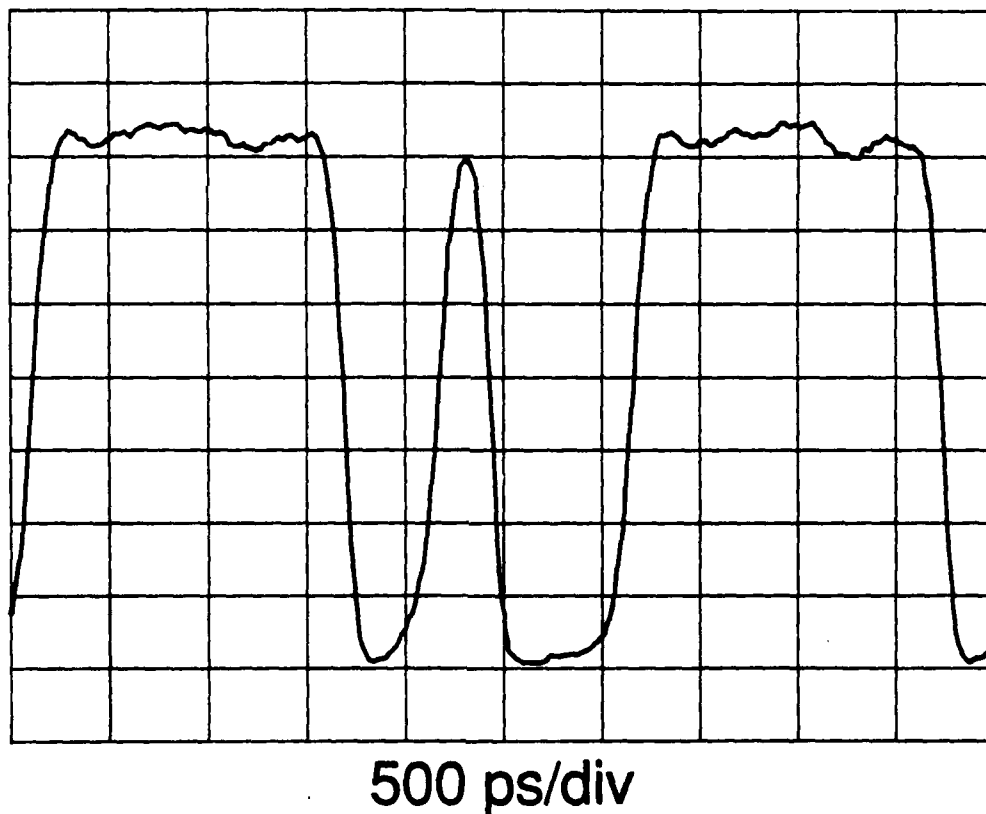


Fig. 4.10. Serial output waveform of a 2.7 GHz, 8-bit multiplexer [4.7] measured by electrooptic sampling. The data word is 11110100.

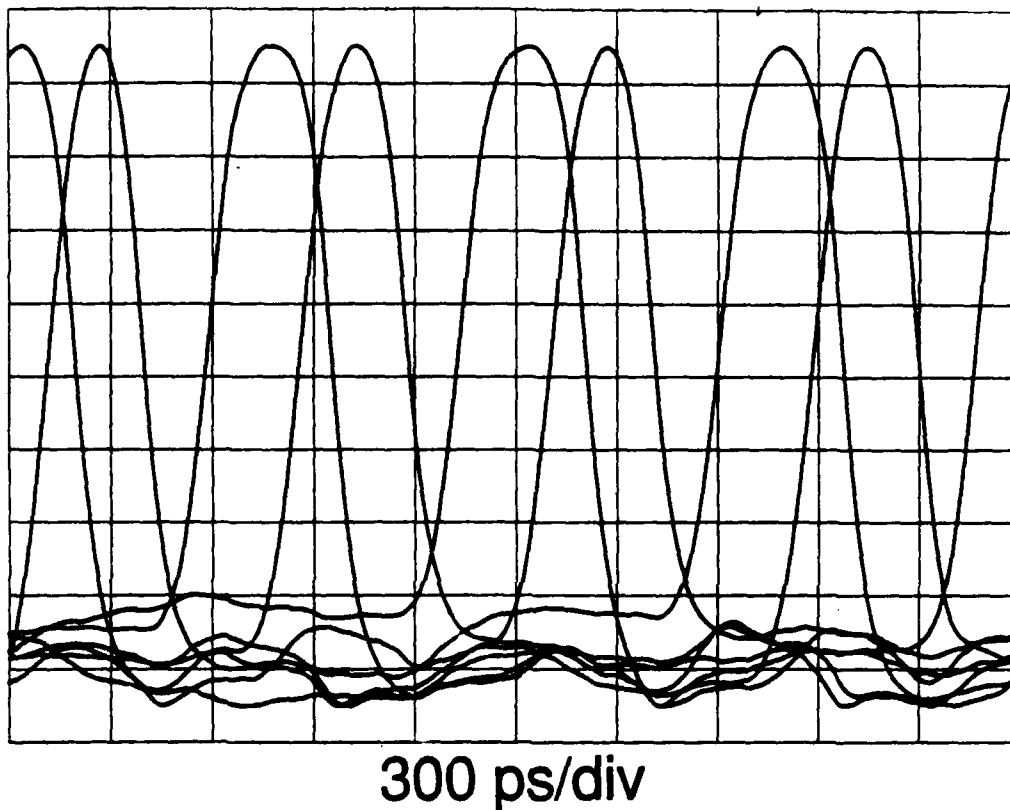


Fig. 4.11. Eight-phase clock waveforms on the multiplexer clocked at 2.7 GHz. An asymmetrical clock input results in timing skew in the 8-phase counter. These data were measured using the phase modulation technique discussed in Section 2.5.3.

### 4.3. Microwave Circuit Measurements

At microwave and millimeter-wave frequencies, where conductor lengths and circuit element sizes often become large with respect to the electrical wavelength, direct measurements of conductor voltages and currents are difficult, particularly with conventional electrical test instrumentation. Directional couplers and directional bridges separate the forward and reverse traveling waves on a transmission line. Standard microwave test instruments use these devices to measure the incident and reflected waves at the ports of a microwave device or network. The relationship between these waves is expressed as the *scattering parameters* [4.11]. The electrooptic sampler directly measures voltages, but not currents, preventing a direct measure of two-port parameters. However, measuring the voltage as a function of position with the optical probe [4.12], similar to a slotted-line measurement, permits calculation of the incident and reverse waves on the transmission lines connected to devices (Section 2.2.2 and Appendix B). From this information the scattering parameters can then be determined.

### 4.3.1. One-Port Measurements

The traveling-wave coefficients on lossless transmission lines are measured as described in Section 2.2.2 and Appendix B. For a one-port transmission line the ratio of the traveling wave coefficients  $V^+$  and  $V^-$  is the reflection coefficient  $\Gamma$ , or  $S_{11}$ , the return loss. An example of such a measured vector standing wave and the calculated reflection coefficient for an unterminated CPW transmission line at a drive frequency of 40 GHz is shown in Fig. 4.12, and a similar measurement with an matched load terminating the line at 20 GHz is shown in Fig. 4.13.

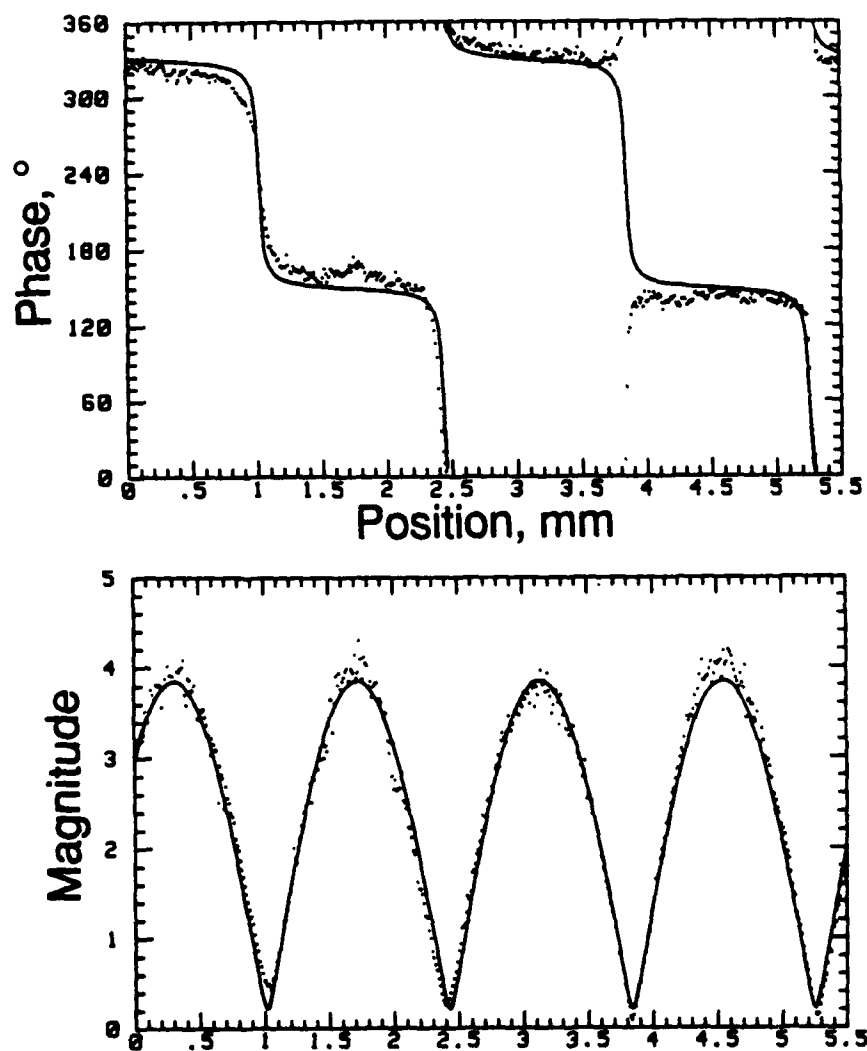


Fig. 4.12. 40 GHz voltage standing wave on an open-terminated GaAs coplanar waveguide transmission line, magnitude (top) and phase (bottom). The points are the data and the solid line is the fitted curve. From this measurement a reflection coefficient of 0.90 @  $-80^\circ$  is calculated. Note that each division of  $10^\circ$  in phase equals 0.7 ps in time.

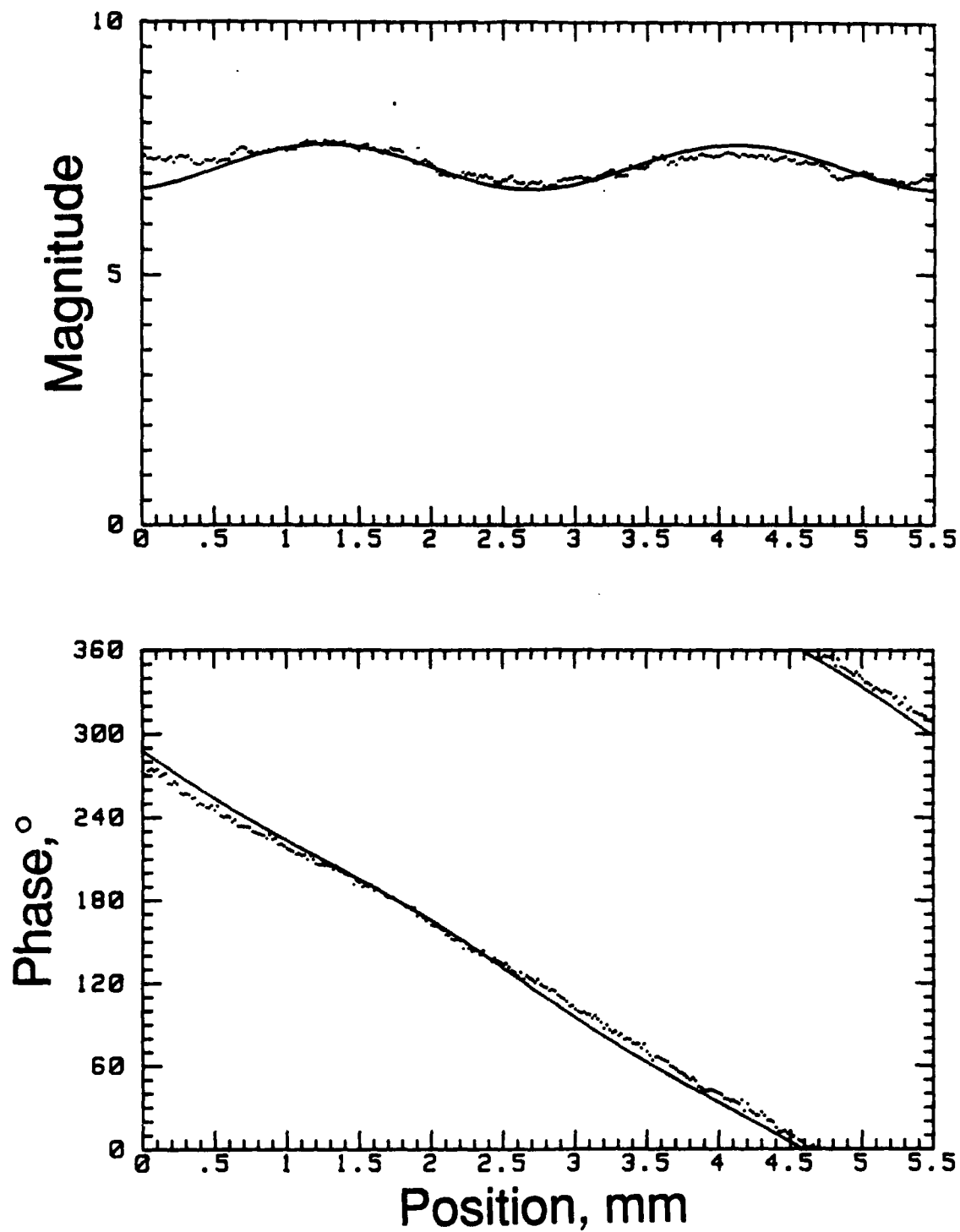


Fig. 4.13. 20 GHz voltage standing wave on a GaAs coplanar waveguide transmission line terminated in  $50 \Omega$  (nominally), magnitude (top) and phase (bottom). The points are the data and the solid line is the fitted curve. From this measurement a reflection coefficient of  $0.06 @ -160^\circ$  is calculated.

### 4.3.2. Two-port S-parameter Measurements

Extending the one-port measurement to calculate the incident and reflected waves on the input and output ports of a network allows for calculation of the S-parameters with a reference plane on the integrated circuit. Figure 4.14 shows a general test structure for S-parameter measurement, consisting of a device with transmission lines connected to its input and output. The  $a$ 's represent traveling waves propagating toward the DUT and the  $b$ 's represent traveling waves propagating away from the DUT. Applying an input signal, the electrooptic probe is scanned along the input and output transmission lines and the traveling wave coefficients are determined. With an ideal test structure, the transmission line characteristic impedance  $Z_0$  equals the load impedance  $Z_L$  and the S-parameters can be calculated directly from the measured traveling waves.

$$S_{11} = \left. \frac{b_1}{a_1} \right|_{a_2=0} \quad S_{21} = \left. \frac{b_2}{a_1} \right|_{a_2=0} \quad (4.1)$$

$$S_{12} = \left. \frac{b_1}{a_2} \right|_{a_1=0} \quad S_{22} = \left. \frac{b_2}{a_2} \right|_{a_1=0}$$

For example, with a drive signal applied to the input, any traveling wave  $b_2$  transmitted by the DUT is absorbed by the load, assuring  $a_2=0$ . However, in a practical test structure, the load impedance is determined by wafer probes with cabling or some other test fixture, and will not exactly match  $Z_0$ , resulting in a reflected wave  $a_2$ . The measured traveling waves must be corrected for this error term.

Figure 4.15 is an error model for the source and load mismatch of the test setup. With the drive signal applied to the input of the device, the actual S-parameters (designated by the  $a$  subscript) are

$$S_{11a} = \frac{b_{1f} - S_{12a} a_{2f}}{a_{1f}} \quad (4.2)$$

$$S_{21a} = \frac{b_{2f} - S_{22a} a_{2f}}{a_{1f}}$$

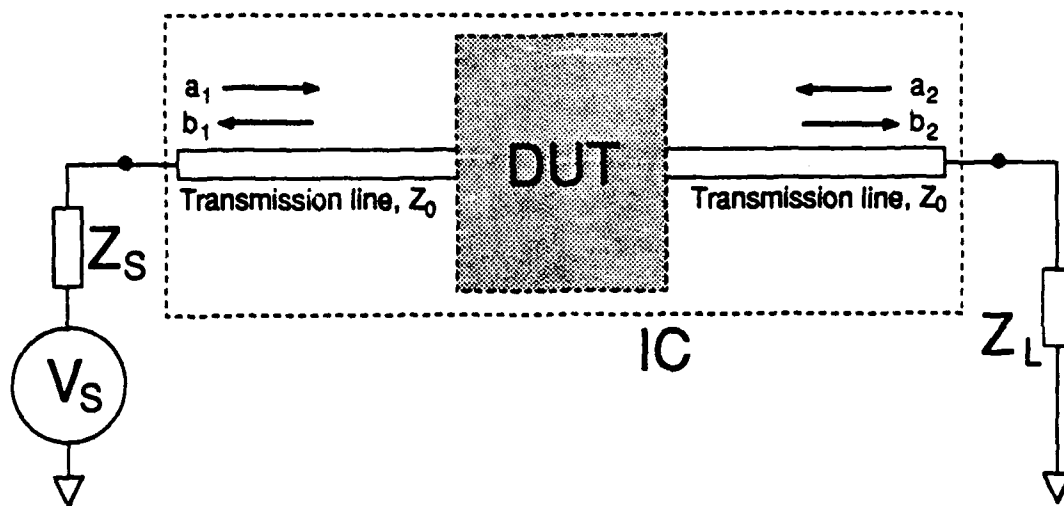


Fig. 4.14. Integrated circuit S-parameter test structure for the electrooptic probe.

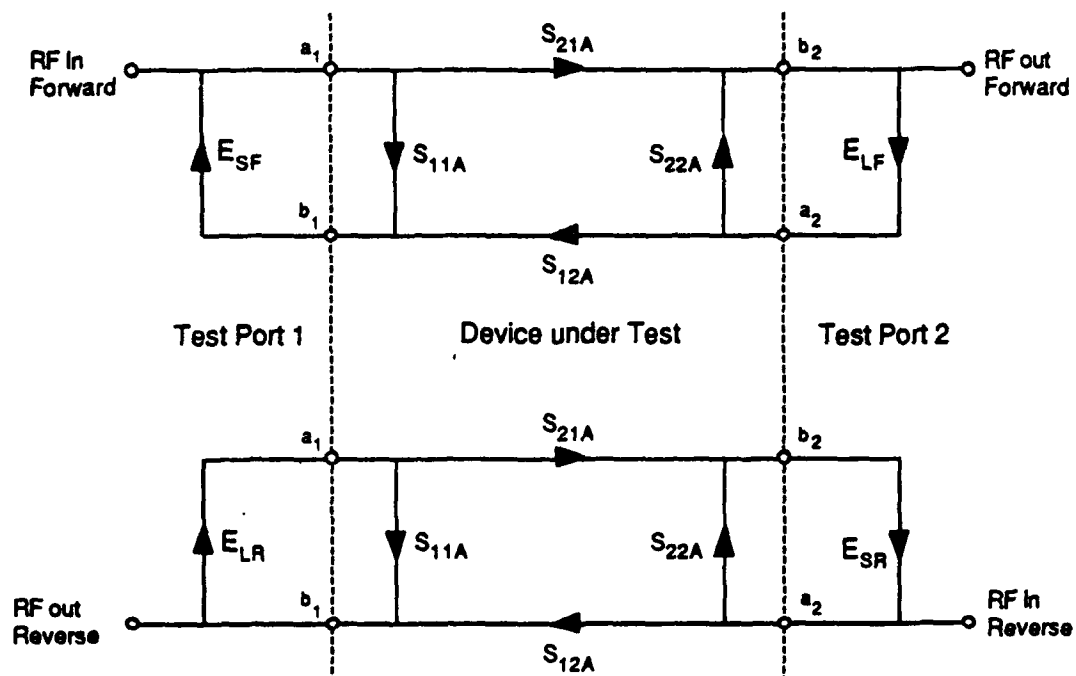


Fig. 4.15. Error model for the S-parameter test structure of Fig. 4.14. Only the forward and reverse load match, corrected for as shown in (4.5), contribute errors to the measurement.

where the  $f$  subscript indicates the drive signal is applied to the forward or input side of the DUT. Similarly, with the drive signal applied to the reverse (output) side of the DUT,

$$S_{22a} = \frac{b_{2r} - S_{21a} a_{1r}}{a_{2r}} \quad (4.3)$$

$$S_{12a} = \frac{b_{1r} - S_{11a} a_{1r}}{a_{2r}}$$

Now, the equations for  $S_{11a}$  can be substituted into the equation for  $S_{12a}$ , and vice versa, and  $S_{22a}$  can be substituted into the equation for  $S_{21a}$ , and vice versa, to obtain equations for the actual S-parameters in terms of the measured  $a$  and  $b$  values. The following defined variables are then substituted for ratios of the  $a$ 's and  $b$ 's

$$\begin{aligned} S_{11m} &= \frac{b_{1f}}{a_{1f}} & S_{12m} &= \frac{b_{1r}}{a_{2r}} \\ S_{21m} &= \frac{b_{2f}}{a_{1f}} & S_{22m} &= \frac{b_{2r}}{a_{2r}} \end{aligned} \quad (4.4)$$

$$E_{Lf} = \frac{a_{2f}}{b_{2f}} \quad E_{Lr} = \frac{a_{1r}}{b_{1r}}$$

where the  $m$  subscript represents the measured values of the S-parameters, with no error correction, and  $E_{Lf}$  and  $E_{Lr}$  are the forward and reverse load match, respectively. The resulting error equations for electrooptic probing are

$$\begin{aligned} S_{11a} &= \frac{S_{11m} - E_{Lf} S_{21m} S_{12m}}{1 - E_{Lf} E_{Lr} S_{21m} S_{12m}} \\ S_{22a} &= \frac{S_{22m} - E_{Lr} S_{21m} S_{12m}}{1 - E_{Lf} E_{Lr} S_{21m} S_{12m}} \\ S_{21a} &= \frac{S_{21m} (1 - E_{Lf} S_{21m} S_{12m})}{1 - E_{Lf} E_{Lr} S_{21m} S_{12m}} \\ S_{12a} &= \frac{S_{12m} (1 - E_{Lr} S_{21m} S_{12m})}{1 - E_{Lf} E_{Lr} S_{21m} S_{12m}} \end{aligned} \quad (4.5)$$



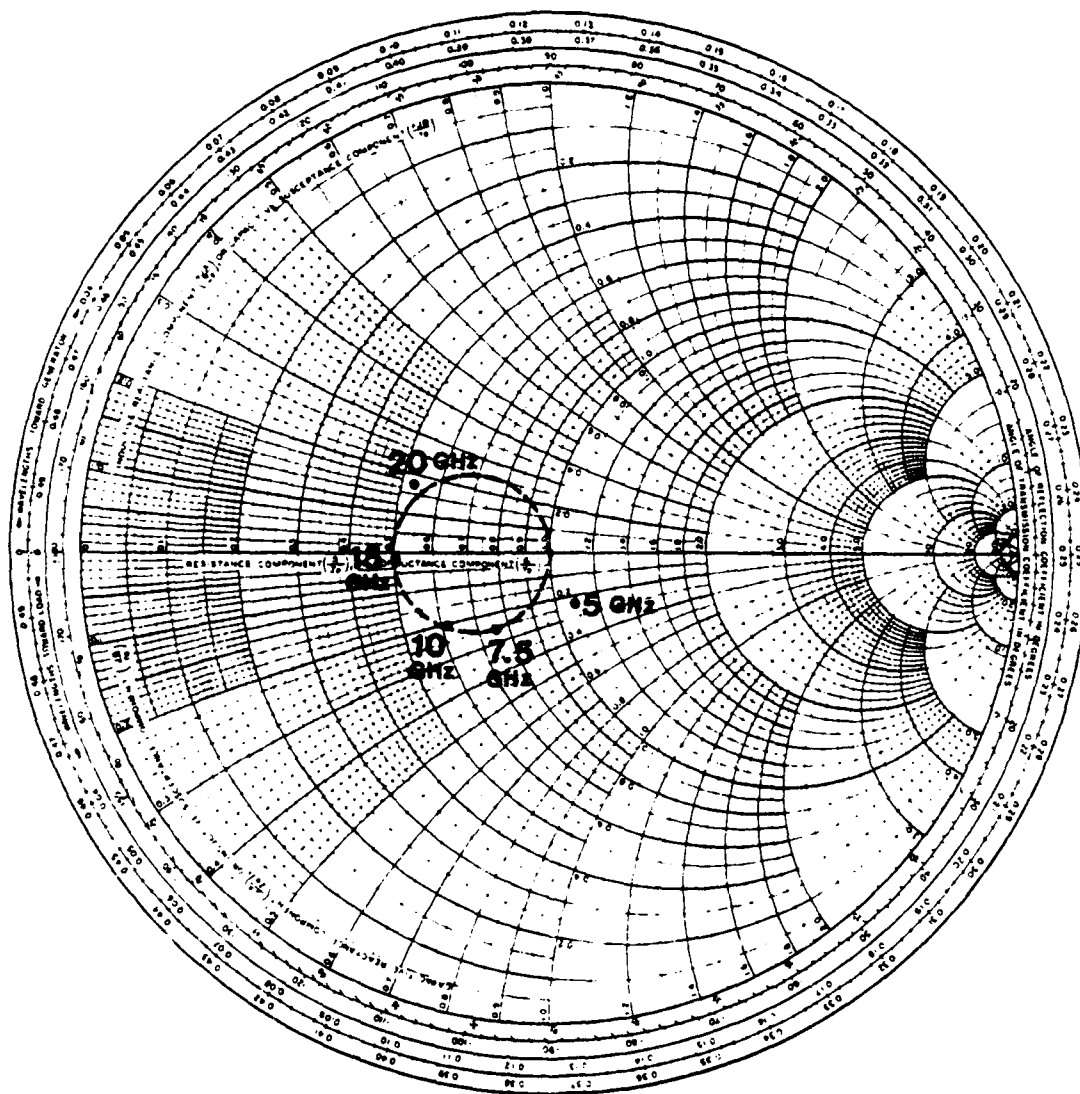


Fig. 4.16. Measured  $S_{11}$  for a test structure consisting of a section of  $35 \Omega$  CPW transmission line  $1600 \mu\text{m}$  in length with  $2500 \mu\text{m}$  length sections of  $50 \Omega$  CPW on its input and output. The dashed-line circle is the theoretical  $S_{11}$  for a  $35 \Omega$  transmission line.

Using this technique, the S-parameters of simple microwave test structures have been measured. Figure 4.16 shows the measured  $S_{11}$  for a test structure consisting of a section

of  $35 \Omega$  CPW transmission line  $1600 \mu\text{m}$  in length with  $2500 \mu\text{m}$  length sections of  $50 \Omega$  CPW on its input and output. The drive signal is applied to the input side, the probe beam is scanned along the input and output sections of  $50 \Omega$  line, the traveling waves are calculated, and  $S_{11m}$ ,  $S_{21m}$ , and  $E_{Lf}$  are determined. Then, the drive signal is applied to the output side, the probe beam is scanned along the same sections of  $50 \Omega$  line, the traveling waves are calculated, and  $S_{22m}$ ,  $S_{12m}$ , and  $E_{Lr}$  are determined. Finally, the corrected S-parameters are calculated using (4.5).

This technique has several important features for S-parameter measurements. First, the measurement is on-chip, with the phase reference points determined by the probe beam position with respect to the DUT. Secondly, the technique requires no separate calibration standards, such as precision  $50 \Omega$  terminations, opens, and shorts required with conventional network analyzers. The calibration standard by which the S-parameters are defined is the characteristic impedance  $Z_0$  of the input and output transmission lines. The accuracy and repeatability these lines, integrated into the IC fabrication, can be precisely controlled. Finally, the optical system's bandwidth allows measurements into the millimeter-wave frequency range.

A disadvantage of this approach is the size of transmission lines required, which use valuable space on the IC. Roughly an eighth of a wavelength is required to make a reasonable measurement with the optical system's current level of (multiplicative) intensity noise. Also, the intensity noise sets an effective directivity slightly more than 20 dB. Stabilizing the laser intensity noise will improve the S-parameter measurement performance and allow for measurements on shorter sections of transmission line.

#### 4.3.3. Potential Mapping for Circuit Modeling

The optical probe can be used to map the vector potential on and around IC conductors. For example, the magnitude and phase transverse to a microstrip transmission (Fig. 4.17) shows the falloff from the conductor and a change in phase indicative of a non-TEM<sub>00</sub> mode. The wavelength on a conductor can be directly measured, to characterize dispersion or measure the change in wavelength between different waveguide modes, such as the even and odd modes of CPW [4.13]. One proposal was recently published [4.14] for field mapping by varying the angle of incidence of the probe beam to obtain information allowing calculation of the three-dimensional field. The experimental feasibility of this technique, however, remains to be demonstrated.

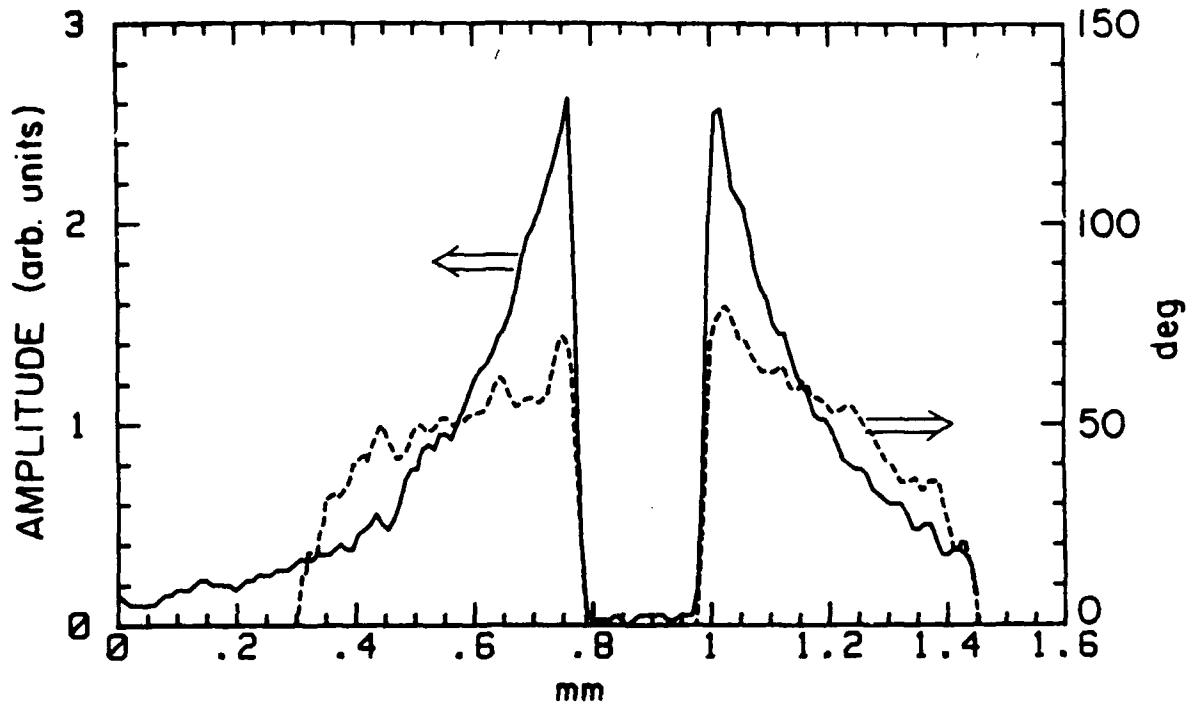


Fig. 4.17. Transverse potential measured on a GaAs microstrip at a drive frequency of 30 GHz. The magnitude shows the falloff in the potential and the curvature to the phase is indicative of non-TEM mode propagation.

#### 4.3.4. Microwave Amplifiers

On GaAs microwave amplifiers and similar MMIC's, the propagation of microwave signals internal to the circuit can be measured. Figure 4.18 is a monolithic 2-18 GHz MESFET distributed amplifier from Varian Research Labs [4.15,16] with coplanar-waveguide transmission line interconnects. In the distributed amplifier, a series of small transistors are connected between two high-impedance transmission lines. The high-impedance lines and the FET input and output capacitances together form a synthetic transmission lines of 50  $\Omega$  characteristic impedance. Series stubs are used in the drain circuit, equalizing the phase velocities of the two lines and providing some matching between the low impedance of the output line and the higher output impedances of the FET's at high frequencies, peaking the gain.

Measurements to better understand the circuit's operation include the relative drive levels to each FET as influenced by the loss and cutoff frequency of the synthetic gate line, the small-signal voltage at the drain of each FET, and identification of signal saturation leading to amplifier gain compression. Figure 4.19 shows the electrooptically measured

small-signal gate voltages versus frequency for the CPW distributed amplifier. The rolloff beyond 18 GHz is due to the cutoff frequency of the periodically-loaded gate line, the slow rolloff with frequency is due to the gate line attenuation arising from the FET input conductance, and the ripples with frequency are due to standing waves resulting from mitermination of the gate line (the load resistance was not equal to the synthetic line's characteristic impedance due to a fabrication variance).

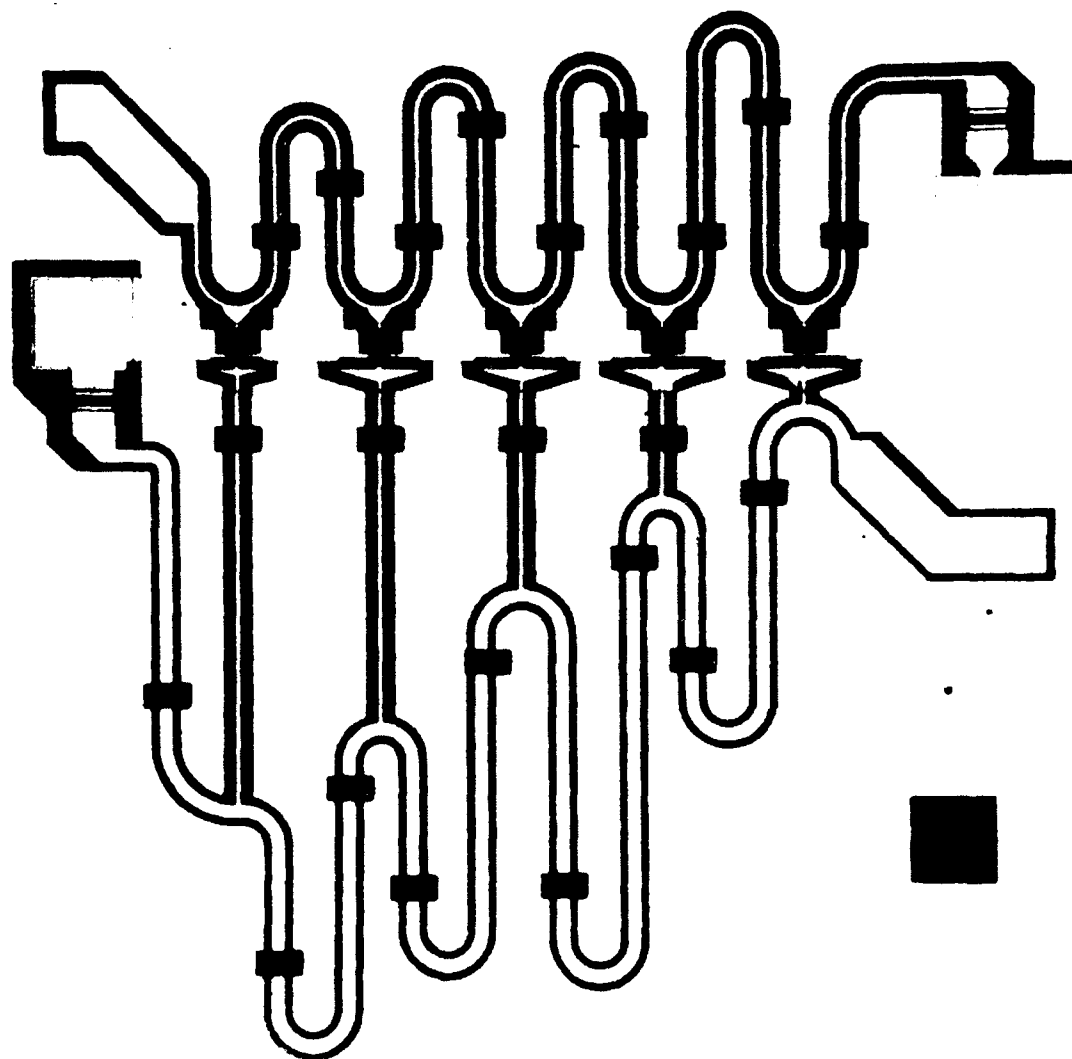


Fig. 4.18. Distributed amplifier using coplanar waveguide transmission line interconnects [4.13]. Photo courtesy of M. Riazat, Varian Research Center.

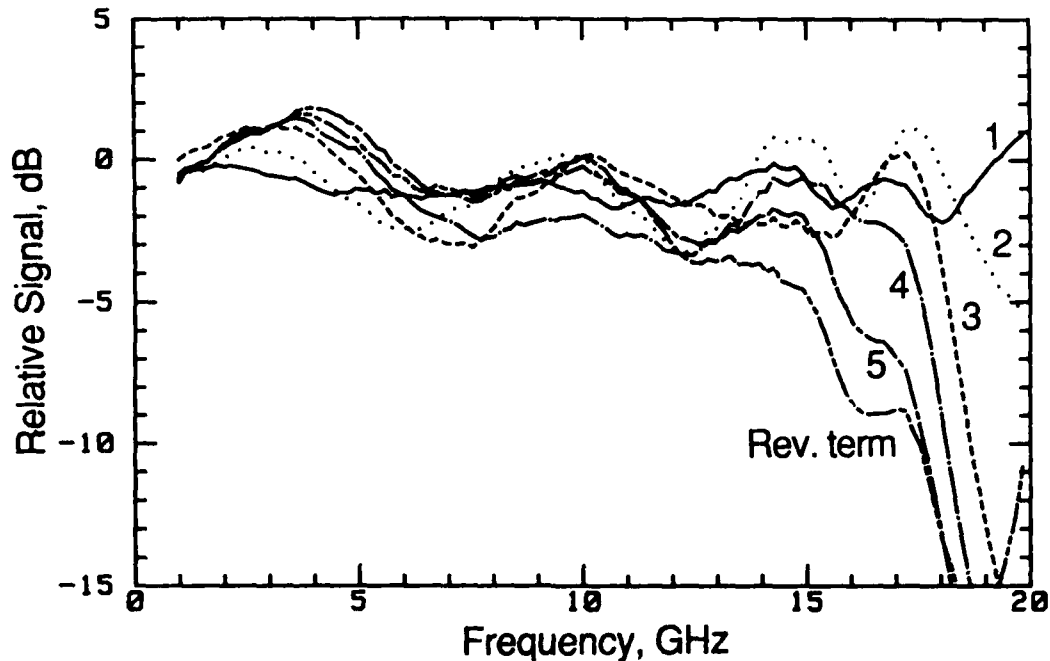
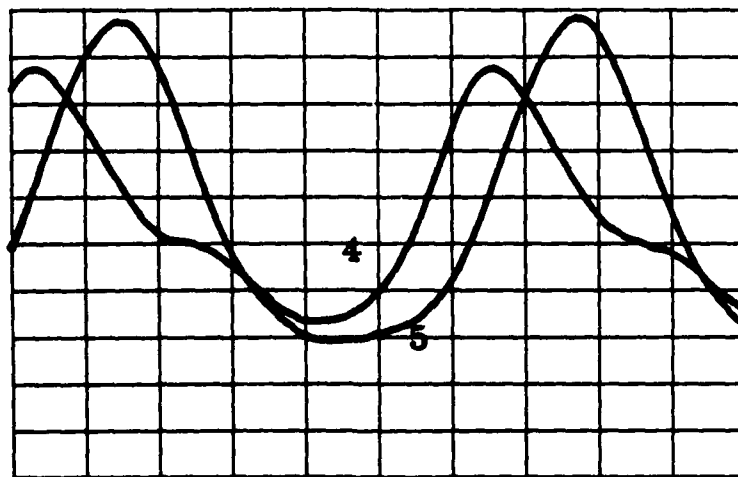


Fig. 4.19. Small-signal voltages on the coplanar 2-18 GHz distributed amplifier of Fig. 4.18, at the five gates and at the gate line termination resistor.

Figure 4.20 shows the voltage waveforms at drains 4 and 5 of a microstrip distributed amplifier operated at 10 GHz and 7 dBm input power, the 1 dB gain compression point. For this amplifier at frequencies above 5 GHz, gain saturation is predominantly from drain saturation (i.e. reduction of  $V_{dg}$  the gate to drain voltage to the point where the drain end of the channel is no longer pinched off) of the fourth and fifth FET's. Saturation at drive frequencies as high as 21 GHz has been observed, as in Fig. 4.21.

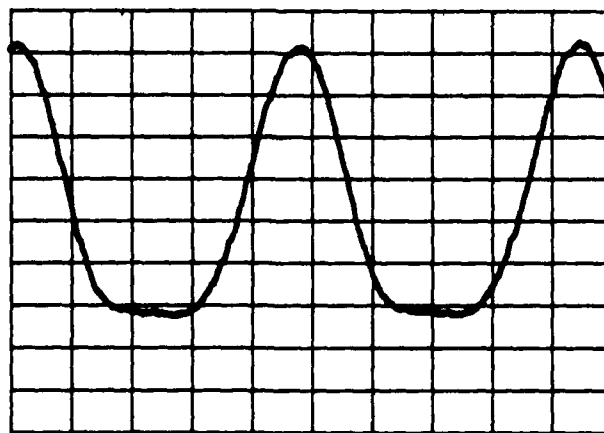
#### 4.3.5. Nonlinear Transmission Line

The capabilities of the electrooptic sampler are essential for measuring electrical signals with less than 10 ps transients, because both its intrinsic time resolution, and its on-chip probing capability to avoid the difficult problem of propagating picosecond signals from the IC to coaxial connectors. In an ongoing research project in Ginzton Laboratories, GaAs IC structures are being fabricated to generate picosecond switching signals [4.17]. The structure consists of a transmission line periodically loaded with Schottky diodes from center conductor to ground. The nonlinear, voltage-dependent capacitance of the diodes creates a propagation velocity on the transmission line that depends on the signal voltage.



16 ps/div.

Fig. 4.20. Saturation at drains 4 and 5 of a microstrip distributed amplifier at a drive frequency of 10 GHz and 7 dBm input power, the amplifier's 1 dB compression point.



10 ps/div.

Fig. 4.21. Saturation at drain 3 of a microstrip distributed amplifier at 21 GHz drive frequency.

With the diode polarity in the fabricated structures, more negative voltages travel at a slower speed, so that the falltime of a negative voltage swing decreases as the signal propagates down the line.

On the first such structure fabricated, consisting of 42 diodes uniformly separated by  $160\ \mu\text{m}$  on a CPW transmission line and fabricated with  $10\ \mu\text{m}$  design rules, signal falltimes of 7.8 ps (Fig. 4.22) were measured with the electrooptic sampler and an falltime compression factor of 3.7 (Fig. 4.23) was measured with two cascaded lines. The series resistance of the shunt diodes was found to be the limiting factor in the signal falltime, and a second design to reduce the diode resistance has generated falltimes of 5 ps. Further scaling of the structure should allow for signal falltimes approaching one picosecond.

#### 4.4. Summary

This chapter presented measurements made with the optical probe to characterize the speed and response of a number of digital and analog IC's. A wide variety of circuit types, such as ion-implanted MESFET's, MBE-grown MESFET's, MODFET's, and HBT's, have been electrooptically probed.

On digital IC's, signal propagation delays and risetimes were measured on test circuits such as inverter chains and frequency dividers. The propagation delays in the frequency dividers were correlated to the circuits' maximum clock frequency operation. On a multiplexer circuit of medium-scale integration complexity, the multiplexed output signal and timing of the 8-phase clock were measured. In addition to quantitative signal timing measurements, the capability to measure time waveforms in order to verify large-signal switching at internal nodes is an important feature for testing digital IC's at multi-gigahertz clock rates.

For small-signal microwave measurements, a method to measure S-parameters was described. One-port measurements of standing wave ratios to 40 GHz drive frequency and initial measurements of the insertion loss of a simple microwave test structure were made. On distributed amplifiers, the small-signal internal-node response was measured, allowing observation of gate line cutoff, attenuation, and standing waves from a mismatched termination. Large-signal measurements were made on the distributed amplifiers to determine their saturation mechanisms, and on nonlinear transmission lines to measure generation of 7.8 ps signal falltimes.

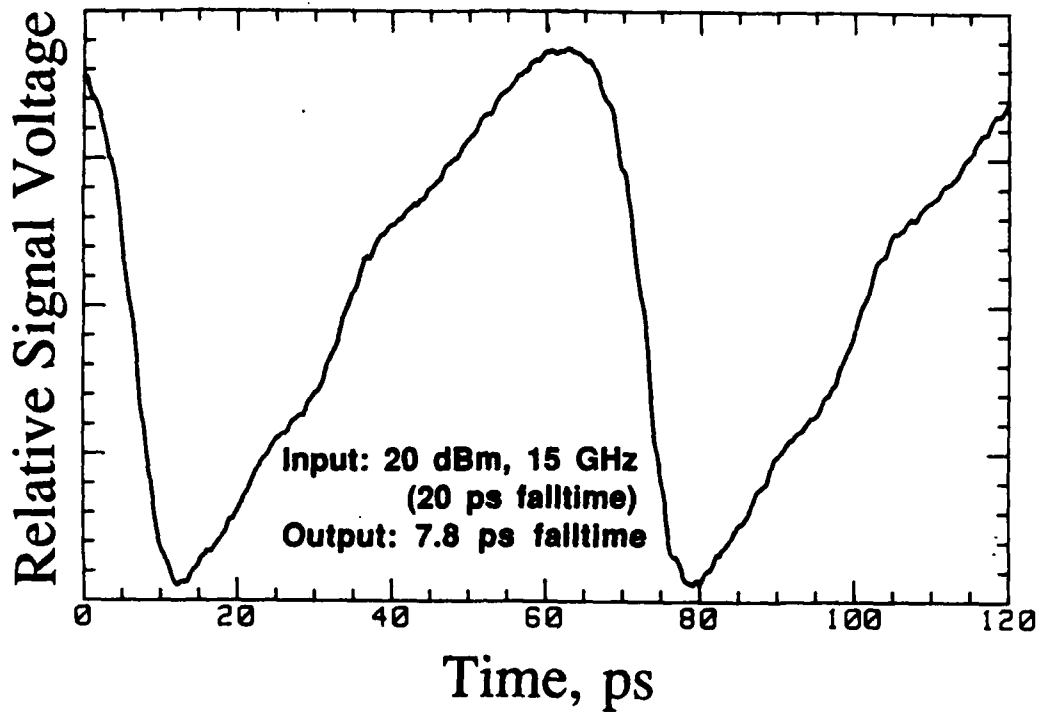


Fig. 4.22. Shock-wave formation/falltime compression on the nonlinear transmission line with a sinusoidal input waveform.

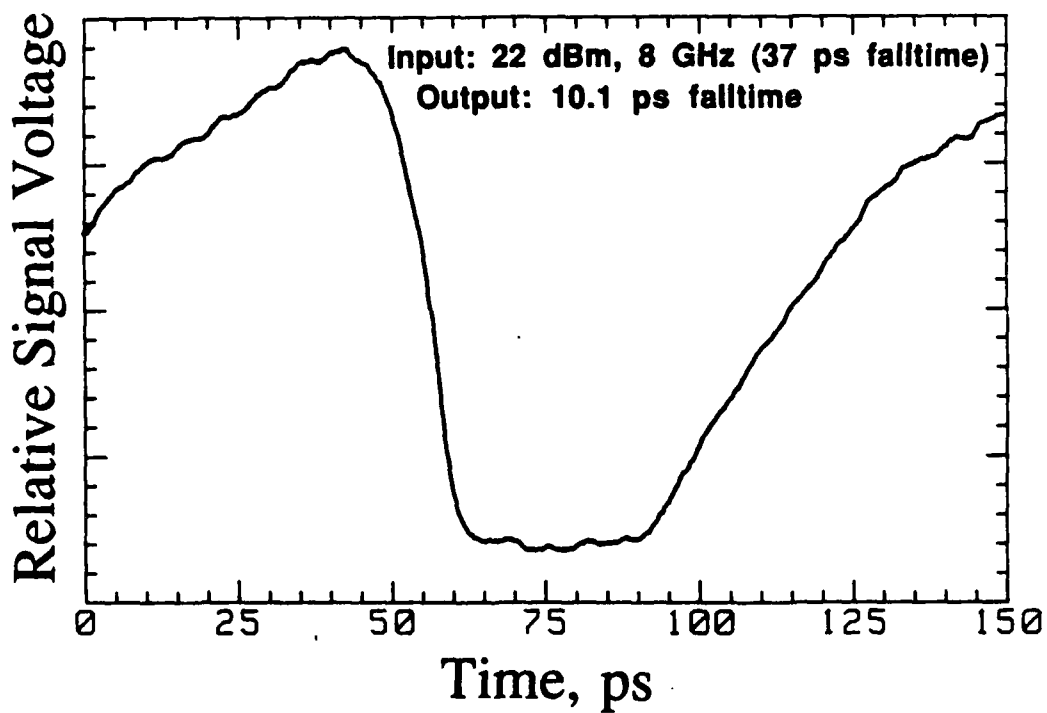


Fig. 4.23. Shock-wave formation/falltime compression on two cascaded nonlinear transmission lines.



#### 4.5. References for Chapter 4

- 4.1 S. Swierkowski, K. Mayeda, and C. McConaghy, "A sub-200 picosecond GaAs sample-and-hold circuit for a multi-gigasample/second integrated circuit," *Technical Digest of the 1985 International Electron Devices Meeting*, pp. 272-275
- 4.2 M.J.W. Rodwell, K.J. Weingarten J.L. Freeman, and D.M. Bloom, "Gate propagation delay and logic timing of GaAs integrated circuits measured by electrooptic sampling," *Elect. Lett.*, vol. 22, pp. 499-501, 1986
- 4.3 X.-C. Zhang and R. K. Jain, "Measurement of on-chip waveforms and pulse propagation in digital GaAs integrated circuits by picosecond electro-optic sampling," *Elect. Lett.*, vol. 22, pp. 264-265, 1986
- 4.4 J.F. Jensen, L.G. Salmon, D.S. Deakin, and M.J. Delaney, "Ultrahigh-speed GaAs static frequency dividers," *Technical Digest of the 1987 International Electron Devices Meeting*, pp. 476-479
- 4.5 J.F. Jensen, K.J. Weingarten, and D.M. Bloom, "Development of 18 GHz static frequency dividers and their evaluation by electrooptic sampling," *Picosecond Electronics and Optoelectronics*, New York: Springer-Verlag, 1987
- 4.6 J.F. Jensen, L.G. Salmon, D.S. Deakin, and M.J. Delaney, "26 GHz GaAs room-temperature dynamic divider circuit," *Proceedings of the 1987 GaAs IC Symposium*, Portland, Oregon, pp. 201-204
- 4.7 G.D. McCormack, A.G. Rode, and E.W. Strid, "A GaAs MSI 8-bit Multiplexer and Demultiplexer," *Proceedings of the 1982 GaAs IC Symposium*, pp. 25-28
- 4.8 X.-C. Zhang, R.K. Jain, and R.M. Hickling, "Electrooptic sampling analysis of timing patterns at critical internal nodes in GigaBit GaAs multiplexers/demultiplexers," *Picosecond Electronics and Optoelectronics*, New York: Springer-Verlag, 1987
- 4.9 K.C. Wang, P.M. Asbeck, D.L. Miller, and F.H. Eisen, "Voltage comparators implemented with GaAs/(GaAl)As heterojunction bipolar transistors," *Elect. Lett.*, vol. 21, pp. 807-808, 1985
- 4.10 K.C. Wang, P.M. Asbeck, M.F. Chang, G.J. Sullivan, and D.L. Miller, "A 20 GHz frequency divider implemented with heterojunction bipolar transistors," *IEEE Elec. Dev. Lett.*, vol. EDL-8, pp. 383-385, 1987
- 4.11 R.E. Collins, *Foundations of Microwave Engineering*, New York: McGraw-Hill, 1966
- 4.12 K.J. Weingarten, M.J.W. Rodwell, J.L. Freeman, S.K. Diamond, and D.M. Bloom, "Electrooptic sampling of gallium arsenide integrated circuits," *Ultrafast Phenomena V*, ed. by G.R. Fleming and A.E. Siegman, Springer Ser. Chem. Phys., Vol. 46, New York: Springer-Verlag, 1986, pp. 98

- 
- 4.13 R. Majidi-Ahy, K.J. Weingarten, M. Riazat, B.A. Auld, and D.M. Bloom, "Electrooptic sampling measurement of coplanar waveguide (coupled slot line) modes," *Elect. Lett.*, vol. 23, 1987
- 4.14 Y.H. Lo, M.C. Wu, Z.H. Zhu, S.Y. Wang, and S. Wang, "Proposal for three-dimensional internal field mapping by cw electro-optic probing," *Appl. Phys. Lett.*, vol. 50, pp. 1791-1793, 1987
- 4.15 M.J.W. Rodwell, M. Riazat, K.J. Weingarten, B.A. Auld, and D.M. Bloom, "Internal microwave propagation and distortion characteristics of travelling-wave amplifiers studied by electro-optic sampling," *IEEE Trans. Microwave Theory Tech.*, vol. MTT-34, pp. 1356-1362, 1986
- 4.16 G. Zdasiuk, M. Riazat, R. LaRue, C. Yuen, and S. Bandy, "Enhanced performance ultrabroadband distributed amplifiers," *Picosecond Electronics and Optoelectronics*, New York: Springer-Verlag, 1987
- 4.17 M.J.W. Rodwell, "Picosecond electrical wavefront generation and picosecond optoelectronic instrumentation," *Ph.D. Thesis*, Stanford University, Stanford, CA, 1987.